Determination and understanding of the role of alloying elements on the passive behavior of Ni-based alloys by electrochemical investigation

Zhiheng Zhang

To cite this version:

Zhiheng Zhang. Determination and understanding of the role of alloying elements on the passive behavior of Ni-based alloys by electrochemical investigation. Materials. Université de Lyon, 2021. English. NNT : 2021LYSEI050 . tel-03394931

HAL Id: tel-03394931

https://theses.hal.science/tel-03394931v1

Submitted on 22 Oct 2021

N°d'ordre
NNT:2021LYSEI050

THESE de DOCTORAT DE L'UNIVERSITE DE LYON

opérée au sein de
L'Institut National des Sciences Appliquées de Lyon

Ecole Doctorale N° ED34
L'École Doctorale Matériaux de Lyon

Spécialité : Science et génie des matériaux

Soutenue publiquement le 19/07/2021, par :
Zhiheng Zhang

Determination and understanding of the role of alloying elements on the passive behavior of Ni-based alloys by electrochemical investigation

---

Devant le jury composé de :

PEBERE, Nadine	Directrice de Recherche	CNRS (CIRIMAT), Toulouse	Rapporteur
BOJINOV, Martin	Professeur des Universités	University of Chemical Technology and Metallurgy, Sofia (Bulgaria)	Rapporteur
MARCUS, Philippe	Directeur de Recherche	CNRS (Chimie ParisTech), Paris	Président du jury
COUET, Adrien	Maître de Conférences	University of Wisconsin –Madison, Madison (USA)	Examinateur
NORMAND, Bernard	Professeur des Universités	INSA de Lyon, Villeurbanne	Directeur de thèse
TER-OVANESSIAN, Benoît	Maître de Conférences	INSA de Lyon, Villeurbanne	Co-directeur de thèse
MARCELIN, Sabrina	Ingénieure de Recherche	INSA de Lyon, Villeurbanne	Invitée

Département FEDORA – INSA Lyon - Ecoles Doctorales

SIGLE	ECOLE DOCTORALE	NOM ET COORDONNEES DU RESPONSABLE
CHIMIE	**CHIMIE DE LYON** **https://www.edchimie-lyon.fr** Sec. : Renée EL MELHEM Bât. Blaise PASCAL, 3e étage secretariat@edchimie-lyon.fr	**M. Stéphane DANIELE** C2P2-CPE LYON-UMR 5265 Bâtiment F308, BP 2077 43 Boulevard du 11 novembre 1918 69616 Villeurbanne **directeur@edchimie-lyon.fr**
E.E.A.	**ÉLECTRONIQUE, ÉLECTROTECHNIQUE, AUTOMATIQUE** **https://edeea.universite-lyon.fr** Sec. : Stéphanie CAUVIN Bâtiment Direction INSA Lyon Tél : 04.72.43.71.70 secretariat.edeea@insa-lyon.fr	**M. Philippe DELACHARTRE** INSA LYON Laboratoire CREATIS Bâtiment Blaise Pascal, 7 avenue Jean Capelle 69621 Villeurbanne CEDEX Tél : 04.72.43.88.63 **philippe.delachartre@insa-lyon.fr**
E2M2	**ÉVOLUTION, ÉCOSYSTÈME, MICROBIOLOGIE, MODÉLISATION** **http://e2m2.universite-lyon.fr** Sec. : Sylvie ROBERJOT Bât. Atrium, UCB Lyon 1 Tél : 04.72.44.83.62 secretariat.e2m2@univ-lyon1.fr	**M. Philippe NORMAND** Université Claude Bernard Lyon 1 UMR 5557 Lab. d'Ecologie Microbienne Bâtiment Mendel 43, boulevard du 11 Novembre 1918 69 622 Villeurbanne CEDEX **philippe.normand@univ-lyon1.fr**
EDISS	**INTERDISCIPLINAIRE SCIENCES-SANTÉ** **http://ediss.universite-lyon.fr** Sec. : Sylvie ROBERJOT Bât. Atrium, UCB Lyon 1 Tél : 04.72.44.83.62 secretariat.ediss@univ-lyon1.fr	**Mme Sylvie RICARD-BLUM** Institut de Chimie et Biochimie Moléculaires et Supramoléculaires (ICBMS) - UMR 5246 CNRS - Université Lyon 1 Bâtiment Raulin - 2ème étage Nord 43 Boulevard du 11 novembre 1918 69622 Villeurbanne Cedex Tél : +33(0)4 72 44 82 32 **sylvie.ricard-blum@univ-lyon1.fr**
INFOMATHS	**INFORMATIQUE ET MATHÉMATIQUES** **http://edinfomaths.universite-lyon.fr** Sec. : Renée EL MELHEM Bât. Blaise PASCAL, 3e étage Tél : 04.72.43.80.46 infomaths@univ-lyon1.fr	**M. Hamamache KHEDDOUCI** Université Claude Bernard Lyon 1 Bât. Nautibus 43, Boulevard du 11 novembre 1918 69 622 Villeurbanne Cedex France Tél : 04.72.44.83.69 **hamamache.kheddouci@univ-lyon1.fr**
Matériaux	**MATÉRIAUX DE LYON** **http://ed34.universite-lyon.fr** Sec. : Yann DE ORDENANA Tél : 04.72.18.62.44 yann.de-ordenana@ec-lyon.fr	**M. Stéphane BENAYOUN** Ecole Centrale de Lyon Laboratoire LTDS 36 avenue Guy de Collongue 69134 Ecully CEDEX Tél : 04.72.18.64.37 **stephane.benayoun@ec-lyon.fr**
MEGA	**MÉCANIQUE, ÉNERGÉTIQUE, GÉNIE CIVIL, ACOUSTIQUE** **http://edmega.universite-lyon.fr** Sec. : Stéphanie CAUVIN Tél : 04.72.43.71.70 Bâtiment Direction INSA Lyon mega@insa-lyon.fr	**M. Jocelyn BONJOUR** INSA Lyon Laboratoire CETHIL Bâtiment Sadi-Carnot 9, rue de la Physique 69621 Villeurbanne CEDEX **jocelyn.bonjour@insa-lyon.fr**
ScSo	**ScSo*** **https://edsciencessociales.universite-lyon.fr** Sec. : Mélina FAVETON INSA : J.Y. TOUSSAINT Tél : 04.78.69.77.79 melina.faveton@univ-lyon2.fr	**M. Christian MONTES** Université Lumière Lyon 2 86 Rue Pasteur 69365 Lyon CEDEX 07 **christian.montes@univ-lyon2.fr**

*ScSo : Histoire, Géographie, Aménagement, Urbanisme, Archéologie, Science politique, Sociologie, Anthropologie

《 Ne jamais dire jamais, il y a toujours quelque chose à tenter. 》

-Le film 'Les Choristes'

Abstract

Ni-based alloys are widely used in various engineering applications, such as oil and gas, nuclear power plant and chemical process, due to their excellent corrosion resistance and good mechanical properties at elevated temperature. To extend the sustainability and the versatility of Ni-based alloys, development of new grades or improvement of the existing ones is still ongoing. To carry out the alloy design, the study on the role of alloying elements on nickel-based alloys properties and corrosion resistance remains the best scientific approach. Within this framework, the main objective of this thesis is to develop a methodology based on electrochemical characterization and analysis for understanding the role of the alloying elements on the corrosion behavior and on the passive film properties of Ni-based alloys. The proposed methodology relies on successive electrochemical impedance spectroscopy measurements and advanced analyses of the impedance data, to follow the evolution of the passive film properties grown on different binary (Ni-Cr) and ternary (Ni-Cr-Fe) alloys at different potentials. The obtained impedance diagrams were interpreted with enhanced graphical method and fitted with Power-Law Model for giving physical meanings to passive film. This experimental procedure provides supplementary data from conventional polarization curves, such as evolution of the passive film thickness and resistivity profiles through the film.

In this work, the role of alloying elements, especially chromium and iron, on the passive film properties and reactivity is studied. Understanding how alloying elements act on the passive film nature, structure and properties will provide some guidelines to engineers and scientists for designing or choosing the more adapted alloys. Finally, the proposed experimental method is also applied on certain commercial alloys. Their responses are compared with that of the closest binary and ternary alloys to evidence the discriminating factors that control the passive behavior.

Key words: Ni-based alloys; Passivation; Electrochemical Impedance Spectroscopy

Résumé

Les alliages base nickel sont largement utilisés dans divers domaines d'application, tels que le pétrole et le gaz, le nucléaire et la chimie, grâce à leur excellente résistance à la corrosion et leurs bonnes propriétés mécaniques à haute température. Dans le but de prolonger la durée de vie de certains composants stratégiques, de nombreuses études sur l'influence des éléments d'alliage sur les propriétés et la résistance à la corrosion des alliages base nickel ont été réalisées ou sont toujours en cours. Dans ce cadre, l'objectif principal de cette thèse est de développer une méthodologie basée sur la caractérisation et l'analyse électrochimique permettant de comprendre l'effet des éléments d'alliage sur les propriétés du film passif des alliages base nickel. La méthodologie proposée se base sur des mesures successives de spectroscopie d'impédance électrochimique et sur une analyse approfondie des diagrammes d'impédance, permettant de suivre l'évolution des propriétés du film passif formé sur différents alliages binaires (Ni-Cr) et ternaires (Ni-Cr-Fe) à différents potentiels. Les diagrammes d'impédance obtenus ont été interprétés avec une méthode graphique avancée et ajustés par le modèle en loi de puissance fournissant ainsi des informations caractéristiques du film passif. Cette méthodologie permet ainsi de déterminer et d'obtenir des informations complémentaires aux traditionnelles courbes de polarisation, telles que l'évolution de l'épaisseur du film et des profils de résistivité au travers de son épaisseur. Cette méthodologie a aussi été appliquée à des alliages commerciaux. Leurs réponses ont été comparées à celles obtenues pour les alliages binaires ou tertiaires dont les compositions sont les plus proches afin de mettre en évidence quels sont les paramètres microstructuraux ou chimiques les plus discriminants.

Dans ce travail, le rôle des éléments d'alliage, en particulier le chrome et le fer, sur les propriétés et la réactivité du film passif a été étudié. Comprendre comment les éléments d'alliage agissent sur la nature, la structure et les propriétés du film passif fournira quelques lignes directrices aux ingénieurs et scientifiques pour la conception ou le choix des alliages les plus adaptés.

Mots clés: Alliages à base de Nickel; Passivation; Spectroscopie d'Impédance Electrochimique

Remerciements

Tout à bord, je voudrais remercier sincèrement le jury pour leur temps, leur lecture, correction et commentaires afin d'améliorer ma thèse et leur présence à ma soutenance.

Je voudrais remercier mon directeur de thèse Bernard qui m'a toujours supporté au niveau scientifique ainsi que financier. Je voudrais également remercier mon co-directeur de thèse Benoît qui est toujours disponible pour discuter et me guider dans la direction de ma recherche. Ils m'ont beaucoup appris en corrosion et passivation. Je voudrais remercier Sabrina et Jules pour leur aide sur l'analyse de l'impédance et XPS. Puis, je voudrais remercier Marion qui m'a recruté pour commencer ma thèse en France. Je voudrais aussi remercier Yasmina pour ses aides administratives. Je suis reconnaissant à Sheng, Nicolas et d'autres permanants de CorrIS et MATEIS de leur aide.

Un grand merci aux collègues Amandine, Dwaipayan, Elizaveta, Imen, Hela, Quentin, Nicolas, Yushi et d'autres collègues et amis de CorrIS, Chloé, Kathleen, Phillipe et Ying qui étaient arrivés au laboratoire en même temps que moi, aux nouveaux doctorants, Hugo, Jonathan et d'autre collègues qui sont arrivés plus tard que moi. Merci pour leurs aides, supports et coopérations. Je voudrais aussi remercier les amis chinois faisaient leurs thèses à INSA-Lyon.

Je voudrais tenir mon remerciement à Adrien et son équipe pour leur accueil chaleureux pendant fin de ma thèse aux Etats-Unis.

Je voudrais remercier mon directeur et directrice de thèse de master, Junlei et Yingying, qui m'ont guidé au domaine de corrosion. Donc j'aurais pu avoir de la chance de finir ma thèse en France.

Je voudrais remercier China Scholarship Council (CSC) pour le financement.

Au final, je voudrais remercier ma famille et mes amis sont loin de moi mais toujours me soutiennent.

Contents

General introduction

Nowadays, Nickel-based alloys are the best candidates for structural and high values applications, such as energy, chemical and food processing etc. Sometimes Nickel-based alloys are even the only choice under the circumstance where is not for the stainless steel or other specific alloys. It is important to understand why such interest.

The face-centered cubic (*fcc*) structure of nickel makes it a ductile metal. However, nickel has a capacity to provide a high strength for its alloys with excellent corrosion resistance that could operate at 1000°C, resulting in a wide possible development of different Nickel-based alloys. Moreover, alloying of nickel with other elements, like chromium, aluminum, and molybdenum etc., greatly broadens its use in engineering applications. Figure Intro.1 displays the relationship between the alloying elements added to the Ni matrix and the obtained corrosion properties. It also mentions the commonly known alloy grades according to the main addition elements.

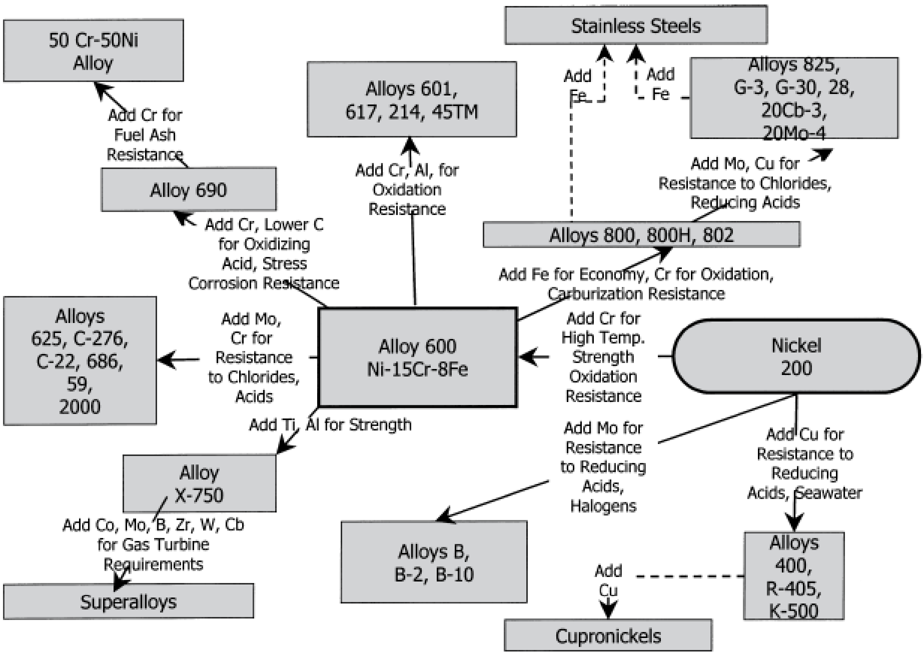

Figure Intro. 1 Compositional and property linkages for nickel alloys [1].

In the first place, typical nickel 200 (min Ni 99% wt.) is used in massive applications. For example, food and chemical processing equipment, electrical and electronic parts, aerospace components, caustic handling equipment etc. [2]. With copper adding, forming Alloy 400, Alloy R-405 etc. which are resistant to reducing acids and seawater. The Cupronickels could be obtained with a further addition of copper. If the molybdenum was added into nickel, Alloy B (like Alloy B-2, Alloy B-3 etc.) could be formed. The series of Alloy B is a binary alloy of nickel and molybdenum. It was found that this alloy has an excellent corrosion resistance to reducing acids and halogens (like Cl^- and Br^-). The third base for the Nickel-based alloy branch is Alloy 600, namely Ni15Cr8Fe (mass weight). With addition of 15% wt. Cr, the corrosion resistance at high temperature could be strengthen. From this Ni-Cr alloys family, five ways of alloy design could be proposed on purpose. Firstly, for the economical reasons, more irons are added. Maintaining a good corrosion resistance, Alloy 800, Alloy 800H and Alloy 802 are formed. In fact, Alloy 800 is no longer the Nickel-based alloy but could be considered Iron-based alloy. Since the maximum iron content in the alloy reaches at 39.5 % wt., while that for nickel is just 35 % wt. In the base of Alloy 800, with extra addition of molybdenum or copper, Alloy 825, Alloy G-3, Alloy G-30 were designed for a special utilization in medium containing chloride. With much more addition of iron, the stainless steels are obtained. Secondly, with increase of chromium and addition of aluminum, there would be Alloy 601, Alloy 617 for high temperature applications. Thirdly, with the chromium content increases from 14% wt. to 30% wt., Alloy 690 is made to resist to oxidizing acid and to prevent Stress Corrosion Cracking (SCC). When the addition of chromium reaches up to 50 % wt., 50Ni50Cr is often used for fuel ash resistance. Fourthly, the Alloy 625, Alloy C-276 etc. have an increase of chromium and molybdenum, in comparison with Alloy 600. Those kinds of alloys are used in the acid environment with chloride ions. Finally, the mechanical properties of alloys are strengthened by adding titanium and aluminum. Alloy X-750 is formed. The superalloys could be formed with different elements, like cobalt, zirconium, tungsten etc. These last alloys are interesting because they provide tunable mechanical properties and good corrosion resistance even at high temperatures and in harsh environments.

With this short context, it is obvious that alloying nickel with other elements is the main way to make Nickel-based alloys with enhanced corrosion resistance or mechanical properties. Chromium is one of the most important alloying elements which tends to form a stable passive film on the surface of alloys preventing a degradation of the alloy. However, the corrosion resistance or the properties of passive film do not increase linearly with the chromium content in the alloys. In addition, an exceeded chromium in the alloy which might influence other properties, like mechanical properties, or manufacturability of alloys. Consequently, other elements could be added to promote the mechanical properties, the production process or the welding ability. Therefore, the study of the role of alloying elements on Nickel-based alloys properties and corrosion resistance is always ongoing, for new alloy designing and service life prolonging.

In this framework, the present study will focus on the passive behavior of Ni-based alloys and consider the role of alloying elements (specifically chromium and iron) on the passive film properties and reactivity. Consequently, the main objective of this work is to understand the role of the alloying elements on the passive film properties of Ni-based alloys. For that it was opportunity to develop a methodology based on electrochemical characterization and analysis. The proposed methodology is using successive electrochemical impedance spectroscopy measurements to follow the evolution of the passive film properties grown on different binary (Ni-Cr) and ternary (Ni-Cr-Fe) alloys at different potentials. The analysis of the impedance diagrams obtained are based on recent advanced data analysis (as described in Chapter II) and completed with microstructural characterization and X-ray Photoelectron Spectroscopy. Understanding how these alloying elements act on the passive film nature, structure and properties will give some guidelines to engineer and scientist for designing or choosing the more adapted alloys.

The thesis is composed of six chapters:

Chapter I presents a bibliographical introduction of the definition of passivity, the thermodynamics and kinetics of passivation, and the mechanisms of nucleation, growth and breakdown of passive film.

It is followed by the description of the most known models often used for passivation or oxidation study and prediction of passivity formation and breakdown.

Chapter II is devoted to the description of the different characterization techniques employed in this work. It includes the technique for microstructural observation, surface analysis and electrochemical analyses. The principal theoretical approach for impedance diagram analysis will also be presented in this chapter.

Chapter III is mainly focused on the development of methodology for analysis of passive film with the successive impedance measurements. Different experimental parameters, including dwell times, step sizes, scanning direction and the electrolyte aeration, were studied. Then passivation behavior of a Ni-Cr model alloy in various solution with different pH values was studied using this method with validated and optimized parameters. It reveals that this experimental procedure provides supplementary data, such as the evolution of the passive film thickness, resistivity profiles through the film, in comparison with conventional polarization curves.

Chapter IV is dedicated to the study of the role alloying elements on the passivation behavior of Ni-Cr based alloy on both passivation and secondary passivation domain. The role of the alloying elements on the process of the secondary passivation and especially on the chemical composition of the passive film was discussed. The result shows that the dissolution is increasing with higher Cr content in secondary oxidation domain and this phenomenon can be hindered by the addition of Fe.

Chapter V shows the results of the application of method on commercial alloys, namely GILPHY 80, Inconel 600 and Inconel 625. One the one hand, the comparison of corrosion behavior of the alloys with the same chemical compositions was made. On the other hand, the cause of different corrosion behavior between model alloys and commercial alloys was discussed. It is found that the structure might have huge influence on passivation behavior when the composition of alloys is the same.

To conclude, All the significant results of this work will be summarized. Also, some perspectives and future works are proposed in last chapter.

Chapter 1 Bibliographical review

Chapter I firstly presents a bibliographical introduction of passivation: its definition and the mechanisms related to the nucleation, growth and breakdown. Then, a short review of the most commonly known models used for describing the passive state is introduced and discussed regarding the experimental technics.

1.1 The passivity and passive film

Faraday firstly reported the passivation phenomenon in his iron-in-nitric acid experiment in 1836. In this experiment, an iron bar corrodes concomitantly with the evolution of H_2 in dilute nitric acid solution, while there is no reaction apparently observed in concentrated nitric acid [3]. Then, it is also evidenced that when there is anodic polarization applied on the metal in acid or neutral solution, the dissolution could be much limited. The presence of the oxidant or the polarization on the electrode in positive direction may promote that the metal surface reaches from an unstable state to a stable state. The phenomenon is called the passivation, the corrosion-resistant state is called passive state [4]. Passivity of metals or alloys is considered to be a key role in their use, since passive films formed on their surface give excellent protection against corrosion [5]. Generally, passive films have a duplex or bilayer chemical structure. The inner layer is mainly oxide, while the outer layer is hydrated composed by hydroxides or oxi-hydroxides, as shown in Fig.1. 1.

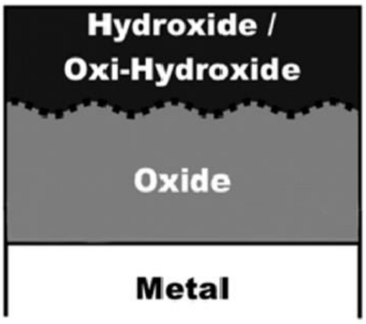

Fig.1. 1 Representation for the bilayer structure of passive films [6].

Whatever the passive material considered, the passive films present common particularities [7]. Firstly, the passive films are generally very thin. Their thickness can vary from nanometers to micrometers, relying on the materials, the electrolyte and other film forming conditions. The thickness of passive films formed on transitions metals, like Fe, Cr, Ni, Co and Mo, is less than 10 nm (Fig.1. 2 (a)), while that formed on non-transitions and valve metals, such as Al, Ti, Zn, Cd, Cu, Mg and Pb, could be much thicker. Some examples of a passive film grown on steel and an anodic film on aluminum are presented in Fig.1. 2 (b). Secondly, the passive films should exhibit relatively low ionic conductivity, preventing the migration of ions (cations or anions) through the passive film and the transfer of cations in the electrolyte. Their electronic conductivity is also limited as they are oxides. Actually, the passive films are mainly made up of metallic oxides or hydroxides which are envisaged to possess semi-conductive properties or to behave as insulator. The oxides in passive films are often non-ideal or non-stoichiometric. The deviation from ideal oxide or stochiometric oxide could come from the structure of the passive layer, polycrystalline or amorphous, or may result from the overall factors involved in the film forming conditions (substrate chemical composition, physicochemical conditions…). The non-stoichiometry of the oxides corresponds to the presence of defects which act like dopants, inducing an additional charge into the oxide. An increase of defects, from the point of view of semi-conductivity, modifies the conductivity of the passive layer. For example, a positively charged oxygen vacancy or an interstitial cation within the oxide lattice could lead to an excess of electrons carried by the adjacent ions. This doping corresponds to n-type semiconductors, such as the passive film on Fe [8] and W [9], with a very high donor concentration. Conversely, a cation vacancy leads to a local deficit of electrons, causing extra electron holes. It results in as p-type semiconductors, like passive film on Ni [10] and Cr [11] etc., with acceptor concentration. Therefore, greater number of defects is, the more conductive the oxides are. In most of the studies, the densities of the majority charge carriers are of the order of 10^{20} - 10^{21} cm^3 suggesting that passive films are highly disordered semiconductors. Those electronic properties are expected to be crucially important in understanding the protective characters against corrosion of passive layer [12]. Hence, the study of the semi-conductivity of passive metals makes it possible to apprehend not only their ability to conduct current, but also their structure, as well as certain intrinsic properties, such as predominate sort of defect and defects densities etc. [13]. Thirdly, the passive films have also very low chemical solubility, and are stable under a wide potential range. Finally, the passive films generally have certain mechanical properties to resist to scratching, abrasion, deformation...

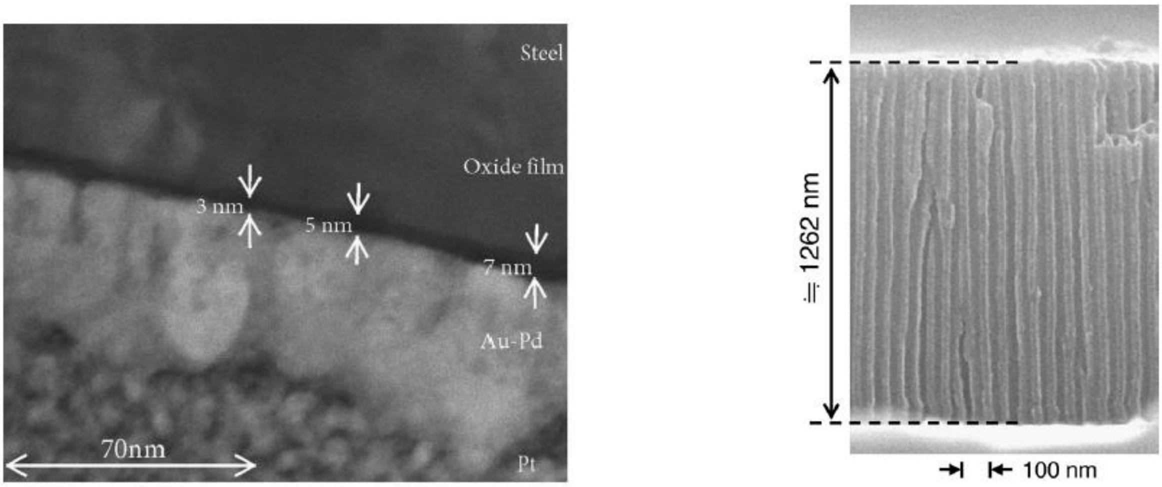

(a) (b)

Fig.1. 2 (a) HAADF-STEM images of ASTM A416 steel following 24 hours immersion in simulated pore solution [14] *and (b) SEM side view image of porous anodized aluminum oxide film* [15].

Going further, different metals present different passivation ability. By considering their fundamental properties, P. Marcus [16] classified some metallic elements into two categories, namely passivation promoters and dissolution moderators. Since the combination of metal with O^{2-} or OH^{-} occurs after the breakdown of metal-metal (M-M) bond, the metallic elements that provide a strong metal-oxygen (M-O) or (M-OH) bond energy are passivity promoters. While the dissolution moderators must have a high metal-metal (M-M) bond energy to avoid the formation of the metal-oxygen (M-O) or (M-OH) bond. The classification of two types of metallic elements is show in Fig.1. 3. It is worth mentioning that this classification is not only interesting for pure material but also for designing alloys.

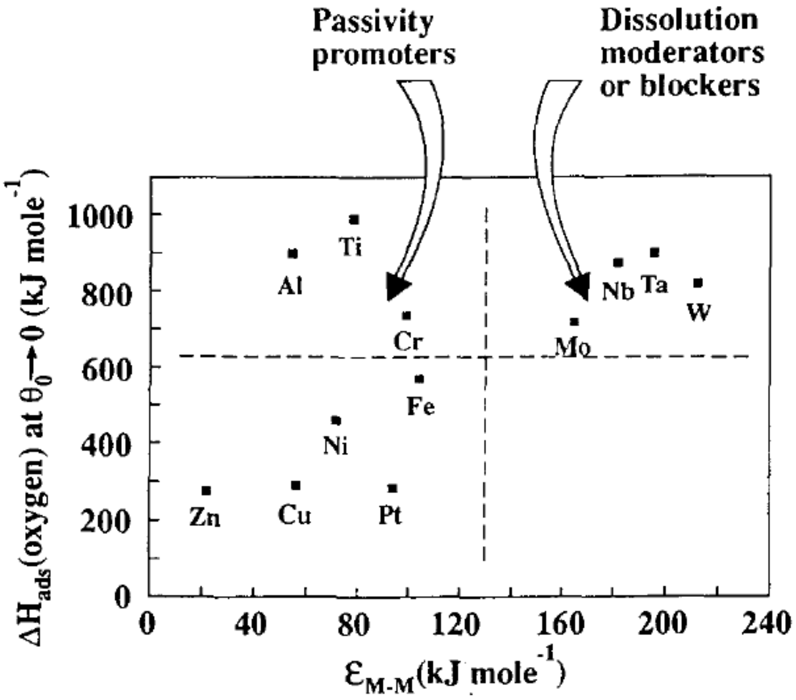

Fig.1. 3 Classification of passivity promoters and dissolution moderators based on the synergy between the heat of adsorption of oxygen and the strength of metal-metal bonds [16].

Passivity promoters and dissolution moderators are separated by the relationship between the heat of adsorption of oxygen (ΔH_{ads}) and metal-metal bond energy (ε_{M-M}). It is clear that the metals in the upper left of the diagram (Cr, Al, and Ti), who exhibit an excellent combination ability of high heat of adsorption of oxygen and relatively lower metal-metal (M-M) bond strength, are ideal elements to promote the passivation. It is easy to break the metal-metal (M-M) bond and adsorb the oxygen (or OH), which is in favor of the nucleation of a passive film. On the contrary, another part in the diagram located in the upper right is for the dissolution moderators or blockers. The alloying elements in this area, like molybdenum, niobium, tantalum, display much higher heat of adsorption of oxygen (ΔH_{ads}) and metal-metal bond energy (ε_{M-M}) comparing with the elements of passivity promoters on the left. In other word, the metal-metal (M-M) bond of the dissolution moderators is much difficult to break. Moreover, it is also possible for the dissolution moderators to become passivity promoters, due to their high heat of adsorption of oxygen (ΔH_{ads}). Lastly, it is interesting to mention that the elements of the lower left corner, such as iron, nickel, zinc and copper, are often used to be the base of alloys.

1.2 The mechanism of passivation

The dissolution-precipitation process is one of the possible mechanisms of formation of passive film. There are two steps involved, namely the dissolution of metal ions and the formation of the oxide on the metal surface. The two process could be concluded as (according to Fig 1.4 and 1.5 a divalent metallic cation is considered in the following equations):

$$M_{metal} \rightarrow {M_{aq}}^{2+} + 2e \qquad (1.1)$$

$$ {M_{aq}}^{2+} + H_2O_{aq} \rightarrow MO(ox) + 2{H_{aq}}^{+} \qquad (1.2)$$

Generally, the passive film is in some extent hydrated. In the nucleation stage, the passive film is completely hydrated. However, the film will become dehydrated and deprotonated once the precipitated film is growing on the metal surface. Especially, the inner face contacting with the metal is dehydrated because of the existence of high anodic electrical field [4]. The formation of passive film depends on the interfacial dynamic reactions, particularly anodic reactions that rely on the potential difference between metal and electrolyte, and also the pH value of electrolyte. The bipolar mechanism proposed by Sato [17] considering the process from active dissolution to the passive state is presented in Fig.1. 4.

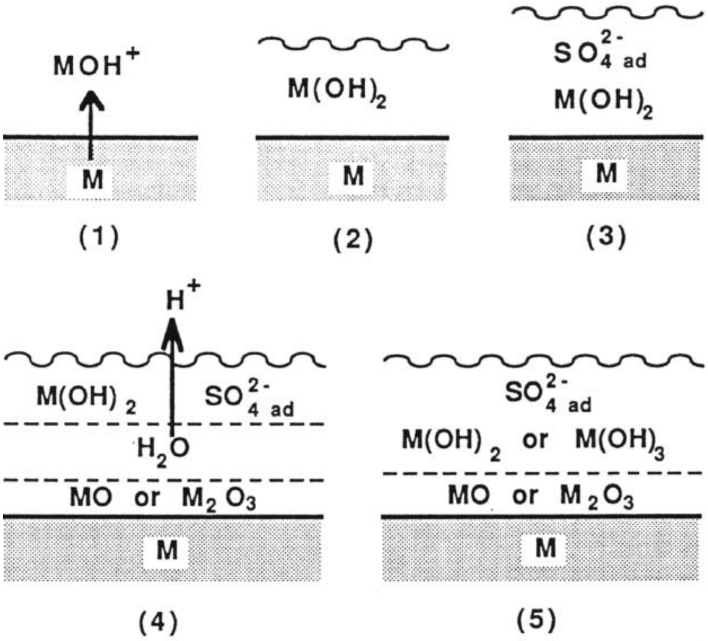

Fig.1. 4 The bipolar mechanism for metal passivation: (1) metal dissolution, (2) metal hydroxide precipitation, (3) formation of bipolar precipitates, (4) deprotonation and (5) formation of double layer [17].

As depicted in Fig.1. 4, the first step of the passivation is dissolved metal ions combine with hydroxyl ions to form MOH^+, assembling near the metal surface. The MOH^+ will form metal hydroxide $M(OH)_2$ with a porous sol-gel structure, or salt precipitated film. Then, the non-aggressive oxyanions, like SO_4^{2-}, could be adsorbed on the solution side of the precipitated film. The outermost layer would convert from an anion-selective phase to a cation-selective phase, making the film become bipolarized, as presented in Fig. 1.4 (4). Finally, the precipitated film is modified as a metal dehydrated oxide film of MO or M_2O_3 with an outer hydrated layer $M(OH)_2$ or $M(OH)_3$. The outer hydroxide is supposed to be dissolved in acidic solution.

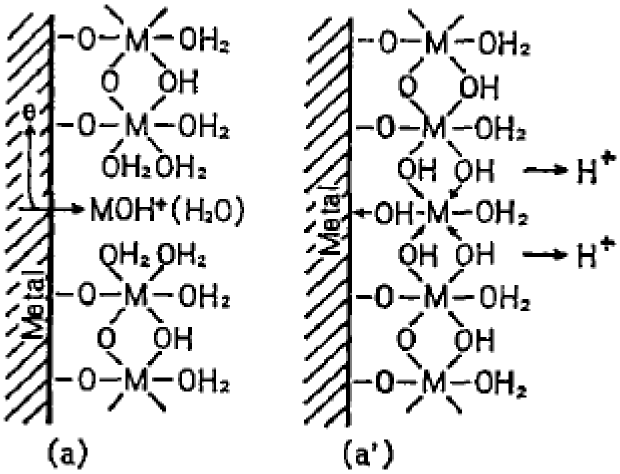

Fig.1. 5 Schematic representation of the film formation by metal ions dissolution (a) dissolved metal ions are captured to form the film (a') bridging OH bonds between neighboring sites [18].

Okamoto [18,19] proposed another model for explaining the effect of the potential and ageing for dry and wet corrosion conditions, as presented in the Fig.1. 5. First, the passive film generated in aqueous is assumed with a gel-like structure, containing bound water. The proton within the passive film will be ejected during the process of ageing or in presence of anodic polarization. After partial deprotonation, the dissolved metal ions form an intermediate MOH^+, shown in the Fig.1. 5 (a). Then, since intermediate MOH^+ is supposed to be captured by the neighboring water molecules, the surface of metal will be covered by solid film, which is illustrated in the Fig.1. 5 (a'). There are different connected bounds that could form between metallic ions and water, such as H_2O-M-H_2O, -HO-M-HO- and also -O-M-O-, considering the stage of deprotonation. In which, H_2O-M-H_2O structure is the most reactive part, while the least reactive part in the film is -O-M-O-. The final film composition will be reached after the successive deprotonations, according to the reactions: $H_2O \rightarrow OH^- + H^+$ and $OH^- \rightarrow H^+ + O^{2-}$.

1.3 Thermodynamics and kinetics of passivation

1.3.1 Thermodynamics of passivation: Pourbaix Diagrams

Marcel Pourbaix has proposed to collect and represent the thermodynamic information for metal-solvent system for different pH values as a function of potentials into a potential/pH diagram (also called Pourbaix diagram). Pourbaix diagram defines regions of pH and potential where the metal undergoes corrosion, is passivated or staying at a metallic state (immunity domain) [20]. The example of the Pourbaix diagram for iron in water is presented in Fig.1. 6.

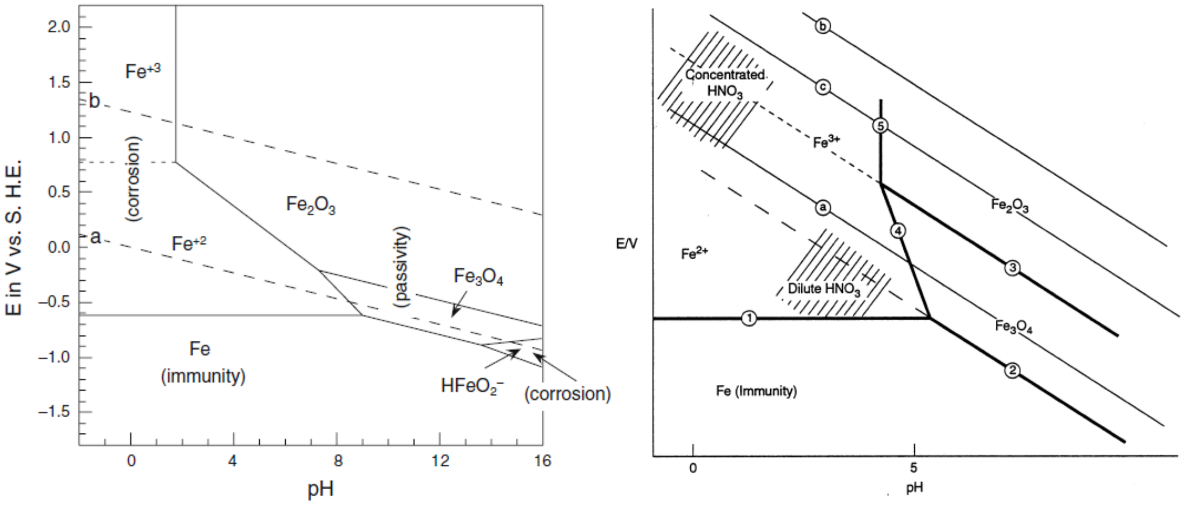

(a) (b)

Fig.1. 6 (a) Pourbaix diagram for iron at 25°C [21] *and (b) Schematic Pourbaix diagram for iron illustrating the resolution of the Faraday paradox in the corrosion of iron in nitric acid* [22].

First of all, when iron is in presence of water (deaerated or aerated), it reacts. Indeed, the metallic state is not thermodynamically stable with water and oxygen. In acidic or neutral solutions, the iron is corroded in the region as Fe^{2+} or Fe^{3+}, as a function of the potential. Separately, corrosion will also happen in basic solutions by forming the complex anion $HFeO_2^-$. In other cases, like with pH value between 8 and 14, the Fe_2O_3 and Fe_3O_4 iron oxides provide the passivity.

Even though the Pourbaix diagram for iron indicates that iron is in the state of corrosion for pH lower than 8, it is experimentally found that there is a metastable passive state even for lower pH. This suggests that the existence of passive state is not only governed by thermodynamic considerations. Fig.1. 6 (b) presents the case of iron in nitric acid to illustrate that point (Faraday's experiments). In the region where marked 'dilute HNO_3', the iron is supposed to be at the state of Fe^{2+} due to weak oxidizing agent property of dilute HNO_3, while the Fe^{3+} is assumed in 'concentrated HNO_3' because of oxidizing property of concentrated HNO_3. In this last case, NO_3^- is reduced to HNO_2 and this reaction is fast inducing the extension of the passivity region. It is then possible to form a metastable phase of Fe_3O_4, resulting in passivity. Moreover, Fe_2O_3 might evolve as an additional metastable phase of Fe_3O_4, if the potential is more positive. When the rate of formation or dissolution processes of metastable phase reaches an equilibrium, then a quasi-steady state can be achieved [22].

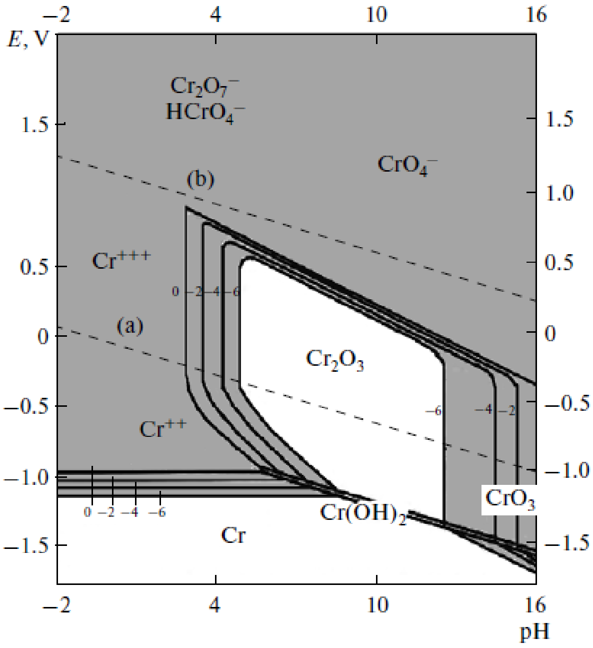

Fig.1. 7 Pourbaix diagram for chromium at 25°C [23].

Another example is given in Fig.1. 7, presenting the Pourbaix diagram for chromium. On one hand, it is evident that the passivate state of Cr_2O_3 is thermodynamically stable only at pH values above pH 3–5. However, it is experimentally proved that chromia may exist as a metastable state in highly acidic solutions, since chromium contained stainless steel is used in concentrated acid environment [24]. Consequently, the plotted region for the passivity of Cr_2O_3 under equilibrium conditions from Pourbaix diagram led to wrong conclusion for the use of chromium in acidic environment [23]. On the other hand, the Pourbaix diagram of chromium reveals that the chromium oxide is dissolve and out of stability with increased anodic potential (over 0.7 V vs. SHE). Hence, the chromium could be in state of corrosion as chromate ions, like CrO_4^{2-}. The dissolution of passive film at anodic potentials is named transpassive dissolution and will be discussed later.

Pourbaix diagrams are very useful tools for researchers and engineers. However, the Pourbaix diagrams exhibits limitations. One of these limitations remains in that they are often rigorously calculated for single elemental metals. In more complicated case as for alloys, Pourbaix diagrams can be superimposed onto each other in terms of different elements or determined from electrochemical polarization measurements [21]. However, the results of this superimposition are not always satisfying because the different kinetics of the reactions, preferential dissolution and the kinetics limitations are not taken into account.

1.3.2 Kinetics of passivation

As mentioned above, Pourbaix diagrams are helpful to find the corrosion behavior of various metals in many different systems. However, Pourbaix diagrams do not give any information about kinetics which are crucial to understand passivity. The passivity cannot be only determined from thermodynamic approaches. Furthermore, it is kinetic factors that define the passive state rather than thermodynamic equilibrium properties. Kinetic Stability Diagram (KSD) is developed to be alternative to the classical

Pourbaix diagrams, showing kinetic stability of passive state. A schematic KSD for a chromia oxide passive layer is illustrated in Fig.1. 8 [25].

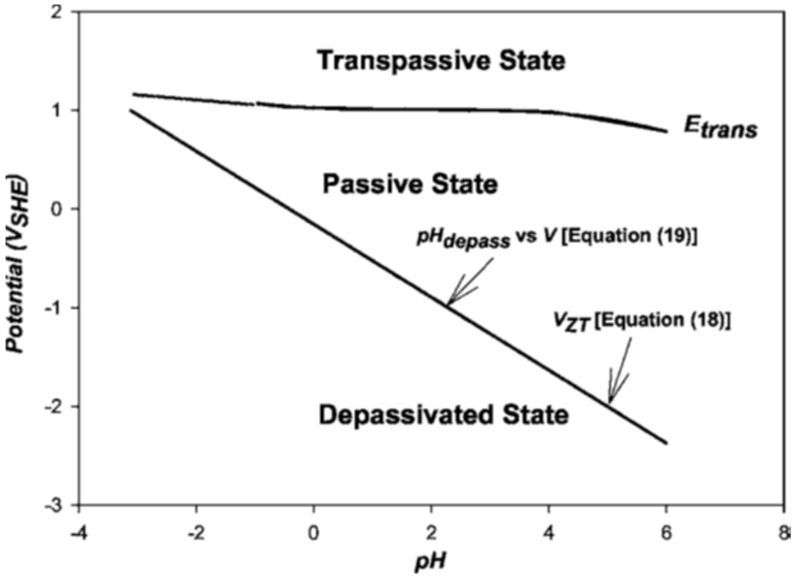

Fig.1. 8 Primitive kinetic stability diagram for a hypothetical alloy with similar properties to Ni-Cr-Mo-W-Fe alloys acidic solution with 6.256 m NaCl at 50°C. The passive state can exist only in the region indicated [25].

Fig.1. 8 could be divided into three parts. The top part is the transpassive state in increased anodic potential region, while the bottom part is the depassivated state at the most negative potentials for acidic solution. The passive film is stable between the depassivated and transpassive state. The boundary between the passive and depassivated states is defined by the pH or voltage, which is considered to be two independent variables. KSD indicates a passivated state at very low pH and within a wide range of potential while chromium is in state of corrosion at very acidic and cathodic potential range, according to Pourbaix diagrams of chromium in Fig.1. 7. In addition, KSD shown in Fig.1. 8 is used for predicting chromium oxide layer of alloy X (a hypothetical alloy with similar properties to Ni-Cr-Mo-W-Fe alloys), and it is supposed to be employed for pure chromium but also for chromium-containing alloys. Since a chromia passive layers can be expressed with a formula of $Cr_{2+x}O_{3-y}$, forming on many chromium-containing alloys such as stainless steels, Ni–Cr based alloys etc. [25].

However, even though KSDs are kinetic descriptions of the passive state, they do not provide kinetics information about the passive ability, behavior and steady state. Hence, to better understand the kinetics related to the passivation process, polarization curves are generally used to quantify the behaviors of metals under various conditions and determine the existence domain of passive state and the current density associated with the steady state passivity. Polarization curves for passive systems may show active/passive and/or passive/transpassive transitions, even secondary passivation domain and oxygen evolution. A schematic polarization curve is given in Fig.1. 9 below.

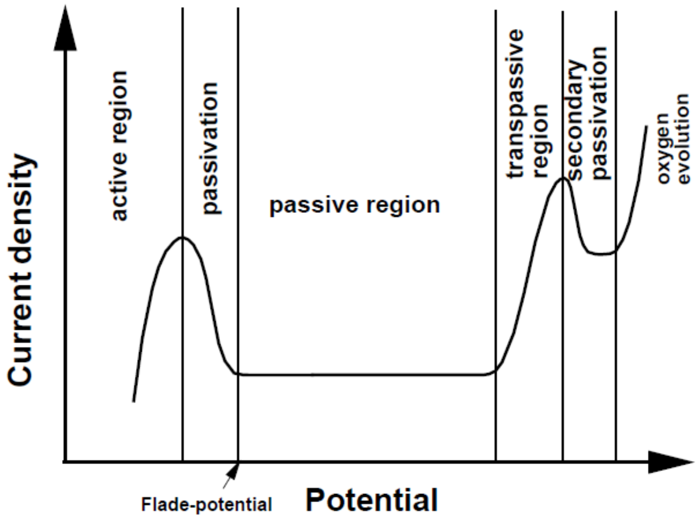

Fig.1. 9 State of a metal electrode (e.g.Cr, Fe) during voltammetric measurement [26].

From cathodic to anodic potential, the electrode begins to oxidize in active region associated with an increase of current. It corresponds generally to the first step of the passive film formation (Eq. 1.1). With a more anodic applied potential, the current starts to reduce, forming passive film (Eq. 1.2). During the passivation, the surface of electrode is covered progressively by the passive film according to the model proposed by Sato or Okamoto. When the current reaches its minimum value, the potential here is called Flade-potential. The passive film is completely covering the electrode. The passive domain is then defined by the length of the plateau with minimum current (in the order of magnitude of μA cm^{-2}). If the electrode is a Ni-Cr based or Fe-Cr based alloy, the current will start to increase again when higher potentials is applied on its surface, and the electrode enters into the transpassivation region. The metal ions constituting the passive film will be oxidized to higher valences, which might cause change of film composition and/or the dissolution of film. It is hard to observe the potential thresholds between different reactions, since the corrosion current increases quickly in this region. After the transpassivation region, either the surface of electrode begins to passivate again (it will enter in secondary passivation region) or the dissolution still occurs. Finally, the oxygen evolution takes place and the current density of all the anodic reactions are added. In some cases, passive film is no more existing in this potential region according to the KSD. Fig.1. 10 evidences also that the passive ability of a material is closely related to the solution considered.

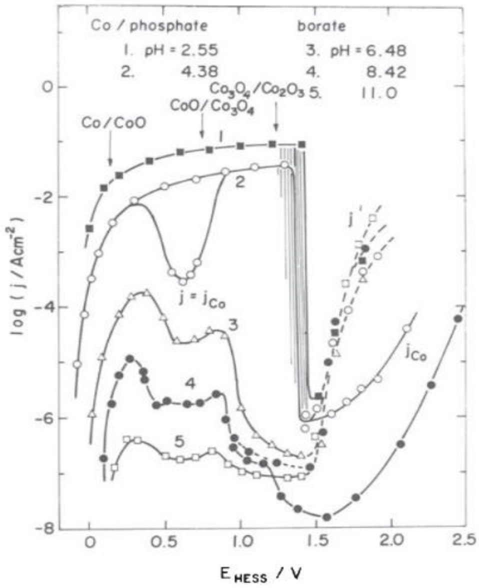

Fig.1. 10 Potentiostatic anodic polarization curves of cobalt in 1 h steady state in 0.15 M phosphate and 0.15 M borate solutions with acidic and basic pH values [4].

The shape of the polarization curves for a selected material is dependent on the experimental conditions. For example, as a function of the cathodic reaction, the active-passive transition is not always observed. Another example, the secondary passivation is not always detected and is closely related to the oxyanions nature or pH value [27,28].

1.4 The breakdown of passivity

As previously mentioned, even if the material is protected by a passive film, the protection can be lost with time or change of environment. The breakdown of a protective passive film can lead to the exposure of bare material surface to corrosive media and even accelerate dissolution of materials. Hence, the passivity breakdown is an important practical issue as well as a tricky scientific problem. The passivity can breakdown under some certain conditions. There are many reasons that may cause the chemical or electrochemical breakdown of passive film.

1.4.1 Anodic dissolution

As mentioned in the previous part, the transpassivation is activated at high anodic potential and linked to the anion presence and pH of the electrolyte. In this process, supplementary electrochemical reactions may take place and break the electrochemical equilibrium reached during the steady-state. The transpassive dissolution is the oxidation of the element in the passive film to a higher valence. These higher valence ions are generally more soluble or forming complex soluble ions. For example, the trivalent chromium in the passive film is oxidized to soluble hexavalent chromium in the transpassive potential range [20,29]:

$$Cr_2O_3 + 4H_2O \rightarrow Cr_2O_7^{2-} + 8H^+ + 6e^-, \; E_0 = 1.259 - 0.0788pH + 0.0197\log(HCrO_4^-) \quad (1.3)$$

Consequently, the passive film is gradually dissolved into electrolyte in the transpassive potential range. Generally, the transpassive dissolution is more observable at substrate grain boundaries. In this potential range, the material is no more protected.

1.4.2 Cathodic breakdown

As shown in the KSD, at low potential, when system reaching the hydrogen evolution, it is also possible to weaken and modify the passive film. Yet, this reaction is often observed at more negative potentials in presence of passive layer, due to overvoltage limitation. Hydrogen are generated from proton reduction. Protons could be discharged at interface between the electrolyte and passive film, and pass through the film to the metal surface by tunneling electrons or enlarging conductivity from weaken spots [30,31]. On the one hand, the solved hydrogen can weaken and reduce the oxide or make it dissolved into the electrolyte. On the other hand, the formation of hydrogen bubbles at the interface between oxide and metal can make the delamination of passive film. Furthermore, this process is generally associated with a local increase of pH value and current density.

1.4.3 Localized corrosion

If anodic and cathodic breakdowns could be considered electrochemical limitations of passive film existence, then localized corrosion is one of the most problematic issues regarding passivity breakdown. The passive films are susceptible to many kinds of localized corrosion, like pitting corrosion, crevice corrosion and intergranular corrosion etc. In the following part, the different mechanisms involved in localized corrosion are described.

1.4.3.1 Pitting corrosion

In some cases where there is the presence of aggressive ions in the electrolyte, like chloride, bromide, iodide or perchlorate ions, the passive film might breakdown and dissolve at exceeded critical potential value, because of the pitting corrosion. The aggressive ions might penetrate the passive film under high potential field by passing through the defects in the passive film. Once the film is locally destroyed, the dissolution from the bare metal happens. Pitting is a hazardous form of corrosion. Indeed, the nucleation and growth of pits is difficult to predict [32].

The pitting susceptibility is influenced not only by the halides in electrolyte, but also by the chemistry of passive film which is related to the composition of alloys. For Ni-Cr alloy, it is reported that the 16 wt.% Cr alloy was the most susceptible to metastable and stable pitting, whereas the alloy was almost unaffected by metastable or stable pitting when the chromium content increases up to 28 wt.% in the alloy [33]. Preferential interactions between Cl^- and Ni^{2+} ions, which are incorporated in the passive film, are responsible for the increased pitting sensitivity. Hence, it is possible to evaluate the pitting susceptibility of the Ni-Cr alloys by measuring the ratio of chromium oxide and nickel oxide in the passive film.

In addition, the role of nanostructure of passive films is also considered for the passivity breakdown. The metastable pits of Ni (111) single-crystal surface in atomic scale were studied by Electrochemical Scanning tunneling microscopy (ECSTM). The STM topographic images of the metastable pits formed on passivated Ni (111) exposed to chloride were illustrated in Fig.1. 11. In Fig.1. 11 (a), local areas where the substrate has been attacked were observed, while Fig.1. 11 (b) shows a magnified image of the nucleation site of a single pit.

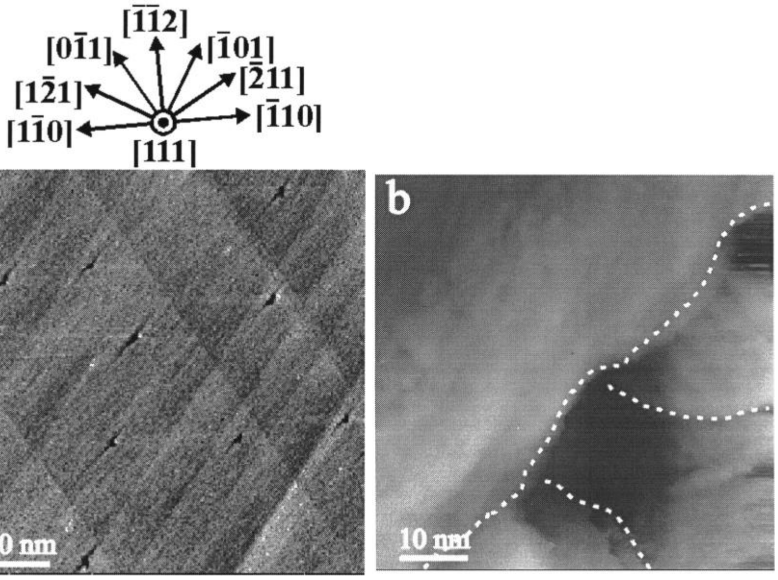

Fig.1. 11 STM topographic images of the metastable pits formed on passivated Ni(111) in acidic 0.05 M NaCl. The indicated crystallographic directions and marked the grain boundaries of the passive film are also reported [34].

The STM topographic images illustrate the formation of pits at the grain boundaries of the passive film. A representation of the pitting corrosion mechanism is shown in Fig.1. 12.

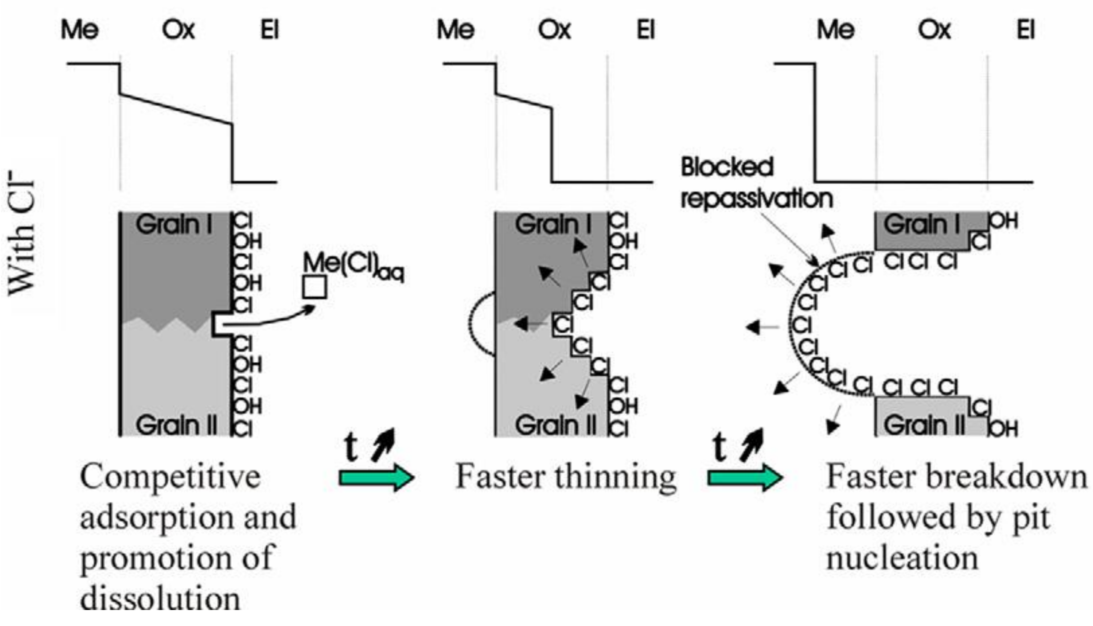

Fig.1. 12 The effect of chlorides on the local breakdown of passivity driven by the potential drop at the oxide/electrolyte interface of an intergranular boundary of the barrier layer [35].

Cl^- ions tend to compete with OH^- for adsorption on metals or alloys surface. The soluble complexes of Me–Cl^- or MeO(H)–Cl^- form, once Cl^- are adsorbed on the oxide surface. As a result, the dissolution rate at local sites increases while the growth of passive film is hindered. It leads to a faster thinning of the passive layer and localized depassivation in the less resistive sites. After local passive film rupture, Cl^- continues to compete with OH^- for adsorption on surface site. It is easier for Cl^- to adsorb on substrate depassivated surface, due to stronger electronegativity of Cl^- than that of OH^-. Consequently, repassivation of matrix becomes difficult because Cl^- blocked the supply of OH^- and pits may grow.

1.4.3.2 Intergranular corrosion

Intergranular corrosion is a form of corrosive attack that progresses preferentially at grain boundaries. In general, a significant material loss may not occur. To identify this type of corrosion, microstructure examination under a microscope is usually required. The attack of intergranular corrosion results from local differences in composition or grain boundary precipitation. For stainless steel or Ni-Cr alloys, intergranular chromium carbides precipitation is mainly responsible for intergranular corrosion. The precipitation of chromium carbides consumed neighboring chromium along the grain boundary, resulting in chromium depletion zone which may play a role in anode during corrosion process. While the core of the grain nearby or the carbide itself act as cathode. Consequently, chromium depletion regions will be attacked preferentially during corrosion. Moreover, the passive film grown on the chromium depleted zone do not exhibit the same properties than elsewhere resulting in a greater susceptibility to breakdown. Fig.1. 13 depicts the formation of the Cr depleted zone around the Cr carbides precipitates.

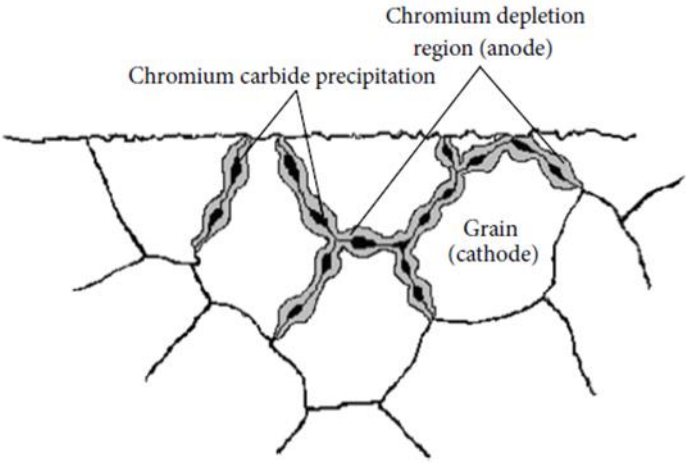

Fig.1. 13 Representation of chromium carbide $Cr_{23}C_6$ precipitation and associated chromium depletion at the grain boundaries [36].

There are many factors that have influence on susceptibility to intergranular corrosion, carbides precipitation, grain to grain disorientation, grain boundaries chemical quality… Li *et al.* found that susceptibility to intergranular corrosion of a sensitized 316L stainless steel decreases as the grain size increased [37]. The observed surface obtained after a Double Loop Electrochemical Potentiokinetic Reactivation (DLEPR) test on 316L stainless steel with various grain sizes are displayed below. It is found that no intergranular corrosion is observed in the sample of 173 µm. Besides, precipitations are decreasing with increasing of average grain size.

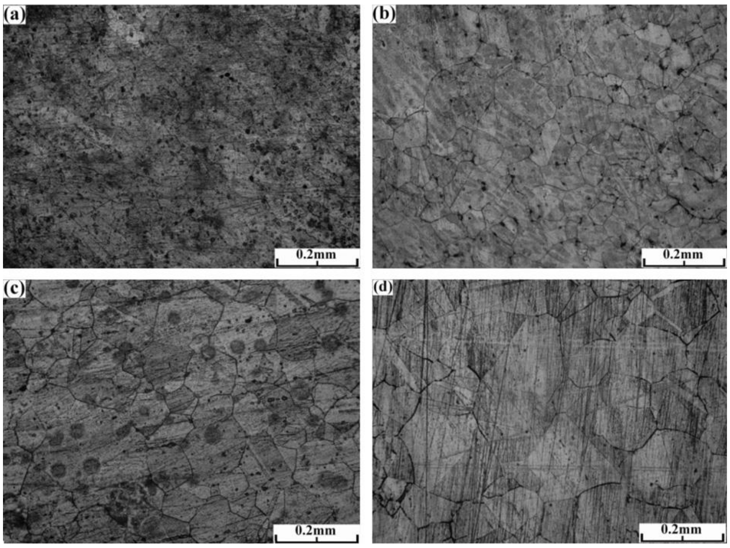

Fig.1. 14 Microstructures of sensitized at 650°C for 50 h 316L stainless steel with different grain sizes (a) 55 µm (b) 77 µm (c) 110 µm (d) 173 µm after the DLEPR test [37].

In addition, different microstructures will also affect susceptibility to intergranular corrosion. It reported that intergranular corrosion on austenitic stainless is much slower than that on ferritic stainless steel, due to slow kinetics of diffusion and precipitation [38].

Some solutions could be adopted to prevent or decrease the susceptibility of intergranular corrosion. For example, it was found that intergranular corrosion could be reduced by decreasing carbon content to around 0.002 wt.% [38]. Also, addition of stabilizer elements, like Ti, can promote better intergranular corrosion resistance. Because precipitation of titanium carbides can reduce the formation of chromium carbides [39]. Moreover, performing heat treatment that can decrease the carbides precipitation and susceptibility of alloys to intergranular corrosion [40].

1.4.3.3 Crevice corrosion

Crevice Corrosion is a localized corrosion occurring at gap or crevice between two joining surfaces. It can happen on metal-metal or metal-non-metal junctions. Crevice corrosion is generally initiated by a difference in composition between the occluded and the bulk solutions, especially in terms of O_2 concentration [41]. It results in an electrochemical concentration cell (differential aeration cell in the case of oxygen). A representation of crevice corrosion is given in Fig.1. 15.

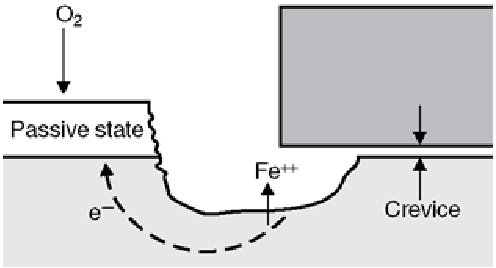

Fig.1. 15 Schematic of crevice corrosion [42].

Besides, there are other considered factors that have important effects on crevice corrosion, including crevice type, composition of alloys, crevice geometry and solution, electrochemical reactions and mass transport process etc. The information in detail is show in Fig.1. 16.

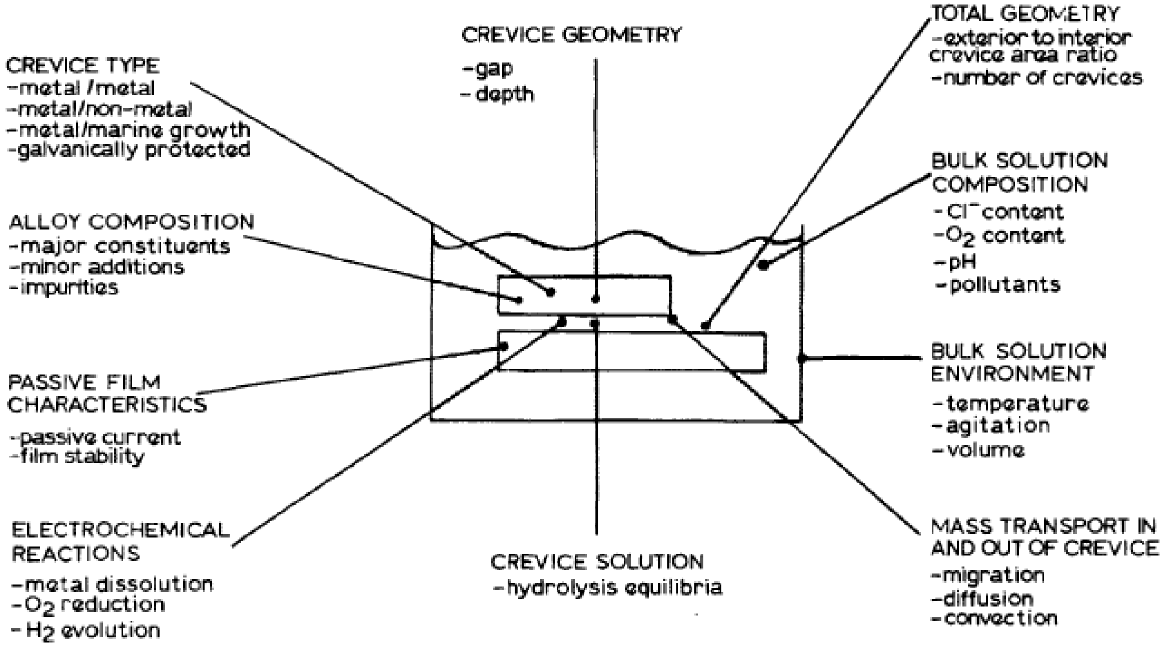

Fig.1. 16 Considered important factors for crevice corrosion [43].

Crevice corrosion is dangerous because even passivatable alloys used for mechanical joints in engineering structures could be rapidly destroyed due to crevice corrosion [44]. A great number of studies concerning crevice corrosion of stainless steels and nickel alloys were performed, especially the role of alloying elements [43,45,46]. It is known that Cr may enhance corrosion resistance of alloys under oxidizing conditions, while Mo is a beneficial alloying element for reducing conditions. It is found that Cr content is more responsible for limiting the crevice corrosion initiation, whereas Mo content will affect the corrosion damage within the occluded crevice. The corrosion propagates preferentially parallel to surface when there is high Mo content, while the corrosion will grow into the alloy if there was low Mo content in the alloy [43]. Among other alloying elements, W can impact initiation and repassivation crevice temperatures [46], and Cu has no obvious effect on crevice corrosion resistance [47].

1.4.4 Synergetic effect inducing passive film breakdown

When the materials are exposed in a certain working environment, the passive film might breakdown because of aggressive species from the environment or mechanically assisted factor, and their synergetic interactions.

1.4.4.1 Stress Corrosion Cracking (SCC)

The breakdown of passive film related to the SCC involves both mechanical and chemical contributions. Indeed, SCC occurs on a certain given working environment [48] : the concept of the multicomponent combination of material, environment and stress loading is displayed in Fig.1. 17. Note that SCC occurs in combined and synergistic interactions among environment, material and stress state, indicated by the common area of three circles. SCC study concerned with the link among the three essential factors, since SCC only occurs when three prerequisite conditions are satisfied simultaneously. SCC process will be affected once one of these factors is changed.

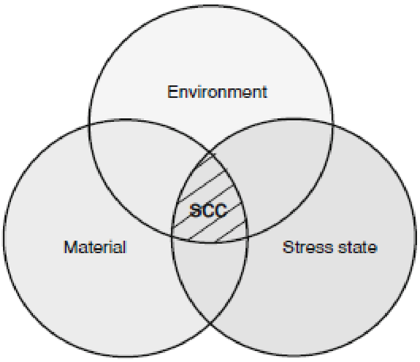

Fig.1. 17 Environment-material- stress combining system and susceptible domain of SCC occurrence.

Regards to the process of SCC, the schematic is shown in Fig.1. 18. SCC process consists of three parts, namely incubation period, crack initiation and crack propagation.

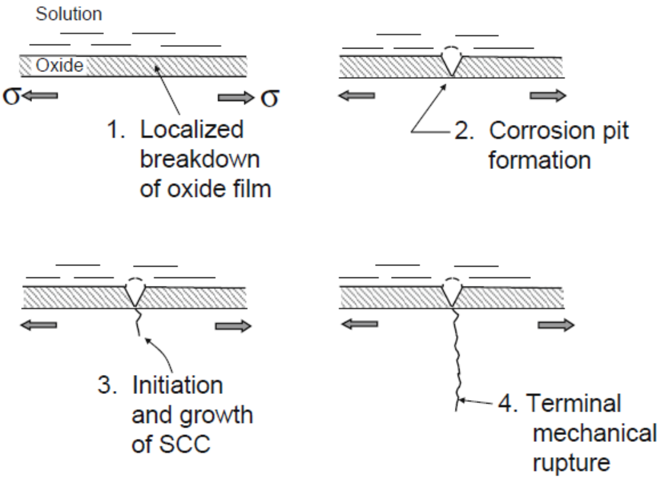

Fig.1. 18 The four stages in the initiation and propagation of stress corrosion crack [21].

Crack initiation and propagation involve four steps as depicted in Fig.1. 18 (in which σ is the direction of applied stress). The first step is localized breakdown of the passive film due to mechanical damage or to chemical attack by aggressive ions. The second step concerns to the pit or defect formation after the rupture of passive film and without a repassivation process, followed by the third step related to initiation and growth of a stress-corrosion crack. Finally, the last step is more about the propagation of the crack that may provoke rupture of the material. The crack growth rate is strongly dependent on the applied stress intensity. Note that some systems do not tend to pit, such as titanium, but a SCC will nucleate from fatigue crack [21]. In SCC process, there is always a competition between dissolution and repassivation, and also between crack growth rate and repassivation.

Metallurgical variables, such as alloy composition [49], microstructure [50], grain size [51], and microchemistry [52] can have influence on SCC resistance. The strength of alloys can be controlled by composition and microstructure, and SCC susceptibility generally increases with increasing strength [53]. An example of the correlation between the SCC resistance and strength is given below. X70 steel becomes less resistant to SCC after water-quenching treatment with enhanced strength. Moreover, physicochemical conditions, including pH value, oxygen concentrations or temperature affects straightforwardly the SCC resistance [53].

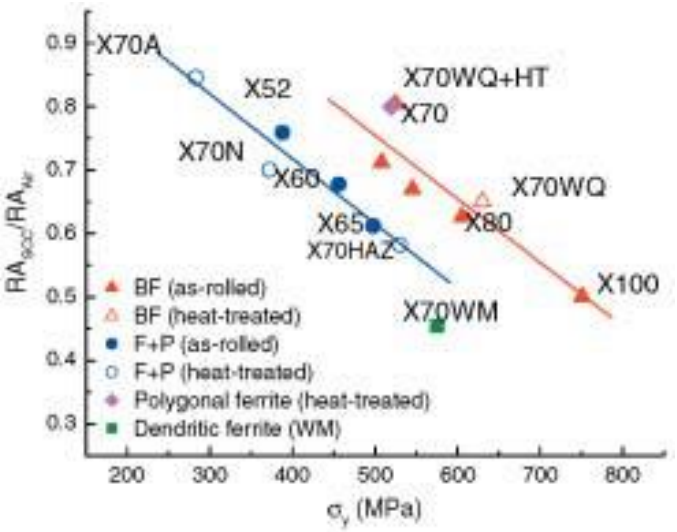

Fig.1. 19 SCC resistance evolution trend with strength of pipeline steels [50].

1.4.4.2 Corrosion fatigue

Generally, the fatigue failure happens after a large amount of cycles of loading. The fatigue failure is mainly owing to the critical crack which could not sustain the next cycle of mechanical load anymore [54]. Localized plastic deformation will cause fatigue crack during cyclic straining. The main question concerning to the fatigue corrosion is the fatigue crack initiation. In recent literature, crack incubation and crack formation are also used interchangeably to describe this process [54]. It is not like SCC that can be either intergranular or transgranular. In general, fatigue is transgranular unless it is coupled to SCC. Moreover, true corrosion fatigue must display the typical striations of fatigue, which could be ductile or brittle [55]. The comparison among corrosion fatigue and other modes of corrosion is shown in Fig.1. 20. The characteristic ductile or brittle striations are also displayed. Brittle striations form planes corresponding to single grains all together to the maximum tensile stress direction, while ductile striations present concentric circles departing from the initiation site [55].

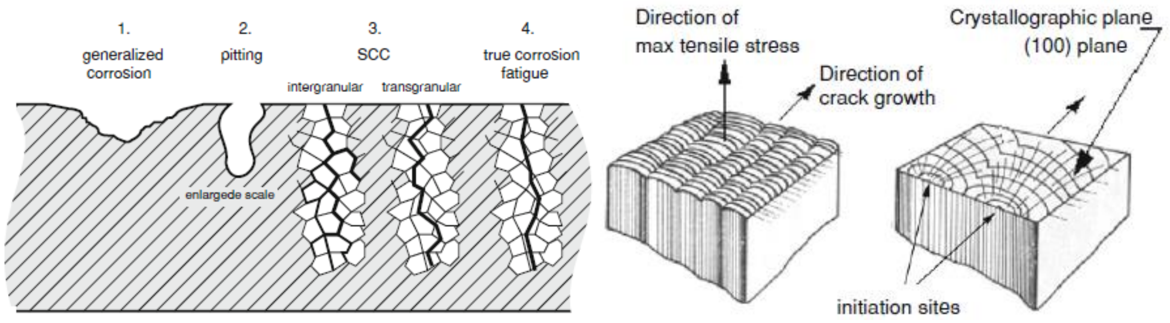

(a) (b)

Fig.1. 20 Representation of (a) true corrosion fatigue comparing with other modes of environmental aggression and (b) difference between ductile (left) and brittle (right) striations [55].

1.4.4.3 Tribo-corrosion

Tribo-corrosion is defined as the degradation of a material caused by simultaneous mechanical and chemical or electrochemical removal [56]. In general, when a passivatable metal or alloy is subjected to sliding wear in a corrosive environment, the surface will be scratched and the underneath material dissolves. In some cases, a new oxide film grows quickly and limits the dissolution. The degradation caused by tribo-corrosion is often expected occurring when mechanic and environment act synergistically. The local abrasion of the passive film, the corrosion products during abrasive action and the plastic deformation of the surface layer could be factors that accelerate or reduce the wear processes [56]. In Fig.1. 21(a), the passive material can generate passive layer on its surface. When the passive layer is removed by mechanical movement, bare material is exposed resulting in corrosion. Then a new passive film will grow again on the surface when the mechanical wear stops. Fig.1. 21(b) depicts the case of abrasion caused by corrosion products. In this case, solid corrosion products from mechanical wear in Fig.1. 21(a) was left on the surface. The debris are called 'third body', and they are considered to cause abrasions on bare material [57].

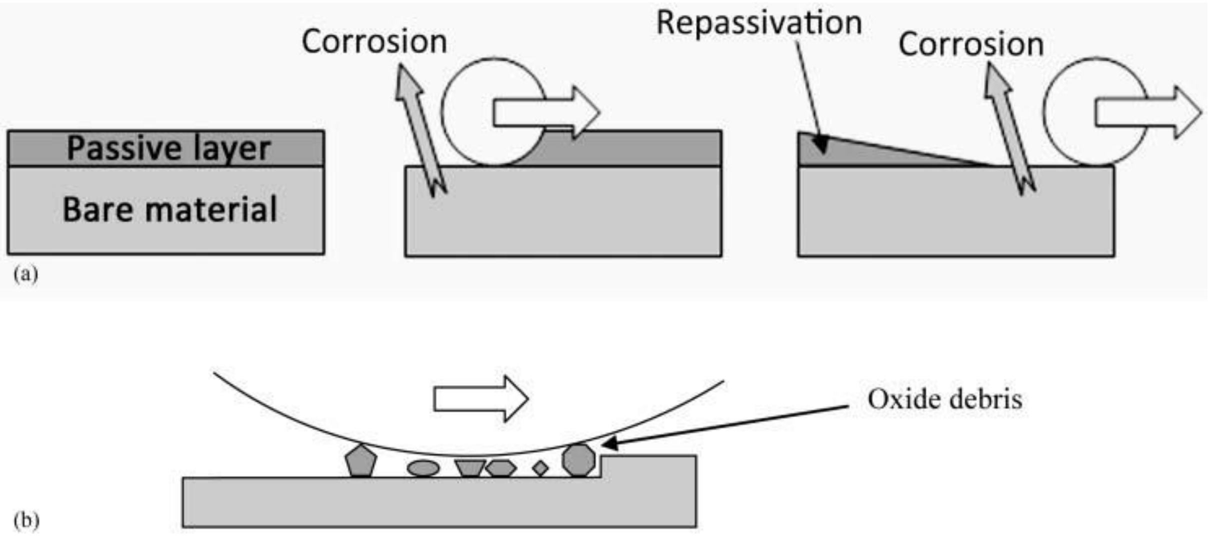

Fig.1. 21 Synergistic effect of corrosion on wear and vice versa. (a) Corrosion accelerated by friction. (b) Abrasion accelerated by corrosion products [57].

To study tribo-corrosion, many mechanical parameters need to be taken into account, including sliding distance, sliding velocity, normal load and roughness of the counterpart. For example, the depassivation rate is critically affected by the sliding velocity and roughness of the counterpart [58]. An example is given in Fig.1. 22 below. The wear track formed on AISI430 steel against by rough and smooth counterpart is presented in Fig.1. 22. It is found that there are obvious scars on the surface of AISI430 after rubbing with rough alumina ball. Furthermore, there is plenty of debris particles left after the test. As described above, these third bodies will also have influence on depassivation of materials. By contrast, the surface of sample is much smoother and less debris particles remained after rubbing with smooth ball, showing in Fig.1. 22 (b). Besides, the microstructure of material [59], passive layer properties [60] and the electrolyte pH values [61] influence consequently the tribo-corrosion process. Moreover, the tribo-corrosion damaging process could also be time-dependent. With variation of pH, surface reactivity, film thickness and chemistry can be modified during the experiment, resulting in a modification of the wear behaviour [62].

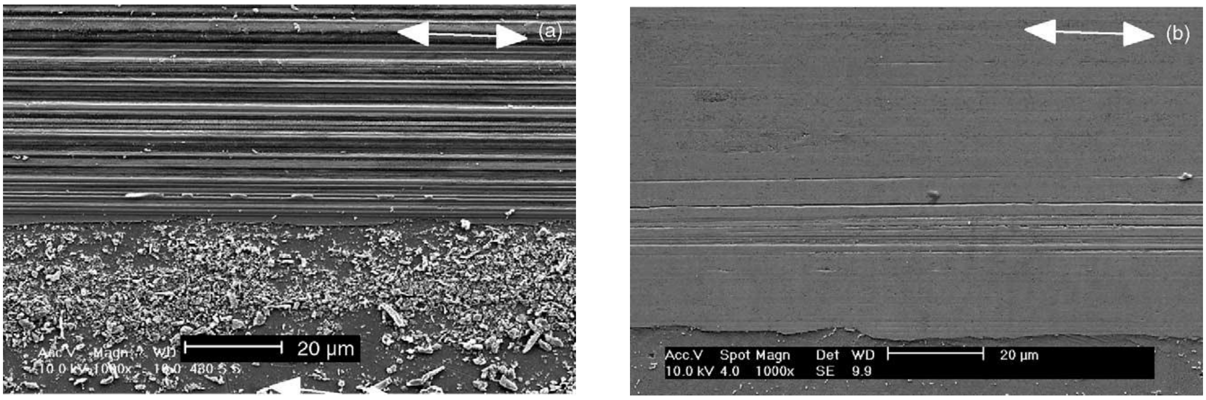

Fig.1. 22 SEM images of wear track on AISI430 steel after rubbing against a rough (a) and a smooth (b) alumina counterpart with 10 N normal force in acidic solution. The sliding direction is indicated by arrows [58].

1.4.4.4 Microbiologically induced corrosion (MIC)

In the environment where bacteria are present, the passivity could also be affected. The sulphate-reducing bacteria (SRB) are considered as the main corrosive species involved in microbiologically induced corrosion (MIC) materials' degradation [63]. With the increase number of bacteria prolifering, the interface between passive film and electrolyte is changed, resulting in inducing or accelerating the corrosion process [64]. Indeed, the bacteria will release metabolites when they are in contact with the surface. Furthermore, the structure and properties of the passive film could be also changed, with the influence of sulfidation from SRB [65]. A schematic of corrosion and biofilm formation process on X80 steel in SRB inoculated seawater is shown below in Fig.1. 23.

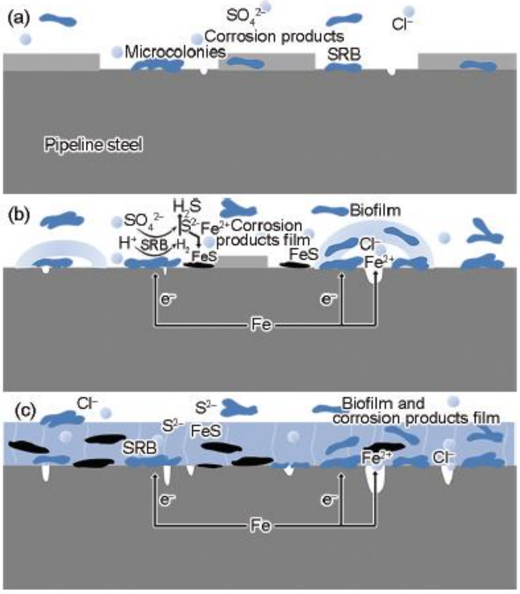

Fig.1. 23 Representation of biofilm formation and corrosion process at (a)the early stage, (b)middle stage and (c) final stage of X80 steel in SRB inoculated seawater [66].

In the first stage depicted in Fig.1. 23 (a), the bacteria mainly float in the solution, and gradually form microbial colonies producing extracellular polymer substances (EPS) which are resistant to corrosive ions and inhibit the corrosion of X80 steel. Then, in the second step, uneven biofilm forms on the steel surface with quick proliferation of bacteria. Meanwhile, S^{2-} reacts with Fe^{2+}, and forming FeS which adheres to the surface of the substrate, resulting in a localized corrosion cell. When there is existence of Cl^- in the solution, formation of pitting will be induced in the localized cell. In the last stage, SRB metabolites deposit on the steel surface, and a complete biofilm formed, which can inhibit uniform corrosion process in some extent. However, the biofilm is loose and porous. This heterogeneity can facilitate pit nucleation.

1.5 The models to study passivation behavior

In the previous part, the concept of passivity has been described. Thermodynamic and kinetic approaches were presented to define the existence of passive film. And finally, the nucleation, growth and breakdown mechanisms were displayed. However, to complete our understanding of the passivity, it is necessary to develop conjointly experimental procedures, data analysis and numerical modelling.

Nowadays, the main purpose of passivation studies relies on a better understanding of both physical and chemical properties of passive films by various techniques. As mentioned before, passive films are generally very thin and not visible to naked eyes. They must be studied by special surface analytical techniques to characterize their composition, their thickness and their structure. X-ray photoelectron spectrometry (XPS) can provide the information about the elemental compositions and the detected oxidation state [67–69]. X-ray absorption spectroscopy (XAS) presents the information about metallic, oxides and hydroxides separately [70,71]. The secondary ion mass spectrometry (ToF-SIMS) could be used for the chemical profiling of thick layers and their chemical imaging [72–74]. The atomic force microscope (AFM) could be for the analysis of passive layer morphology at the nanometric scale [75,76]. While it is possible to employ the scanning tunneling microscopy (STM) to characterize crystalline structure [77,78]. The electrochemical techniques contribute to characterize the resistance to corrosion but also evidence some physical properties of the passive layer as well as its reactivity. Linear sweep voltammetry (LSV) could be used to obtain the polarization curves [79,80], and electrochemical impedance spectroscopy (EIS) helps to determine the corrosion resistance and electronic/physical properties [81–83]. Mott–Schottky (M-S) is employed for determining their semi-conductive properties [84,85]. With the help of characterization techniques for studying passive film, the relationships among compositions of passive film, passive state and even type of semi-conductivity and defects concentration could be postulated. The analyses of these experimental data can provide crucial information on the passive behavior of materials and the properties of passive film but are often limited by the experimental conditions (short durations tests, applied potential, scan rate…) and do not allow to predict long term behavior of a material (even more in a fluctuating environment). Consequently, it is necessary to develop models that allow to put into equations the different processes occurring during nucleation, growth, steady state and breakdown of passive film, to predict the behavior of passive material. In the following part, the most common model use to describe the passive state and behavior are briefly reported.

1.5.1 High-Field Model (HFM)

In the High Field Model, it was firstly assumed that there is a high electric field in the film acting as driving force for change carriers transport, and the potential drop across the oxide film [86]. N. Cabrera and N. F. Mott [87] proposed a hypothesis that a strong field exists in the oxide film, due to a potential difference between metal and adsorbed oxygen on its surface, which enables the metal ions to move through it. A schematic diagram for the mechanisms is illustrated in Fig.1. 24.

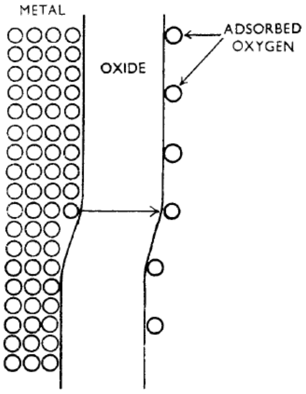

Fig.1. 24 Representation of the mechanisms by which ions leave a metal and pass through the oxide layer [87].

From their point of view, the formation of passive film at low temperature follows a logarithmic growth law,

$$1/X = A - B \ln t \tag{1.4}$$

X being the thickness at time t.

For sufficiently high temperatures, the films tend to be thicker, the oxidation will conform to the parabolic law, and expressed as:

$$X^2 = 2At \tag{1.5}$$

where X is the thickness of film at a time t after exposure to air and A is a constant.

Some assumptions were made to deduce the parabolic law:

- Both metal and oxygen are soluble within the oxide. There is a local thermodynamic equilibrium at both interface metal/oxide and oxide/air.

-The diffusion of metal or oxygen through the oxide layer under a concentration gradient which is proportional to $1/X$; the rate of growth dX/dt is thus proportional to $1/X$, and integration gives the parabolic law.

$$A = 2D_e\Omega[n_e(0) - n_e(X)] \tag{1.6}$$

Where D_e is the diffusion coefficient of the interstitial ions, $n_e(0)$ is the concentration of metal atoms, X is the thickness and $n_e(X)$ is the concentration of dissolved metal at the oxide-air interface.

According to the statements, electrons can pass the film easily, but ions can only penetrate it and migrate in the presence of a very strong electric field which supposed to be constant.

1.5.2 The Point Defect Model of the passive state (PDM)

The first generation Point Defect Model (PDM) was proposed by Digby D. Macdonald and his group in the early 1980s [88,89]. PDM is one of the main predictive models for passivation, it is used to describe the maintenance of passive film from growth to a steady state and even failure in the corrosive medium.

From the PDM point of view, passive films are described as a bilayer structure, consisting of a compact inner oxide layer generated at the metal surface and a porous outer hydroxide layer between the primary passive layer and the solution as presented in Fig.1. 25. Most of the electrochemical reactions take place at the metal/primary passive film and primary passive film/upper layer film interfaces.

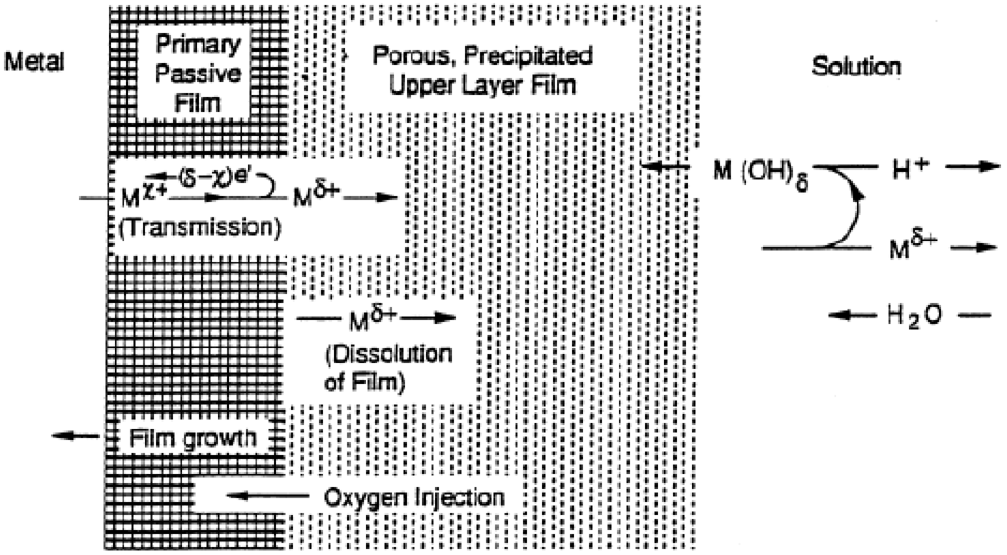

Fig.1. 25 Schematic of formation processes of bilayer passive films on surface of metal [90].

The PDM has been developed from the first to the third generation, the main assumptions of the three generations are listed below [88,89,91,92]:

- The passive film is composed of the inner oxide (a barrier layer containing defects, cationic vacancies, anionic vacancies or even interstitial cations) and an outer layer without defect, resulting from the precipitation of cations on the surface.
- The defects are generated and annihilated at the interface between the substrate and oxide film (barrier layer), or at the interface between the oxide film and the outer layer. The schematic reaction for the seven point-defect reactions occurring at the interfaces of the barrier layer is presented in Fig.1. 26.
- The strength of the electric field is constant in the film and does not vary with the potential. Thus, the variation of potential in the film is linear with the distance.
- The potential gradient is considered through the passive film. Moreover, the potential drop varies linearly with pH and applied voltage.
- The thickness of oxide film also varies linearly with pH and applied voltage.
- The current at steady state for n-type oxide film is independent of the applied voltage, while that for p-type oxide is exponentially dependent with the applied voltage.

- The outer layer of passive film also contributes to potential difference and passive current density.

- The ohmic potential-drop (IR) is partially responsible for the potential difference which is the driving force for film growing.

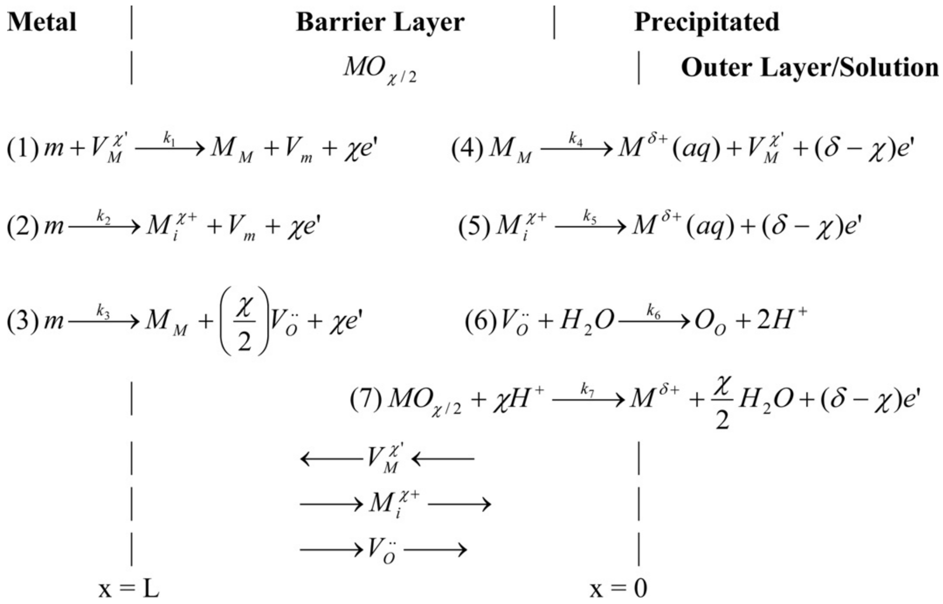

Fig.1. 26. Summarized PDM-II for the description of defect generation and annihilation at the interfaces of oxide layer and metal. $V_M^{x'}$ ≡ cation vacancy, $M_i^{x^+}$ ≡ cation interstitial, V_m ≡ vacancy in metal phase, $V_{\ddot{O}}$ ≡ oxygen (anion) vacancy, $M^{\delta+}$(aq) ≡ cation in outer layer/solution interface, M_M ≡ cation in cation sublattice, O_O ≡ oxide ion in anion site on the anion sublattice, $MO_{x/2}$ ≡ stoichiometric barrier layer oxide.

In Fig.1. 26, reactions 1-3 happen at the interface between the metal and the barrier layer, while reactions 4-7 occur at the interface between the barrier layer and the precipitated layer. In reaction 1, metal vacancies in the oxide are consumed at the interface between the metal and barrier film by the oxidation of the substrate. There are amounts of generated electrons that equal to the oxidation state in the oxide, corresponding to the charge of the metal vacancies (χ). These metal vacancies $V_M^{x'}$ are produced at the interface between the outer layer and solution by the reaction 4 where the metal ions from oxide are ejected. The charge of the dissolved species(δ) at the interface between the outer layer and solution are produced. Consequently, (δ-χ) electrons are generated. The reaction 2 is concerning to the injection of metal interstitials at the interface between the metal and barrier film into the oxide network. The cations are injected into the interstitial site of oxide crystal, generating electrons. In parallel, like reaction 4, the reaction 5 reveals the process of the transfer of these interstitial ions from oxide film to outer layer. The growth process of barrier layer into the metal is concluded by the reaction 3. During this process, oxygen vacancies $V_{\ddot{O}}$ and electrons are generated. The oxygen vacancies are consumed at the interface between the barrier layer and electrolyte, as seen in reaction 6. Finally, the dissolution of passive film is demonstrated in reaction 7. The film dissolves at the interface between the barrier layer and the electrolyte. It is noting that reactions 1, 2, 4, 5 and 6 are conservative whereas reactions 3 and 7 are nonconservative. The conservative reactions concerning the transport and movement of ions within the passive film, while nonconservative reactions are to maintain finite thickness of passive films. Reaction 3 is for the generation of film whereas reaction 7 results in the dissolution of passive film.

There are over 30 kinetics, physics and diffusion parameters involved for modelling passive process with PDM [93]. It obviously increases the difficulties for modelling since each change of parameters could make the ideal fitting results far away from the experimental data. Nevertheless, the PDM has been successfully employed for the study of passive films formed on different materials such as iron [94], tungsten [95], zinc [96], titanium [97–100] and 316L stainless steel [101], and also different types of corrosion cases [88,102–106].

1.5.3 The Mixed Conduction Model (MCM)

The Mixed Conduction Model (MCM) was developed for assessing quantitative information for the transport parameters of passive film, and it was mainly applied on studying electrochemical behavior of nickel and iron based alloys [107,108]. Also, this theory has been introduced to study the oxide film formed at high temperature [109,110]. The MCM takes basic concepts from the PDM, but there are a few other assumptions proposed, making it different from the PDM.

The passive film is considered as a homogenous single-phase oxide, and hydroxide is excluded in the MCM. In the MCM, the transport of ionic species is influenced by the electric field strength. Furthermore, the MCM emphases on low potential field at room temperature, whereas the high potential field is used at high temperature. The MCM considers that the conductivity of the passive film is linearly dependent on the concentration of ionic defect. For general transport description, the Fromhold–Cook equation are employed instead of the Nernst–Planck equation. The simplified schematic system for the MCM is illustrated in Fig.1. 27 below:

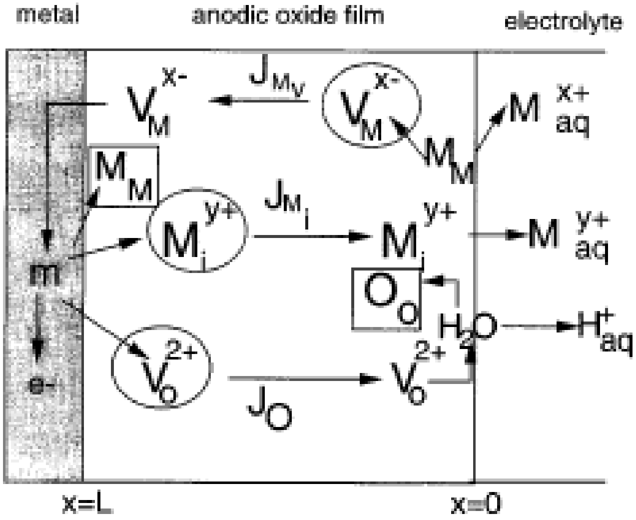

Fig.1. 27 The schematic reactions at interface between oxide film and metal and interface between oxide film and electrolyte [107].

At the interface between the metal and anodic oxide film, the annihilation of metal vacancies occurs concomitantly with the injection of interstitials metal ions and oxygen vacancies. The migration of defects is supposed to proceed in the anodic oxide film, with the assistance of high electrical field. At the interface between the oxide film and electrolyte, cation vacancies are generated from the ejection of metal ions from their positions in the oxide lattice in reaction (1.7.1). The dissolution of interstitials is presented in (1.7.2).

$$M_M^{III} \overset{k_3}{\rightarrow} V_M^{3-} + M_{aq}^{3+} \tag{1.7.1}$$

$$M_i^{2+} \overset{k_{3,i}}{\longrightarrow} M_{aq}^{x+} + (x-2)e^- \tag{1.7.2}$$

The dissolution of the oxide film is illustrated in reaction (1.8) to keep the balance between the steady state of the oxide film and growth reaction.

$$M_2O_3 + 6H^+ \overset{k_4}{\rightarrow} M_{aq}^{3+} + 3H_2O \tag{1.8}$$

1.5.4 The Generalized Model (GM)

The GM was developed for modelling the oxide growth kinetics, considering the evolution of the interfacial potential drops during the oxide growth. It is worth mentioning that the parameters relative to the substrate composition and the limited growth because of the flux of oxygen vacancies through the film are considered in GM, in comparison with PDM. The generalized oxide growth model considers the non-stationary conditions of oxide growth, for example, potential drop evolution at the interface between the oxide and electrolyte, and evolution of the electric field within the film during oxide growth. Also, it includes all the reactions occurring at the interface between the metal and oxide film and the interface between oxide film and electrolyte. Finally, the balance between the oxide film growth and release of alloying elements into the solution is considered as well. The interfacial reaction scheme is presented in Fig.1. 28.

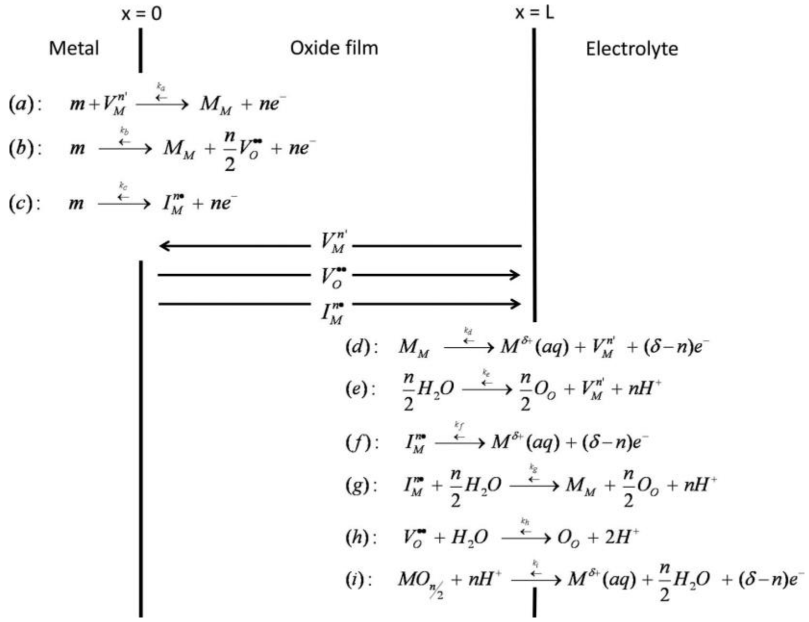

Fig.1. 28 Schematic for reaction and transport processes at metal/oxide and oxide /electrolyte interfaces during the growth of the oxide layer [111].

Several interfacial reactions are presented in the scheme. At the interface between the metal and oxide film, (a) Insertion of cations into a cation vacancy, (b) Formation of oxygen vacancies and (c) Insertion of cations into an interstitial site of the oxide. At the interface between the oxide film and electrolyte, (d) Cationic dissolution with creation of vacancies, (e) Formation of cation vacancies, (f) Dissolution of cations in interstitial position, (g) Growth of the oxide by reaction of an interstitial cation with H_2O, (h) Insertion of oxygen by replacement of an oxygen vacancy and (i) Electrochemical dissolution of the oxide.

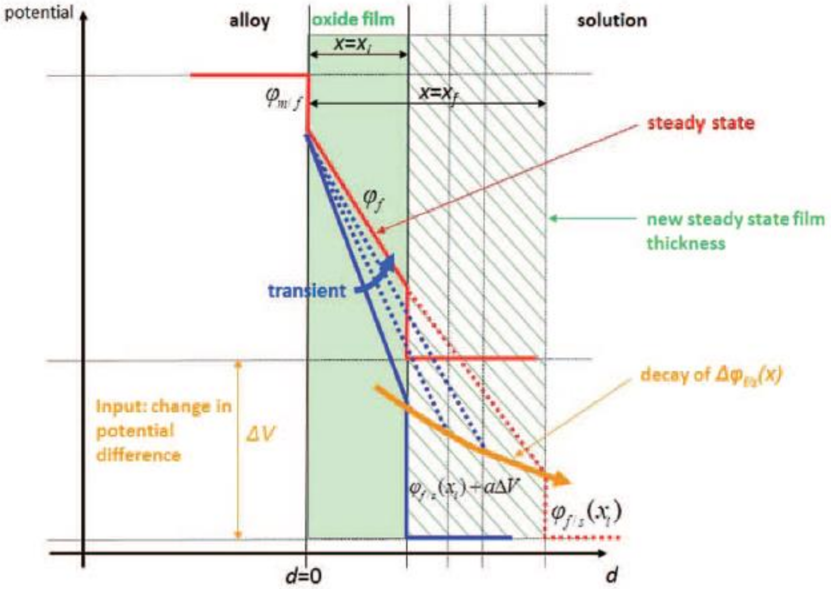

Fig.1. 29 Change of the steady state when increasing the electrode potential [112].

Fig.1. 29 shows the principal hypothesis on the evolution of the potential drop across the oxide film. The electric field in the film is constant at steady state (in red), while that changes under non-steady transient state (non-steady, in blue) conditions. The potential drop will go back to its original place once steady state is reached again. During this process, the ions transport will be introduced with the increase of the electric field, resulting in the increase of the film thickness. In addition, the dissolution of oxide might occur at the interface between the film and electrolyte, leading to an increase in the electric field. As a result, the oxide thickness increases. The steady state will be achieved again when the dissolution rate of oxide equals to the formation rate at the considered electric field.

1.5.5 Diffusion Poisson Coupled Model (DPCM)

The Diffusion Poisson Coupled Model (DPCM) is the model developed, and aiming to modelling the corrosion behavior of iron based alloy for nuclear waste repository under anaerobic conditions in anoxic groundwater [113]. DPCM is similar to PDM and MCM except for the potential profile through the oxide. PDM and MCM consider that the potential linearly changed with the distance within the oxide whereas that for DPCM is calculated with the Poisson equation given below, and the potential profile is presented in Fig.1. 30.

$$\nabla^2\emptyset = -\frac{F}{\chi\chi_0}\sum_i z_i c_i - \frac{\rho_{hl}}{\chi\chi_0} \tag{1.9}$$

Where ∇^2 is the Laplacian. χ and χ_0 is corresponding to the dielectric constant of the oxide and the vacuum dielectric constant, respectively. F is the Faraday constant. c_i is the concentration profile of the charge carrier within the oxide and z_i is its charge. ρ_{hl} is the net charge density of the lattice which is assumed to be homogeneous.

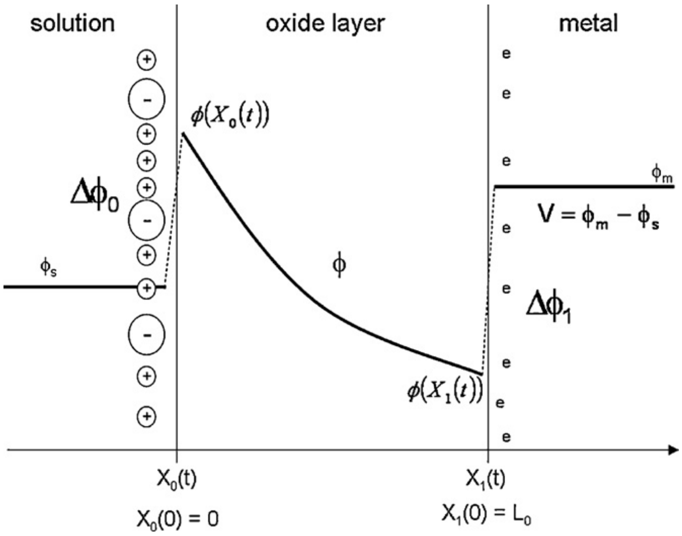

Fig.1. 30 Potential profile in the solution/oxide layer/metal system from DPCM [113].

In the DPCM, the interfaces of the iron oxide layer are moving. They are denoted by the outer interface $X_0(t)$ (oxide/solution) and the inner interface $X_1(t)$ (oxide/metal). There are three charge carriers taken into account within the oxide layer, they are electrons, cations (Fe^{3+}) and oxygen vacancies ($V_O^{\cdot\cdot}$). The boundary conditions for densities of these three charge carriers are linear convection–diffusion and coupled with a Poisson equation for the electrical potential. The boundary conditions for the Poisson equation considered that the metal and the solution could be charged because of their electronic and ionic properties and this accumulation of charges is described with the Gauss law. Moreover, these accumulations of charges depend on the voltage drop at the interface by the usual Helmholtz law which links the charge to the voltage drop through a capacitance. Finally, the evolutions of a dense oxide layer, corrosion rate etc. with pH value and time were obtained proving the efficiency of the model [114].

1.5.6 The Coupled Current Charge Compensation model (C4)

The Coupled Current Charge Compensation (C4) model is developed for describing differentiated oxidation kinetics in zirconium based alloys [115]. The C4 model assumes that space charges are created by doping of zirconium oxide or by alloying elements, which creates oxygen anion vacancies in the oxide. The C4 model mainly based on the framework of Fromhold for describing mobility equation relating the fluxes to the electric field and charged species concentrations. The relation is defined in the equation (1.10) and schematic of the oxidation process of zirconium alloys is shown in Fig.1. 31.

$$J_s = g(E, C_s) \tag{1.10}$$

Where g is an integral function.

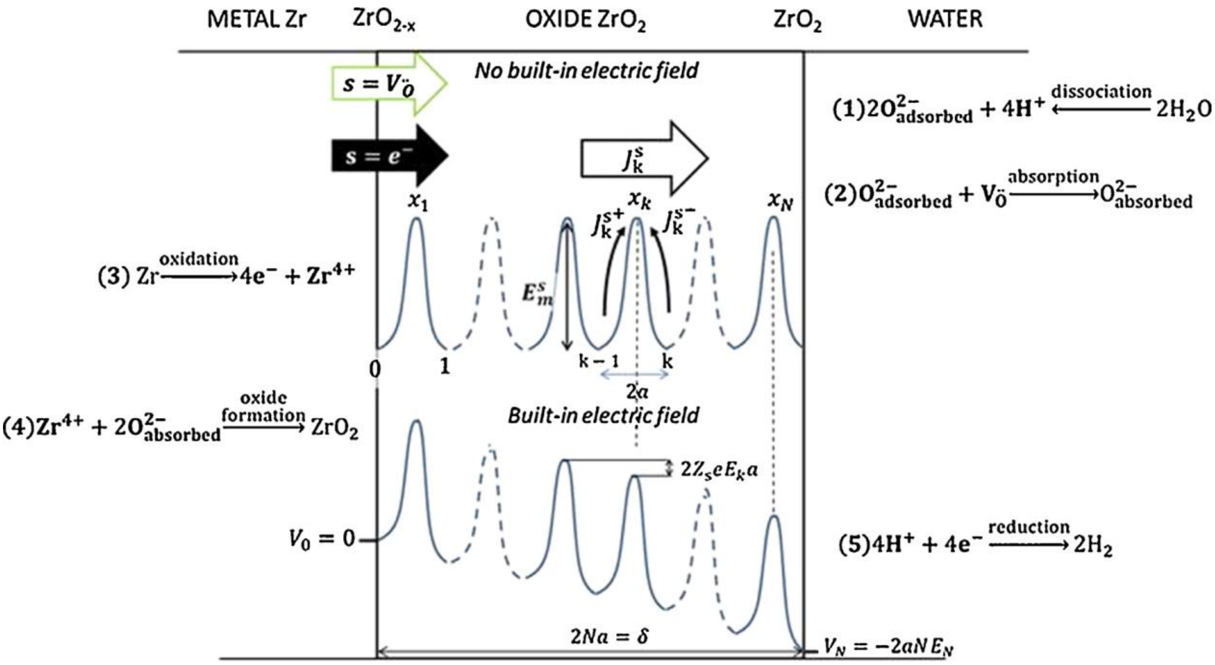

Fig.1. 31 Scheme of the discrete lattice and the effect of the built-in electric field on the potential energy diagram [115].

The oxidation process can be conceptually divided into several steps, as presented in Fig.1. 31. Firstly, oxygen in the water molecule dissociates and is adsorbed onto the oxide layer surface (Fig.1. 31, reactions 1 and 2). Because of the defect concentration gradient, the oxygen anions diffuse either through the bulk of the oxide or along the oxide grain boundaries. When the oxygen anion reaches the oxide–metal interface, it reacts with Zr cations to form new oxide (Fig.1. 31, reactions 3 and 4). The formation of this new oxide releases electrons, which then migrate through the oxide to reduce the hydrogen ions at the cathodic site (Fig.1. 31, reaction 5)

The C4 model proved that the effect of space charges is compensated by oxidized Nb^{3+} in solid solution, resulting in near parabolic oxidation kinetics. On the contrary, if there are no enough oxidized alloying elements presented in the oxide to compensate space charge, it was expected having sub-parabolic kinetics in the case of Zircaloy alloys. Moreover, the C4 model has also been successfully applied on oxidation and hydriding kinetics of Zr–0.5Nb and Zr–1.0Nb alloys for hydrogen pickup, which considered the proton migration energy closed to transition in oxidation kinetics [116].

1.5.7 Short conclusions on model for passive phenomenon

From the first proposed passive film growth model of HFM to the three generation of PDM, and later MCM, DPCM and GM, even C4, the development of growth model for passive film has been conducted by international researchers and are still ongoing. In the first, HFM was fail to account steady-state and pH effect, but also complex alloys. Then both PDM and MCM are restricted to certain applications due to the free adjustable parameters electric field and outer layer polarizability [113]. Later, the DPCM was proposed to integrate Poisson equations for the electric potential. GM is the model dedicated for non-stationary system while other models consider quasi-steady-state. C4 is the model that takes into account the creation of space charge which is one of most important parameters for passive film properties, but this model is only used on Zr alloy yet. For further development of models, more experimental data might be needed and the schematic for synergy between models, passivation mechanisms and experimental data could be displayed as below.

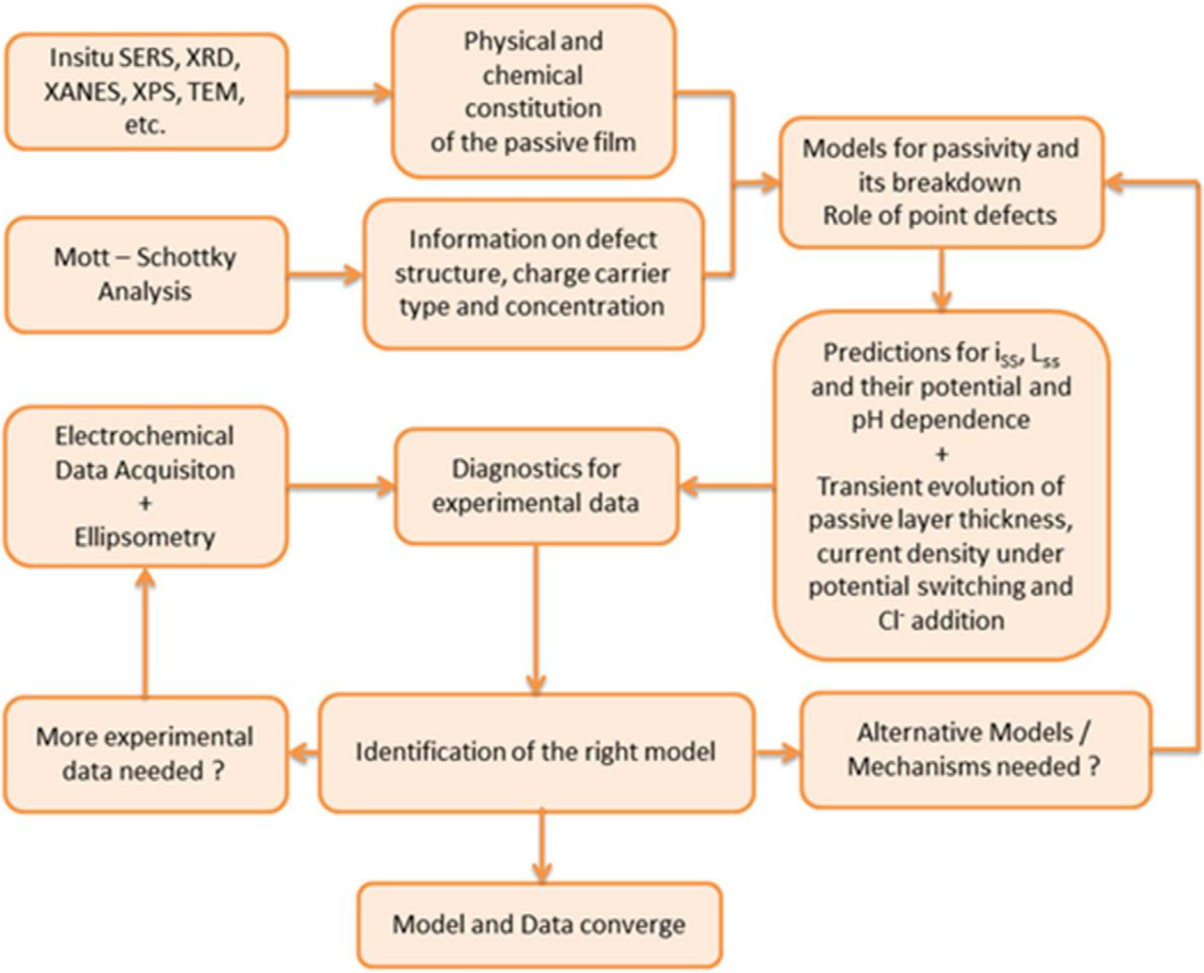

Fig.1. 32 The flowchart for synergy relationship among models, mechanisms and data [117].

It is found that to model corrosion mechanism, the process of data gathering is important. The characterization techniques, like XRD, XPS, XANES and TEM etc., help to recognize valence states of ions, chemical compositions and structure of passive film. With the help of Mott-Schottky analysis, the carrier type of the semiconducting oxide as n-type or p-type is able to be found, and also defects or charges concentrations in the passive films can be calculated. As a result, this information is helpful for the model prediction. While electrochemical tests provide information about passive potential, passive state, passive current density, passivity break-down potential etc., which provides massive data for modelling. These data can be obtained from polarization curves. Moreover, it is possible to have kinetics parameters, like transfer coefficients and rate constants, from EIS measurements [118]. However, since EIS data is model-dependent, it is important to investigate the analysis EIS data by looking for analytical procedure that provide physical parameters.

Numerical models tried to explain variation of the passive current density and thickness of the passive film with applied potential, pH and different ions in the solution, and it is supposed to be distinguished from the transient evolution [117]. Therefore, the experimental data, especially the evolution of passive current density, thickness of passive film with applied potential or electrolyte condition, is helpful to identify the right models allowing model and data converging.

1.6 Conclusion

The present bibliographic review begins with the history and definition of passivity. Then, the common properties of passive films are listed. After that, possible mechanisms for formation of the passive film were presented, followed by thermodynamics and kinetics of passivation. At the end, the breakdown of passive film in different situations, such as anodic dissolution, cathodic breakdown because of hydrogen, localized corrosion, mechanical or biological effects etc. are presented. Moreover, some models are introduced briefly, including the High-Field Model (HFM), the Point Defect Model (PDM), the Mixed Conduction Model (MCM), the Generalized Model (GM), Diffusion Poisson Coupled Model (DPCM) and the Coupled Current Charge Compensation model (C4). Even though those models were firstly developed for different uses in specific situation, they provide various ideas for describing the oxidation kinetics or predicting lifespan of passive films.

The main goal of researchers who work either on experimental or modelling on corrosion behavior of alloys, is to understand corrosion, to improve corrosion resistance, and enhance corrosion prevention or monitoring. They should consider the cost of maintenance, service life, replacement costs. However, better designing the composition of materials from the first step of design could be a first economic practice. Hence, to reach this goal, it is necessary to better understand the role of alloying elements content on corrosion behavior. Considering how could we better understand it, both experiments and modelling are needed. To be able to model passivation of alloys, plenty of information about passive films is required. For instance, the composition and structure of passive films, formation potential on passive state, type and concentrations of defects in the passive etc. Extracting more information about passive film by electrochemical methods, especially passive film structure or other physical properties, in order to collect and provide possible relevant data for numerical modelling is the main purpose of this thesis.

Chapter 2 Experimental details

2.1 Introduction

This chapter is devoted to the description of information about materials used in the experiments, the presentation of different electrochemical techniques employed for passive film studies and surface characterization technique for passive film composition analysis.

2.2 The materials for experiment

2.2.1 Composition of the materials

The binary model alloys Ni-xCr (x= 16, 20, 24 and 28) were used to study the effect of chromium content on their passivation behavior. Furthermore, the ternary model alloys Ni-xCr-8Fe (x= 14, 22 and 30) have been also employed to study the role of iron in passivation behavior, especially in secondary oxidation process. These model alloys were supplied by Sumitomo Metal Industries, Ltd, Japan, prepared by the method of hot-rolling plates. Then, homogenizing at 1230°C for 10 hours and solution annealed at 1180°C for 30 minutes, finally quenched with water. In parallel, the commercial alloys Inconel 600, 625 and GILPHY 80(Ni80Cr20) were also found to compare their passivation behavior with that of model alloys. In which, the alloy Inconel 600 is from the company Goodfellow, the alloy Inconel 625 is the product of company ArcelorMittal, while GILPHY 80 is from Aperam Alloys Imphy. The chemical composition of all the materials was reported in Table 2. 1 below.

Table 2. 1 Chemical composition (wt. %) of the different alloys.

Materials	C	Si	S	Cr	Mn	Fe	Mo	Ti	Nb+Ta	Ni
16Cr	0.006	<0.001	<0.001	15.7	0.049	0.015	-	-	-	Bal.
20Cr	0.008	0.009	<0.001	19.8	0.045	0.018	-	-	-	Bal.
24Cr	0.004	0.008	<0.001	23.8	0.047	0.027	-	-	-	Bal.
28Cr	0.006	0.006	<0.001	27.6	0.045	0.024	-	-	-	Bal.
14Cr8Fe	<0.001	0.02	<0.001	14.7	0.05	7.81	-	-	-	Bal.
22Cr8Fe	<0.001	0.02	0.001	21.6	0.05	7.84	-	-	-	Bal.
30Cr8Fe	<0.001	0.02	0.001	29.4	0.05	7.85	-	-	-	Bal.
600	<0.15	0.5	<0.015	15.5	<1.0	7	-	0.2	-	Bal.
625	<0.05	<0.05	<0.01	20.6	<0.5	<5	8-10	0.4	3.15-4.15	Bal.
G80	<0.15	1-1.6	-	20	<1	<1	-	-	-	Bal.

2.2.2 Preparation of the materials

All the mirror polished specimens were followed the steps below for surface preparations: the samples were firstly ground with SiC papers from grit 80, successively through 180, 400, 800, 1200 and 2400 up to grit 4000, then followed by mirror polishing to 3 µm and 1 µm with diamond paste. The specimens were cleaned with deionized water in an ultrasonic bath for 5 minutes before each grinding and polishing step. Finally, they were cleaned in ethanol and dried with argon. The polished samples could be used for electrochemical tests. While those for structure observation, the materials are needed to polished up to 0.03 µm with suspension SPM (colloidal silica), and then chemically etched for 90 seconds in the mixed acid solution at room temperature. The acid solution composes of acetic acid ($C_2H_4O_2$), hydrochloric acid (HCL) and nitric acid (HNO_3), with the volume ratio of 2:1:2, respectively. Etched coupons were subsequently ultrasonically cleaned in pure water and dried with argon flow.

2.2.3 Structure characterizations

The microstructures were observed with the optical microscopy of Olympus, the observed microstructure is presented in the Fig. 2. 1.

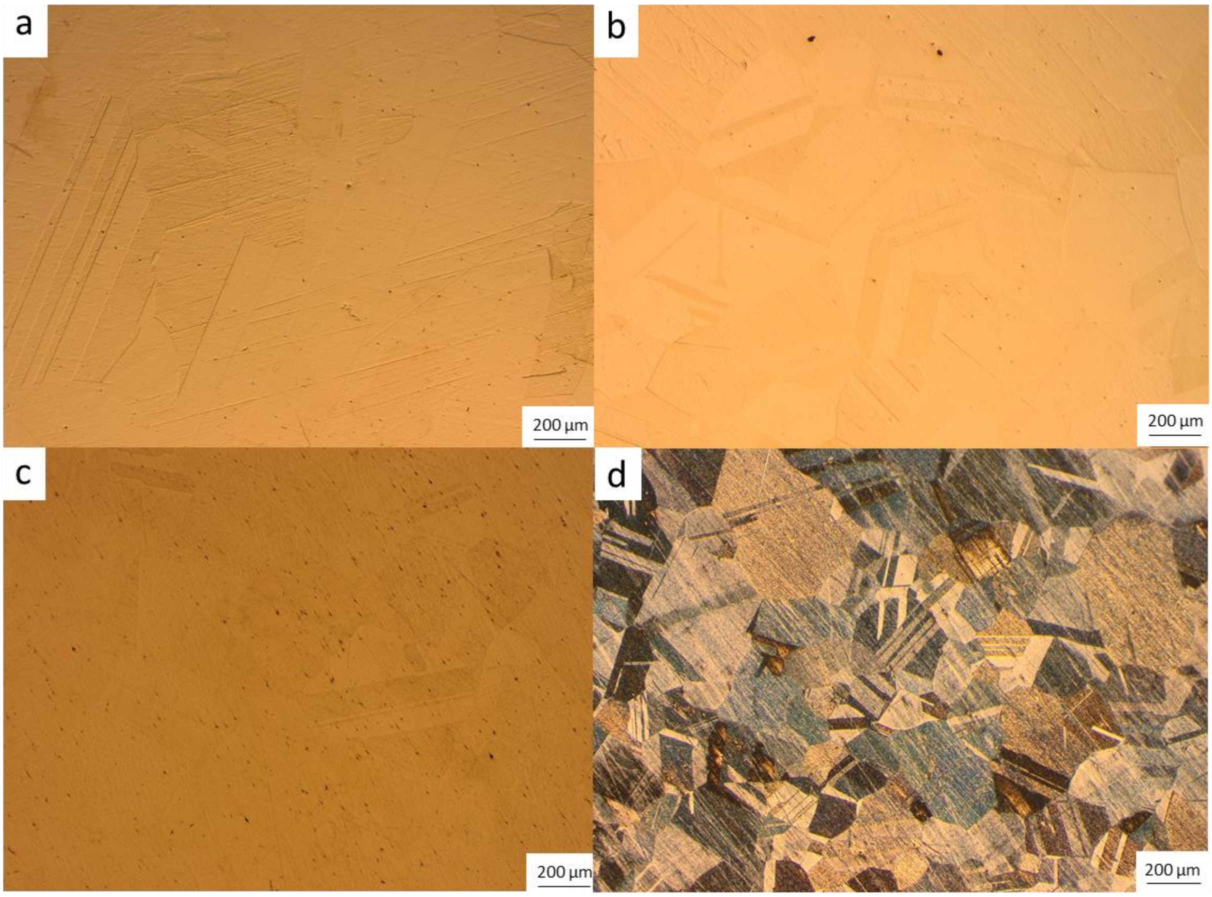

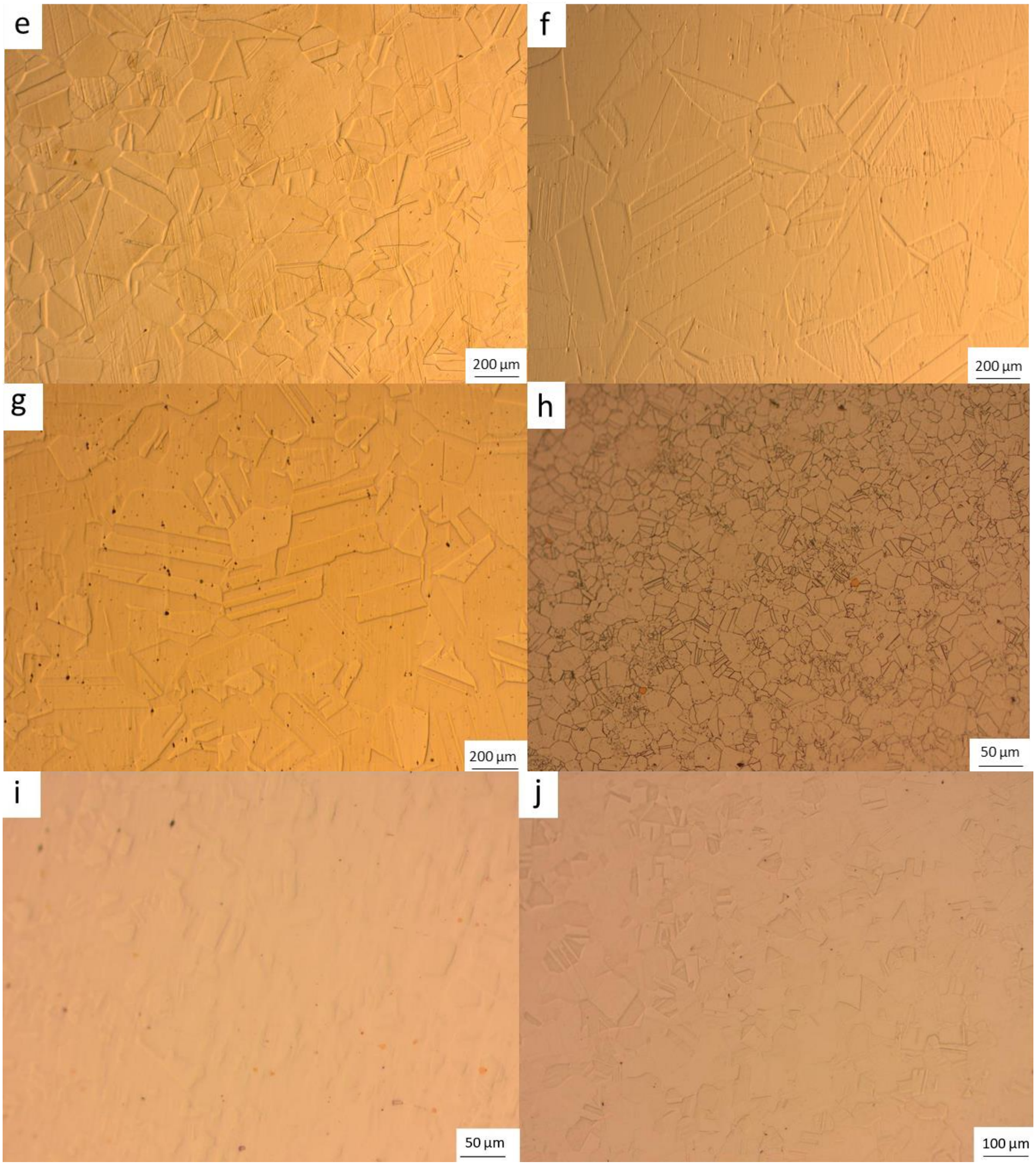

Fig. 2. 1 The microstructure of chemically etched samples: (a) Ni-16Cr, (b)Ni-20Cr, (c) Ni-24Cr, (d) Ni-28Cr, (e) Ni-14Cr-8Fe, (f) Ni-22Cr-8Fe, (g)Ni-30Cr-8Fe, (h) Inconel 600, (i) Inconel 625 and (j) GILPHY 80

The samples characterized in Fig. 2. 1 all exhibit a single austenite phase. Annealing twins are also characterized, indicating that the materials were deformed and then annealed. Scanning Electron Microscopy (SEM, ZEISS SUPRA 55VP) was employed in the study, to characterize the surface morphology of specimens with Secondary Electrons (SE=10 eV) after chemical etching. Energy Dispersive X-ray Spectroscopy (EDS, OXFORD system with X-Max 50 mm^2 detector) was used to determine the compositions of etched samples. With regard to EDS analysis, no carbides were found in the model alloys. On the contrary, carbides $Cr_{23}C_6$ and TiN were found in the commercial Inconel 600, while TiN/NbN were found as the precipitated phase in the commercial Inconel 625.

2.2.4 Calculation of grain size

The average grain size was estimated with the reference from Lineal Intercept Procedure from ASTM-E112 -96 (2004) [119]. The main idea of this method is that by using a certain length of straight line to cut through the grains. Then it is possible to calculate the average length of straight line through a grain, namely, the average grain size expressed as below:

$$Average\ grain\ size = \frac{L}{N} \tag{2.1}$$

where L is the length of straight line, and N corresponds to the total number of intercepted grain boundaries. It is noting that the number of grain boundary was focused for grain size calculation. The schematic description for the grain size measuring is shown in the Fig. 2. 2.

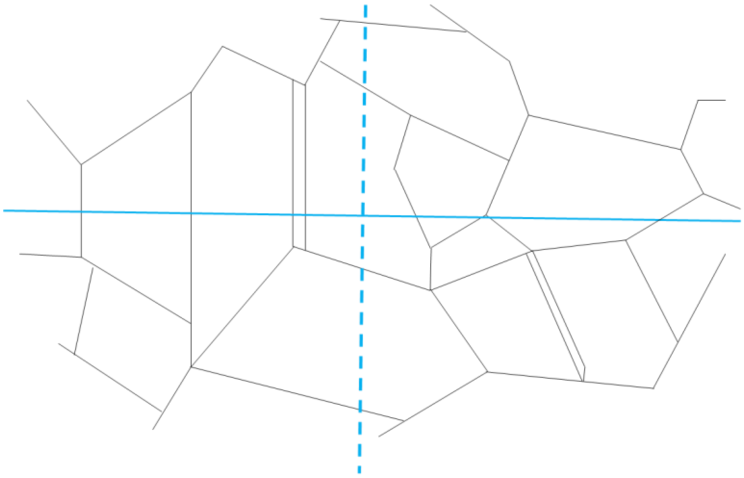

Fig. 2. 2 The schematic description of Lineal Intercept Procedure for grain size.

In Fig. 2. 2, the line in the horizontal direction crosses five grain boundaries, that is, four grains could be counted. In this situation, the line which crosses on twining caused by solution annealing process is not considered as one grain boundary. On the other hand, both ends of the line do not pass through the entire crystal grain, thus these two grains are not considered. Then, with the help from the software Image J, the length of the cross-section could be recorded, and the average grain size could be calculated from equation (2.1). The same measurement was performed three times in the horizontal direction and the vertical direction (presented in dashed line), respectively. Consequently, the presented average grain size for each sample is the average value of six measurements. The calculated grain size of different samples is listed in the Table 2. 2.

Table 2. 2 Calculated grain size of different samples

Materials	Grain size/ µm
16Cr	281±65
20Cr	265±37
24Cr	308±16
28Cr	186±13
14Cr8Fe	150±29
22Cr8Fe	301±52
30Cr8Fe	220±22

Inconel 600	16±2
Inconel 625	29±5
GILPHY 80	61±6

It is found that the model alloys have generally much bigger grain size in comparison with the commercial alloys.

2.3 Electrolyte for electrochemical measurements

The solution of 0.05 M H_3BO_3 + 0.075 M $Na_2B_4O_7$ $10H_2O$ (pH=9.2) was specifically selected for studying passive film because the solubility of the Cr-rich oxide is generally low, while the oxygen has a high solubility in the borate solution [120–122]. Other two aerated solutions of different pH were used for the electrochemical tests: 10 g/L Na_2SO_4 buffered with H_2SO_4 (pH=2), 0.01 M Na_2SO_4 (pH=5.8), and these solutions were selected to study the passive behavior in acidic, neutral, and basic solution. All the electrochemical measurements were performed at room temperature (22 ± 3°C).

2.4 Electrochemical analysis

2.4.1 Electrochemical test setup

The conventional three-electrode cell was used for the electrochemical measurements. The schematic illustration of the experimental setup is presented in the Fig. 2. 3 below.

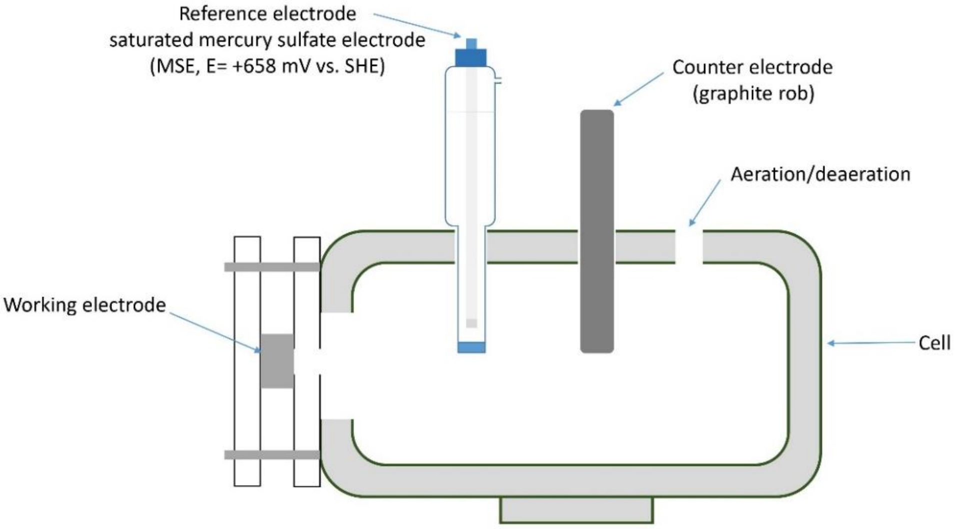

Fig. 2. 3 The schematic illustration of the setup for the electrochemical test (with 50 mL electrolyte).

The different alloys (exposure area = 0.56 cm^2) were used as the working electrode. A large graphite rod was used as the counter electrode, and a saturated mercury sulfate electrode (MSE, E= +658 mV vs. SHE), from Radiometer analytical®, was used as the reference electrode. The electrochemical measurements were carried out with the Gamry Reference 600™ electrochemical potentiostat.

2.4.2 Open circuit potential (OCP)

Open circuit potential (OCP) is the mixed potential where the anode current and the cathode current are equal. The working electrode's potential is measured with respect to the electrode in reference. There are no current flows to or from it, or potential existing in the cell. It characterizes the nobility of the material. When the value of OCP become stable, the following electrochemical tests could be carried out. In general, OCP could provide preliminary information about the metal/passive film system. Its evolution evaluates the stationarity of the system. OCP monitoring indicates if the working electrode have reached a stationary state. This helps to decide the immersion time before launching impedance or other techniques. In this thesis, 24 hours of OCP was performed on each specimen to be sure that the passive film reaches its steady state.

2.4.3 Linear sweep voltammetry (LSV)

Linear sweep voltammetry measurement gives access to current-voltage curves. By applying linearly varied potential on the working electrode, starting from a given potential up to a cathode or anode final potential. The corresponding current densities are continuously recorded. In general, polarization curves are shown as the plots of log |i| vs. E, which is the basic kinetic law for the electrochemical reactions. Respecting certain conditions, it also provides a means of identifying important electrochemical parameters such that the corrosion current density, the Tafel slope as well as the diffusion coefficient of species taking place in electrochemical kinetics. In the experiments, the linear sweep voltammetry was performed from cathodic direction −0.2 V vs. E_{OCP} to anodic 1.2 V vs. E_{OCP}, with a scan rate of 0.5 mV/s.

2.4.4 Electrochemical impedance spectroscopy (EIS)

2.4.4.1 The theory of the electrochemical impedance

The electrochemical impedance spectroscopy is a non-destructive measuring method, which is usually performed when the system is in the stationary state. A response of current could be observed after a weak sinusoidal electrical potential is imposed into a stationary system. The input potential could be written as $E = E_0 + \Delta E\,\sin(\omega t)$, thus a sinusoidal current $I = I_0 + \Delta I\,\sin(\mathrm{\omega t} - \varphi)$ is measured. The operation principal of EIS is shown in Fig. 2. 4 below.

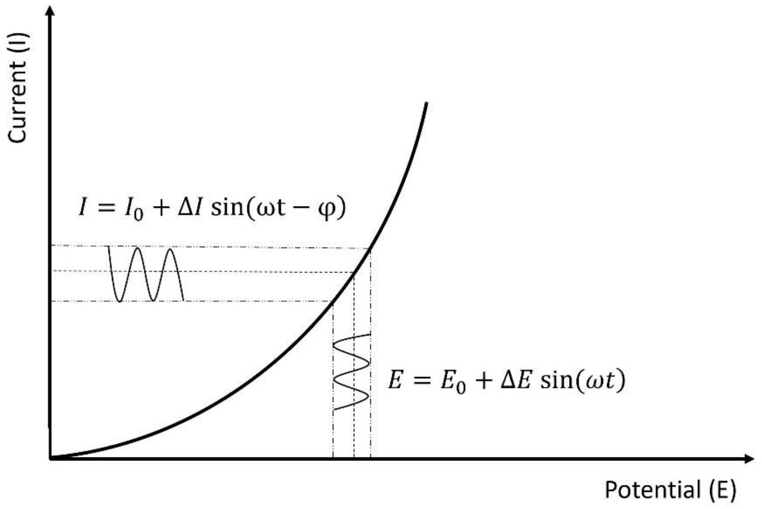

Fig. 2. 4 The representation of the measured electrochemical impedance spectroscopy.

ΔE and ΔI represent the amplitudes of the signals, E_0 and I_0 are the stationary components, ω corresponds to the pulse signal, and finally φ is the phase angle. Then, the impedance $Z(\omega)$ corresponds to:

$$Z(\omega) = \frac{E}{I} = |Z|\, exp(j\omega) \tag{2.2}$$

The real part Z' and the imaginary part Z'' compromise the complex value of impedance $Z(\omega)$, presented by the module $|Z|$and the phase φ :

$$Z(\omega) = Z'(\omega) + jZ''(\omega) \tag{2.3}$$

$$|Z| = \sqrt{((Z')^2 + (Z'')^2)} \tag{2.4}$$

$$\varphi = tan^{-1}\frac{Z''}{Z'} \tag{2.5}$$

The causality, the linearity and the stability must be satisfied for the measured system [123].

(a) The causality. There must be a causal relationship between the disturbance and the response within the system. In other words, the output signal could be only from the input signal in the system, and other irrelevant signal must be ignored.

(b) The linearity. The measured system must be a system with linear function: the output signal should be as the function of the input signal.

(c) The stability. The system must be stable regarding with the input signal, that is to say, the system could get recovered when the disturbing signal stopped. The input disturbing signal would not change the structure of the system.

The linearity is ensured by the use of a low amplitude signal, while the causality and stability are guaranteed by the former OCP monitoring before the impedance measurement. What's more, with the help of Kramers—Kronig transforms, the electrochemical impedance data could be validated with reference to the condition of linearity and stability [124].

In the experiment, impedances performed at OCP measured in the frequency range of 10 kHz to 0.05 Hz with 8 points per decade and a sine wave with 10 mV amplitude. While the impedances performed at other potentials measured the frequency range of 10 kHz to 0.1 Hz with 8 points per decade and a sine wave with 10 mV amplitude.

2.4.4.2 Interpretation of the impedance diagrams for passive films

In blocking system, constant-phase element (CPE) is often observed and used to fit impedance diagram which response follows CPE behavior. CPE parameters are considered to arise from a distribution of time-constants. The CPE impedance is expressed in terms of model parameters [125]:

$$Z_{CPE} = \frac{1}{(j\omega)^{\alpha} Q} \tag{2.6}$$

Under the assumption that the dielectric constant is independent of position and permittivity along the film thickness is uniform, M. Orazem and B. Tribollet et al. [126,127] put forward Power-Law Model (PLM) for the passive film, assuming the conductivity through passive film following a normal power-law distribution. This model was verified by both numerical simulations and experimental results. The resistivity distribution to follow a power-law as:

$$\frac{\rho}{\rho_{\delta}} = \xi^{-\gamma} \tag{2.7}$$

where $\xi = {}^{\gamma}/_{\delta}$ is the dimensionless position, γ is corresponding to the position through the film, δ is the thickness of passive film. ρ_{δ} represents the resistivity where $\xi = 1$. γ is a positive constant about the resistivity variation. Then the resistivity at where $\xi = 0$ is expressed as:

$$\frac{\rho}{\rho_{\delta}} = \left(\frac{\rho_{\delta}}{\rho_0} + \left(1 - \frac{\rho_{\delta}}{\rho_0}\right)\xi^{\gamma}\right)^{-1} \tag{2.8}$$

Where ρ_0 and ρ_{δ} are the resistivity at the interface between the metal or alloy and film, the interface between the film and the electrolyte, respectively. An example of power-law distribution of resistivity versus the dimensionless distance.

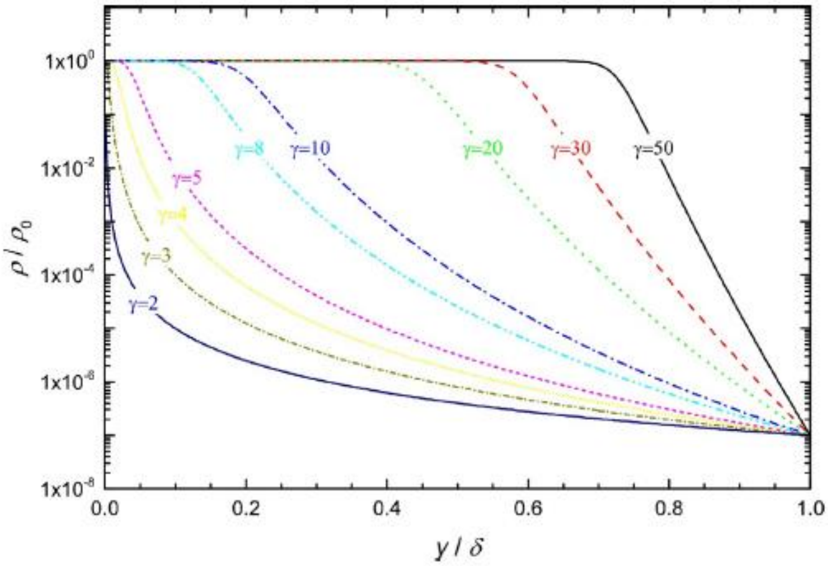

Fig. 2. 5 Normalized resistivity from the equation (2.8) as a function of dimensionless with γ as a parameter [128].

When the applied condition is under $\rho_0 \gg \rho_\delta$ and $f < (2\pi\rho_0\varepsilon\varepsilon_0)^{-1}$, the equation could be expressed as:

$$Z = g(\gamma)\frac{\delta\rho_\delta^{1/\gamma}}{(\rho_0^{-1} + j\omega\varepsilon\varepsilon_0)^{(\gamma-1)/\gamma}} \tag{2.9}$$

where g is a function of γ. If the form of CPE is applied on the equation (2.9):

$$Z = \frac{1}{j\omega^\alpha Q} = g\frac{\delta\rho_\delta^{1/\gamma}}{j\omega\varepsilon\varepsilon_0^{(\gamma-1)/\gamma}} \tag{2.10}$$

In which,

$$\alpha = \frac{\gamma - 1}{\gamma} \tag{2.11}$$

$$g = 1 + 2.88(1-\alpha)^{2.375} \tag{2.12}$$

Hence, the integrated expression of equation (2.9) can thus be written as follows [126]:

$$Z(\omega) = g\frac{\delta\rho_\delta^{1-\alpha}}{(\rho_0^{-1} + j\omega\varepsilon\varepsilon_0)^\alpha} \tag{2.13}$$

the relationship among the CPE parameters Q and α, the thickness of passive film δ, resistivity ρ_δ at the interface between passive film and the electrolyte and the dielectric constant ε of oxide could be concluded as:

$$Q = \frac{(\varepsilon\varepsilon_0)^\alpha}{g\delta\rho_\delta^{1-\alpha}} \tag{2.14}$$

Finally, the capacitance could be expressed as:

$$C_{film,PL} = gQ(\rho_\delta\varepsilon\varepsilon_0)^{1-\alpha} \tag{2.15}$$

Or

$$C_{film,PL} = (gQ)^{1/\alpha}(\delta\rho_\delta)^{(1-\alpha)/\alpha} \tag{2.16}$$

The detailed interpretation process for impedance data with PLM is explained as following: firstly, the high-frequency part of an electrochemical impedance diagram obtained in the presence of a passive film is generally represented by a CPE [129]. The CPE parameters (α and Q_{eff}) were determined using an enhanced graphical method [130]. The effective CPE exponent α was estimated from a modified phase angle-frequency Bode representation after estimation of the electrolyte resistance ($R_{e,est}$):

$$\varphi_{adj} = tan^{-1}\left(\frac{Z''}{Z' - R_{e,est}}\right) \tag{2.17}$$

The electrolyte resistance ($R_{e,est}$) could be estimated from the Nyquist impedance diagram, as presented in Fig. 2. 6. The value of electrolyte resistance is supposed to be the value of intersection between the Nyquist plots with real part.

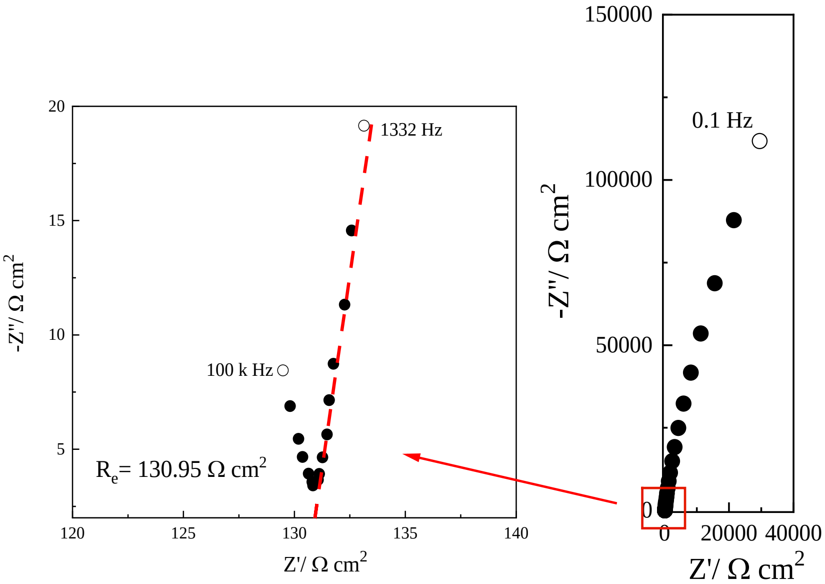

Fig. 2. 6 Estimation of electrolyte resistance ($R_{e,est}$).

where ϕ_{adj} is the phase angle corrected by the electrolyte resistance from the Bode plot, shown in Fig. 2. 7 (a) and Z' and Z'' are the real and imaginary part of the impedance, respectively. For α≠1, the CPE parameter α can be calculated using the following equation:

$$\varphi_{adj}(HF) = -90°\alpha \tag{2.18}$$

The effective coefficient of the CPE (Q_{eff}) can be determined from Z'' , with ω = 2πf:

$$Q(\omega) = \sin\left(\frac{\alpha\pi}{2}\right)\frac{-1}{Z''\omega^\alpha} \tag{2.19}$$

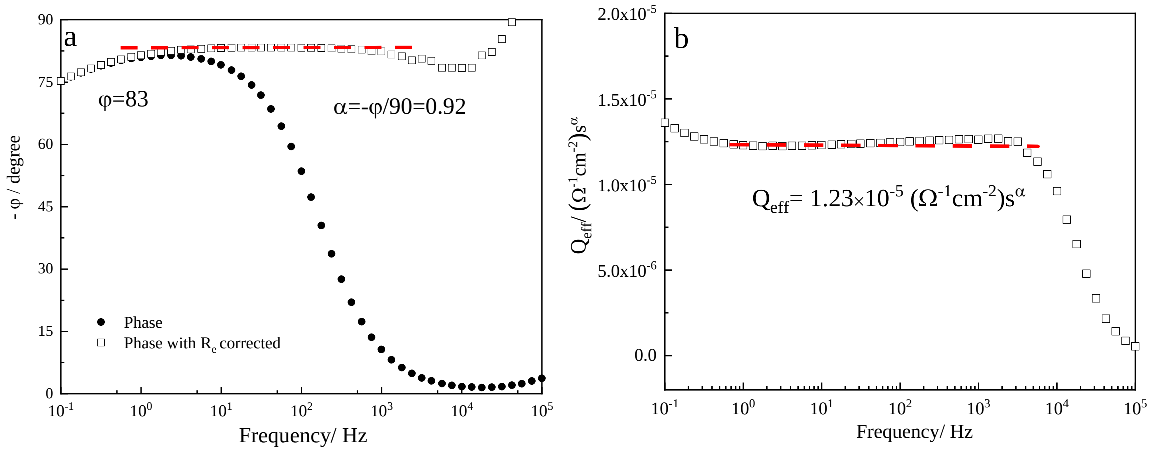

Fig. 2. 7 Estimation of α by corrected phase angle and effective coefficient of the CPE (Q_{eff}).

As the capacitance governs the impedance at very high frequency, the resistance behavior can be neglected. Thus, the complex capacitance representation emphasizes values at high frequency, enabling determination of the high-frequency limit of the real part of the complex capacitance [125]. The high-frequency-limit capacitance here is related to the dielectric field within the passive film [131]. Hence, the thickness of the passive film (δ) can be estimated from the capacitance from the complex representation (C_∞).

The complex representation (Cole-Cole representation) can be expressed as:

$$C^* = \frac{1}{j\omega(Z - R_{e,est})} \tag{2.20}$$

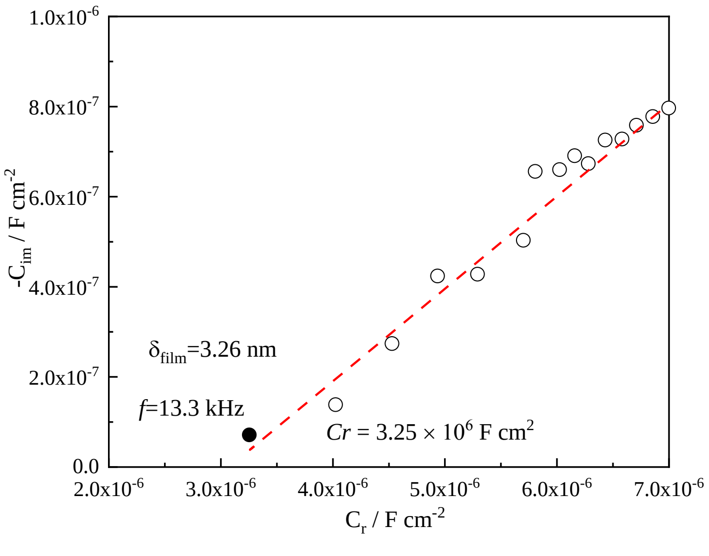

Fig. 2. 8 Estimation of thickness of passive film with infinite capacitance(C_∞) from the complex representation.

C_∞ is the estimated limiting capacitance at high frequency from the complex capacitance representation. Thus, δ can be determined using the formula

$$\delta = \frac{\varepsilon\varepsilon_0}{C_\infty} \tag{2.21}$$

where δ is the calculated thickness of the passive film, ε is the dielectric constant of the oxide (ε=12 for Cr_2O_3) [132], and ε_0 is the vacuum permittivity (8.85×10^{-14} F cm^{-1}). The example of estimation for thickness of passive film from the complex representation is given in Fig. 2. 8. The calculated thickness of a passive film has shown good agreement with that determined using other techniques [133]. Hence, thanks to the enhanced graphical representation, it was beneficial in determining four parameters used for fitting with the PLM (by reducing the number of unknown parameters). There are CPE relevant parameters α and Q_{eff}, infinite capacitance C_∞ and calculated thickness of passive film. Moreover, the resistivity at interface between passive film ρ_δ can be calculated to obtain calculated resistivity $\rho_{\delta,c}$ from equation (2.14).

To sum up, the theoretical approach and methodology are shown in Fig. 2. 9.

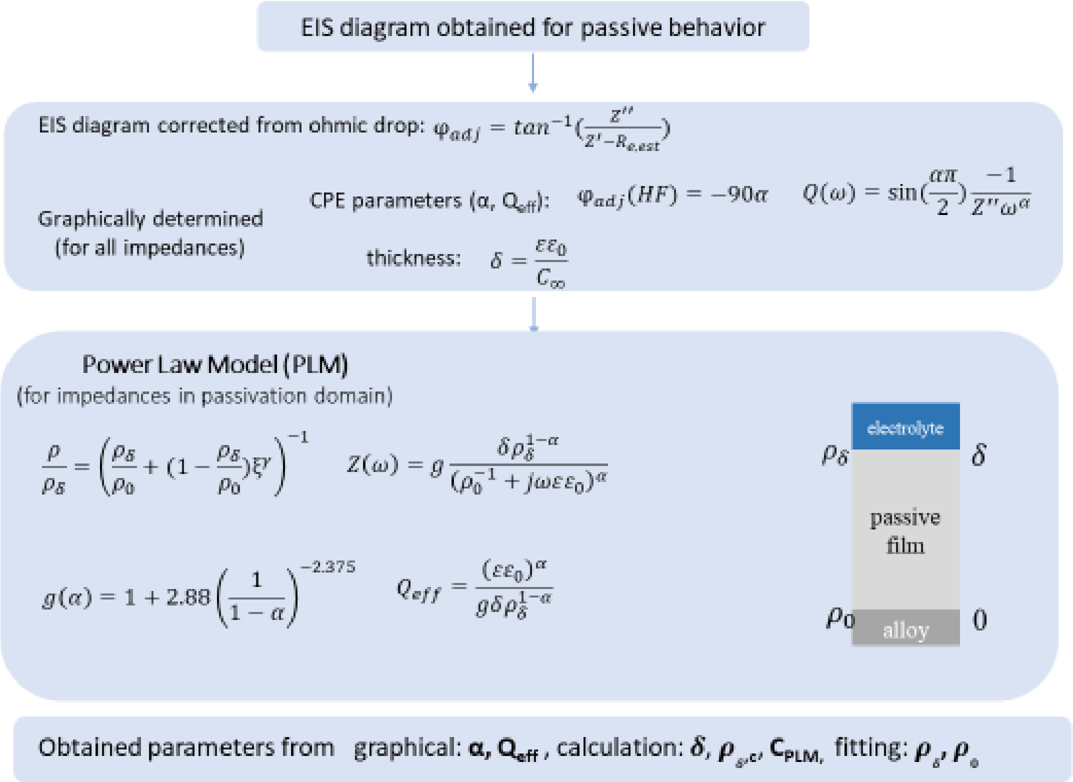

Fig. 2. 9 Adopted theoretical approach and methodology.

2.4.4.3 Electrical equivalent circuit

The electrical equivalent circuit (EEC) of the overall model used to describe the oxidized metal/electrolyte interface is presented in Fig. 2. 10.

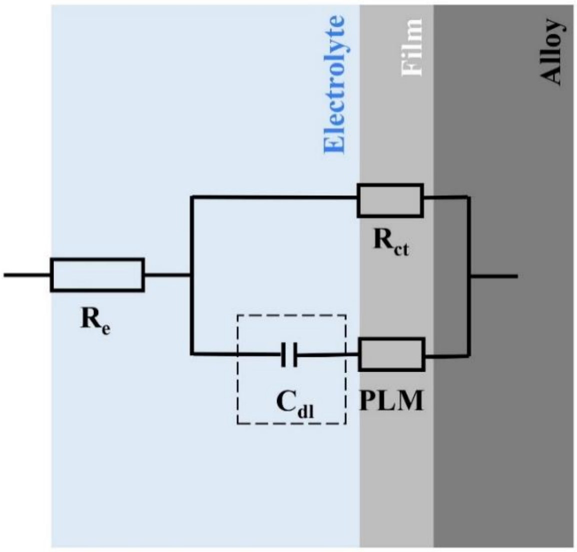

Fig. 2. 10 Electrical equivalent circuit (EEC) used to fit impedance diagrams.

R_e represents the resistance of the electrolyte. PLM is the element corresponding to equation (2.13) used to describe the passive film response to the anodic non-faradaic contribution. The passive film is considered a dielectric layer. The CPE behavior can be attributed to the normal distribution of resistivity throughout the passive film, adjusted by the PLM [129]. C_{dl} is the capacitance of the electrochemical double layer. Generally, C_{dl} is approximately on the order of 50 μF/cm^2, causing an error of 5%–10% in the estimated value of the oxide capacitance [129]. However, in this study, C_{dl} was neglected during the entire fitting process. R_{ct} is the charge-transfer resistance, which is attributed to the faradaic contribution. For the impedance data acquired from the cathodic domain to the beginning of the anodic domain (−0.1 to 0.1 V vs. E_{OCP}), the contribution of the cathodic reaction has been considered within the charge-transfer resistance. For more anodic potentials, this resistance R_{ct} can be considered infinite because the cathodic reaction becomes negligible. In the more anodic potential domain, the contribution of the faradaic branch can also be neglected for transport phenomena in the passive film. Within the impedance data obtained in this potential range, the charge-transfer resistance was removed from the equivalent circuit. Each impedance diagram was fitted using the non-commercial software SIMAD developed at the LISE UMR 8235 CNRS, Sorbonne University, Paris. However, in basic borate electrolyte, when transpassivation or second oxidation occurs on the samples, the EEC proposed for fitting is no longer suitable for the studied system, since the process of dissolution and oxidation contains a lot of ions transports.

2.5 Surface analysis – X-ray photoelectron spectroscopy (XPS)

X-ray photoelectron spectroscopy (XPS) is a widely used technique for the investigation of the chemical composition of surfaces. The sample for analyzing is irradiated by the X-rays with a known energy, and then the energy of the emitted electrons is analyzed. Generally, the X-rays used for XPS, their photons can interact with atoms in the sample surface, due to their limited penetrating power in solid (in order of 1 -10 micrometers), resulting in emitting electrons by the photoelectric effect. Consequently, limited electrons from sample surface will be detected. The emission process for atoms is shown in Fig. 2. 11 [134]. During the process of emission, not only will photoelectrons be emitted, but also the Auger electrons might be emitted, because of relaxation of the excited ions remaining after photoemission.

In the process of Auger emission, an electron in the outer layer falls into the inner orbital vacancy, which emits a second electron carrying off the excess energy. Hence, there are two electrons generally emitted after photoionization process. They are a photoelectron and an Auger electron. The total kinetic energies of the emitted electrons cannot exceed the energy of the ionizing photons.

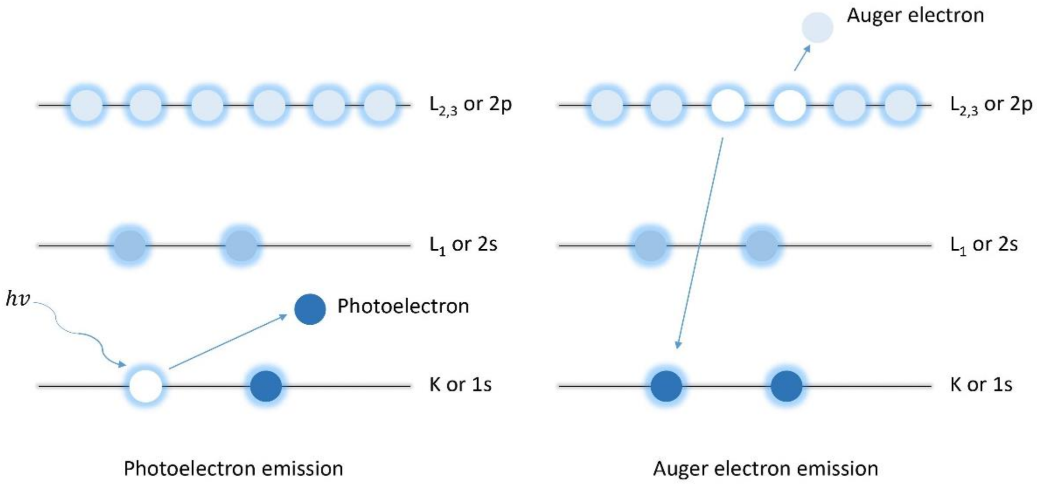

Fig. 2. 11 The illustration of XPS emission process remade from [134].

The emitted photons energy is measured from the equation 2.22 below:

$$hv = E_k + E_b + \varphi_{spectro} \tag{2.22}$$

where hv is the energy of the X-ray photons being used, E_k presents the kinetic energy of the electron as measured by the instrument, E_b corresponds to the binding energy of the electron measured relative to the chemical potential, and $\varphi_{spectro}$ is the spectrometer work function. It is possible to identify the surface composition, since the binding energy of the atomic orbital is specific for each element. Meanwhile, the binding energy could be calculated from the measured kinetic energy of the emitted electrons equation (2.22). Consequently, the amount of photo electrons could be measured as a function of their kinetic energy and obtained spectra.

In the thesis, the chemical compositions of the passive films were characterized using XPS on a PHI Quantera SXM with monochromatic Al Kα (1486.6 eV). A take-off angle of 90° was used and was not changed during the experiments. Charge compensation was performed throughout the experiments using a dual-beam neutralizer, and the remaining charge was adjusted using the aliphatic carbon peak at 284.8 eV of adventitious carbon in the C1s region. For high-resolution spectra, a pass energy of 23 eV was used. The obtained spectra were fitted with the software XPSPEAK41 and CASA XPS. Moreover, a Shirley background was applied for the specta. The spectra of XPS fitted with the method reported by Mark C. Biesinger *et al.* [135], especially for the chromium. Firstly, it is found that a series of single peaks to represent each different chemical species could cause the species being disordered. For instance, Cr(0) with the broadened peak shape for Cr(0) and $Cr(OH)_3$ could lead to incorrectly attributing to Cr(VI) species [136]. Secondly, employing multiple peaks to represent the various Cr(III) peak for the multiplet structure could be resolved with updated instruments. Thirdly, considering the oxides in passive film are often poly-crystallinity or non-stoichiometric, it reasonable to consider that the oxide in passive film are multiplet structures. Fitting parameters for Cr 2p3/2 spectra are presented in Table 2. 3. The data in table are based on spectra taken from certain well-characterized standard compounds. It is noting that chromium oxide shows multiplet structure whereas the hydroxide shows one peak.

Table 2. 3 Cr 2p$_{3/2}$ spectral fitting parameters: binding energy (eV), percentage of total area, FWHM value (eV) for each pass energy, and spectral component separation (eV) [135]

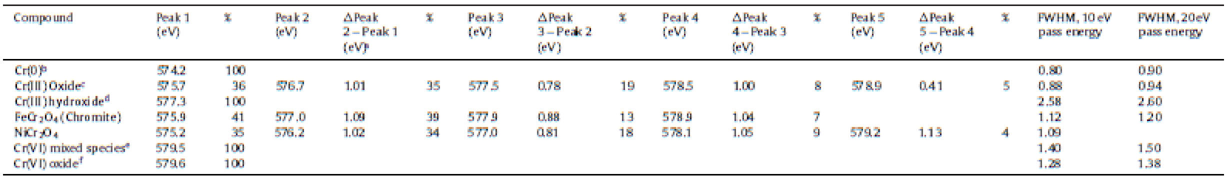

Compound	Peak 1 (eV)	%	Peak 2 (eV)	ΔPeak 2 – Peak 1 (eV)[a]	%	Peak 3 (eV)	ΔPeak 3 – Peak 2 (eV)	%	Peak 4 (eV)	ΔPeak 4 – Peak 3 (eV)	%	Peak 5 (eV)	ΔPeak 5 – Peak 4 (eV)	%	FWHM, 10 eV pass energy	FWHM, 20eV pass energy
Cr(0)[b]	574.2	100													0.80	0.90
Cr(III) Oxide[c]	575.7	36	576.7	1.01	35	577.5	0.78	19	578.5	1.00	8	578.9	0.41	5	0.88	0.94
Cr(III) hydroxide[d]	577.3	100													2.58	2.60
$FeCr_2O_4$ (Chromite)	575.9	41	577.0	1.09	39	577.9	0.88	13	578.9	1.04	7				1.12	1.20
$NiCr_2O_4$	575.2	35	576.2	1.02	34	577.0	0.81	18	578.1	1.05	9	579.2	1.13	4	1.09	
Cr(VI) mixed species[e]	579.5	100													1.40	1.50
Cr(VI) oxide[f]	579.6	100													1.28	1.38

The same method was employed for fitting nickel and its oxides and hydroxides. Here, the passive films were relative thicker and the information about oxides and hydroxides of nickel is more evident. The spectra were fitted with the data in Table 2. 4. The data presented for Ni metal, NiO and $Ni(OH)_2$ in the Table 2. 4 derived from standard samples.

Table 2. 4 Ni 2p$_{3/2}$ spectral fitting parameters: binding energy (eV), percentage of total area, FWHM value (eV) for each pass energy, and spectral component separation (eV) [135]

Compound	Peak 1 (eV) a)	%	Peak 1, FWHM, 10 eV pass energy	Peak 1, FWHM, 20 eV pass energy	Peak 2 (eV)	Δ Peak 2 – Peak 1 (eV)[a]	%	Peak 2, FWHM, 10 eV pass energy	Peak 2, FWHM, 20 eV pass energy	Peak 3 (eV)	Δ Peak 3 – Peak 2 (eV)	%	Peak 3, FWHM, 10 eV pass energy	Peak 3, FWHM, 20 eV pass energy	Peak 4 (eV)	Δ Peak 4 – Peak 3 (eV)	%	Peak 4, FWHM, 10 eV pass energy	Peak 4, FWHM, 20 eV pass energy
Ni Metal from [5][a,d]	852.6	79.6	1.00	1.02	856.3	3.65	5.6	2.48	2.48	858.7	2.38	14.8	2.48	2.48					
Ni Metal - New Line Shape[c,d]	852.6	81.2	0.94	0.95	856.3	3.65	6.3	2.70	2.70	858.7	2.38	12.5	2.70	2.70					
NiO	853.7	14.3	0.98	1.02	855.4	1.71	44.2	2.04	3.25	860.9	5.44	34.0	3.85	3.76	864.0	3.10	3.6	1.97	2.04
$Ni(OH)_2$	854.9	7.4	1.12	1.16	855.7	0.77	45.3	1.5	2.29	857.7	2.02	3.0	1.59	1.59	860.5	2.79	1.4	1.06	1.06
Gamma NiOOH	854.6	13.8	1.40		855.3	0.70	12.4	6.50		855.7	0.36	9.7	1.40		856.5	0.78	20.7	1.40	
Beta NiOOH (3+ Portion)[e]	854.6	9.2	1.40		855.3	0.70	8.3	5.30		855.7	0.36	6.4	1.40		856.5	0.78	13.8	1.40	
Beta NiOOH (2+ Portion)[e]	854.9	2.5	1.12		855.7	0.77	15.1	1.5		857.7	2.02	1.0	1.59		860.5	2.79	0.5	1.06	
$NiCr_2O_4$	853.8	7.0	1.22	1.30	855.8	1.95	20.5	1.82	1.86	856.5	0.71	24.7	3.91	7.01	861.0	4.50	2.3	1.27	1.33
$NiFe_2O_4$	854.5	17.3	1.35	1.36	856.0	1.52	38.2	3.03	2.98	861.4	5.41	38.5	4.49	4.50	864.7	3.29	2.8	3.04	3.01

Compound	Peak 5 (eV)	Δ Peak 5 – Peak 4 (eV)	%	Peak 5, FWHM, 10 eV pass energy	Peak 5, FWHM, 20 eV pass energy	Peak 6 (eV)	Δ Peak 6 – Peak 5 (eV)	%	Peak 6, FWHM, 10 eV pass energy	Peak 6, FWHM, 20 eV pass energy	Peak 7 (eV)	Δ Peak 7 – Peak 6 (eV)	%	Peak 7, FWHM, 10 eV pass energy	Peak 7, FWHM, 20 eV pass energy
Ni Metal from [5][a,d]															
Ni Metal - New Line Shape[c,d]															
NiO	866.3	2.38	3.9	2.60	2.44										
$Ni(OH)_2$	861.5	1.00	39.2	4.64	4.65	866.5	4.96	3.7	3.08	3.01					
Gamma NiOOH	857.8	1.33	8.7	1.90		861.0	3.20	23.3	4.00		864.4	3.38	11.4	4.40	
Beta NiOOH (3+ Portion)[e]	857.8	1.33	5.8	1.90		861.0	3.20	15.6	4.00		864.4	3.38	7.6	4.40	
Beta NiOOH (2+ Portion)[e]	861.5	1.00	13.1	4.64		866.5	4.96	1.2	3.08						
$NiCr_2O_4$	861.3	0.26	39.4	4.34	4.31	866.0	4.73	6.1	2.07	2.13					
$NiFe_2O_4$	867.0	2.27	3.2	2.61	2.66										

2.6 Conclusion

The materials and experimental details are presented in this chapter. The structures of alloys (both model and commercial alloys) were characterized and the grain sizes were calculated as well. The device and instrument to study electrochemical behavior were introduced. The electrochemical techniques including OCP monitoring, EIS and LSV were used in the thesis. In particular, the process of enhanced graphical method and theory of Power-Law Model (PLM) for abstracting parameters and fitting for impedance diagrams were explained in detail. Moreover, the XPS, as a supplementary method to analyze the compositions of passive films, were introduced as well. The Cr 2p3/2 and Ni 2p3/2 spectral were fitted with the method developed by Mark C. Biesinger.

Chapter 3 The development of the methodology for passive film characterizations

The main results in this chapter has been published in the journal of *Electrochimica Acta*, referenced as:

Z. Zhang, B. Ter-Ovanessian, S. Marcelin, B. Normand, Investigation of the passive behavior of a Ni–Cr binary alloy using successive electrochemical impedance measurements, Electrochim. Acta. 353 (2020) 136531. https://doi.org/10.1016/j.electacta.2020.136531.

Regarding to the development of the methodology, more details were studied and discussed in this chapter.

3.1 Introduction

As stated by D.D. Macdonald in 1999 [22], passivity should be considered "the key to our metals-based civilization". Today, research and development on passive materials continues to lead to scientific and technological improvements and improved material design in many industrial fields, including the energy, transport, and health sectors. Because passivity plays a crucial role in material applications, investigations of passive behavior remain topical issues in corrosion science.

The long-term stability of passive materials, even sometimes in harsh environments, is mainly attributed to the growth of an extremely thin passive film (a few nanometers in thickness) protecting the metal. Observation of this passive film using conventional equipment is challenging, even using transmission electron microscopy (TEM). Moreover, this passive film is commonly considered a complex multilayer structure closely related to the material underneath as well as the physico-chemistry of the environment. This complexity makes it difficult to attain a complete understanding of the passivity. Nevertheless, over the past few decades, several analytical methods and techniques have been developed to study passive films. Among surface analytical techniques, X-ray photoelectron spectroscopy (XPS), which provides semi-quantitative information on the chemical composition of passive films, is one of the most frequently used [137–139]. Several other analytical techniques are also often employed such as scanning tunneling microscopy (STM) [16,140,141] and ellipsometry [142–144]. In addition to these methods, different sets of electrochemical techniques are used to determine the kinetic parameters related to the growth, steady state, and breakdown of the passive film and permit a ranking to be established and materials to be selected based on their passive behavior.

The potentiodynamic polarization technique (potential sweep) — cyclic or not — is one of the most frequently used techniques for studying the electrochemical behavior of a passive material. From the resulting polarization curves, the ability to achieve passivity, the passive potential region, the passive current density, the potential of breakdown, and the relative stability of the passive film can all be determined. Even though this data is necessary to study passive materials, this information remains insufficient to fully describe the passive film behavior and its resistance. The rate-determining step hinders the overall passivation analysis. Moreover, for a specific corrosion mode, the results are dependent on the scan rate. For example, it is commonly known that the determination of the pitting potential is very sensitive to the sweep rate [79]. Another point of vigilance is the evolution of the passive film with the sequence of experiments that are performed. Indeed, for certain materials, several days are required to attain stability or reach the steady state of the passive material/solution interface; consequently, the results obtained after only a few minutes of immersion in an electrolyte are not representative of the long-term passive system.

To complete the analysis of a passive material/solution interface, electrochemical impedance spectroscopy (EIS) is a suitable complementary electrochemical technique that generally contributes to the description of the interface in terms of mechanisms and kinetics. Although EIS analysis is mainly performed at the open-circuit potential (OCP), it is not rare to use EIS at different applied potentials (selected from the polarization curves) to investigate the evolution of the passive film and determine physical parameters, kinetic constants, and migration/diffusion coefficients based on descriptive or predictive models of the evolution of the passive state. For example, the point defect model (PDM) [93,145,146] was developed to predict the growth and breakdown of passive films. In this model, EIS is used to explore the properties of passive films as a function of applied potential and pH [147,148] using various parameters, such as interfacial rate constants and the electrical field strength, as variables [145]. The mixed conduction model (MCM) [109,110,149] also uses EIS to emphasize the coupling between ionic and electronic defect structures in steady-state passive films and to predict the local conductivity within the film. In this model, the point-defect formation and transport are caused by the exponential evolution of the conductivity between the metal/film and film/solution interfaces. By considering a passive film to be a highly disordered semiconductor, the complementary Mott–Schottky approach, the determination of the semiconductive properties of a semiconductor in the presence of an electrolyte, can be transposed to the study of passive films. The obtained properties, including the semiconductive type, flat band potential, and charge carrier densities, can provide information about the relation between the electronic properties and passive film growth, steady state, and susceptibility to breakdown. In the PDM, the point defects are the semiconductor charge carriers. Their evolution with the applied potential is a required input in the calculation. However, the main deviation of the results obtained using the Mott-Schottky approach results from the differential capacitance measurement during a scan of potential, generally at a single frequency. Recently, the use of multi-frequency measurements, which avoids the issue of frequency selection and dependency, has generated interest [12,150].

On the basis of these preliminary remarks and considering that EIS can provide more information about passivation phenomena, successive EIS measurements were used in the current work on a nickel-based alloy, known to be a passive material, from the cathodic to anodic domain, to obtain a traditional potentiodynamic polarization curve. This procedure was applied in an attempt to provide continuous information on the passive material/electrolyte interface during potential-step polarizations. In addition, the evolution of each physical parameter extracted from the impedance diagrams, for example the thickness and resistivity within the passive film, could be discussed [130,151–153].

The chapter consists of two parts. The first part is devoted to validation of the methodology. In this part, the effects of experimental parameters on potentiostatic polarization curves, namely the dwell time at each potential step, the potential step size, the scan direction and the aeration of the solution, were studied. The aim was to optimize the experiment, find a good compromise between time and accuracy, and ensure that the measurements were performed under steady-state conditions. The second part of the study is focused on the use of this technique, termed successive EIS (SEIS), to characterize the passive behavior of a binary model Ni–Cr alloy containing 20 wt.% Cr (Ni20Cr) in different electrolytic solutions using the optimized experimental parameters.

3.2 Validation of the methodology

As presented in chapter 2, the impedance diagrams were interpreted using the recent impedance interpretation approach [130,151–153] to highlight the behavior of the passive film during the overall polarization process. A preliminary investigation was performed to optimize the experimental parameters in accordance with a conventional polarization curve, ensuring that the conditions of stationarity of the interface phenomena were respected. First, the effect of dwell time at each step of potential was studied. The potential step size was fixed at 50 mV, and different polarization dwell times (30, 120, 600 s, and 7200 s) were tested. After that, two different step sizes (25 and 50 mV) were tested, with the dwell time fixed at 120 s.

3.2.1 Influence of dwell time

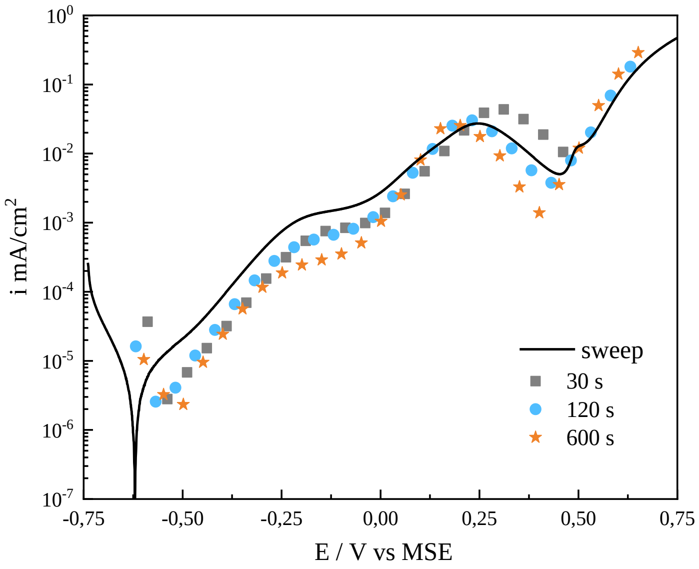

Fig. 3. 1 Comparison of potentiodynamic polarization curve (straight line, 0.5 mV/s) and potentiostatic curves for Ni–20Cr alloy in solution pH=9.2 for different dwell times

In Fig. 3. 1, the solid line corresponds to the potentiodynamic polarization curve, whereas each point of the dotted curves is the last value of the current density reached during potentiostatic polarization. The current density criterion (lower than 1×10^{-5} mA s^{-1}) for the impedance measurements was considered as the steady-state condition for the different sets of experimental conditions. For all the curves, the corrosion potentials fell in the small range between −0.62 and −0.50 V vs. MSE. Characteristics of a passive material in a basic solution after 24 h of passive film growth are observed in all the curves: a cathodic branch, a slight increase in current density, a plateau, and a dissolution–

repassivation–redissolution process in the potential range more positive than 0.0 V vs. MSE [27,28]. This finding indicates that all the curves characterized the same electrochemical reactions for substantially identical current densities. Comparison of the potentiodynamic and potentiostatic polarization curves revealed that the testing dwell time and step size did not result in any significant deviation. To confirm this conclusion, impedance diagrams obtained during the successive impedance measurements at four potential steps corresponding approximately to potentials of −0.50, −0.25, 0, and 0.25 V vs. MSE are presented, interpreted, and compared in Fig. 3. 2 (a1, b1, c1, d1). Meanwhile, evolution of current density as function of polarized dwell time is also presented in Fig. 3. 2 (a2, b2, c2, d2).

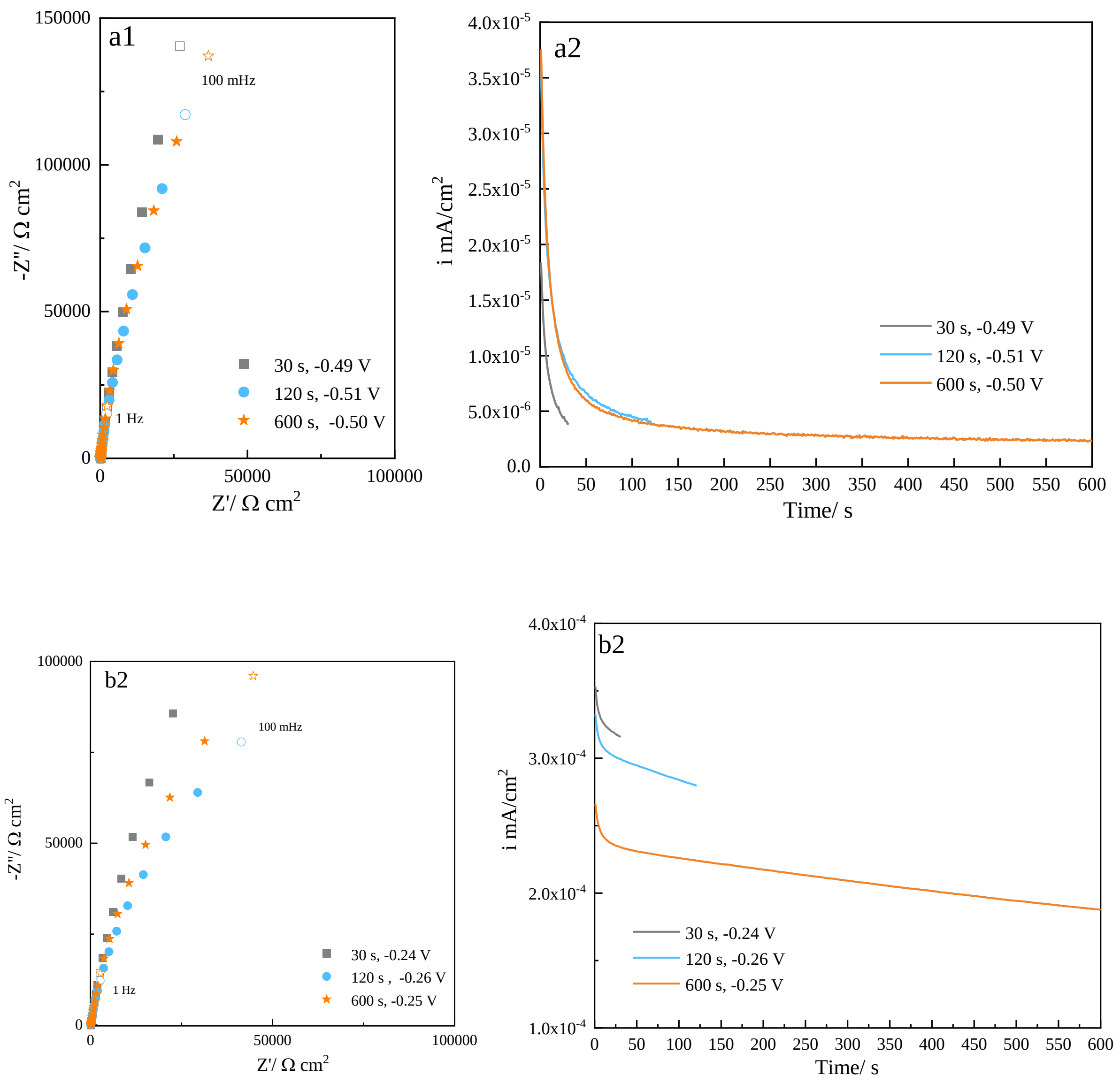

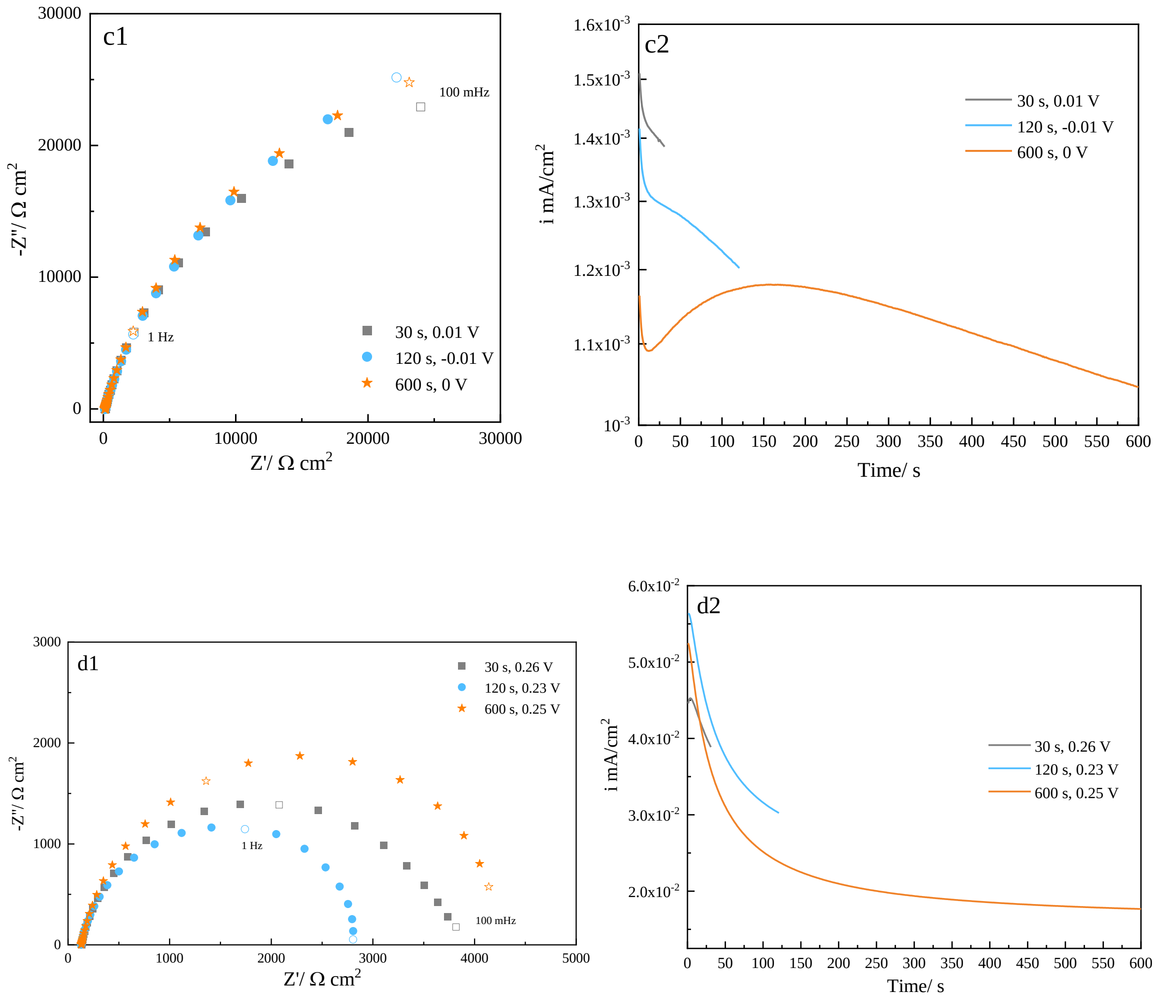

Fig. 3. 2 Nyquist diagrams (a1-d1) and current density vs. dwell time(a2-d2) for Ni–20Cr alloy obtained at different potentials for different dwell times in aerated 0.05 M H_3BO_3 + 0.075 M $Na_2B_4O_7$ $10H_2O$ borate buffer solution (pH=9.2): a) near –0.50 V vs. MSE, b) near –0.25 V vs. MSE, c) near 0.0 V vs. MSE, and d) near 0.25 V vs. MSE.

Fig. 3. 2 presents Nyquist plots obtained at different selected potential steps from successive EIS tests with different dwell times, as well as current density as function of polarized time. As observed in Fig. 3. 2(a1)–(c1), the Nyquist diagrams were similar for each tested condition. A conventional truncated and depressed semicircle classically seen for a passive film/electrolyte interface was observed for all the samples. Whereas it is found that current density near –0.50 and –0.25 V vs. MSE arrives almost quasi-stationary steady state. At potential around 0 V vs. MSE, a longer polarization time is needed to be at this state due to beginning of dissolution of passive films. There was more discrepancy between the Nyquist diagrams in Fig. 3. 2(d1) as a function of the tested parameters, most likely because of the significant increase of the current density near this potential. This state maybe changed by a longer polarization according to the record of current density evolution in Fig. 3. 2(d2). The dissolution–repassivation–redissolution process occurring within this potential range is sensitive to small differences in potential. In any case, the impedance values remained of the same order of magnitude. The analyzed results from the impedance diagrams are listed in Table 3. 1.

3.2.2 Influence of the long term staying

To discriminate the method between long term and short term staying, an experiment considering the dwell time of 7200 s (2 h) and the step size of 50 mV were performed, and the result is presented in Fig. 3. 3 below.

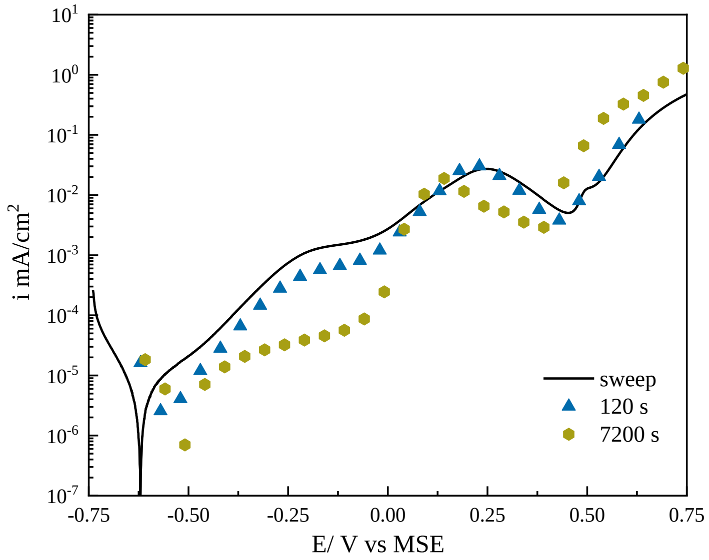

Fig. 3. 3 Comparison potentiostatic curves for Ni–20Cr alloy in solution pH=9.2 of 0.05 M H_3BO_3 + 0.075 M $Na_2B_4O_7$ $10H_2O$ for short term (120 s) and long term (7200 s) dwell time.

The potentiostatic polarization curve for the dwell time of 7200 s presents the corrosion potential of -0.5 V vs. MSE, close to -0.54 V vs. MSE for the dwell time of 120 s. The experiment with the dwell time of 7200 s exhibits the current density with magnitude of 10^{-4} mA/cm^2 at stable passivation domain while that for the experiment with dwell time of 120 s is about 10^{-3} mA/cm^2. Hence, the sample with a longer dwell time exhibits lower current density since the surface of the sample was polarized longer at each potential. This result indicates that for shorter dwell time, the steady-state is not totally achieved, whereas for longer dwell time, the passive film is intrinsically modified due to the applied potential. On the other hand, it is also found that the secondary oxidation begins near 0 V vs. MSE for both samples, indicating that the longer dwell time would not change the potential for secondary oxidation occurrence and the current density within the secondary oxidation potential range. However, the critical potential for dissolution was detected at slightly different potential with longer dwell time. In addition, the longer dwell time seemed to decrease the current density at secondary repassivation domain as in the passivation domain. The Nyquist plots obtained at different four selected potentials for the two experimental conditions are compared in Fig. 3. 4(a)–(c).

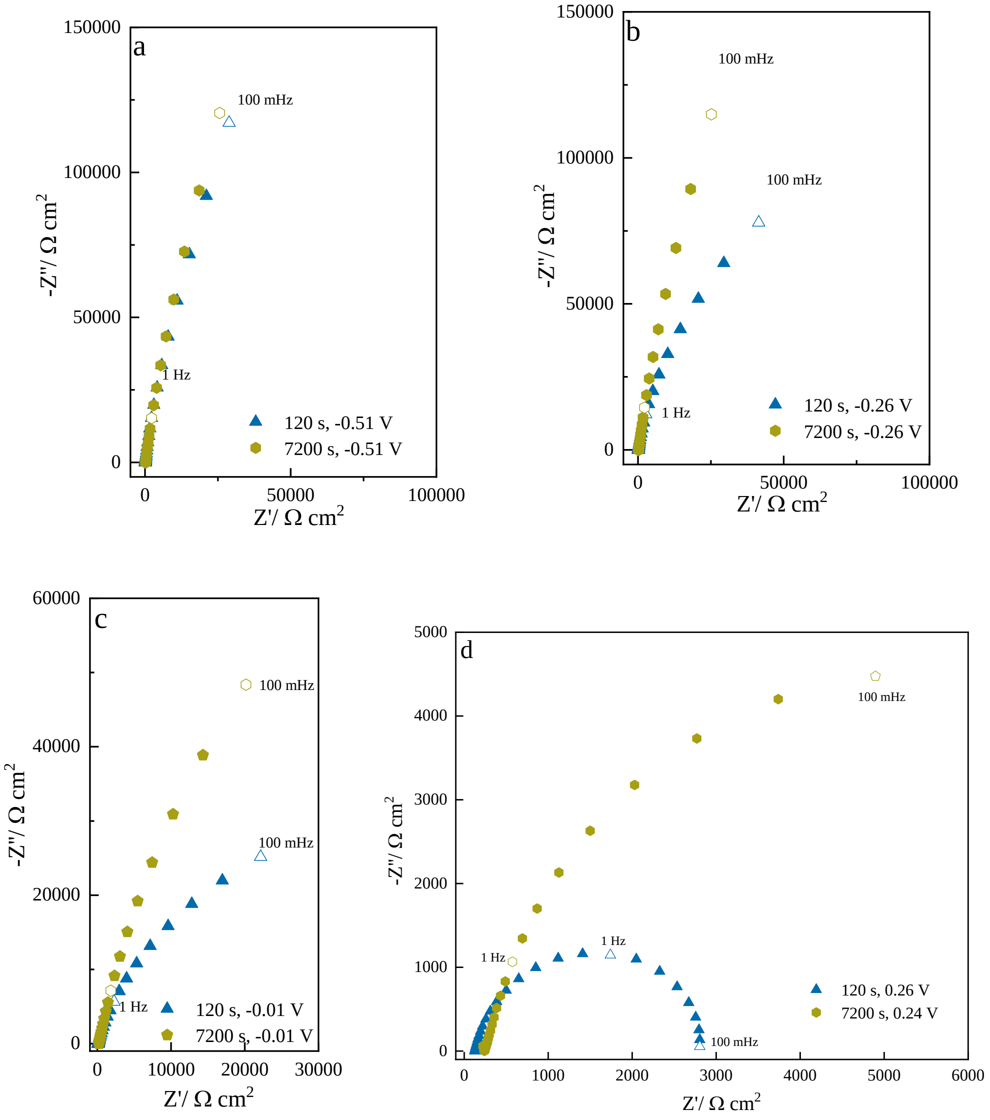

Fig. 3. 4 Nyquist diagrams for Ni–20Cr alloy obtained at different potentials for dwell time of 120 s and 7200 s in 0.05 M H_3BO_3 + 0.075 M $Na_2B_4O_7$ $10H_2O$ borate buffer solution (pH=9.2): a) near –0.50 V vs. MSE, b) near –0.25 V vs. MSE, c) near 0.0 V vs. MSE, and d) near 0.25 V vs. MSE.

The Nyquist diagrams obtained near -0.5 V vs. MSE in Fig. 3. 4(a) are very similar. On the contrary, the Nyquist plots for the sample with dwell time of 7200 s presents larger semicircle at other three potentials, comparing with the sample with shorter dwell time. It could be caused by the longer polarization allowing the achievement of the equilibrium in terms of charge migration and rates of the interface reactions at each potential or a densification of the passive layer. The fitted results for two samples are listed in Table 3. 1 and will be discussed later.

3.2.3 Influence of step size

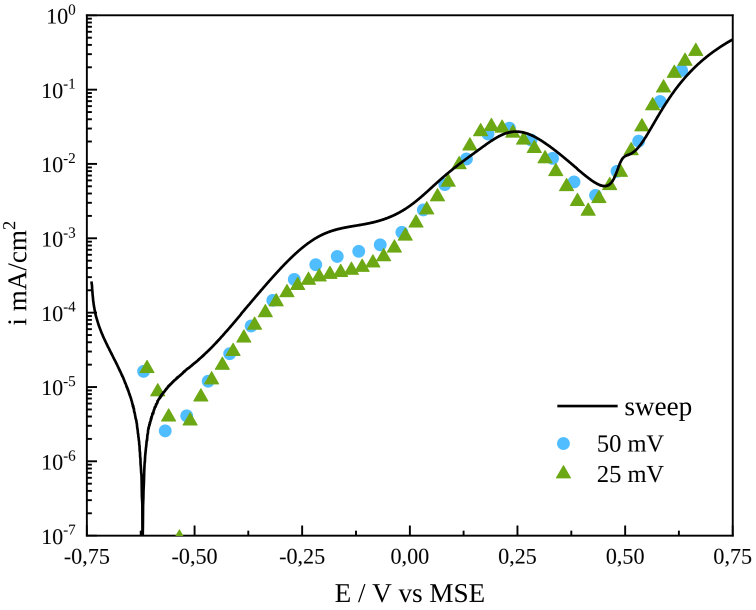

Fig. 3. 5 Comparison of potentiodynamic polarization curve (straight line, 0.5 mV/s) and potentiostatic curves for Ni20Cr alloy in solution pH=9.2 for different step sizes.

Fig. 3. 5 presents potentiodynamic polarization curve and the potentiostatic polarization curve obtained from SEIS tests, with different potential step sizes. It is obvious that the dotted plots recording the potentiostatic polarization curves do not miss any information in comparison with potentiodynamic curve (line curve). For the static polarization curves performed with different step size, no significant difference is observed, indicating that no influence of step size on potentiostatic polarization curve affects the results. EIS diagrams performed on several potentials (-0.50, -0.25, 0 and 0.25 V vs. MSE) with different step sizes are presented in Fig. 3. 6 (a)–(c).

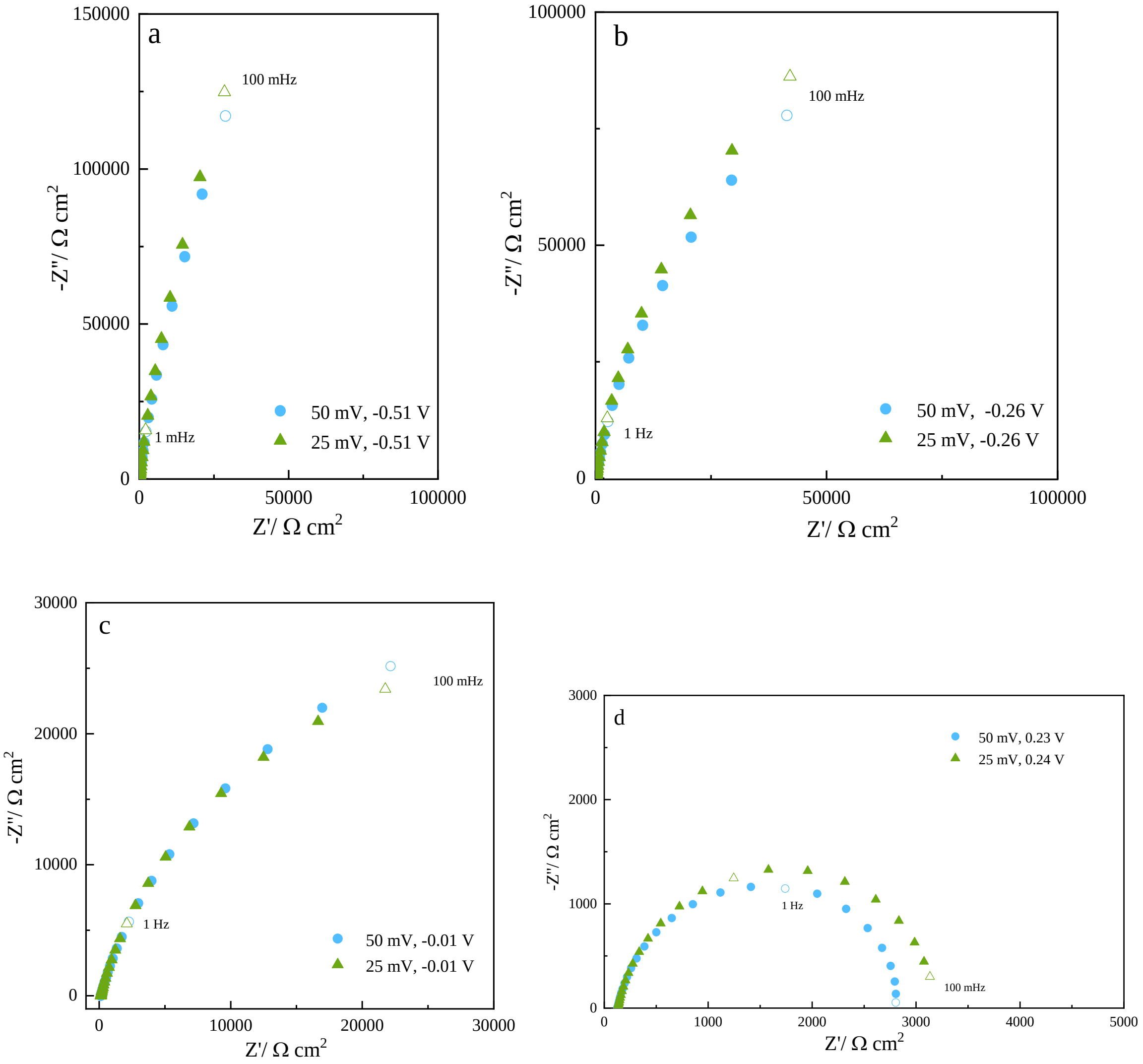

Fig. 3. 6 Nyquist diagrams for Ni–20Cr alloy obtained at different potentials for different step sizes in aerated 0.05 M H_3BO_3 + 0.075 M $Na_2B_4O_7$ $10H_2O$ borate buffer solution (pH=9.2): a) near –0.50 V vs. MSE, b) near –0.25 V vs. MSE, c) near 0.0 V vs. MSE, and d) near 0.25 V vs. MSE.

As previously observed, A conventional truncated and depressed semicircle classically seen for a passive film/electrolyte interface was observed for all the samples. For the four tested potentials, the impedance diagrams obtained with both step sizes are very similar.

3.2.4 Inversed scanning direction

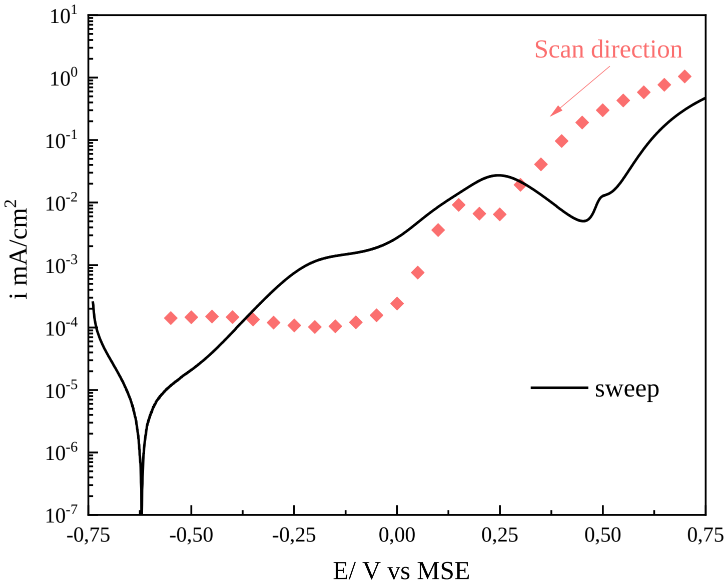

Fig. 3. 7 Comparison of potentiodynamic polarization curve (straight line, 0.5 mV/s) and potentiostatic curves from inverse direction for Ni20Cr alloy 0.05 M H_3BO_3 + 0.075 M $Na_2B_4O_7$ $10H_2O$ borate buffer solution (pH=9.2).

SEIS measurement could be compared with differential capacitance measurement commonly used to apply the Mott-Schottky analysis. In the latter, the validity of the Mott-Schottky approach required that the experiment must be performed quickly to limit the modification of the interface and maintain the reversibility of the reactions. For this reason, the results obtained have to be independent of the direction of the potential scan. With SEIS, this condition is not fulfilled. Indeed, Fig. 3. 7 compares Inverse scanning direction of the potentiostatic polarization curve obtained from the successive impedance test with the conventional polarization curve. It is obvious that the dotted plots related to potentiostatic polarization curves does not match with potentiodynamic curve. Since the successive impedance test started from the transpassive dissolution region, the passive film formed after 24 h at OCP was firstly modified and eventually removed, concomitantly with oxygen evolution reaction. With this reverse scanning to the cathodic potentials, the domain of dissolution occurred until the potential at 0 V vs MSE. The fluctuation around 0.2 V vs MSE could be explained as reduction of Cr^{6+} ions. After that, the stable passivation was obtained on the potential range of 0 V to -0.5 V vs MSE. The current density was then lower than for the potentiodynamic curve because the anodic film forming conditions affect the passive film structure. Consequently, the method used in this work is obviously dependent of the scan direction. Hence, all the presented results are only comparable with the scan direction from cathodic to anodic potentials. The evolution of the passive film parameters is considered according to the conventional scan direction generally used in polarization studies.

3.2.5 Influence of the electrolyte aeration

Another testing parameter could be the aeration of the electrolyte, as oxygen reduction may play a role on the passive behavior. The successive impedance measurements were performed on the sample in aerated or deaerated electrolyte, to understand the effect of oxygen on the methodology. For this study, a dwell time of 120 s and a step size of 50 mV were selected. In addition, to remove the native passive film formed in the air, the sample was firstly cathodically polarized at -1.5 V vs. MSE for 15 minutes, and then OCP monitoring was followed in deaerated electrolyte. The electrolyte was deaerated with N_2 bubbling during all the measurement. The result is presented in Fig. 3. 8 below.

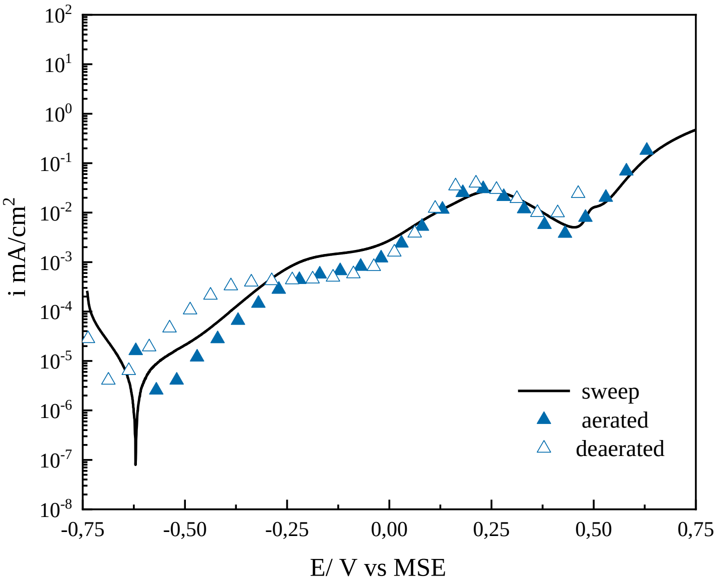

Fig. 3. 8 Comparison between potentiostatic curves for Ni20Cr alloy in deaerated and aerated 0.05 M H_3BO_3 *+ 0.075 M* $Na_2B_4O_7$ *10*H_2O *borate buffer solution (pH=9.2).*

Fig. 3. 8 presents potentiodynamic polarization curve and the potentiostatic polarization curve obtained from the successive impedance test, in deaerated and aerated borate buffer solution. It is obvious that the potentiostatic polarization curves performed in deaerated buffer solution has a negative potential shift, in comparison with other two performed in aerated solution. In aerated solution, cathodic reduction reaction is mainly related with dissolved oxygen in the electrolyte [154]

$$O_2 + H_2O + 4e^- \rightarrow 4OH^- \tag{3.1}$$

Consequently, the main cathodic reaction is weakened because of lack of oxygen in the deaerated solution. By contrast, the anodic reaction was strengthened. Hence, a longer passivation plateau was observed. Moreover, the polarization curves obtained in both solutions presented the same information in the secondary oxidation domain.

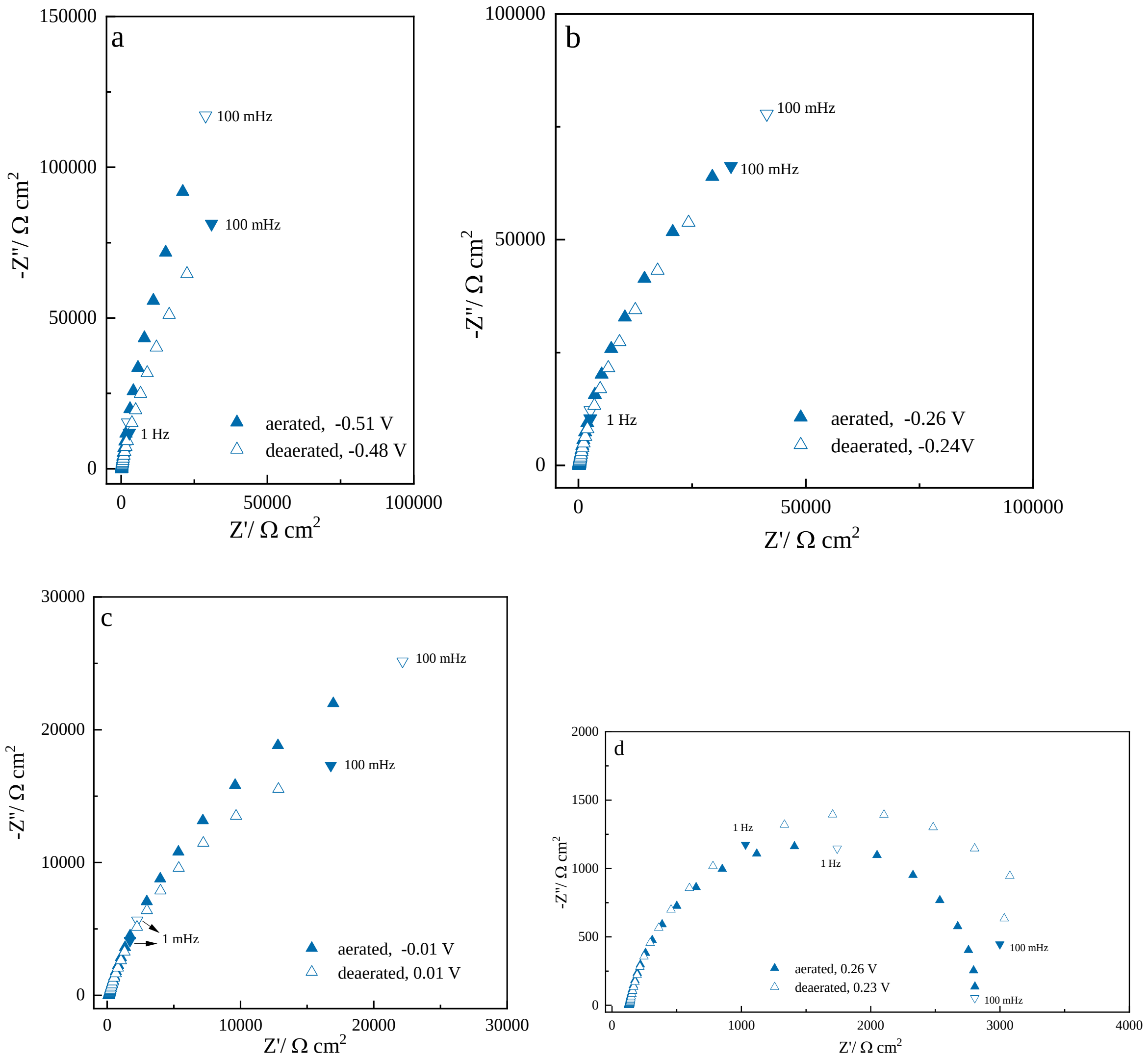

Fig. 3. 9 Nyquist diagrams for Ni–20Cr alloy obtained at different potentials for step sizes of 50 mV and dwell time of 120 s, in aerated and deaerated 0.05 M H_3BO_3 + 0.075 M $Na_2B_4O_7$ $10H_2O$ borate buffer solution (pH=9.2): a) near –0.50 V vs. MSE, b) near –0.25 V vs. MSE, c) near 0.0 V vs. MSE, and d) near 0.25 V vs. MSE.

Fig. 3. 9 presents Nyquist plots obtained at different selected potential steps in aerated and deaerated borate solution. As shown in Fig. 3. 9(a)–(c), the Nyquist diagrams were very similar for each potential, especially near -0.25 V vs. MSE. The difference is more significant at potential of 0.25 V vs MSE in Fig. 3. 9 (d), which is related by the slight difference in the current density. Consequently, it is found that with or without dissolved oxygen in the electrolyte, the observed impedances follow the same trend as other process. Hence only the cathodic contribution is modified, but it does not affect electrochemical response when the potential reaches more anodic potential. The measured impedances are fitted and the results are presented in Table 3. 1.

Table 3. 1 Capacitance and thickness of passive film, corresponding parameters of CPE, and resistivity (ρ_δ) at the interface of the passive film and electrolyte

Potential applied (V vs. MSE)	Step size (mV)	Dwell time (s)	C_∞ ($\mu F/cm^2$) *	α*	Q_{eff} ($\mu F/cm^2 s^{1-\alpha}$) *	δ (nm) **	f_δ (MHz) **	$\rho_{\delta,c}$ (kΩcm) **	C_{PLM} ($\mu F/cm^2$) **	R_{ct} (kΩcm²) ***	ρ_δ (kΩcm) ***
-0.50	50	30	2.8	0.93	10	3.7	12	13	3.0	3.68×10^3	25
	aerated	120	3.3	0.92	12	3.2	12	13	3.2	2.30×10^3	26
	deareated	120	3.8	0.89	16	2.8	0.1	2530	3.8	-	2000
		600	3.5	0.94	10	3.0	1	162	3.5	1.82×10^3	28
		7200	2.8	0.92	12	3.9	14	11	2.8	4.97×10^5	12
	25	120	3.9	0.93	11	2.7	1	107	3.9	2.85×10^3	89
-0.25	50	30	3.0	0.89	16	3.1	0.1	363	2.9	-	410
	aerated	120	3.4	0.89	15	3.1	3	940	3.3	-	380
	deareated	120	4.1	0.88	18	2.6	0.1	1777	4.0	-	1549
		600	3.0	0.90	13	3.6	0.5	320	2.9	-	317
		7200	2.8	0.91	13	3.8	10	15	2.8		14
	25	120	4.0	0.91	14	2.6	2	710	4.0	-	336
0.0	50	30	4.1	0.83	46	2.5	0.3	523	4.1	-	826
	aerated	120	3.9	0.84	42	2.4	0.4	276	3.9	-	974
	deareated	120	5.5	0.82	50	1.9	0.1	2847	5.4	-	2709
		600	3.7	0.83	43	2.8	0.3	436	3.6	-	718
		7200	3.4	0.87	28	3.1	2	87	3.4		86
	25	120	4.5	0.84	36	2.3	0.1	1667	4.5	-	1637
0.25	50	30	10.5	0.86	79	1.7	0.2	14	7.5	-	27
	aerated	120	5.9	0.86	74	1.8	0.2	10	5.8	-	10
	deareated	120	10.2	0.85	130	1.1	7	21	10.5	-	24
		600	6.2	0.87	79	1.7	55	3	6.0	-	6
		7200	5.6	0.84	193	1.9	1189	0.1	5.7		0.2
	25	120	8.1	0.85	109	1.3	5	23	8.2	-	16

* From graphical method, ** From calculation equations (4, 8, 9, 10), *** From fitting

The parameters for interpreting the EIS diagrams are reported as a function of the experimental conditions in Table 3.1: C_∞ is the capacitance obtained from the complex capacitance representation, δ is the calculated thickness of the passive film according to Eq. (2.21), the values of α and Q_{eff} were determined from enhanced graphical representation, $\rho_{\delta,c}$ is the calculated resistivity according to Eq. (2.15), which was used to calculate the characteristic frequency using the following equation:

$$f_\delta = \frac{1}{2\pi\rho_{\delta,c}\varepsilon\varepsilon_0} \tag{3.2}$$

Here, f_δ is the characteristic frequency, indicating the limit of the frequency domain of validity of the PLM ($[f_0; f_\delta]$). The fitted value of resistivity at the interface between the passive film and electrolyte, ρ_δ, is also reported and compared with the calculated value. R_{ct} and C_{PLM} are the charge-transfer resistance and calculated capacitance with PLM formula, respectively. R_{ct} was only considered at the potential of −0.50 V vs. MSE for aerated conditions. Consistent with previous observations, even though the values of the EIS parameters were not identical, they were still of the same order of magnitude, in most of the experimental conditions. First, because the experiments were conducted using an overpotential relative to E_{OCP}, it is possible that the potentials for each specimen were not exactly −0.50, −0.25, 0.0, and 0.25 V vs. MSE. In addition, the differences in the values is mainly included in the standard deviation of such tests. It is also worth mentioning that for some cases, the values of the fitted resistivity and the calculated one are different for the same experimental conditions. This difference is most likely linked to the sensitivity of ρ_δ, which is closely related to the determination of δ, α, and Q_{eff}. Except for ρ_δ and $\rho_{\delta,c}$, the step size and the short dwell durations did not appear to significantly affect the values of the EIS parameters.

From the result of polarization curve obtained in the different conditions, it is obvious that the results in Fig. 3. 1, Fig. 3. 2, Fig. 3. 5, Fig. 3. 6 are similar. For all the presented potentials, the deviations for α and Q_{eff} were very narrow. At −0.50 and −0.25 V vs. MSE, the capacitance estimated from the complex capacitance representation and the calculated thickness of the passive films were quite close for the different experimental conditions. The capacitance was approximately 3 μFcm^2, and the thickness of the passive film was approximately 3 nm. At the potential of 0.0 V vs. MSE, the estimated capacitance increased and the thickness of the passive film was reduced to less than 3 nm. Finally, at the potential of 0.25 V vs. MSE, the capacitances increased to higher than 5 μFcm^2 and the calculated thicknesses of the passive films were below 2 nm. According to the polarization curves in Fig. 3. 1 and Fig. 3. 5, the potential of 0.0 V vs. MSE is the starting potential of the second oxidation process, which is consistent with an increasing capacitance and a decreasing thickness. For the last potential, no clear tendency could be extracted from the comparison of the capacitance and thickness under the different experimental conditions.

In the case of long term (7200 s) polarization, the passive films formed at each potential are slightly thicker than for others conditions. In addition, the value of charge-transfer resistance for dwell time of 7200 s has two orders of magnitude more than others. By contrast, the values of resistivity ρ_δ formed at different potentials for dwell time of 7200 s are lower than that of others, indicating that the surface state and composition has been changed a lot due to polarization for long time in comparison with that of 120 s. However, further investigations have to be performed to better understand such evolutions.

Note that the impedance measured at -0.5 V vs. MSE in deaerated electrolyte was without considering resistance of charge transfer. Since the impedance measured here is far away from open circuit potential, charge transfer is neglectable. The values of thickness and α are relatively lower than that of in aerated electrolyte. The value of ρ_δ are very large for the passive film formed in the deaerated electrolyte. This finding indicates that ρ_δ is sensitive to the electrochemical reaction occurring at passive film/electrolyte interface. In addition, in the work of Chen et al. [155], Mott–Schottky measurement indicated that higher oxygen content in electrolyte would result in larger donor densities in passive film formed on 316L stainless steel. Consequently, the passive film formed in deareated solution has higher resistivity.

In conclusion, the validity of the SEIS method was confirmed in this part: the reconstructed potentiostatic polarization curves and potentiodynamic polarization curves shown in Fig. 3. 1, Fig. 3. 5, Fig. 3. 7, Fig. 3. 8 and Fig. 3. 3 (In particular, Fig. 3. 1 and Fig. 3. 5) exhibit the same tendency, the same potential of transition, and similar current densities. Moreover, the impedance data do not show any significant dependence on the experimental conditions (dwell time and step size). The current densities measured using the potentiostatic method were close for each dwell time and lower than those measured using the potentiodynamic method, suggesting that steady state was reached. The results obtained with longer dwell time indicate that we must deal with pseudo-steady-state rather than steady-state for shorter dwell times. However, the impedance diagrams in the considered frequency range are reliable. Furthermore, during successive electrochemical impedance measurements, the high frequencies were principally investigated (100 kHz–0.1 Hz) because the capacitive behavior of a passive film mainly contributes at high frequencies. These results indicate that the basic prerequisites of compliance of linearity, stability, and causality necessary to perform EIS analysis were satisfied [123]. Finally, the overall testing time for each impedance measurement (100 kHz–0.1 Hz) was ~2 min. As the dwell times and step sizes used in this study had no significant effect on the EIS results, a dwell time of 120 s and a step size of 50 mV were selected to minimize the duration of the experiment while maintaining the accuracy of the analysis. To facilitate also the measurement, the experiments were conducted in naturally aerated solution.

3.3 Application of the method in different electrolytes

3.3.1 Characterization of passive films at the OCP

The previously validated method was used to study the electrochemical behavior of the Ni20Cr alloy in three different solutions: 10 g/L Na_2SO_4 acidified with H_2SO_4 (pH=2), 0.01 M Na_2SO_4 solution (pH=5.8), and 0.05 M H_3BO_3 + 0.075 M $Na_2B_4O_7$ $10H_2O$ borate buffer solution (pH=9.2).

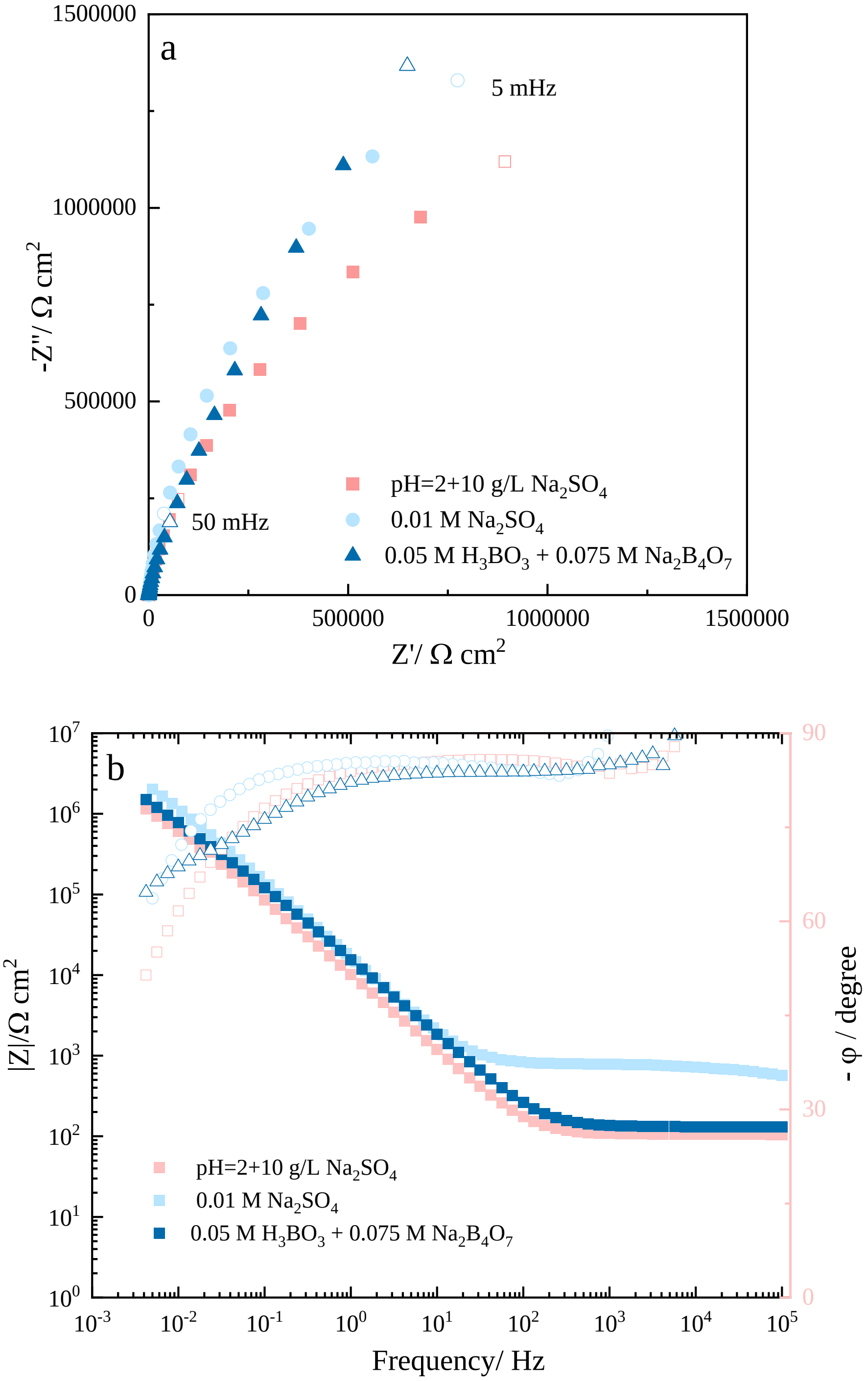

Fig. 3. 10 (a) Nyquist and (b) Bode diagrams obtained at the OCP for Ni–20Cr alloy in the three aerated solutions at pH=2, pH=5.8, and pH=9.2.

Table 3. 2 Capacitance and thickness of passive film, corresponding parameters of CPE, and resistivity at the interface of the passive film and electrolyte obtained at OCP.

Parameters	pH=2	pH=5.8	pH=9.2
E_{OCP} (V vs. MSE)	−0.52	−0.48	−0.38
C_∞ (μF cm^{-2})	5.2	4.5	3.4
α	0.94	0.95	0.92
Q_{eff} (μF cm^{-2}s$^{1-\alpha}$)	12	11	12
δ (nm)	2.0	2.3	3.1
f_δ (MHz)	1	4	3
$\rho_{\delta,c}$(kΩ cm)	166	41	48
C_{PLM} (μF cm^{-2})	5.1	4.5	3.1
R_{ct} (kΩ cm^2)	3.57×10^3	3.60×10^3	2.34×10^3
ρ_δ (kΩ cm)	124	39	17
$R_{e,est}$ (Ω cm^2)	104	789	131

Initially, the samples were immersed for 24 h in the different solutions to allow the growth of the passive film and steady state to be reached. The Nyquist plots are presented in Fig. 3. 10, and the results obtained using the enhanced graphical method and fitting are presented in Table 3. 2. The electrochemical impedance diagrams for the three solutions were characterized by truncated and depressed semicircles. The values of the impedance at low frequencies were high, consistent with the presence of a passive film. With increasing pH of the electrolyte, C_∞ decreased and the thickness increased. For both the acidic and near-neutral solution, the calculated capacitance from the complex representation was approximately 5 μFcm^{-2} and the estimated passive film thickness was approximately 2 nm. Notably, the passive film grown in the borate buffer solution had a smaller capacitance and higher thickness. For the CPE parameters (α and Q_{eff}) estimated from the graphical representation, there was no significant differences among the values. The α values were higher than 0.9. These results indicate the high homogeneity and capacitive behavior of the passive film formed at OCP in the three different solutions. The fitted value of ρ_δ decreased with increasing pH, suggesting modification of the outer layer of the passive film in terms of charge carrier density or hydroxide/oxide ratio. Except for the passive film grown in borate buffer solution, no obvious deviation between the fitted and calculated values of ρ_δ was observed. However, for the three experimental conditions, the calculated capacitance from the PLM was comparable to the value estimated from the graphical representation, validating the consistency of this approach. For the charge-transfer resistance (R_{ct}), the values were of the same order of magnitude (10^6 Ωcm^2), which is consistent with the existence of a protective passive layer [14].

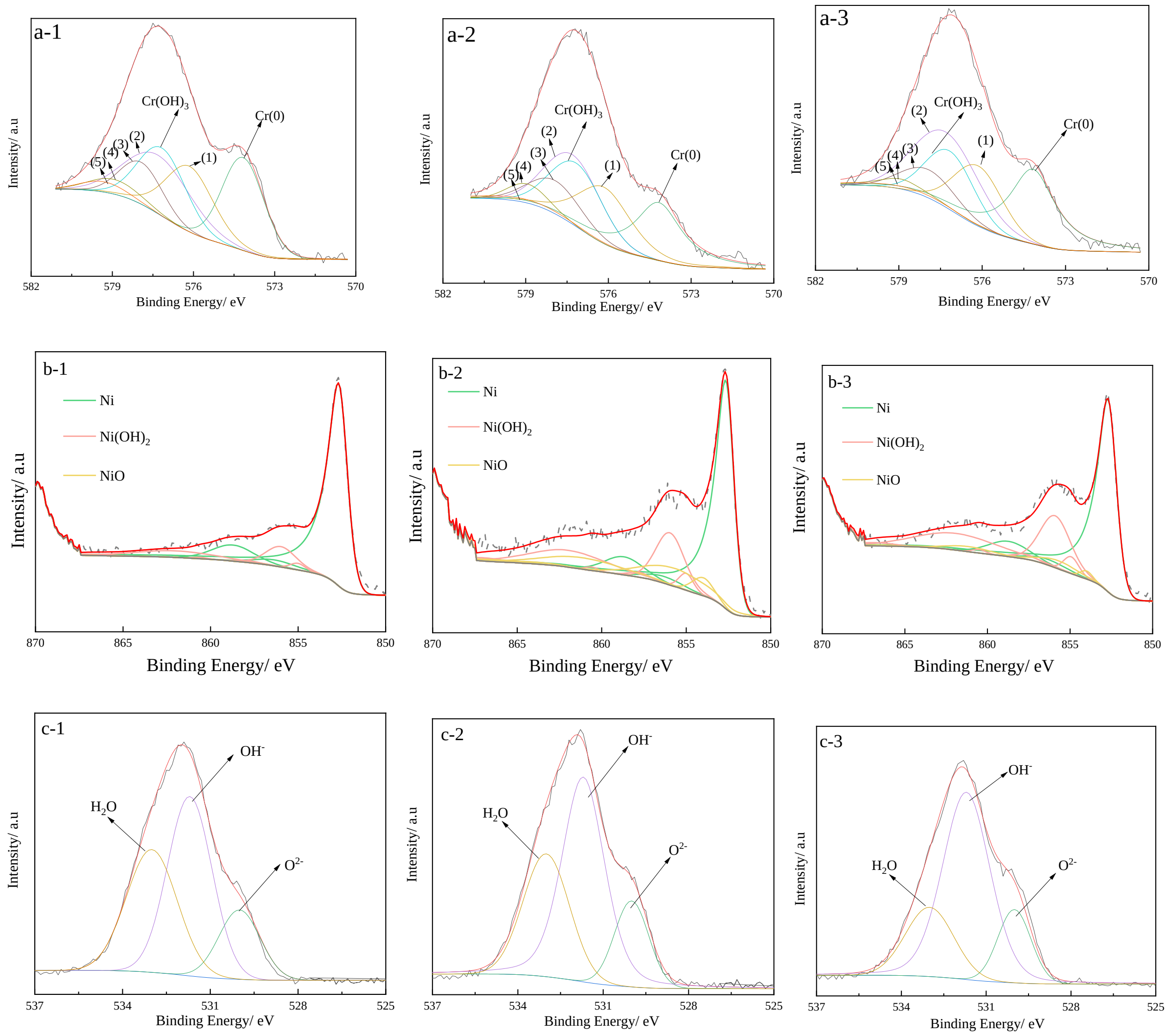

Fig. 3. 11 XPS spectra of (a) Cr 2p3/2, (b) Ni2p3/2, and (c) O 1s of the passive film formed on Ni–20Cr in solution with (1) pH=2, (2) pH=5.8, and (3) pH=9.2.

XPS was employed to determine the compositions of the passive films. Fig. 3. 11 presents high-resolution spectra of the Cr $2p_{3/2}$, Ni $2p_{3/2}$, and O 1s regions of the Ni–20Cr alloy passive film after 24 h of immersion in the different solutions.

The Cr $2p_{3/2}$ spectra were fitted using the method presented by Biesinger et al. [135]. The Cr $2p_{3/2}$ spectra were fitted with seven peaks, shown in Fig. 3. 11(a). The peaks at low binding energy at approximately 574.2 eV correspond to metallic Cr(0), and those at the higher bonding energy of 577.4 eV can be assigned to chromium hydroxide $Cr(OH)_3$. The remaining five peaks at bonding energies of 575.7, 576.7, 577.5, 578.5, and 578.9 eV are attributed to chromium oxide Cr_2O_3.

The $2p_{3/2}$ region of Ni was fitted according to data found in the literature [135]. The ones at the low binding energy of 852.6 eV, 856.3 eV and 858.7 can be attributed to Ni in the metallic state. There are five different peaks to account for nickel oxide NiO at 853.7 eV, 855.4 eV, 860.9 eV, 864.0 eV and 866.3 eV. The last six peaks corresponded to hydroxide $Ni(OH)_2$ locate at 854.9 eV, 855.7 eV, 857.7 eV, 860.5

eV, 861.5 eV and 866.5 eV, respectively. Ni metal is usually fitted with an asymmetric line shape because Ni metal conducts electrons [156].

The O 1s spectra were fitted with three components of oxide O^{2-}, hydroxide OH^-, and water H_2O. The peak at 530.2 eV corresponds to O^{2-}, which can be attributed to the metallic oxides in the passive film. However, the peaks at 531.8 and 533 eV correspond to OH^- of metallic hydroxides and bonded water/adsorbed water or impurities on the surface of the sample [157,158].

The $Cr_2O_3/Cr(OH)_3$ ratio in the acidic, neutral, and basic solutions was 2.5, 2.1, and 1.7, respectively. and the $NiO/Ni(OH)_2$ ratio was 0.5, 0.6, and 0.2, respectively. Notably, the ratios of the Cr oxides formed in acidic and neutral solution were close; however, the ratio decreased in basic solution. This result indicates that the compositions of passive films formed in acidic and neutral solutions are closer, consisting of many more oxides than hydroxides. This finding could be confirmed by the ratio of O^{2-}/OH^- from the spectra. The O^{2-}/OH^- ratio of the passive film formed in acidic, neutral, and basic solutions was 0.34, 0.3, and 0.24, respectively. The evolution of the passive film with the pH of the solution observed in this study is consistent with that reported in other works using XPS or other analytical surface techniques [159,160].

3.3.2 Analysis of passive film properties from successive impedance diagrams

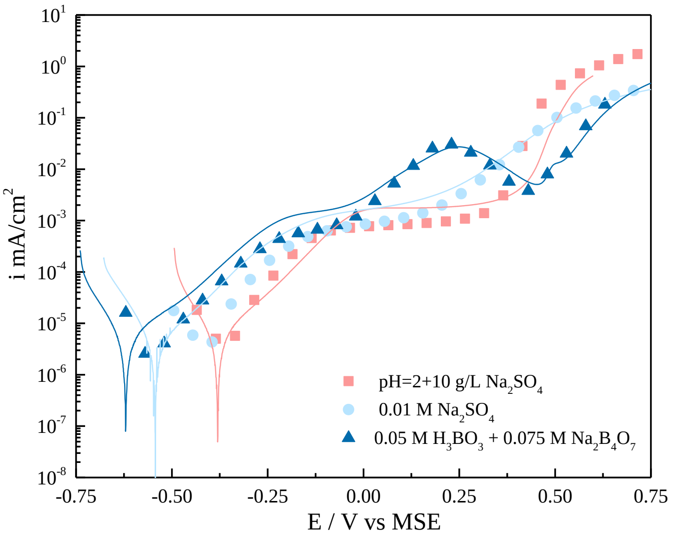

Fig. 3. 12 Potentiodynamic polarization curves obtained at a scan rate of 0.5 mV/s (line) and from potentiostatic measurements (symbol) for Ni–20Cr alloy in the three aerated solutions with pH=2, pH=5.8, and pH=9.2.

The measured potentiostatic polarization curves in the three solutions are presented in Fig. 3. 12 and the potentiodynamic curves are shown for comparison. As described before, the shape of the polarization curves obtained using the SEIS method were similar to those of the dynamic polarization curves, and the current densities were of the same order of magnitude.

In the three solutions, passive behavior was observed for both the potentiodynamic and potentiostatic polarization curves. The corrosion potentials increased in the positive direction with decreasing pH. In acidic solution, the corrosion potential was approximately −0.37 V vs. MSE, and the transpassive region began at 0.3 V vs. MSE. Similarly, for the neutral solution, the corrosion potential shifted to −0.52 V vs. MSE, and the passive–transpassive transition region was smoother and detected at 0.22 V vs. MSE. The curve obtained in basic solution had secondary oxidation peaks, as discussed before. The corrosion potential was approximately −0.65 V vs. MSE, and the secondary oxidation started at 0 V vs. MSE.

According to the polarization curves, the analysis of the impedance diagrams using the PLM model was only applied in the potential domain of existence of the passive film. Thus, for the basic solution, the evolution of the resistivity in the potential range corresponding to secondary oxidation and the transpassive phenomenon are not discussed. Another EEC must be developed for this potential range.

In the passive domain, each impedance diagram was analyzed using the enhanced graphical method and fitted with SIMAD according to the EEC presented in Chapter 2. The charge-transfer resistance was used to fit the first four potentials when the cathodic reaction was considered. However, as the charge-transfer resistance tended to an infinite value, it is not taken into account. The evolution with applied potential of all the other parameters obtained by the analysis is reported in Fig. 3. 13.

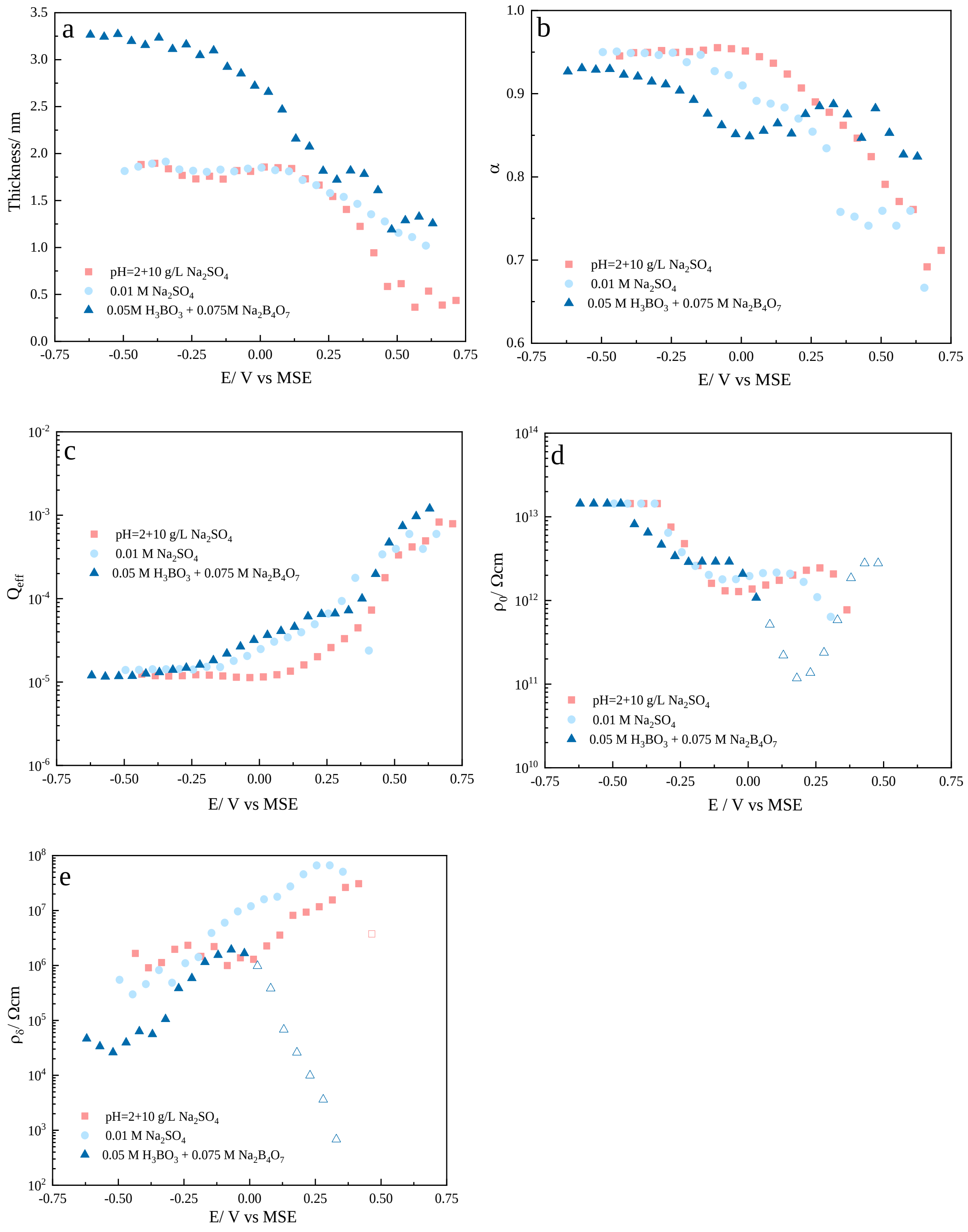

Fig. 3. 13 Evolution of physical parameters: (a) calculated thickness of passive film, (b) CPE exponent α, (c) CPE parameter Qeff, (d) resistivity ρ0 (alloy/passive film interface), and (e) resistivity ρδ (passive film/electrolyte interface) for the Ni–20Cr alloy in the three aerated solutions with pH=2, pH=5.8, and pH=9.2.

Fig. 3. 13 (a) shows the evolution of the thickness of the passive film with the applied potential. The passive film formed in borate buffer solution was the thickest, with those formed in the acidic and neutral solutions having similar thicknesses. This result can be attributed to the presence of a large

amount of hydroxide in the passive film at high pH [161]. The thickness of the passive film formed in acidic solution (pH=2) was stable and close to 1.7 nm up to the potential of 0.1 V vs. MSE. When the applied potential was over 0.1 V vs. MSE, the thickness decreased sharply to less than 1 nm. The thickness of the passive film formed in the neutral solution of 0.01 M Na_2SO_4 (pH=5.8) changed less when the potential reached more anodic values, maintaining a value between 1.5 and 2.0 nm in the potential range from −0.5 to 0 V vs. MSE. Beyond that range, for more anodic applied potentials, the thickness decreased. The calculated thickness of the passive film in borate buffer solution decreased from 3.2 nm at a potential near −0.6 V vs. MSE to 1.5 nm at a potential of 0.5 V vs. MSE. In all the cases, a decrease of the passive film thickness occurred before the sharp increase in current density related to the secondary oxidation of Cr. This finding indicates that the thickness of the passive film evolves even if the measured current density remains constant. The decrease of the thickness with increasing potential may be related to the semiconductor properties of Cr oxide grown on Ni–Cr alloys [12]. Effectively, as Cr oxide acts as a p-type semiconductor, the generation of cation vacancies promoted by the increase of potential results in a thinning effect of the passive layer.

The evolution of the CPE parameters (α and Q_{eff}) with potential is shown in Fig. 3. 13(b) and (c). Similar trends were observed for the evolution of α in acidic and neutral solution. In the range of potentials lower than −0.1 V vs. MSE, a plateau was observed. The value of α remained approximately 0.95 in the plateau region, indicating that the distribution within the passive film did not change with applied potential in this range. When the applied potential was more anodic than −0.1 V vs. MSE, α significantly decreased from 0.95 to 0.8 for potentials between −0.1 V vs. MSE and 0.50 V vs. MSE. This result indicates that continuous evolution of the passive film occurred during the polarization and occurred before the transpassive potential. In addition, the potential applied in the anodic direction over −0.1 V vs. MSE, Q_{eff}, continuously increased with imposed anodic potential and exceeded 10^{-4} $\mu Fcm^{-2}s^{1-\alpha}$ at 0.50 V vs. MSE.. A similar result was observed for the borate buffer solution. The value of α remained stable at approximately 0.92 in the potential range [−0.6 V vs. MSE; −0.25 V vs. MSE], followed by a decrease to 0.85 at 0.05 V vs. MSE. In the potential range of secondary oxidation, the value of α increased again, reaching approximately 0.89 at 0.3 V vs. MSE, suggesting the formation of a new oxide layer at the surface. When the potential was nobler than 0.3 V vs. MSE, α decreased continuously. The variation of α indicates a change of the structure of the passive film with applied potential. The decrease of α generally indicates an increase of the dispersion of time constants related to surface heterogeneity or chemical composition distribution within the passive film [162]. It may also suggest the transition from a protective passive layer to a reactive surface at transpassive potentials.

The evolution of the resistivity ρ_0 at the interface between the Ni–Cr alloy and passive film with potential in the three electrolytes is shown in Fig. 3. 13 (d). In the potential range from −0.1 to 0.1 V vs. OCP, the impedances were fitted with the equivalent circuit considering the contribution of the charge-transfer resistance. There was no obvious change of resistivity ρ_0 (interface between the Ni–Cr alloy and passive film) resulting from the cathodic reaction. With further increase of the applied potential, ρ_0 decreased, reached a plateau, and finally decreased again. The evolution of ρ_0 is closely related to the evolution of the current density (Fig. 3. 12), and the transition potentials are similar. The evolution of ρ_0 suggests modification of the Ni–Cr/passive film interface by the presence of more point defects locally decreases the resistivity. This finding indicates that ρ_0 and the measured current density are closely related to the transport of point defects and the electrochemical kinetic constants at this inner interface.

The evolution of the resistivity ρ_δ at the interface between the passive film and electrolyte with potential is shown in Fig. 3. 13 (e). The value of ρ_δ was fitted using the PLM and was drastically lower than ρ_0. The ρ_δ value in the acidic solution was $10^6\ \Omega$ cm at approximately −0.49 V vs. MSE and remained steady until the applied potential reached 0.0 V vs. MSE. Then, ρ_δ increased to $10^7\ \Omega$ cm at a potential of 0.35 V vs. MSE. The evolution of ρ_δ in the neutral solution followed a similar trend to that in the acidic solution. The first fitted value of ρ_δ at −0.50 V vs. MSE was approximately $10^6\ \Omega$ cm, and the value remained almost stable up to −0.1 V vs. MSE. After that, ρ_δ increased with increasing potential. Conversely, a different trend was observed for the evolution of ρ_δ in the boric buffer solution. The first fitted value for ρ_δ at −0.60 V vs. MSE was approximately $10^5\ \Omega$ cm, which is smaller than that in the other two media. Then, upon further increase in the applied potential, ρ_δ continued increasing to approximately $10^6\ \Omega$ cm at a potential of 0.0 V vs. MSE. The value of ρ_δ in boric acid solution was lower than that in the acidic and neutral solutions. This difference was caused by the different chemical compositions of the passive film in solutions of different pH, as confirmed by the XPS results. The evolution of ρ_δ indicates continuous modification of the outer oxide layer with the applied potential, suggesting variation of the oxide/hydroxide ratio or densification of this outer layer.

3.3.3 Evolution of resistivity profiles as a function of polarization and pH

Using the values of α, ρ_0, and ρ_δ, resistivity profiles throughout the passive film were constructed for each tested potential using Eq. (2.8). The calculated distributions of resistivity within the passive films grown in the different solutions are shown in Fig. 3. 14. A dimensional thickness and normalized resistivity were selected to highlight the common tendency of passive film variation with applied potential for all the tested solutions.

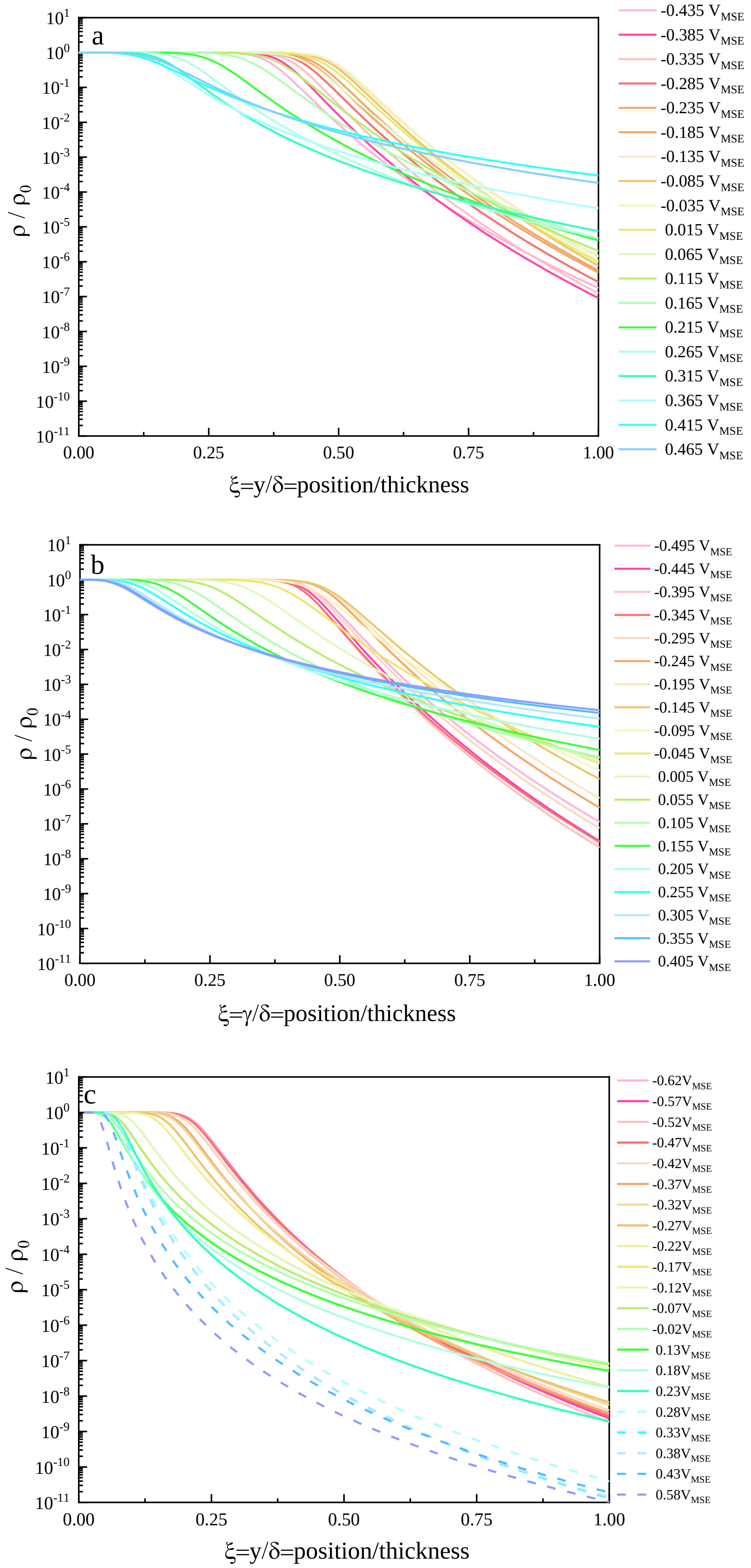

Fig. 3. 14 Normalized resistivity of passive film of Ni–20Cr alloy in solution of (a) pH=2, (b) pH=5.8, and (c) pH=9.2 from Eq. (4) as a function of dimensionless position with ξ as a parameter.

For all the cases, the resistivity distribution profile consisted of two separate parts. From the alloy/passive film interface, the first part consisted of a plateau with ρ equal to ρ_0. The second part reflects power-law decay of the resistivity, reaching the passive film/solution interface resistivity ρ_δ. This dual distribution of the resistivity can be understood from the dual structure of the passive film with an inner dense oxide layer and an outer hydrated and hydroxide layer. As the value of ρ_0 is high and close to the resistivity of the bulk oxide, the length of the plateau may be related to the size of the inner chromium oxide layer and the decay may be related to the modified oxide being affected near the electrolyte. It is also interesting that the resistivity distribution profile is similar to the transition layer model proposed by Sato [161]. In the transition layer model, the passivating film consists of an inner anhydrous oxide layer and an outer hydrous oxide layer. There is a critical extent of hydration that depends on the solution pH and decreases with decreasing concentration of OH^- in the solution. In the acidic and neutral solutions (Fig. 3. 14(a) and (b)), the lengths of the plateau were quite similar, almost 50% of the total thickness of the passive layer. The distributions of the resistivity were also similar, indicating that the passive films that formed in the acidic and neutral solutions were similar. This finding is consistent with the XPS results showing that the compositions of the passive films formed in the acidic and neutral solutions were similar. The length of the plateau was shorter (approximately 25% of the total thickness) in Fig. 3. 14(c), indicating that the dense chromium oxide in the passive film formed in basic solution was thinner. This last result is consistent with the presence of more hydroxide in the passive film grown in the borate buffer solution.

The evolution of the resistivity profiles was similar for the three tested solutions. The length of the plateau decreased with increasing applied potential. As ρ_δ increased with the applied potential, the resistivity decay was smoother at higher potential. These results suggest that during the anodic polarization, the passive film is modified in depth: the defectiveness of the inner oxide increases (ρ_0 decreases) as the thickness decreases, and ρ_δ of the outer layer of the passive film increases, suggesting its chemical modification in terms of the density of point defects or the chemistry. This last tendency is more noticeable for the passive film grown in the acidic and neutral solutions. Hence, increasing the applied potential appears to affect the charge-carrier transport and distribution throughout the passive film. This evolution is consistent with the following transpassive phenomenon that relies on a charge-transfer reaction that the passive film is no longer blocking as well as potential dissolution of the film.

3.3.4 *In-situ* analysis of passive film behavior during polarization

One of the most important findings of this work is that the passive film continuously evolves during the polarization test even if the polarization curves show a current density plateau. Another result is that regardless of the pH, the evolution of the passive film properties shows similar trends in the potential range of “passive behavior”. Fig. 3. 15 presents a schematic representation of the evolution of the different parameters measured and determined from the analysis of the impedance diagram for the passive film grown in borate buffer solution. The transitions indicated below (related to modification of the trend in the evolution of the parameters) were also observed for the other tested cases but shifted to less cathodic potentials as the solution pH decreased, which is consistent with the OCP shift.

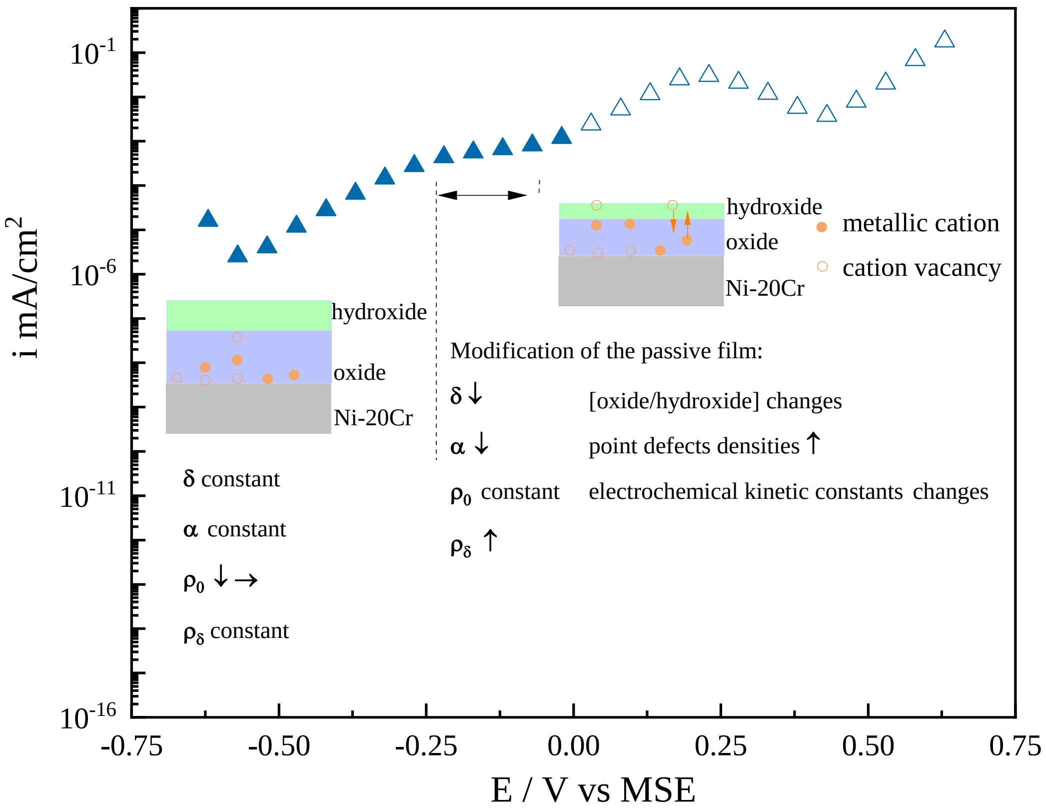

Fig. 3. 15 Schematic representation of the evolution of the different parameters related to the film passive properties.

The potential-step polarization curve reveals three potential domains: one corresponding to the increase of the current density from low current density at E_{OCP} to the current density of the passive plateau, one corresponding to the passive plateau, and one corresponding to the transpassive phenomenon. As previously mentioned, the evolution of ρ_0 is related to the evolution of the current density during polarization. This relation indicates that the metal/passive film interface evolves via the generation and transport of cation vacancies from the electrolyte/passive film interface. The electrochemical kinetic constants are linked to the annihilation of those vacancies. For the passive plateau, although the current density remains constant, α and ρ_δ change after remaining constant with the applied potential. This result indicates that the modifications of the structure of the passive film (thinning of the inner oxide layer) related to its chemical composition (change in oxide/hydroxide ratio) or its reactivity (increase of the point defect densities or mobilities or the balance of the electrochemical reaction kinetics) are promoted before the transpassive phenomenon but also before the thinning. Indeed, the thickness of the passive film decreases while the transpassive potential is not reached. This work demonstrates the evolving character of the passive film. Even if polarization curves indicate the steady-state character of the passive film in a potential range (passive plateau), its structure, chemistry, or properties differ significantly as a function of the potential. Such behavior is generally hidden in conventional potentiodynamic studies. It is also important to notice that by applying SEIS and the proposed analysis methodology to adjust the electrochemical impedance diagrams, the evolutions of the parameters α, ρ_0, and ρ_δ clearly demonstrate that the PLM impedance is related to the anodic contribution of the current density and ionic species distribution and transport through the passive film.

3.4 Conclusion

In this chapter, an electrochemical analysis method combining potentiostatic polarization with electrochemical impedance measurement at each potential step was used to successfully study the passive behavior of Ni–20Cr binary alloy. This method, termed successive electrochemical impedance spectroscopy (SEIS), was tested considering various experimental conditions, not only dwell times and step sizes, but the scanning direction and the electrolyte aeration. The effects of each parameter on the potentiostatic polarization curves and on impedance data were investigated, and the results were validated by comparison with more conventional potentiodynamic polarization curves. The results confirmed that the potentiostatic polarization curves were comparable to the potentiodynamic polarization curves (scan rate of 0.5 mV/s) and that the electrochemical impedance measurements were not significantly affected by the step size, shorter dwell times and aeration of the solution. Longer dwell times and scan direction affect suggestively the results by modifying deeply the passive film structure. The deviation between the potentiostatic and potentiodynamic curves increase when considering these parameters.

In the second part of this chapter, the optimized method was applied for the study of passive films grown on a binary Ni–20Cr alloy in three solutions with different pH values. This method shows great potential for the study of film passivity owing to the interpretation of the impedance data through enhanced graphical representation and the power-law model allowing more parameters related to the passive film properties to be determined. Indeed, the application of SEIS provides a lot of information on the passive film properties and their evolution with the applied potential. For instance, the evolution of thickness of passive film decreases within passivation domain with anodic potential applied. Also, the resistivities of passive films formed in different solution are observed different, resulting from the different composition or structure of passive film. While the resistivities are observed increasing with anodic potential caused by dehydration. Using this proposed methodology, it is possible to explore the evolutionary nature of a passive film. Hence, as a complement to monitoring the evolution of the current density (measured at each potential step), the modification of the thickness, chemical composition, and reactivity can be assessed *in situ* using this original method.

Chapter 4 Role of alloying elements in passive and transpassive behavior

The main results in this chapter has been published in *Journal of the Electrochemical Society*, referenced as:

Z. Zhang, B. Ter-Ovanessian, S. Marcelin, J. Galipaud, B. Normand, Role of alloying elements in passive and transpassive behavior of Ni–Cr-based alloys in borate buffer solution. *J. Electrochem. Soc.* 168(2020) 081503. https://doi.org/10.1149/1945-7111/ac1890

4.1 Introduction

Nickel-based alloys are widely used for critical applications because of their ability to form passive films in aqueous environments and protective oxides with controlled growth rates at high temperature. Moreover, they exhibit favorable and tunable mechanical properties. However, the design of novel nickel-based alloys remains a challenge given the complexity of the chemical and mechanical loadings potentially encountered in advanced applications, such as those in the nuclear and aerospace domains.

The corrosion resistance of these alloys can be greatly improved through the addition of certain alloying elements such as Cr, which acts as a passivity promoter, supporting the nucleation of the oxide [16]. The Cr-rich layer within the passive film is considered the main corrosion-resistance feature of these alloys [163]. The oxide films on Ni–Cr binary alloys have generally been reported to consist of a main Cr oxide network mixed with a minor Ni oxide network or the insertion of a certain concentration of metal ions [164]. Moreover, a dual structure is generally considered to be formed by an inner oxide part and an outer hydroxide part consisting of both metallic elements [165]. Cr(III) is the main cation species in both layers, whereas Cr(VI) and Ni(II) are the minor species.

The minimal concentration of Cr required for passivity in bulk Ni–Cr alloys has been determined to be 8–11 at.% [166]. In acidic solution, the passivation potential is shifted to more negative values with increasing Cr content. The current densities in the active and passive potential ranges decrease with increasing Cr content [167]. However, a critical Cr concentration of 22–26 wt.% in bulk Ni–Cr alloys enables the diffusivity of charge species within the passive film to be tailored, maintaining a low steady-state current density and ensuring good resistance to the passivity breakdown process [12]. In chloride-containing solution, a similar Cr concentration provides good resistance to pitting corrosion, limiting the nucleation and growth of pits [168]. However, the potential range of passivity is affected by the Cr content. Indeed, the transpassive potential is generally lower for Ni–Cr alloys than for pure Ni which exhibits a transpassive region for potential located after thermodynamic water stability [165].

Transpassivation is characterized by a rapid dissolution of metal or alloy when the electrode potential becomes too positive [169]. The transpassive oxidation potential is thermodynamically controlled. It is mainly dependent on the aqueous solution (essentially the pH). For Ni–Cr-based alloys, this thermodynamic phenomenon is linked to the redox potential of Cr(III) to Cr(VI) generally expressed as [165]:

$$Cr_2O_3 + 10OH^- \rightarrow 2CrO_4^{2-} + 5H_2O + 6e^- \tag{4.1}$$

However, in basic solution, the transpassive dissolution rate can be limited by the formation of a new oxide film on the surface that contains chemical species in a higher valence state. This phenomenon is called secondary passivation [170]. Fig.4. 1, adapted from our previous study [171], presents the polarization curves obtained for a synthetic Ni–Cr binary alloy (with 20 wt.% Cr) immersed in 10 g/L Na_2SO_4 acidified with H_2SO_4 (pH=2) (red curve) and in 0.05M H_3BO_3 + 0.075 M $Na_2B_4O_7$ $10H_2O$ (pH=9.2) (blue curve). In acidic solution, the alloy presents a higher corrosion potential and wide passive range and a transpassive process, whereas in borate buffer solution, the alloy exhibits a lower corrosion potential and a transpassivation–secondary passivation transition, as evidenced by the hump in current density after the passive domain. The secondary passivation is not always observed in polarization curves. Mishra *et al.* [27,28] showed that the occurrence and intensity of this phenomenon are closely related to the pH and oxyanion of the solution. They proved that the full process, including the apparent breakdown of the passive film followed by an anodic peak and a secondary passive region, occurs for Cr-containing Ni-based alloys for solutions with pH > 8.6, such as carbonate/bicarbonate or borate buffer solutions. They also reported that for Ni–Cr–Mo alloys, the apparent transpassive potential and anodic peak potential are independent of the chemical composition of the alloy. However, the current densities of the anodic peak and secondary passive plateau are affected by the solution and alloy chemistry.

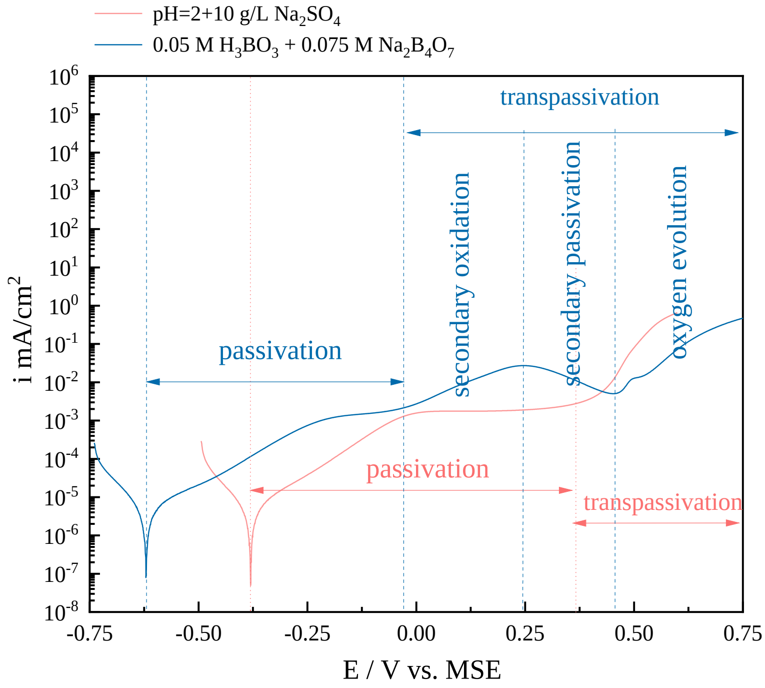

Fig.4. 1 Potentiodynamic polarization curves obtained for Ni–20Cr binary alloy in aerated acidic and buffer solutions (scan rate of 0.5 mV/s after 24 h of immersion).

In the present work, the relation between the passive and transpassive behaviors and the chemical composition of synthetic Ni-based alloys will be addressed, focusing on the role of not only the Cr content but also the Fe content. Indeed, Fe is generally added as an alloying element in Ni-based alloys because it reduces the total cost of the material while improving the machinability and weldability. Even if Fe contributes to the passive film formation, the addition is not straightforwardly beneficial to the corrosion behavior of Ni-based alloys. For example, in acidic solution, adding 8 wt.% Fe to Ni–Cr binary alloys increases the current density of the active peak and the passive plateau [172]. In acidic saline solution, the ternary Ni–Cr–Fe alloy was more sensitive to pitting corrosion than the binary Ni–Cr alloy even though the thickness of the passive film was not remarkably changed and only minor amounts of Fe were detected [173]. In basic solution, Boudin *et al.* [174] confirmed that the passive film thickness was unchanged by the addition of Fe and that the oxidized Fe mainly appeared in the mid-part of the passive film. Moreover, the addition of Fe to Ni-based alloys has been shown to decrease the corrosion currents in the transpassive potential range [175]; however, this finding is not yet well understood.

Considerable research has been conducted on the passivation of binary Ni–Cr and ternary Ni–Cr–Fe alloys [12,163,167,168,175]; however, the growth mechanism and the nature, composition, and structure of the passive films during polarization processes remain largely unexplored. Moreover, most prior investigations on the corrosion behavior of passive alloys have focused on the passive regime, with little attention paid to the transpassive phenomenon and the key parameters governing it. A relatively high potential is required to activate transpassive dissolution; nevertheless, certain service conditions (accidents, radiolysis,…) can shift the potential [176], resulting in transpassive dissolution and consequently shortening the service life of alloys. Moreover, Chiang *et al.* suspected that the susceptibility to stress corrosion cracking may be related to the active dissolution due to transpassivation [177]. Hence, preventing damage from transpassive dissolution is of considerable interest in the corrosion domain [178]. A better understanding of the passivation process and mechanism when the applied potentials change, even in the transpassive and secondary passivation regimes, could provide insight into the key factors of success for the design of new alloys.

The aim of this chapter was to investigate the role of alloying elements in the passivation behavior of Ni–Cr-based model alloys under polarization over a wide potential range. Successive electrochemical impedance measurements were performed on various binary Ni–Cr and ternary Ni–Cr–Fe alloys in borate buffer solution. Thanks to recent advances in the analysis of electrochemical impedance spectra, successive electrochemical impedance measurements provide insight into the chemical processes occurring during passivation and polarization processes [179]. Using this approach, a better understanding of the effect of the alloy composition (Cr and Fe content) on the electrochemical behavior of Ni-based alloys from cathodic potential to the transpassive region was attained. In addition, the roles of the alloying elements in the secondary passivation process and especially in determining the chemical composition of the passive film were studied in detail using X-ray photoelectron spectroscopy (XPS).

The results obtained from the successive electrochemical impedance measurements were intentionally separated into the study of the polarization curves and the investigation of the evolution of the electrochemical parameters determined through analysis of the impedance spectra.

4.2 Current density–potential curves

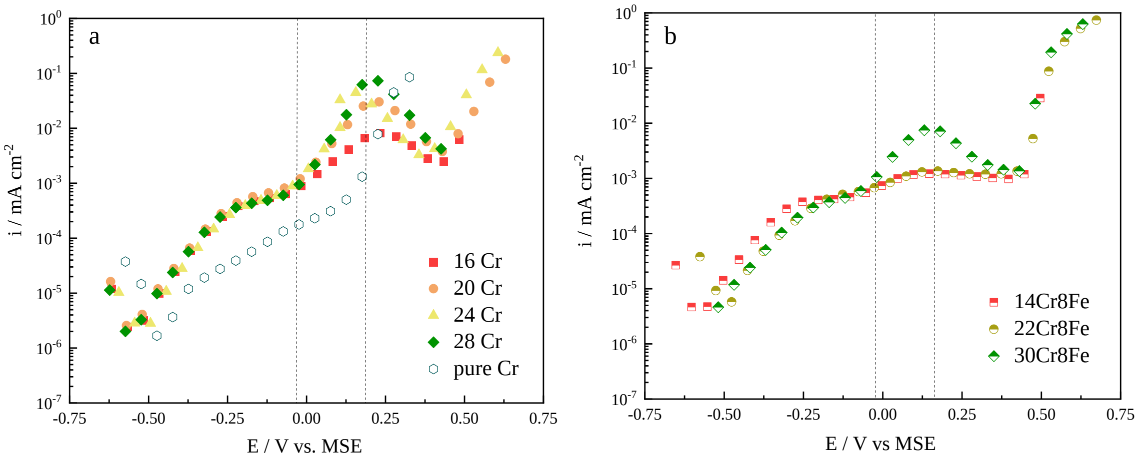

Fig.4. 2 Potentiostatic polarization curve for (a) binary Ni–xCr alloys (x=16, 20, 24, 28 wt%) and pure Cr, (b) ternary Ni–xCr–8Fe alloys (x=14, 22, 30 wt%), obtained in aerated 0.05 M H3BO3 + 0.075 M Na2B4O7 10H2O borate buffer solution at pH=9.2.

Fig.4. 2 (a) presents the polarization curves for the Ni–xCr alloys (x=16, 20, 24, 28) and pure Cr in aerated borate buffer solution obtained by step-by-step potentiostatic measurements. The reported current density is the average value of the last ten measurements for each potential step. For all the curves, the corrosion potential was close to −0.6 V vs. MSE. The shapes of the polarization curves of the Ni–xCr alloys with different Cr contents were similar, especially in the passive domain defined between −0.6 V and 0 V vs. MSE. For more anodic overvoltage, a hump in the current density related to the second oxidation and repassivation followed by a final increase of the current density was observed. Anodic current densities of the same order of magnitude were observed in the passive range regardless of the Cr content in the binary alloy. This result suggests that the passive behavior characterized in the borate buffer solution remains almost independent of the Cr content. However, the critical current density measured at 0.23 V vs. MSE for the Ni–16Cr, Ni–20Cr, Ni–24Cr, and Ni–28Cr alloys was 0.008, 0.03, 0.04, and 0.07 mA cm^{-2}, respectively. Notably, for all the tested materials, the current-density peak increased with increasing Cr content; however, the current density corresponding to the second passivation plateau remained the same. For comparison, the polarization curve for pure Cr was obtained under the same conditions. Notably, no secondary passivation phenomenon was observed in this case. Only transpassive dissolution, indicated by the continuous increase of the current density for potentials higher than 0.20 V vs. MSE, was observed. Consequently, the second oxidation–repassivation transition was induced by the Ni matrix that plays a role in this potential domain, allowing the repassivation phenomenon [180]. It is worth mentioning that in this potential range, Ni remains in a passive state [104,181].

Similar polarization curves were obtained for the ternary Ni–xCr–8Fe alloys (x=14, 22, 30 wt%), as presented in Fig.4. 2 (b). The corrosion potentials for all the alloys were close to the value of −0.6 V vs. MSE of the binary alloys. Moreover, the current-density plateau for the ternary alloys had the same order of magnitude. With the addition of Fe, the corrosion tendency in the passive region was not changed. These findings suggest that the passive film grown in borate buffer solution behaved similarly for all the materials tested within the passive domain and that the barrier property of the passive film should be attributed to a similar inner layer. However, interestingly, the dissolution–repassivation peak for the Ni–14Cr–8Fe and Ni–22Cr–8Fe alloys was almost absent in the secondary passivation domain compared with that of the Ni–Cr binary alloys. For these two materials, a smooth evolution of the current density was observed at 0.0 V vs. MSE before a plateau of 1 µA cm^{-2} was reached, indicating a slight evolution of the interface. In contrast, the dissolution–repassivation peak still existed for the Ni–30Cr–8Fe alloy, and the critical current density near 0.13 V vs. MSE was 7 µA cm^{-2}. Thus, the addition of Fe has a beneficial role in the electrochemical behavior, limiting the current density in the transpassive potential domain, consistent with findings in the literature [175]. This effect is also suggested for the corrosion behavior of stainless steel [182,183].

4.3 XPS characterization

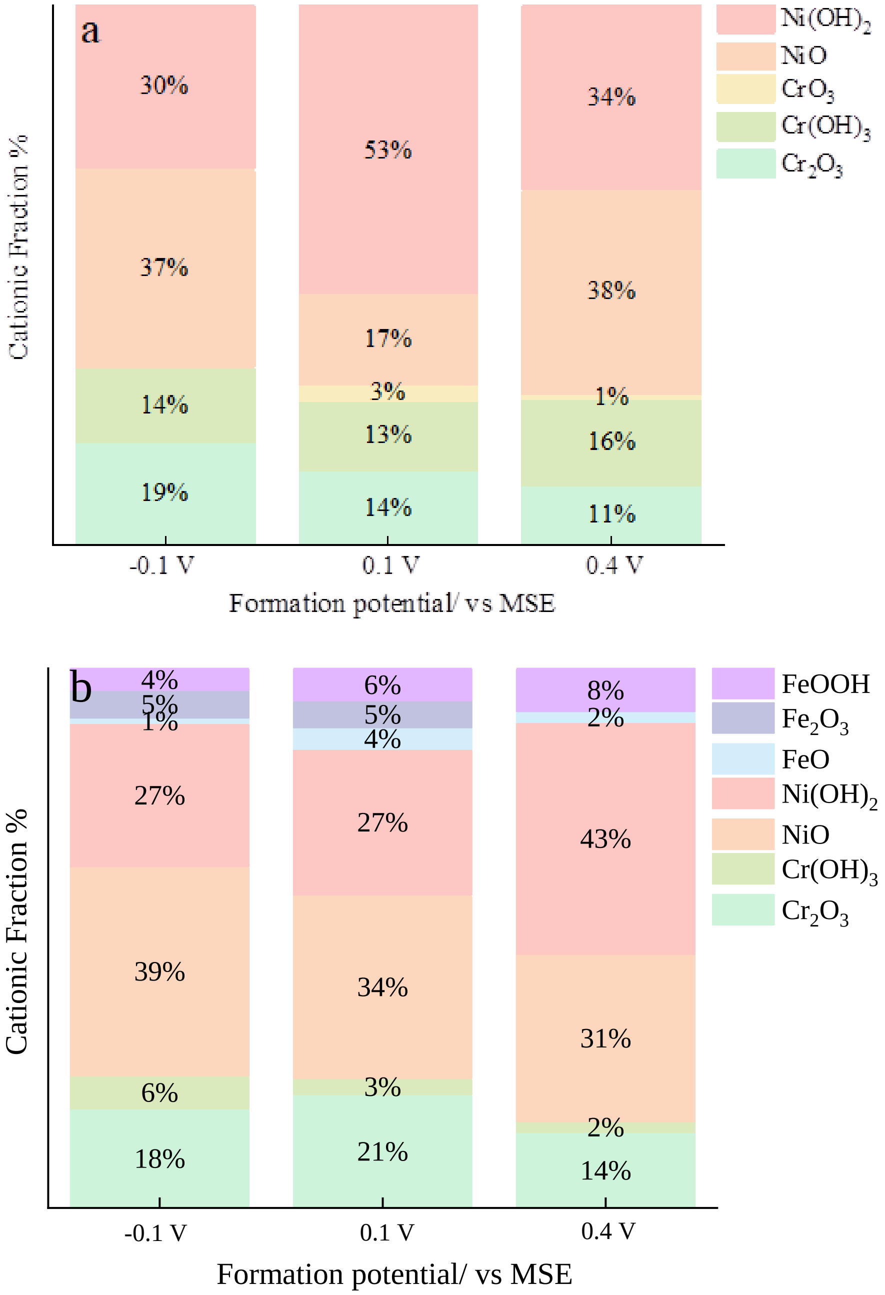

Fig.4. 3 Main components of passive films formed on (a) Ni–16Cr alloy and (b) Ni–14Cr–8Fe alloys under different potentials in aerated 0.05 M H3BO3 + 0.075 M Na2B4O7 10H2O borate buffer solution (pH=9.2).

Table 4. 1 Ratio of oxide to hydroxide for the different metallic elements in passive films formed at different potentials

$M_xO_y/M_{x'}(OH)_{y'}$	−0.1 V vs. MSE	0.1 V vs. MSE	0.4 V vs. MSE
For Cr in Ni–16Cr	1.36	1.31	0.75
For Ni in Ni–16Cr	0.81	0.32	1.12
Total oxide/hydroxide in Ni–16Cr	1.27	0.52	1
For Cr in Ni–14Cr–8Fe	3.0	7.0	7.0
For Ni in Ni–14Cr–8Fe	1.44	1.26	0.72
For Fe in Ni–14Cr–8Fe	1.5	1.5	0.25
Total oxide/hydroxide in Ni–14Cr68Fe	1.7	1.78	1.13

To determine the representative effect of Fe addition on the passive and transpassive behavior, XPS was used to analyze the compositions of the passive films grown at three different potentials on binary Ni–16Cr and ternary Ni–14Cr–8Fe alloys. Indeed, the current density measured on Ni–16Cr revealed the presence of a secondary oxidation peak and secondary passivation, which were not observed for the Ni–14Cr–8Fe alloy (Fig.4. 2). The applied potentials were −0.1 V, 0.1 V, and 0.4 V vs. MSE, corresponding to the domains of passivation, transpassivation, and secondary passivation, respectively. The high-resolution spectra of Cr 2p3/2, Ni 2p3/2, O 1s, and Fe 2p3/2 regions of the passive films were analyzed. The fitted spectra and binding energies corresponding to the different chemical elements are presented in the Appendix Supplementary data. The main components of the passive films formed at different potentials on two samples are summarized in Fig.4. 3. Only information on the oxides and hydroxides was included, and that on the metallic components was excluded. In addition, Table 4. 1 reports the ratio of oxides to hydroxides for the different components in the passive films formed at different potentials.

In Fig.4. 3 (a), at the applied potential of −0.1 V vs. OCP, Cr_2O_3 and $Cr(OH)_3$ were detected for Cr and NiO and $Ni(OH)_2$ were detected for Ni. For the three potentials, the passive films consisted of a mixed oxide–hydroxide layer. The total oxide/hydroxide ratio was close to 1.27 for −0.1 V vs. MSE, decreased to 0.52 at 0.1 V vs. MSE, and increased to 1 at 0.4 V vs. MSE, indicating that more hydroxide formed in the transpassivation process. For the last two potentials, the Cr_2O_3 signal was lower than that at −0.1 V vs. MSE. The Ni hydroxide enrichment was only observed at 0.1 V vs. MSE, corresponding to the dissolution potential. A similar result has been reported in the literature [27,28]. At this potential, the oxide CrO_3 was detected, confirming that Cr^{6+} is generated during polarization at this potential and partially remains within the film. At the potential of 0.4 V vs. MSE, the signal of the metallic state became more pronounced (see Appendix A), indicating that the layer was thin [184]. The passive film was thinner at high anodic potential, and there was less Cr in the film.

XPS analysis of the ternary Ni–14Cr–8Fe alloy, shown in Fig.4. 3 (b), revealed that the chemical composition of the passive layer was more complex. The main oxide–hydroxide networks remained enriched in Cr, Ni, and Fe, contributing to the passive layer in both oxide and hydroxide forms and at different oxidation states. The contents of chromium oxide Cr_2O_3 and hydroxide $Cr(OH)_3$ in the passive film at 0.4 V vs. MSE were lower than those at the other two potentials. It is worth mentioning that CrO_3 was not detected in the passive film formed at the three potentials. Moreover, Ni hydroxide was the main component at 0.4 V vs. MSE. The overall contribution of Fe increased from −0.1 V vs. MSE to 0.1 V vs. MSE. Additionally, Fe_2O_3 was not detected at 0.4 V vs. MSE, and a higher FeOOH content was observed. These results indicate that the combination of Ni and Fe plays a significant role in the passive film behavior at high anodic potentials by modifying the oxide layer and limiting the dissolution of the material, especially forming hydroxides at 0.4 V vs. MSE, thus preserving the passivity.

4.4 Evolution of EIS parameters determined graphically during anodic polarization

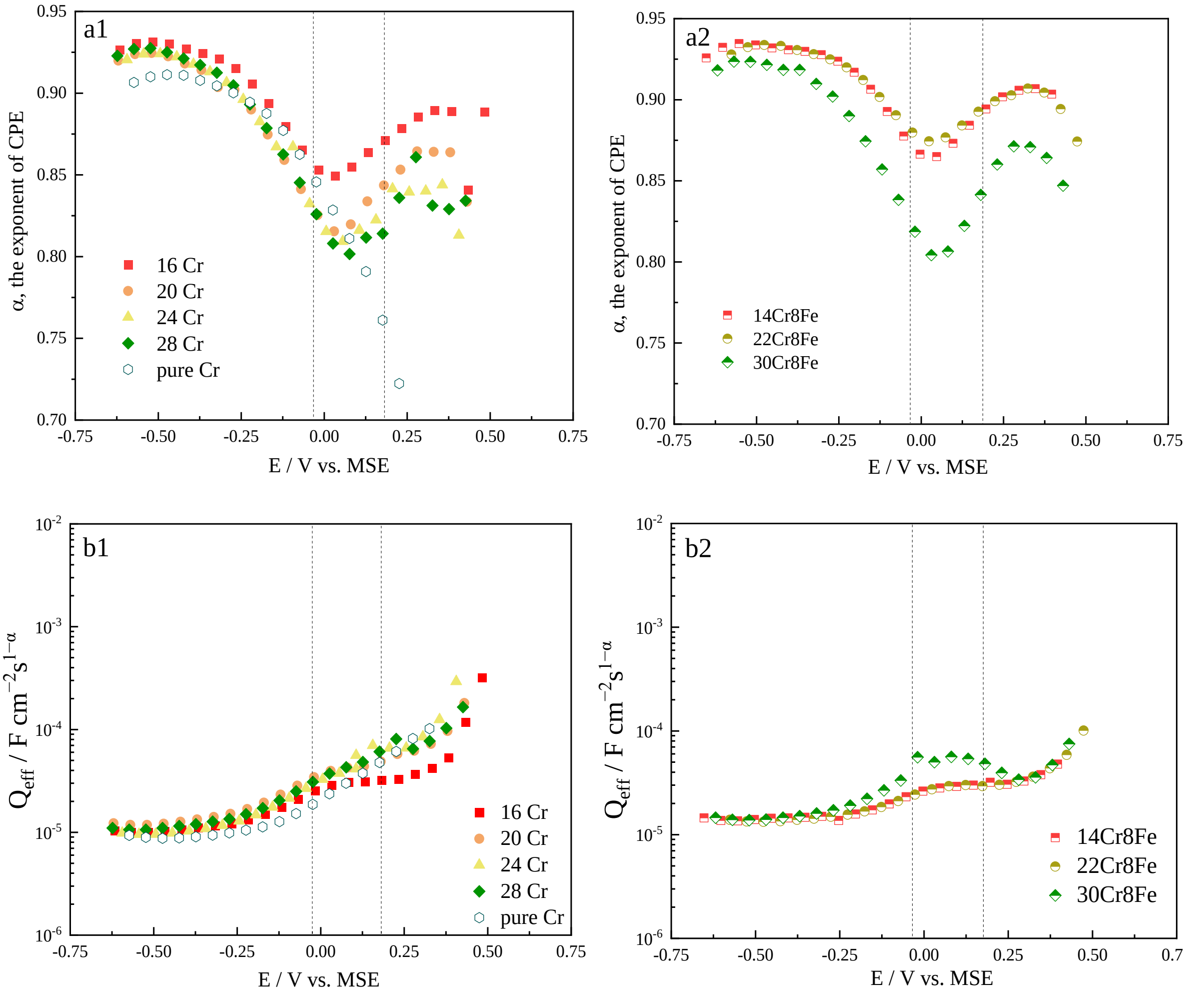

Fig.4. 4 Evolution of CPE parameters α and Qeff with potential for (a) binary Ni–xCr alloys (x=16, 20, 24, 28 wt%) and pure Cr, (b) ternary Ni–xCr–8Fe alloys (x=14, 22, 30 wt%) in 0.05 M H3BO3 + 0.075 M Na2B4O7 10H2O borate buffer solution (pH=9.2).

The evolution of the graphically determined CPE exponent α with potential for the Ni–xCr alloys (x=16, 20, 24, 28 wt%) and pure Cr is shown in Fig.4. 4 a1. Regardless of the chromium content, the α values were similar with the same evolution trend with the applied anodic potential. The CPE parameter remained stable at approximately 0.92 in the potential range between −0.6 V and −0.25 V vs. MSE, followed by a decrease to 0.85 at 0.05 V vs. MSE. In the potential range defined by the secondary oxidation for Ni–Cr alloys, α increased continuously, reaching approximately a plateau at 0.89 at 0.3 V vs. MSE for 16Cr and 0.83 for 28Cr. Finally, for more anodic potential, α decreased again. This evolution provides relevant indications about the reactivity of the Ni–xCr alloys. First, in the passive domain, the passive film was modified when the potential increased, even before the occurrence of the transpassive dissolution, suggesting a continuous alteration of the passive film to breakdown. Then, during the second oxidation, transpassive dissolution occurred and was followed by a novel oxide formation, limiting the current density. The CPE parameter α is linked with the dispersion of time constants related to surface heterogeneity or chemical composition distribution within the passive film. During polarization, both contributions of the passive film structure and electrochemical reactions modify the dispersion of time constants and must be considered. In the potential domain related to second oxidation, α is dependent of the Cr content in the Ni–xCr alloys, suggesting that the structure or chemical composition of the oxide layer is different from that of the original passive film or that the transpassive dissolution kinetics is affected by the Cr content. For comparison, α for the pure Cr remained over 0.9 in this passive potential range but decreased all the time within the transpassive region. No increase of α was observed because no secondary passivation was detected during the measurement. The evolution of the second CPE parameter Q_{eff} with potential for the Ni–xCr alloys and pure Cr presented in Fig.4. 4 b1 is consistent with a continuous evolution of the passive layer up to -0.05 V vs. MSE, followed by a slightly different evolution within the second-oxidation domain. For pure Cr, this second trend was less observable, as no second passivation occurred. The final increase of Q_{eff} is related to the complementary contribution of the double-layer capacitance associated with the reaction of water oxidation.

When Fe was added to the binary Ni–Cr alloy to obtain the Ni–xCr–8Fe alloys (x=14, 22, and 30 wt.%), the CPE parameter α showed a similar trend regardless of the tested material (Fig.4. 4 a2). The value of α remained stable at approximately 0.92 in the potential range of −0.6 V to −0.25 V vs. MSE, followed by a decrease to 0.85 at -0.05 V vs. MSE. In the potential range of secondary oxidation, the value of α increased again, reaching approximately 0.89 at 0.3 V vs. MSE. When the potential was nobler than 0.3 V vs. MSE, α decreased again. Similar to the observation for the binary Ni–Cr alloys, the value of Q_{eff} for the Ni–xCr–8Fe alloys increased with applied potential (Fig.4. 4 b2). These results indicate that the evolution trends of α and Q_{eff} are quite similar for binary and ternary alloys, whereas the polarization curves differ, especially in the domain of the second oxidation potential. However, the values of α in this potential domain were always higher for Ni–14Cr–8Fe and Ni–22Cr–8Fe than for the 30 wt.% Cr-containing alloy, exhibiting a current-density peak. This finding suggests that Fe plays a role in the structure and chemistry of the oxide film within this potential range. When the Cr content was less than 30 wt.%, the dissolution of the passive film or the second oxidation kinetics of Cr was limited by the presence of Fe. Moreover, the higher value of α indicates that Fe contributes to a more homogenous oxide layer in the high potential region.

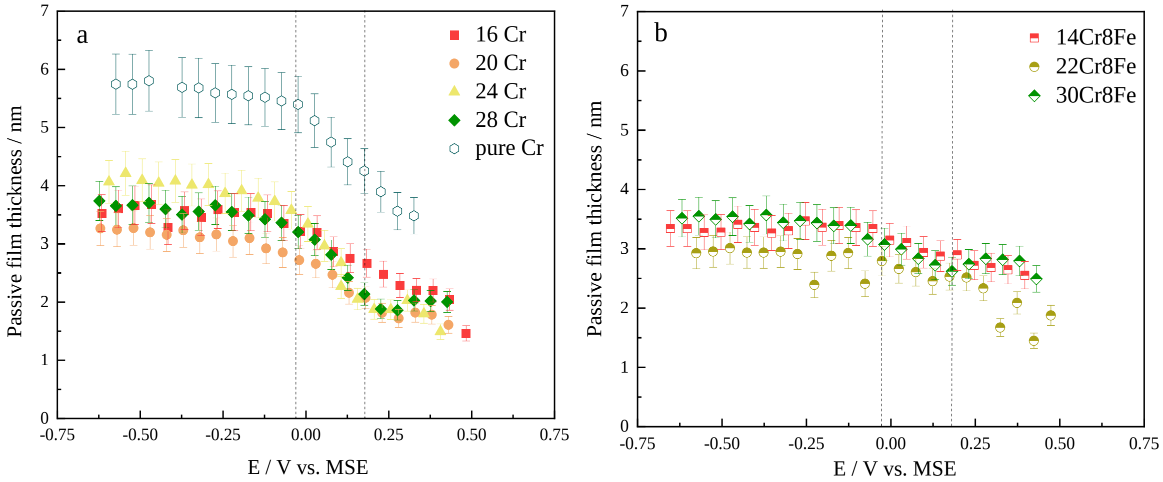

Fig.4. 5 Evolution of calculated passive film thickness as a function of the applied potential for (a) Ni–xCr alloys (x=16, 20, 24, 28 wt%) and pure Cr and (b) Ni–xCr–8Fe alloys (x=14, 22, 30 wt%) in 0.05 M H3BO3 + 0.075 M Na2B4O7 10H2O borate buffer solution (pH=9.2).

The evolution of the evaluated passive film thicknesses with potential for the Ni–xCr alloys (x=16, 20, 24, 28 wt.%) and pure Cr is shown in Fig.4. 5 (a). The deviation for the calculated thickness was approximately 9%. The deviation was calculated from the different estimations from the graphical determination for infinite capacitance. The evolutions of the passive film thicknesses for the four binary alloys show the same trend and can be separated into two parts. For the potentials below 0.0 V_{MSE}, there was no obvious change in thickness (a slight decrease). During polarization, the continuous increase of potential resulted in slight thinning of the passive films within the passive domain. The decrease of the thickness with applied anodic potential might be linked with the properties of the Cr oxide semiconductor grown on the Ni–Cr alloys [185]. Because the Cr oxide generally acts as a p-type semiconductor, the generation of cation vacancies was promoted during the polarization process. In the more anodic potential range (over 0.0 V_{MSE}), the thickness decreased rapidly, which could be linked to the transpassive reaction. The thicknesses were in the range of 3–4 nm for potentials between the cathodic domain and 0 V vs. MSE, whereas that value for pure Cr was up to 6 nm. This result might have been caused by the presence of a larger amount of hydroxide in the passive film formed on pure Cr in basic solution [185] and the calculated thickness of the passive film for Ni–xCr alloys decreased to 1–1.5 nm at a potential of 0.5 V vs. MSE.

Fig.4. 5 (b) shows the evolution of thickness of the passive films with the applied potential for the three ternary alloys. Interestingly, the passive films formed on the different Ni–xCr–Fe alloys were of similar thickness, which was close to that measured on the binary alloys. A similar result was also reported in the literature [186] and indicates that Fe is not the major element contributing to the passive layer. The calculated thickness of the passive films decreased from 3–3.5 nm at a potential near −0.6 V vs. MSE to approximately 2 nm at the potential of 0.5 V vs. MSE. The evolution of the passive layer thickness for the ternary alloys showed the same tendency as that of the binary alloys. The Fe oxide in the passive film is generally considered an n-type semiconductor [187,188]. As the evolution of the thickness trend was not changed by adding Fe, it can be considered that 8 wt.% Fe addition is not significant enough to change the semiconductor properties of the oxide on the Ni–xCr–Fe alloys. That is, the Fe oxide is incorporated in the Cr oxide network, which remains the main structure.

4.5 Resistivity profiles during anodic polarization

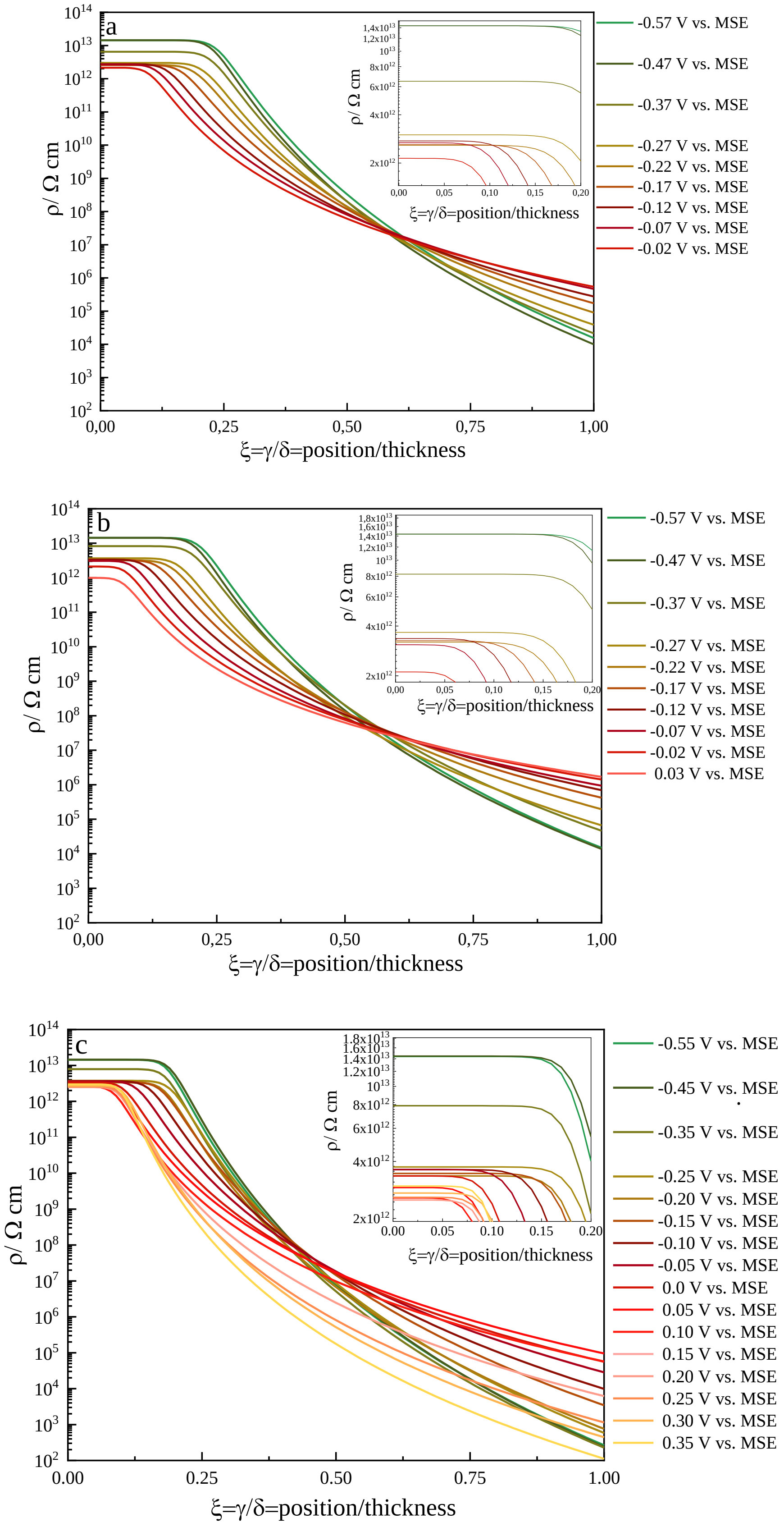

Fig.4. 6 Distribution of resistivity within dimensionless thickness for (a) Ni–16Cr, (b) Ni–28Cr, and (c) Ni–14Cr–8Fe alloys in 0.05 M H3BO3 + 0.075 M Na2B4O7 10H2O borate buffer solution (pH=9.2).

The resistivities at the alloy/passive film interface (ρ_0) and passive film/electrolyte interface (ρ_δ) were obtained by adjusting the impedance diagram using the PLM. The evolution of these parameters could be studied similar to the previously presented parameters or by using a plot of the resistivity distributions within the passive film as a function of the potential. For the sake of clarity, monitoring of the evolution of the resistivity profiles of the Ni–16Cr and Ni–28Cr alloys was selected to study the effect of Cr content on the passivation behavior of Ni–xCr alloys. In addition, the resistivity profiles of Ni–14Cr–8Fe are presented for comparison with those of Ni–16Cr to study the role of Fe in the passivation behavior. For the same reason, certain potentials were selected to highlight the trend. However, it is important to note that regardless of the Cr content, both limit resistivities, ρ_0 and ρ_δ, follow the same tendency and the addition of Fe does not modify the trend of the evolution in the passive range.

Fig.4. 6 shows the evolution of the resistivity distribution through the passive film for a selection of applied potentials for Ni–16Cr (Fig.4. 6 a), Ni–28Cr (Fig.4. 6 b), and Ni–14Cr–8Fe (Fig.4. 6 c). For the three presented cases, the resistivity distribution profiles consist of two segments. The first segment is a plateau, where the resistivity is equal to ρ_0, starting from the alloy/passive film interface. The second segment corresponds to power-law decay of the resistivity, reaching the passive film/solution interface resistivity ρ_δ. This dual evolution of the resistivity can be linked with the dual structure of the passive film with an inner dense oxide layer and an outer hydrous layer. The length of the resistivity plateau can be considered the thickness of the inner dense chromium oxide, whereas the decay can be considered the electrolytic modified oxide–hydroxide.

The resistivity distributions for Ni–16Cr (Fig.4. 6 (a)) and Ni–28Cr (Fig.4. 6 (b)) present similar evolution trends. Both binary alloys have similar plateau lengths (up to 0.20), indicating that the interfaces between the passive film and alloys are similar and that the thickness of the inner layer is not affected by the Cr content. With increasing potential up to −0.07 V vs. MSE, the length of the plateau decreases. There is a thinning effect of the inner layer even in the passive potential range. Concomitantly, ρ_0 also evolves. It decreases when the potential increases up to −0.22 V vs. MSE. Then, between potentials of −0.22 V and −0.07 V vs. MSE (corresponding to the plateau in the polarization curve in Fig.4. 2 (a), the limit resistivity ρ_0 remains stable. Finally, it decreases again close to the transpassivation potential. This evolution of ρ_0 suggests that this parameter is closely related to the anodic electrochemical reaction. Conversely, for both binary alloys, the resistivity ρ_δ at the passive film/solution interface shows an increasing tendency with applied anodic potential. The evolution of the resistivity ρ_δ indicates a continuous modification of the outer layer with the applied potential, suggesting the likely variation of the oxide/hydroxide ratio or the densification of this outer layer. This behavior might be caused by the consumption of more defects, which are present at the interface between the passive film and electrolyte. Moreover, it is also worth noting that the shape of the resistivity decay is smoother within the stable passivation domain, suggesting that the passive film is modified in depth during the anodic polarization and that the transition of the inner–outer layer is smoother. These evolution trends did not change with increasing Cr content.

In the resistivity profile of the ternary Ni–14Cr–8Fe alloy (Fig.4. 6 c), the length of the plateau (up to 0.15) was shortened compared with that of the Ni–16Cr alloy (Fig.4. 6 a). Similarly, as for the Ni–16Cr alloy, the length of the plateau decreased with increasing applied anodic potential and decreasing resistivity ρ_0 until the potential of 0.0 V vs. MSE. In addition, ρ_δ at the interface between the passive film and electrolyte for the Ni–14Cr–8Fe alloy at the initial potential was 10^2 Ω cm, which is much lower than that of Ni–16Cr of 10^4 Ω cm. These findings suggest that Fe contributes to the outer layer of the passive film (likely in the hydroxide form) and acts as a defect, decreasing the local resistivity, but also that the presence of Fe plays a role in the passive film composition and structure by thinning the inner layer and inducing a more defective outer layer. However, the current density measured during polarization was similar, indicating that the inner layer acts as the barrier and that the electrochemical reaction at the metal/passive film interface is the limiting factor. Furthermore, ρ_δ for the Ni–14Cr–8Fe alloy reached a maximum of 10^5 Ω cm at the potential of 0.0 V vs. MSE, which is close to that obtained for the Ni–16Cr alloy. With increasing applied potential, the consumption of defects occurs at the interface between the passive film and electrolyte, as for binary alloys. Because the passivation region of Ni–14Cr–8Fe has a longer passivation potential range than that for the Ni–30Cr–8Fe or Ni–xCr binary alloys, the evolution of the resistivity and resistivity profiles could be monitored over a wider potential range. When the applied potential increased up to 0.35 V vs. MSE, ρ_0 remained constant (slight increase), whereas the length of the plateau decreased again. Concomitantly, a rapid decrease in ρ_δ was observed, indicating another possible change of the composition of the passive film in this potential range, corresponding to the XPS results presented in Fig.4. 3.

4.6 Role of the alloy composition on the passive and transpassive behaviors

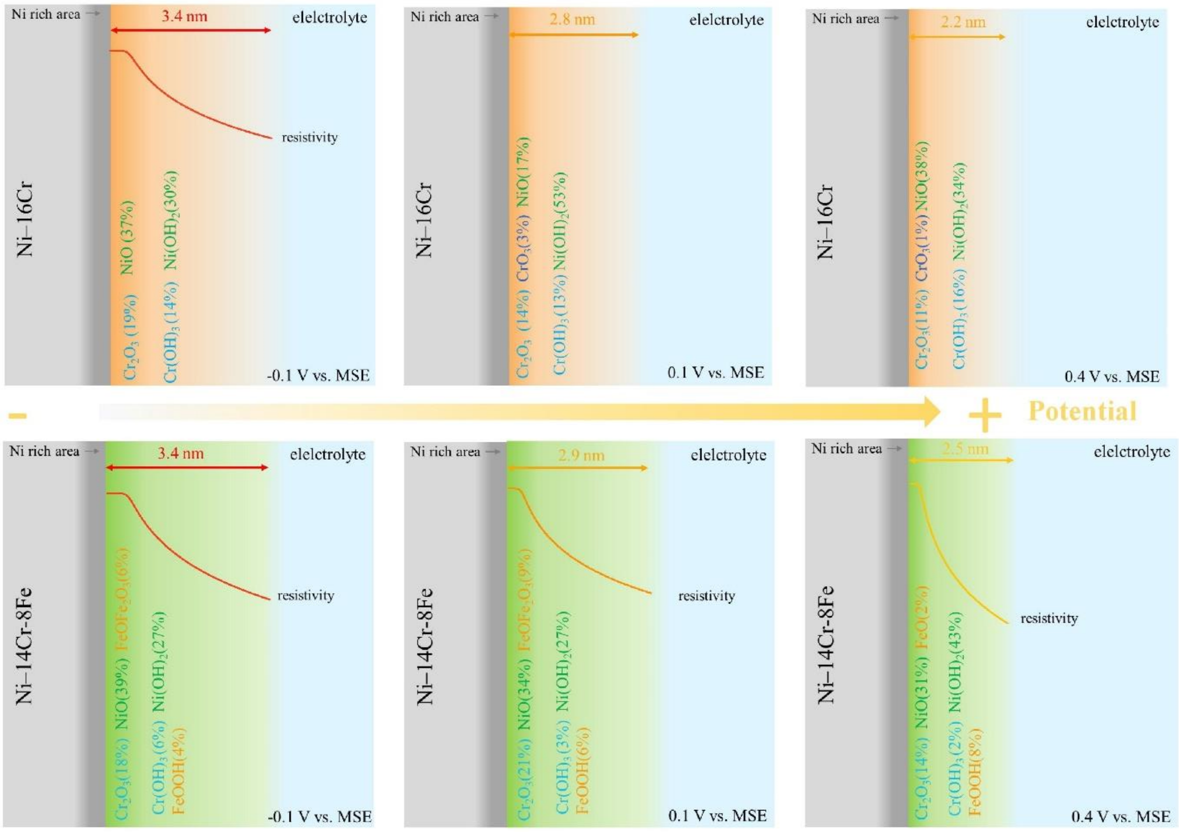

Fig.4. 7 Schematic representation of the evolution of the passive film on Ni–16Cr and Ni–14Cr–8Fe alloy during polarization (from cathodic to anodic domains).

Fig.4. 7 presents schematic representations of the evolution of the passive film grown on Ni–16Cr and Ni–14Cr–8Fe with the applied potential. The representation takes into account the XPS results and the previous discussion on the parameters obtained by analyzing the impedance diagram during

polarization. A duplex representation of the passive film with inner oxide layer and outer hydroxide layer was selected, although it is important to mention that a transition model from a dense oxide to a completely hydrated outer layer would be more accurate. Here in the schematic representation, only global composition of passive film was considered according to XPS results, due to the complexity of further interpreting XPS spectra. Even though a duplex layer of passive film was characterized from electrochemical results.

For Ni–16Cr, the passive film formed in the passive potential domain was composed of Cr oxide and hydroxide, with the contribution of Ni oxide and Ni hydroxide (Fig.4. 3 a). During polarization from OCP to transpassive potential, the thickness of the passive film remained almost stable and was not significantly affected. The thickness of the inner dense layer decreased, and the decay of resistivity through the passive film was smoother. These findings indicate that even if the inner dense layer is thinner, the oxide form in the passive film remains significant. The evolution of the resistivity profiles may be associated with the migration of cation vacancies and cations that progressively modify the inner and outer layers as the applied potential increases. The motion and release of Cr and Ni cations are both involved in governing the steady state. For Ni–14Cr–8Fe, the chemical composition of the passive layer is more complex. The contribution of Fe within the oxide–hydroxide network is non-negligible. During polarization within the passive domain, the impedance parameters obtained for Ni–14Cr–8Fe showed the same evolution as for Ni–16Cr, indicating similar evolution of the passive films. Moreover, if ρ_0 is similar for both materials, ρ_δ is lowest for Ni–14Cr–8Fe, suggesting that the addition of Fe promotes the generation and accumulation of point defects in the outer layer.

When the second oxidation occurs, the dissolution of Cr in the passive layer (according to eq. 4.1) is clearly evidenced for Ni–16Cr by the current density peak in the polarization curves (Fig.4. 2 a) and the presence of CrO_3 in the passive film at 0.1 V vs. MSE. (Fig.4. 2 a). Note that the contribution of the Ni hydroxide also increases between the passive film grown at −0.1 V and 0.1 V vs. MSE. This evolution of chemistry within the passive film is correlated to a decrease of the passive film thickness (Fig.4. 5 a). These results suggest that Ni plays a crucial role in the modification of the passive film during the second oxidation. Indeed, for pure Cr, the thickness and α dramatically decrease, proving that the second oxidation of Cr governs the interface reactivity and causes the thinning of the passive layer. For binary alloys, the presence of Ni compensates the second oxidation of Cr due to the stability of the nickel oxide in this potential range and This effect is greater when the Ni content is higher. Analysis of the XPS data reveals a slight modification of the oxide layer between 0.1 and 0.4 V vs. MSE. Increases of the total oxide/hydroxide ratio and of the $Ni(OH)_2$ contribution are observed. The presence of Ni, which remains passivated in this potential range, delays the dissolution and oxidation of Cr or Cr_2O_3 from the alloy or passive film. This prevention effect is assisted by the presence of the underneath metal layer affected by the preferential oxidation of Cr during the passivation process and Ni enrichment. However, this second passivation was not sufficient to prevent degradation of the alloys: this layer was thin, the current density was rather high, and the metal grain boundaries were etched, suggesting that preferential diffusion and oxidation occurred there.

For Ni–14Cr–8Fe, the transpassive behavior was different. First, no anodic peak appeared on the polarization curve (Fig.4. 2 b). Instead, a singularity followed by a plateau was observed. Moreover, at 0.1 and 0.4 V vs. MSE, CrO_3 was not detected by XPS in the passive film at these potentials. These findings indicate that the second oxidation of Cr is inhibited by the presence of Fe. Moreover, Palotta *et al.* [189] suggested that if CrO_3 is not detected by *ex-situ* XPS analysis, a redox reaction may arise within the passive film between Fe (II) and Cr(VI) when the polarization is performed (reaction 4.2).

$$3Fe(\mathrm{II})_{film} + Cr(\mathrm{VI})_{film} \rightarrow\ Cr(\mathrm{III})_{film+}3Fe(\mathrm{III})_{film} \qquad (4.2)$$

The XPS analysis also revealed some differences between the passive films grown at 0.1 and 0.4 V vs. MSE. The passive film grown at 0.4 V vs. MSE was depleted in Cr (oxide and hydroxide forms) but enriched in Ni hydroxide. These results suggest that Fe within the passive film plays a complementary role, hindering the second oxidation peak and limiting the dissolution of Cr in basic solution. Then, the 8 wt.% Fe in the alloy may have a synergetic effect with Ni to limit the dissolution of the substrate and maintain a second passivation layer at potential higher than the Cr second oxidation potential. However, for Ni–30Cr–8Fe, the amount of Fe was not enough to prevent the anodic dissolution in the transpassive domain (Fig.4. 2 b), resulting in a critical current density of 7 μA cm^{-2}, which is larger than the passive current density of 1 μA cm^{-2} on the Ni–14Cr–8Fe and Ni–22Cr–8Fe alloys.

4.7 Conclusion

The goal of this study was to highlight the role of the chemical composition of Ni-based alloys, essentially the Cr content and the addition of Fe, on their passive and transpassive behaviors in borate buffer solution. The electrochemical characterization was performed using successive impedance measurements over a wide potential range with the incorporation of recent advances in impedance diagram analysis. This innovative and *in-situ* approach enabled monitoring of the evolution of the electrochemical parameters, physical parameters, and XPS data to better understand the modification within the passive film during polarization.

The polarization curves and parameters extracted from the impedance diagrams indicate that the Cr content in the alloy has no obvious effect on the passivation behavior of Ni–xCr in the passive potential domain. The normalized resistivity profiles showed the same duplex distribution and evolution despite the increased Cr content. However, the Cr content straightforwardly affects the electrochemical behavior of the alloys when transpassive dissolution occurs. A higher Cr content in the Ni–xCr alloys results in a higher current density peak in the transpassivation–second passivation processes. The Ni oxide or hydroxide could limit the oxidation of Cr to some extent.

Similarly, the addition of 8 wt.% Fe can diminish the current density peak related to the secondary passivation in the polarization curves. However, the dissolution peak cannot be completely reduced when the Cr content is high. The presence of Fe within the passive film tends to limit the dissolution of the alloys at high anodic potential by maintaining a passive layer at the surface of the alloy. XPS analysis also revealed an enrichment of Ni hydroxide in the passive film composition, indicating a synergetic effect of Fe and Ni to compensate the secondary oxidation of Cr.

With the help of successive impedance measurements and the power-law model, it was possible to obtain more information about passive films within the passivation domain, namely the evolution of the CPE parameters, thickness of the passive film, and resistivity profiles with applied potential. This measurement method might also be employed for the study of commercial alloys or to design new alloys.

Chapter 5 Application of method on the commercial alloys

5.1 Introduction

This chapter is focused on the application of the methodology of successive impedance measurements on commercial Ni-based alloys. Since the commercial alloys are generally composed with more than three alloying elements and traces, the chemistry, structure, and behavior of passive films could differ from the model alloys. In addition, the different microstructure features, as carbides and precipitated phases or grain size, might also have influence on the corrosion behavior. Consequently, it is interesting to compare the passive film properties grown on commercial alloys with their model alloy counterparts in order to highlight the discriminating microstructural factors. The Ni based commercial alloys used in this chapter are GILPHY 80 (Ni80Cr20) compared with NiCr20, Inconel 600 (NiCr14Fe8) compared with NiCr16 and NiCr14Fe8, and Inconel 625 (NiCr20Mo8Nb) compared with NiCr20 and NiCr22Fe8, respectively. The composition and microstructure of the used commercial alloys have already been introduced in the Chapter 2. Note that this chapter presents an opening of the methodology presented previously and some complementary experiments are still required to confirm the proposed assumptions.

5.2 GILPHY 80 (Ni80Cr20)

GILPHY 80 is a Ni-Cr electrical-resistance alloy containing few amounts of Si (less than 1.6 %weight). This alloy has a low coefficient of resistance making it suitable for control resistors. Moreover, it exhibits a good high temperature stability and a well-adhering oxide scale even under cyclic conditions. GILPHY 80 is used for heating elements in domestic appliances and industrial equipment [190].

To compare the different corrosion behavior between model alloy NiCr20 and GILPHY 80, the successive impedance measurements were performed in the solutions of 0.05 M H_3BO_3 + 0.075 M $Na_2B_4O_7$ $10H_2O$ (pH=9.2) and 10 g/L Na_2SO_4 with H_2SO_4 (pH=2).

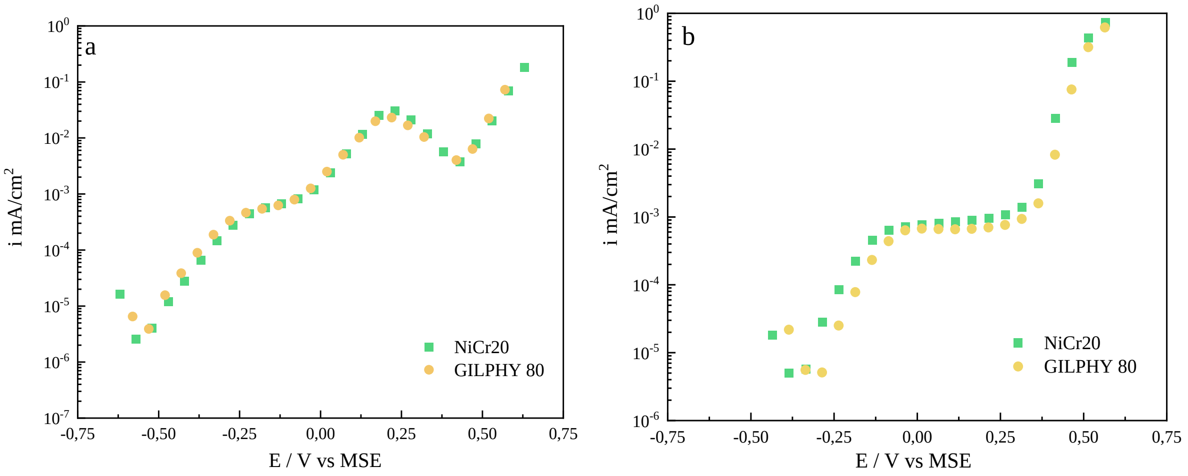

Fig. 5. 1 Potentiostatic polarization curves of NiCr20 and GILPHY 80 in aerated solution of (a) 0.05 M H_3BO_3 + 0.075 M $Na_2B_4O_7$ $10H_2O$ (pH=9.2) and (b) 10 g/L Na_2SO_4 with H_2SO_4 (pH=2)

Fig. 5. 1 (a) shows the potential-step polarization curves for NiCr20 and GILPHY 80 in aerated borate buffer solution. The polarization curves of NiCr20 and GILPHY 80 alloys show similar shapes. For the two curves, the corrosion potentials are very close. The corrosion potential of NiCr20 is -0.54 V vs. MSE whereas that of GILPHY 80 is -0.57 V vs. MSE. The same order of magnitude of anodic current densities is observed on the passivation range for both alloys. For the more anodic over-voltages, the second oxidation and repassivation are observed for both alloys. The measured critical current density at 0.23 V vs. MSE is 0.03 mA cm^{-2} and 0.023 mA cm^{-2} for NiCr20 and GILPHY 80, respectively. In brief, the passive behavior of NiCr20 and GILPHY 80 is similar in terms of current density and potential domains.

Potentiostatic polarization curves of NiCr20 and GILPHY 80 in acidic solution is presented in Fig. 5. 1 (b), the corrosion potential for NiCr20 is approximately −0.36 V vs. MSE whereas that for GILPHY 80 is about −0.31 V vs. MSE. The transpassive region for both alloys begins at 0.3 V vs. MSE. The passive current density for NiCr20 and GILPHY 80 is about 8.08×10^{-4} mA cm^{-2} and 6.5×10^{-4} mA cm^{-2}, respectively.

Impedance diagrams obtained during the SEIS experiment were analyzed. The relevant parameters, such as CPE parameters (α and Q_{eff}), thickness etc. and their evolutions are not presented in detail since there is no significant difference between both alloys (See details in Appendix C). This finding indicates the same tendency than the polarization curves suggesting that the passive films grown on NiCr20 and GILPHY 80 exhibit same properties and same behavior.

Thus, for both test solution, the commercial alloy behaves like the model one. It suggests that:

- As the average grain size of model alloy NiCr20 is 265 µm, whereas that of GILPHY 80 is 61 µm, the grain size does not affect the SEIS measurement. With another point of view, SEIS measurement is not sensitive to the grain size as it is an average measurement on the total exposed surface (which is superior to the grain size).

- The low Si amount in GILPHY 80 alloy does not modify its passive behavior in the test solution of this study.

5.3 Inconel 600 (NiCr14Fe8)

Inconel 600 was often employed as SGs tubing materials in nuclear power plants is now gradually replaced by Inconel 690, due to better SCC resistance of Inconel 690 [191]. However, it is still widely used in a great number of industrial domains, like aerospace, chemical processing, heat treatment industry etc., because of its good resistance to oxidation at elevated temperature. Therefore, it is meaningful to study the passivation behavior of this material to better understand its corrosion resistance. The successive impedance measurements were employed on Inconel 600 in the solutions of 0.05 M H_3BO_3 + 0.075 M $Na_2B_4O_7$ $10H_2O$ (pH=9.2) and of 10 g/L Na_2SO4 with H_2SO_4 (pH=2). The results are compared with that of NiCr16 binary and NiCr14Fe8 ternary alloys.

5.3.1 Inconel 600 passivation behavior in borate buffer solution

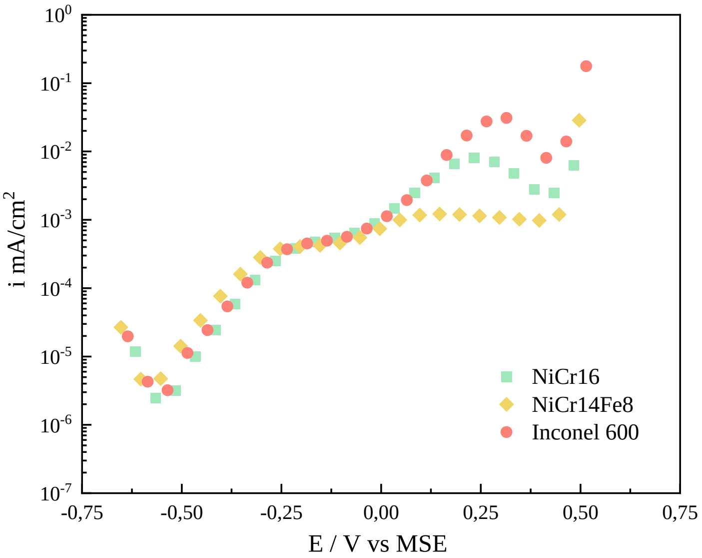

Fig. 5. 2 Potentiostatic polarization curves of NiCr16, NiCr14Fe8 and Inconel 600 in aerated solution of 0.05 M H_3BO_3 + 0.075 M $Na_2B_4O_7$ $10H_2O$ (pH=9.2).

The measured polarization curves for NiCr16, NiCr14Fe8 and Inconel 600 in aerated borate solution is presented in Fig. 5. 2. The curves for NiCr16 and Inconel 600 are quite similar, showing a passive domain and the transpassivation-secondary passivation transition. On the contrary, NiCr14Fe8 does not have this transition as discussed in Chapter 4. Nevertheless, the three samples present the same stable passivation domain. The corrosion potentials for the three samples are very close. The corrosion potential of NiCr16, NiCr14Fe8 and Inconel 600 are -0.54 V, -0.56 V and -0.54 V vs. MSE, respectively. The critical current densities for NiCr16 and Inconel 600 are 0.008 mA cm^{-2} at 0.24 V vs. MSE and 0.03 mA cm^{-2} at 0.32 V vs. MSE, respectively. It is interesting to evidence that Inconel 600 behaves more likely to NiCr16 than NiCr14Fe8. Indeed, NiCr14Fe8 and Inconel 600 have totally different corrosion behavior in the secondary oxidation and repassivation domain, even though they have almost the same chemical compositions. Further analysis and characterizations have been done and are presented below.

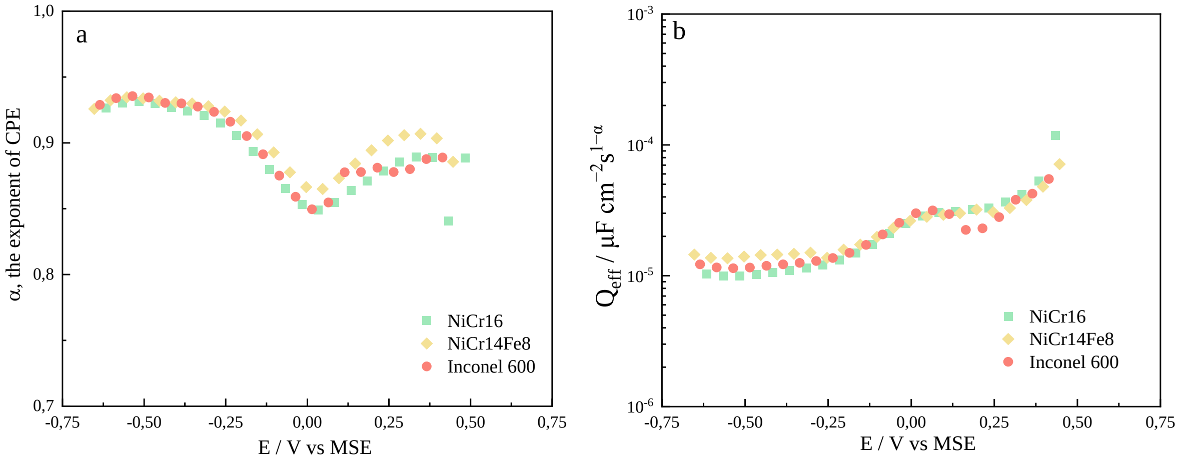

Fig. 5. 3 Evolution of CPE parameters (a) α and (b) Q_{eff} with potential for NiCr16, NiCr14Fe8 and Inconel 600 in aerated solution of 0.05 M H_3BO_3 + 0.075 M $Na_2B_4O_7$ $10H_2O$ (pH=9.2).

Fig. 5. 3 (a) shows the evolution of CPE exponent α with potential for NiCr16, NiCr14Fe8 and Inconel 600 in aerated basic borate solution. Firstly, the value of α is very close for the three samples. The value of α keeps stable about 0.90-0.92 in the potential range between −0.6 V and −0.25 V vs. MSE. Then, the value of α decreases to 0.85 until 0.05 V vs MSE. After, α increases to reach approximately 0.95 at 0.27 V vs. MSE for NiCr16, 0.9 at 0.35 V vs. MSE for NiCr14Fe8 and 0.89 at 0.34 V vs. MSE for Inconel 600. Finally, α decreases again in more anodic potential range. As shown on Fig. 5.3 (b), the evolution tendency of Q_{eff} are quite close for the three samples. The evolution of the parameter Q_{eff} with potential for three samples is consistent with a continuous evolution of the passive layer up to 0.05 V vs MSE, followed by a slightly different evolution within the second oxidation domain, especially for Inconel 600.

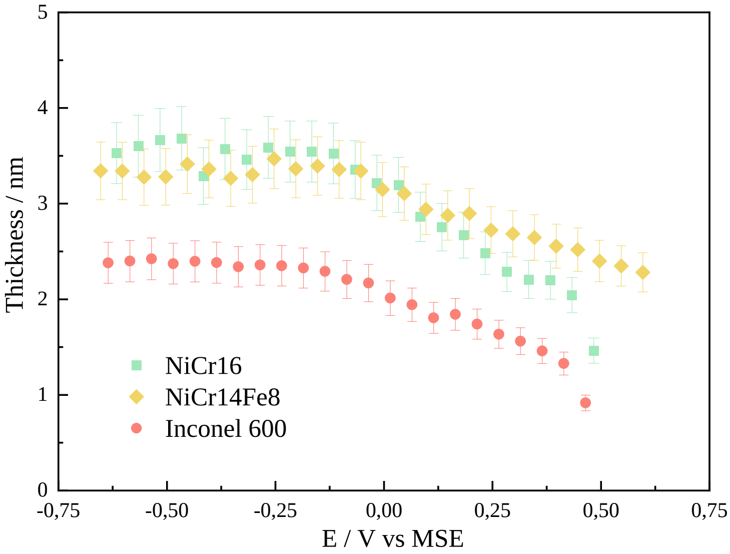

Fig. 5. 4 Evolution of thickness of NiCr16, NiCr14Fe8 and Inconel 600 in aerated solution of 0.05 M H_3BO_3 *+ 0.075 M* $Na_2B_4O_7$ *10*H_2O *(pH=9.2).*

The evolution of thickness of passive films for NiCr16, NiCr14Fe8 and Inconel 600 in aerated solution of 0.05 M H_3BO_3 + 0.075 M $Na_2B_4O_7$ 10H_2O with the applied potential is shown in Fig. 5. 4. The thickness of passive films formed on NiCr16, NiCr14Fe8 has a similar thickness about 3.5 nm, while that for Inconel 600 is about 2.5 nm at the beginning of the test. The calculated thickness of passive films for three samples keeps stable within the potential range of −0.6 V and 0 V vs. MSE. Then the thickness of passive film for NiCr14Fe8 and Inconel 600 reduces gradually up to the potential of 0.5 V vs. MSE. Meanwhile, the thickness of passive film for NiCr16 decreases sharply than the two other samples. It is evident that the decreasing tendency of thickness at higher potential could be hindered by the addition of iron, in spite of differently initial thickness.

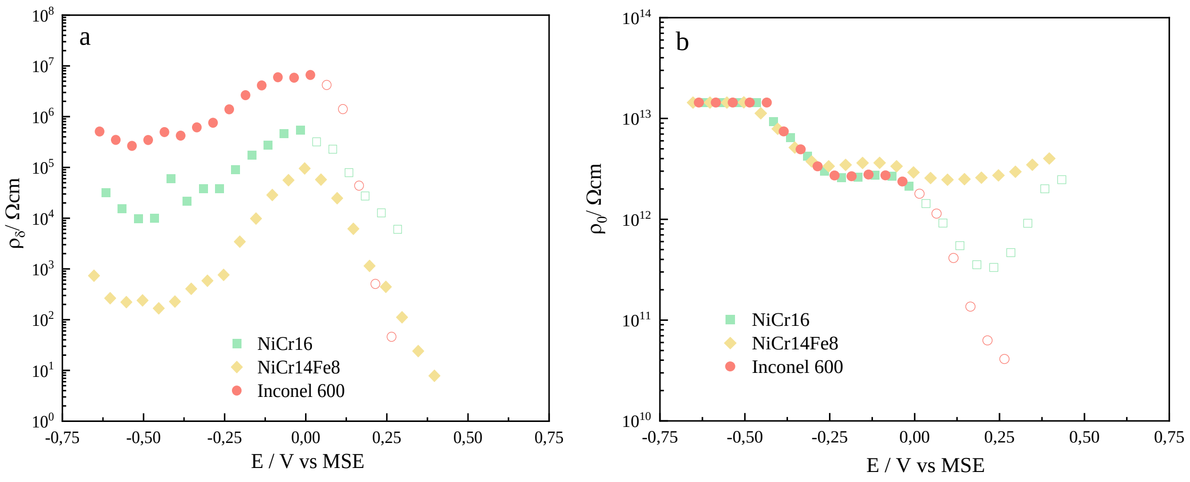

Fig. 5. 5 Evolution of resistivity a) ρ_δ and b) ρ_0 of NiCr16, NiCr14Fe8 and Inconel 600 in aerated solution of 0.05 M H_3BO_3 + 0.075 M $Na_2B_4O_7$ $10H_2O$ (pH=9.2).

Evolution of the fitted resistivities ρ_0 and ρ_δ for NiCr16, NiCr14Fe8 and Inconel 600 are shown in Fig. 5. 5 (a) and (b). Firstly, it is found in Fig. 5. 5 (a) that evolution of the fitted resistivities ρ_δ for three samples exhibits similar trend. The resistivities ρ_δ decreases in the potential domain lower than -0.47 V vs. MSE and increases up to the potential just before the secondary oxidation. The resistivities ρ_δ for NiCr16, NiCr14Fe8 and Inconel 600 are 10^4 Ω cm, 10^3 Ω cm and 10^5 Ω cm in the beginning. This value reaches up to 10^5 Ω cm, 10^4 Ω cm and 10^6 Ω cm, respectively. The evolution values of resistivity ρ_0 of three alloys are very similar, resistivities ρ_0 keep stable, decrease and stay stable again in stable passivation region (in Fig. 5. 5 (b)) with applied anodic potential. However, as mentioned before, the evolution of ρ_0 for alloy NiCr14Fe8 is different with the two other alloys.

To conclude, polarization curves and analysis of the impedance parameters indicate some counter-intuitive results:

- The electrochemical behavior of Inconel 600 is closer to the one of NiCr16 while its chemical composition is close to the one of NiCr14Fe8 as evidenced with the polarization curves and the evolution of ρ_0.

- The thickness of the passive film grown on Inconel 600 is thinner than for the two other alloys.

- The resistivity ρ_δ of the passive film grown on Inconel 600 is higher than for the two other alloys.

These specificities will be discussed later.

5.3.2 Inconel 600 passivation behavior in acidic solution

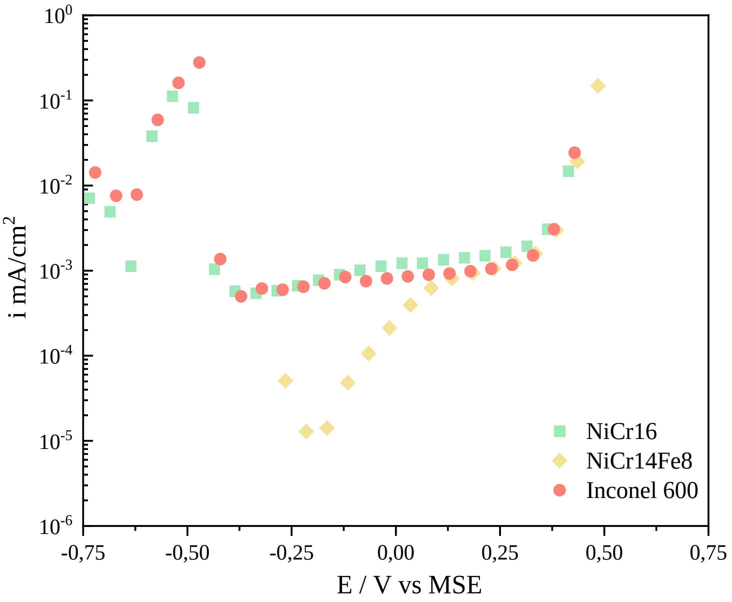

Fig. 5. 6 Potentiostatic polarization curves of NiCr16, NiCr14Fe8 and Inconel 600 in aerated solution of of 10 g/L Na_2SO_4 with H_2SO_4 (pH=2).

The Fig. 5. 6 shows the polarization curves for NiCr16, NiCr14Fe8 and Inconel 600 in aerated acidic solution (pH=2). The curves for NiCr16 and Inconel 600 are quite similar, presenting an active/passive transition and a stable passivation plateau. By contrast, active-passive transition is not observed on NiCr14Fe8. The corrosion potentials of NiCr16, NiCr14Fe8 and Inconel 600 are -0.63 V, -0.18 V and -0.64 V vs. MSE. The passivation current density for NiCr16 and NiCr14Fe8 is about 9 × 10^{-4} mA cm^{-2}, the current density for Inconel 600 is a little bit higher. In addition, no secondary oxidation and passivation peak is observed on the sample in the acidic solution. It is found that the addition of iron in the Ni-Cr alloy could increase the corrosion potential.

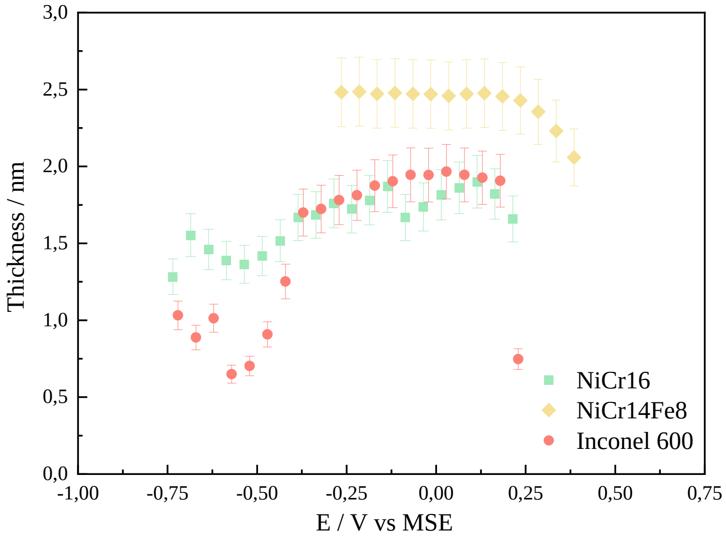

Fig. 5. 7 Evolution of thickness of NiCr16, NiCr14Fe8 and Inconel 600 in aerated solution of 10 g/L Na_2SO_4 with H_2SO_4 (pH=2).

The evolution of thickness of passive films with the applied potential for NiCr16, NiCr14Fe8 and Inconel 600 in aerated acidic solution is shown in Fig. 5. 7. Note that the values of thickness for NiCr16 and Inconel 600 are remarkably low for potentials lower than −0.4 V vs. MSE. It is caused by the active dissolution of these two alloys within this potential range, as seen in the polarization curves in Fig. 5. 6. The thickness of passive films formed on NiCr16 and Inconel 600 has a similar thickness about 1.7 nm at -0.4 V vs. MSE, increasing to 1.9 nm up to 0.2 V vs. MSE. The thickness for NiCr14Fe8 keeps about 2.5 nm within the potential range between -0.27 V and 0.2 V vs. MSE, after that the thickness decreases with more anodic potential applied. This low thickness values confirms that the passive film in acidic solution is thinner and its stability is considered a metastable state, since there is lots of dissolution in less anodic potential and becomes stable passivated after anodic polarization.

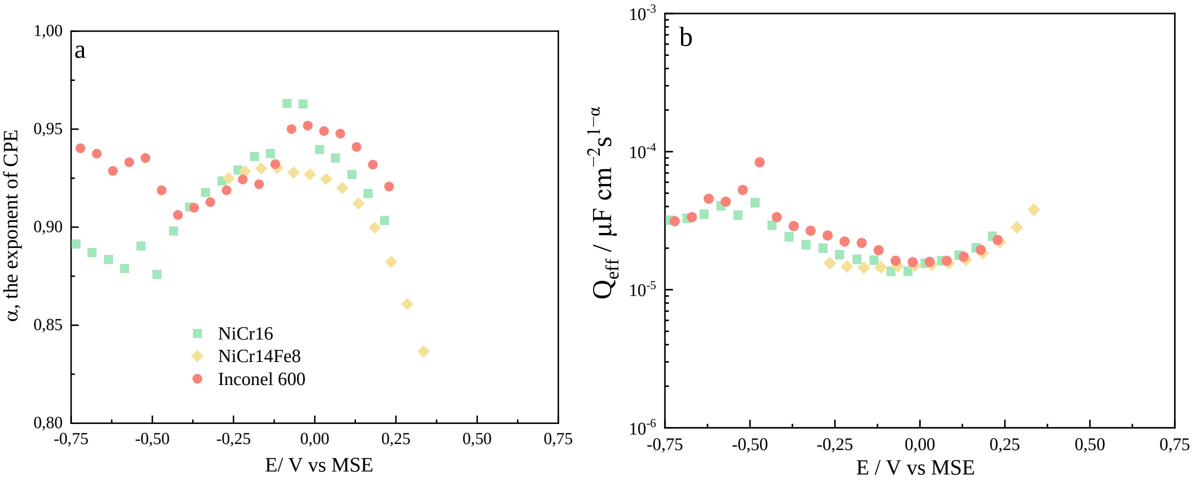

Fig. 5. 8 Evolution of CPE parameters (a) α and (b) Q_{eff} with potential for NiCr16, NiCr14Fe8 and Inconel 600 in aerated solution of 10 g/L Na_2SO_4 with H_2SO_4 (pH=2).

The evolution of CPE parameters of NiCr16, NiCr14Fe8 and Inconel 600 is presented in Fig. 5. 8. It is found that the values of α for NiCr16 and Inconel 600 decrease rapidly, which might be caused by the active-passive transition of the samples in the potential range lower than -0.5 V vs. MSE, seen in Fig. 5. 6. Then, the values of α for these two samples increase with applied anodic potential of 0 vs. MSE and followed by a decrease. While the evolution of α for NiCr14Fe8 keeps stable to 0 vs. MSE and then drops. By contrast, the evolution of Q_{eff} in Fig. 5. 8 (b) presents an opposite trend in comparison with that of α. The values of Q_{eff} for NiCr16 and Inconel 600 increase and decrease and increase again. For NiCr14Fe8, the value of Q_{eff} is stable in the first stage and then increases.

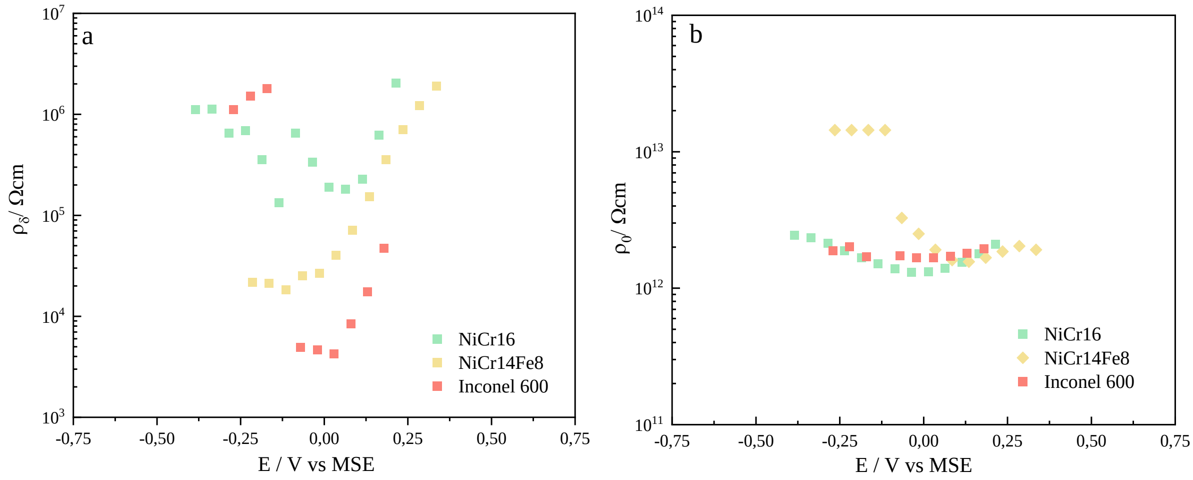

Fig. 5. 9 Evolution of resistivity a) ρ_δ and b) ρ_0 of NiCr16, NiCr14Fe8 and Inconel 600 in aerated solution of 10 g/L Na_2SO_4 with H_2SO_4 (pH=2).

The evolution of limit resistivities of NiCr16, NiCr14Fe8 and Inconel 600 is presented in Fig. 5. 8. The PLM is not used to fit impedance of NiCr16 and Inconel 600 in the active dissolution region, since the stable passive film is not yet formed (or is disturbed). For NiCr16, the measurement of ρ_δ is scattered. Values are included between 10^5 and 10^6 Ω cm. The resistivity ρ_δ for NiCr14Fe8 is constant from the beginning up to 0 V vs. MSE, and then increases. The values of resistivity ρ_δ for NiCr16 and NiCr14Fe8 are very close when the applied potential is greater than 0.15 V vs. MSE. For Inconel 600, the evolution of resistivity ρ_δ is not stable. In the first place, the value of ρ_δ is about 10^6 Ω cm (between -0.25V and -0.15 V vs. MSE), then it is just about 10^3 Ω cm (at -0.1V - 0.05 V vs. MSE), and finally it increases with applied potential to over 10^4 Ω cm. The values of ρ_0 for three samples are close, between 10^{12} Ω cm and 10^{13} Ω cm. ρ_0 remains almost constant for Inconel 600 and NiCr16 alloy.

Like in borate buffer solution, the passive behavior of Inconel 600 is similar to the one of alloy Ni16Cr in the case of acidic solution. Moreover, the values of the impedance parameters extracted on Inconel 600 and Ni16Cr are in the same order of magnitude and follow the same trends with applied potential. Only ρ_δ differs. This last finding needs to be clarified.

5.3.3 Discussion on the reactivity of Inconel 600

Previous results indicate that the passive behavior of Inconel 600 is close to the one of NiCr16 alloy while its chemical composition is closer to the ternary alloy. This finding was observed in both solutions. To better understand that, the relationship between the microstructure and the properties needs to be developed.

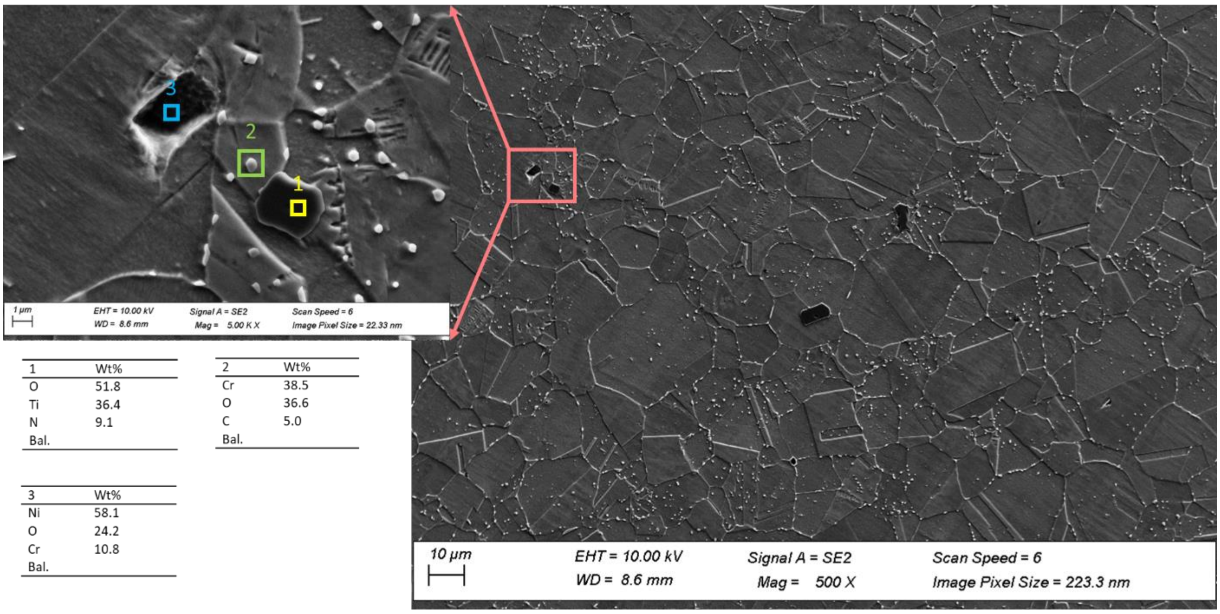

1	Wt%
O	51.8
Ti	36.4
N	9.1
Bal.	

2	Wt%
Cr	38.5
O	36.6
C	5.0
Bal.	

3	Wt%
Ni	58.1
O	24.2
Cr	10.8
Bal.	

Fig. 5. 10 SEM observation for surface microstructure of Inconel 600 after chemical etching and elemental analysis by EDS

Fig. 5. 10 presents the micrographs of surface of Inconel 600 after chemical etching. The etching process has been described in Chapter 2. In addition, a local magnification image is attached with EDS analysis. The austenite microstructure could be observed clearly in the figure, in agreement with the optical micrograph presented in Chapter 2. The matrix grains are decorated by a series of small white precipitates. All along the grain boundary, they are assumed to be chromium carbides $(Fe, Cr)_{23}C_6$. Some of these white precipitates were also detected within the grain. Moreover, there are also black second precipitated phases observed in the micrograph. To confirm the speculation, a local magnification was performed with EDS analysis for knowing the composition. The result is shown in the left part. Different locations were analyzed with EDS in zoomed micrograph. The first one corresponds to the second phase with mostly O, Ti and N content. It could be confirmed that is TiN. The second location EDS analysis is one of the while particles, with 38.5 wt.% Cr, 36.6 wt.% O and 5 wt.% C. Evidently, precipitations of chromium carbide are then evidenced in the micrograph. These carbides are oxidized after the chemical etching inducing the high amount of O detected.

Thus, the existence of $Cr_{23}C_6$ chromium carbides along the grain boundary has been confirmed for the Inconel 600 after chemical etching. It is commonly admitted that this precipitation state, resulting from the thermomechanical past of the sample, induces a sensitized microstructural state. Indeed, during sensitization heat treatments, the precipitates bring chromium from the adjacent austenite and form the chromium carbide $Cr_{23}C_6$ resulting in the formation of chromium depleted zone. The schematic representation of the process is depicted in Fig. 5. 11 below.

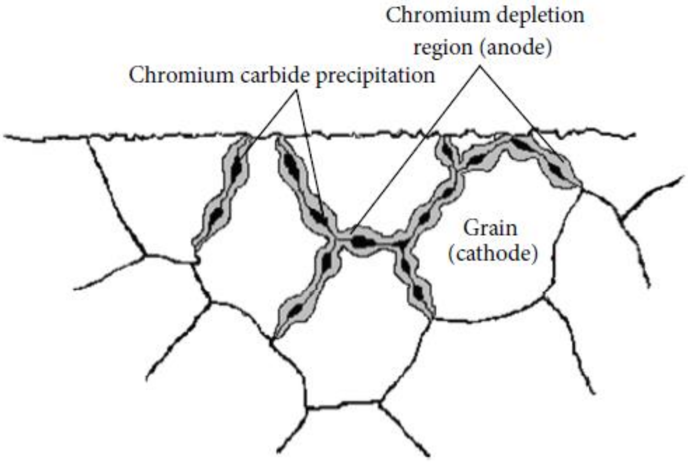

Fig. 5. 11 Schematic representation of precipitation of chromium carbide $M_{23}C_6$ (M=Fe, Cr) at the grain boundaries [36]

The formation of chromium depleted zone near the grain boundary acts as anode whereas grain will play a role of cathode. As a result, a localized breakdown in passivity might happen at the grain boundary causing intergranular corrosion and sometimes stress corrosion cracking. The profile of distribution of chromium concentration at the adjacent of grain boundary is illustrated in Fig. 5. 12.

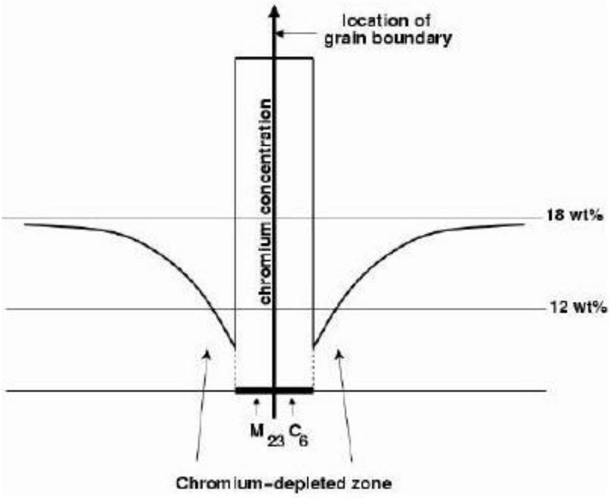

Fig. 5. 12 Distribution of chromium concentration around carbide at the adjacent of grain boundary [192]

It was reported that the minimum chromium concentration reached in the austenite adjacent to the carbide, which in equilibrium with $M_{23}C_6$ is slightly lower than the bulk composition due to multicomponent diffusion effects, the dynamics of the solute fluxes towards the precipitates [192]. The evolution of chromium concentration depends mainly on the aging duration and temperature of producing process [193].

Regarding these microstructural features, it is quite comprehensible that the electrochemical behavior of Inconel 600 in acidic and buffer borate basic solution is compatible to NiCr16 binary model alloy rather than NiCr14Fe8 ternary model alloy. Due to the existence of enriched chromium carbides at grain boundaries in the case of Inconel 600, the concentration of Cr on the subsurface of the material is non-uniform. On the one hand, the passive film formation and growth may differ from one place to another. Generally, it nucleates at the surface of the Cr-rich carbides and then spreads over the surface. This result may explain the fact that in the basic solution, the thickness of passive film formed on Inconel 600 is thinner in comparison with others (in Fig. 5. 4). The effect on the passive film growth results also on resistivity ρ_δ which is larger for Inconel 600 than other two samples, suggesting a thinner but less defective passive film. This phenomenon is less marked in acidic solution due to the active-passive transition occurring during the SEIS. On the other hand, the presence of Cr-rich carbides plays also a role on active-passive transition (acidic solution) and transpassive-secondary passivation transition (basic solution) inhibiting in both cases the role of Fe. The larger dissolution peak occurred in secondary oxidation-repassivation region for Inconel 600 results from the dissolution of the enriched chromium zone. Indeed, as previously presented in Chapter 4, the critical current density of this latter transition is closely related to the Cr content. Fe may reduce this dissolution but its effect is limited for the highest Cr content.

These results prove that the microstructure of the material (precipitation state) plays an important role on the passive behavior of the Ni-based alloys and that this role may hinder the effect of the alloying elements. It could be interesting to perform the SEIS measurement and analysis on the same material but with different heat treatments. This future work may allow to discriminate the role of the alloying elements from the microstructure.

5.4 Inconel 625 (NiCr20Mo8Nb)

Inconel 625 is widely employed in a great number of industries, like oil/gas fields [194], harsh molten-salt environments [195,196] and supercritical water [197] for energy applications etc., due to its excellent strength and corrosion resistance at high temperatures. Moreover, Inconel 625 is one of the candidate materials for future and breakthrough applications, thanks to its good corrosion resistance. Hence, it is critical to study the corrosion resistance of this alloy.

5.4.1 Inconel 625 passivation behavior in borate solution

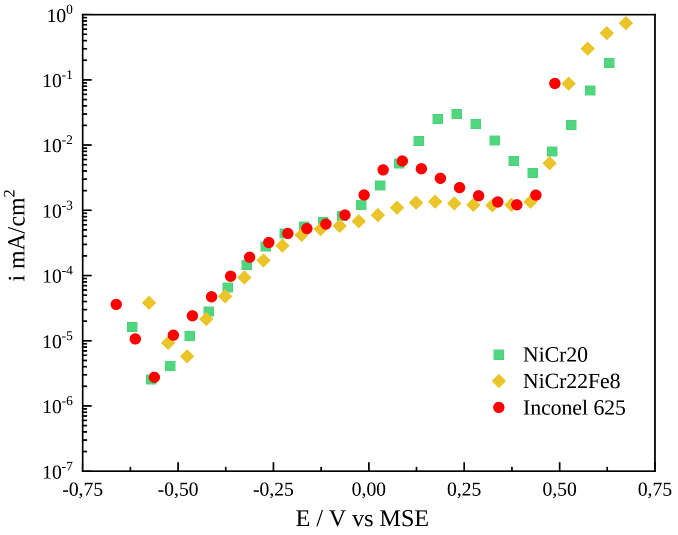

Fig. 5. 13 Potentiostatic polarization curves of NiCr20, NiCr22Fe8 and Inconel 625 in aerated solution of 0.05 M H_3BO_3 + 0.075 M $Na_2B_4O_7$ $10H_2O$ (pH=9.2).

Fig. 5. 13 exhibits the polarization curves for NiCr20, NiCr22Fe8 and Inconel 625 in aerated borate buffer solution with potentiostatic measurement. The corrosion potential of NiCr20 and Inconel 625 is equal to -0.56 V vs. MSE. The corrosion potential of NiCr22Fe8 is a little bit higher with -0.47 V vs. MSE. The anodic behaviour within stable passivation domain for the three samples is very similar. It is found that Inconel 625 presents also a second oxidation and repassivation transition like NiCr20, but the current density peak of Inconel 625 is smaller. The critical current density in secondary oxidation and passivation is 0.05 mA cm^{-2} at 0.23 V vs. MSE for NiCr20 and 0.005 mA cm^{-2} at 0.08 V vs. MSE for Inconel 625. The addition of molybdenum does not hinder the secondary oxidation and passivation peak but limit a further dissolution of chromium.

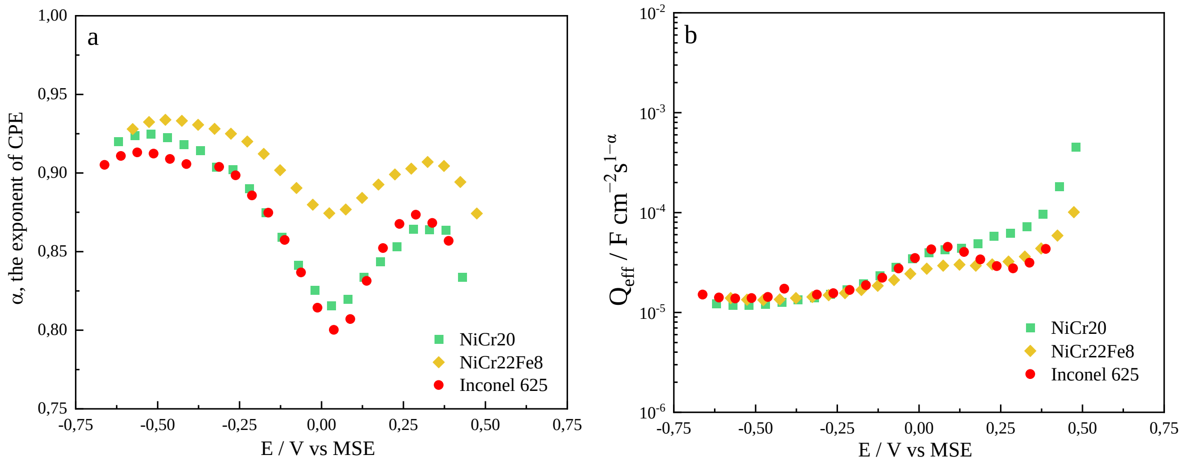

Fig. 5. 14 Evolution of CPE parameters (a) α and (b) Q_{eff} with potential for NiCr20, NiCr22Fe8 and Inconel 625 in aerated solution of 0.05 M H_3BO_3 + 0.075 M $Na_2B_4O_7$ $10H_2O$ (pH=9.2).

The evolution of graphically determined CPE exponent α with potential for NiCr20, NiCr22Fe8 and Inconel 625 is shown in Fig. 5. 14. Evolution trend of α values for NiCr20 and Inconel 625 are very close. The values keep stable about 0.92 in the potential range between −0.6 V and −0.3 V vs. MSE, followed by a continuous decrease to 0.8 until 0.0 V vs. MSE. In the secondary oxidation potentials range α increases continuously to reach approximately 0.87 at 0.29 V vs. MSE. Finally, for potential higher than 0.87 V vs MSE, α decreases again. As previously observed in Chapter 4, α follows the same trends but is always higher for NiCr22Fe8. Evolutions of Q_{eff} with potential for NiCr20, NiCr22Fe8 and Inconel 625 are illustrated in Fig. 5. 14(b). The values of Q_{eff} for the three samples are close, increasing slowly with applied anodic potential up to 0.05 V vs MSE. In the potential range corresponding to the second oxidation, the evolution is different. For NiCr20 and NiCr22Fe8, the values of Q_{eff} increase slowly, while the evolution of Q_{eff} for Inconel 625 exhibit a hump.

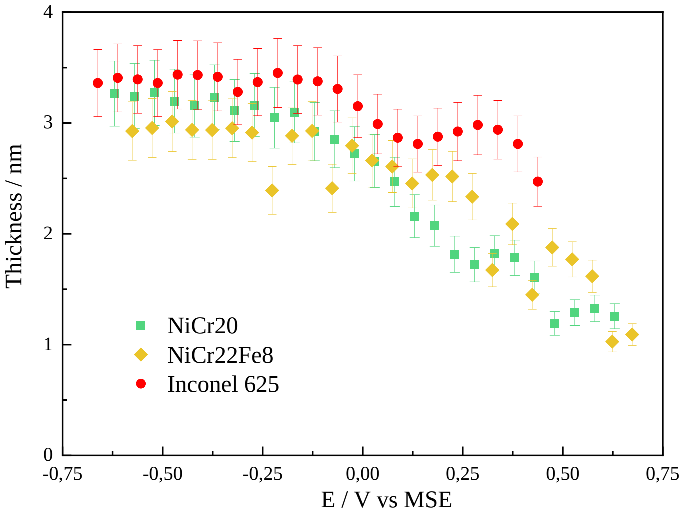

Fig. 5. 15 Evolution of thickness of NiCr20, NiCr22Fe8 and Inconel 625 in aerated solution of 0.05 M H_3BO_3 + 0.075 M $Na_2B_4O_7$ $10H_2O$ (pH=9.2).

Fig. 5. 15 shows the evolution of thickness with potential for NiCr20, NiCr22Fe8 and Inconel 625. This evolution could be divided into two parts. The first part is the plateau where the thickness of passive film does not change with applied anodic potential, whereas the second part is a decrease in thickness. The thickness of passive film for NiCr20, NiCr22Fe8 and Inconel 625 keep at the value of 3.2 nm, 2.9 nm and 3.5 nm respectively within the potential range between -0.66 V and -0.16 V vs. MSE. With more anodic potential applied, the thickness of passive film for NiCr20 decreases quickly to 1.7 nm at 0.42 V vs. MSE. With addition of 8% of iron, the tendency of thinning becomes less sharp to 1.9 nm at 0.48 V vs. MSE. Finally, with addition of 8% of molybdenum, the thickness of passive film for Inconel 625 which decreases to 2.8 nm just at 0.14 V vs. MSE, then it increases to 3 nm at 0.3 V vs. MSE and finally it reduces to 2.5 nm at 0.44 V vs. MSE just before transpassivation. Note that it has been reported that the thickness of the passive film could be increased with the addition of Mo in alloys [198,199]. However, some researcher found that Mo has no remarkable effect on the film thickness [200–202].

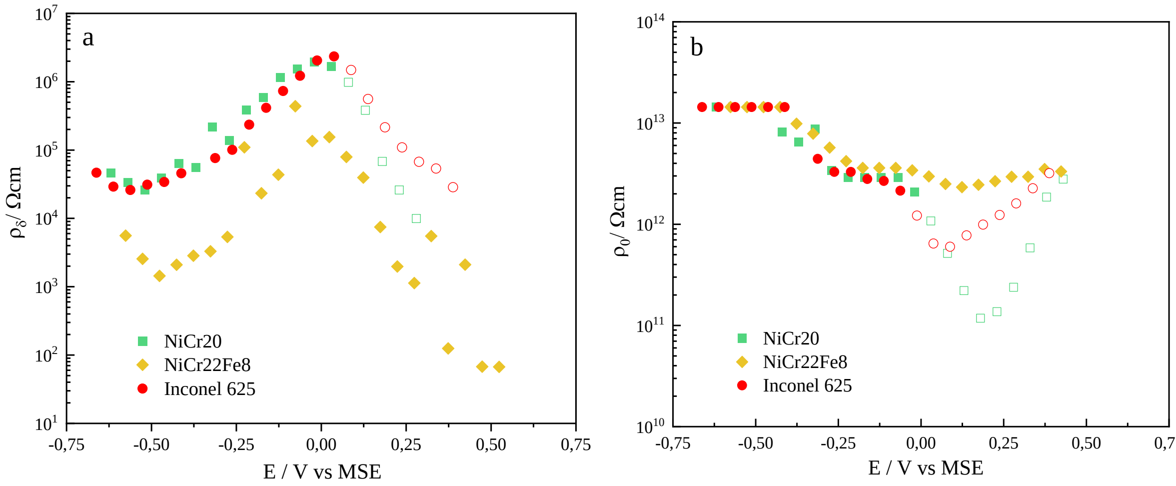

Fig. 5. 16 Evolution of resistivity a) ρ_δ and b) ρ_0 of NiCr20, NiCr22Fe8 and Inconel 625 in aerated solution of 0.05 M H_3BO_3 + 0.075 M $Na_2B_4O_7$ $10H_2O$ (pH=9.2).

Fig. 5. 16 (a) and (b) present the evolution of the fitted resistivities ρ_δ and ρ_0 in basic solution for NiCr20, NiCr22Fe8 and Inconel 625. Obviously, evolution trends of the fitted resistivities ρ_δ for three samples are similar, especially between NiCr20 and Inconel 625. In the first place, the resistivity ρ_δ for NiCr20 and Inconel 625 is about 4.4×10^4 Ω cm at -0.67 V vs. MSE. Then it decreases to about 2.7×10^4 Ω cm at -0.52 V vs. MSE. After it increases up to 2.4×10^6 Ω cm at 0 V vs. MSE just before the secondary oxidation. The resistivity ρ_δ for NiCr22Fe8 is always lower in comparison with other two alloys. It starts with 5.3×10^3 Ω cm at -0.58 V vs. MSE, and then reduces to 1.5×10^3 Ω cm at -0.46 V vs. MSE, finally increases to 1.5×10^5 Ω cm at 0 V vs. MSE. The evolution values of resistivity ρ_0 of the three alloys are very similar in the passivation range. Resistivities ρ_0 keep stable, decrease and stay stable again (in Fig. 5. 16 (b)) with increasing applied potential.

Hence, in borate buffer solution, Inconel 625 behaves like alloy NiCr20 which seems consistent with their Cr content and their similar ability to form the Cr-rich passive film. In the potential range related to the passive domain, the evolutions of the extracted parameters are more or less the same for those two alloys. However, in the secondary oxidation and secondary passivation domain, they behave differently. On the polarization curves, the value of the anodic peak is reduced for Inconel 625 and the second passivation takes place at lower potential than for NiCr20. This difference is also indicated by the evolutions of the thickness and Q_{eff} within this potential range. Then, Mo may play a role in the second oxidation-second passivation process.

5.4.2 Inconel 625 passivation behavior in acidic solution

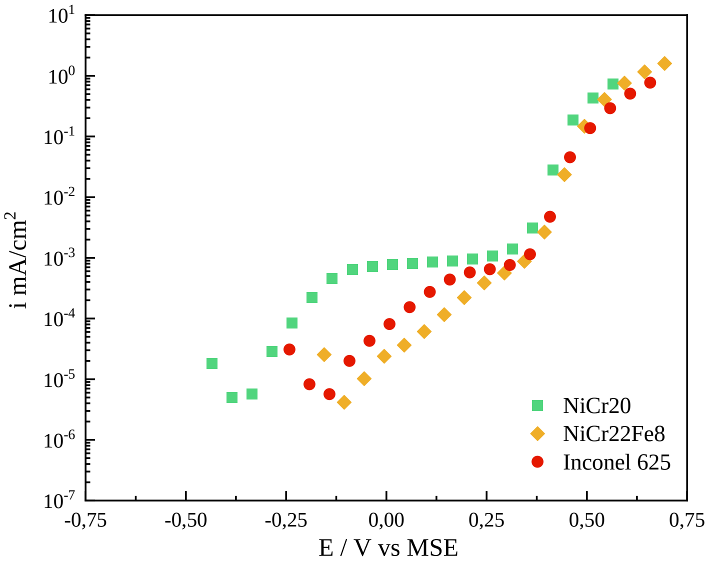

Fig. 5. 17 Potentiostatic polarization curves of NiCr20, NiCr22Fe8 and Inconel 625 in aerated solution of 10 g/L Na_2SO4 with H_2SO_4 (pH=2).

The polarization curves for NiCr20, NiCr22Fe8 and Inconel 625 in aerated acidic solution with pH=2 are shown in Fig. 5. 17. Conversely to the basic solution tendency, Inconel 625 and NiCr22Fe8 alloy exhibit a different polarization curve in this solution from NiCr20 curve. The corrosion potentials for NiCr20, NiCr22Fe8 and Inconel 625 are -0.42 V, -0.14 V and -0.1 V vs. MSE, respectively. The passivation current density for NiCr20 is about 4.5×10^{-4} mA cm^{-2}, the current density for NiCr22Fe8 and Inconel 625 is lower. The plateau in current density is less visible for NiCr22Fe8 and Inconel 625. These findings indicate that the passive state after the 24h of immersion is different for the three alloys. The corrosion potential is shifted by the addition of Fe or Mo. For all the tested samples, neither active-passive transition or secondary oxidation and passivation are detected.

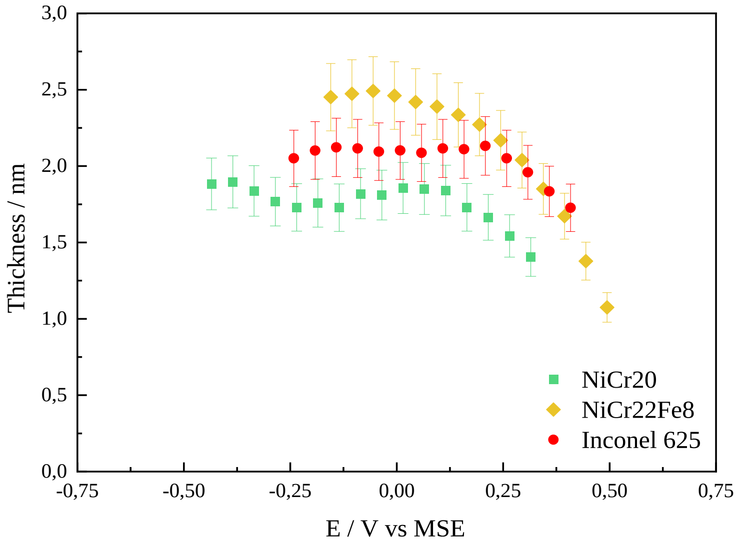

Fig. 5. 18 Evolution of thickness of NiCr20, NiCr22Fe8 and Inconel 625 in aerated solution of 10 g/L Na_2SO_4 with H_2SO_4 (pH=2).

The evolution of the passive film thickness with potential in acidic solution for NiCr20, NiCr22Fe8 and Inconel 625 is shown in Fig. 5. 18. The thickness of passive film for NiCr20 is close to the value of 1.7 nm within the potential range of -0.43 V – 0.11 V vs. MSE and then decreases down to 1.4 nm at 0.32 V vs. MSE. For the case of NiCr22Fe8, the thickness keeps just constant between -0.16 V – 0 V vs. MSE with 2.5 nm and decreases down to 1.7 nm at the potential of 0.4 V vs. MSE. The thickness of passive film for Inconel 625 is close to the value of 2.1 nm in the potential range of -0.24 V and 0.2 V vs. MSE followed by the decrease of passive film to 1.8 nm at 0.36 V vs. MSE. It is found that the plateau of thickness within passivation range is shorter for NiCr22Fe8 comparing with the two other samples.

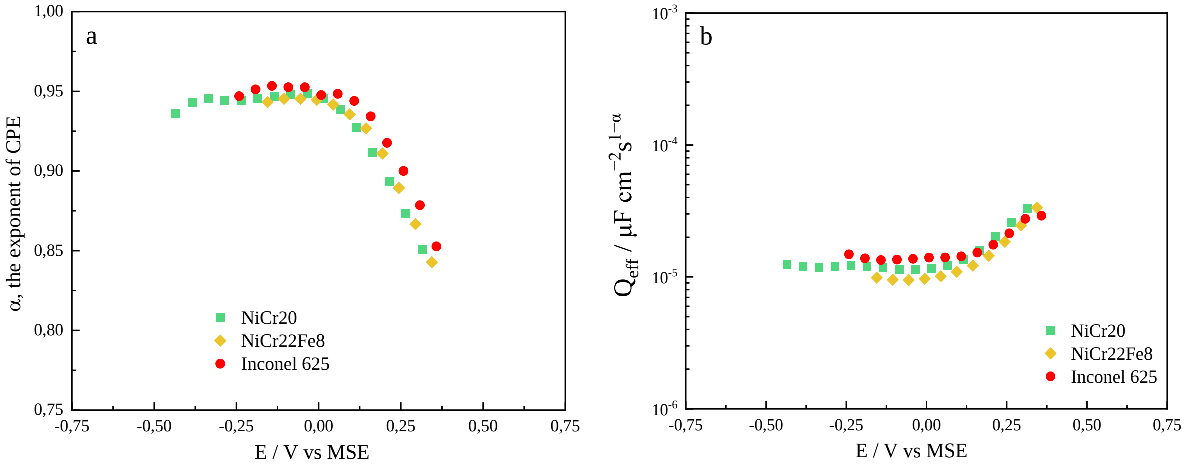

Fig. 5. 19 Evolution of CPE parameters (a) α and (b) Q_{eff} with potential for NiCr20, NiCr22Fe8 and Inconel 625 in aerated solution of 10 g/L Na_2SO_4 with H_2SO_4 (pH=2).

Fig. 5. 19 shows the evolution of graphically determined CPE parameters (exponent α and Q_{eff}) with potential for NiCr20, NiCr22Fe8 and Inconel 625 in acidic solution. In Fig. 5. 19 (a), the evolution trend of α for three alloys are very similar and the values are very close. The values keep stable about 0.95 within the potential range where is negative than 0.05 V vs. MSE. This potential range is longer for

NiCr20 since its corrosion potential is more negative than other two samples. After 0.1 V vs MSE, α continuously decrease to 0.85 at 0.35 V vs. MSE. Evolutions of Q_{eff} with potential for NiCr20, NiCr22Fe8 and Inconel 625 are illustrated in Fig. 5. 19 (b). The values of Q_{eff} for three samples are close, keeping stable with applied anodic potential up to 0.1 V vs MSE, followed by an increase of Q_{eff}.

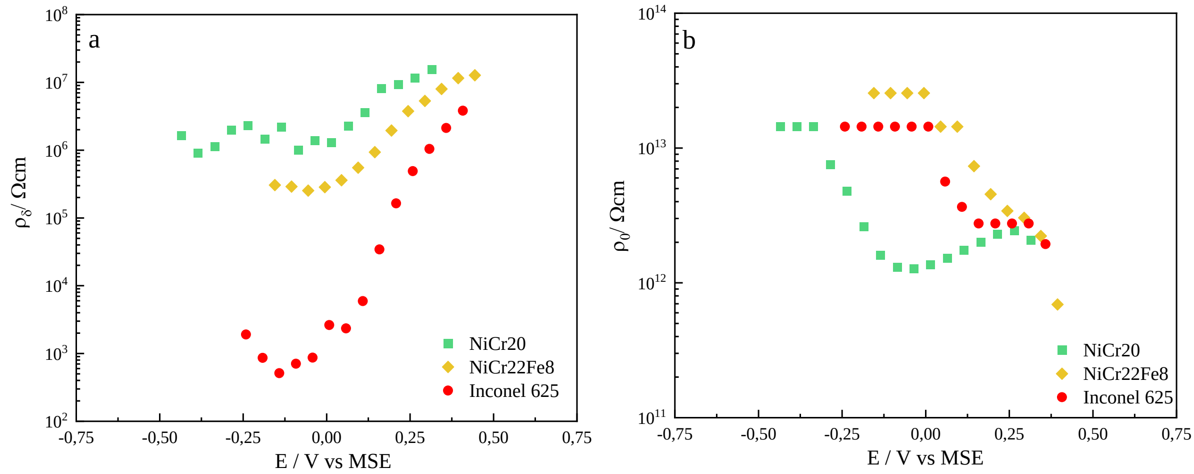

Fig. 5. 20 Evolution of resistivity a) ρ_δ and b) ρ_0 of NiCr20, NiCr22Fe8 and Inconel 625 in aerated solution of 10 g/L Na_2SO_4 with H_2SO_4 (pH=2).

The evolution of the fitted resistivities ρ_δ and ρ_0 in acidic solution for NiCr20, NiCr22Fe8 and Inconel 625 is presented in Fig. 5. 20. It is obvious that the evolution of ρ_δ for the three different samples are different. The value of resistivities ρ_δ for NiCr20 is about 1.7×10^6 Ω cm within the potential range between -0.43 V and 0.02 V vs. MSE, and it increases up to 1.6×10^7 Ω cm at 0.32 V vs. MSE. In the case of NiCr22Fe8, the plateau of the resistivity ρ_δ is shorter and lower in comparison with that of NiCr20. The value keeps stable at 2.8×10^6 Ω cm, then it increases up to 1.3×10^7 Ω cm at 0.4 V vs. MSE. For Inconel 625, the value of resistivity ρ_δ is around 10^3 Ω cm in the beginning and it increases rapidly to 2.1×10^6 Ω cm at 0.36 V vs. MSE. In the present case, it is found that the value of resistivity ρ_δ reduces by the addition of the 8% of iron or molybdenum into the Ni-Cr alloy. This result suggests that the passive film become less resistive at the interface between film and electrolyte. It might be caused by the introduction of defects (other metal ions) into chromium oxide or a modification of the oxide/hydroxide ratio at the interface between the passive film and electrolyte. However, this reduction of resistivity of passive film could be modified by increasing anodic potential and changing the migration rate of vacancies. However, the evolution of ρ_0 for the three alloys are very similar, resistivities ρ_0 keep stable, decrease and stay stable again (in Fig. 5. 20(b)) with applied anodic potential and according to the polarization curves. Hence, the addition of Fe or Mo does not affect significantly the metal/passive interface which may means that the Fe and Mo ions were more located in the outer layer of the passive film.

To conclude, in acidic solution, the passive behavior of Ni-based alloys is modified by the addition of Mo. The corrosion potential is shifted to more anodic potential. Moreover, their contributions to the outer layer of the passive film modify the resistivity profiles through them.

5.4.3 Discussion on the reactivity of Inconel 625

As for Inconel 600, a short study of the microstructure of Inconel 625 before starting the discussion may be required.

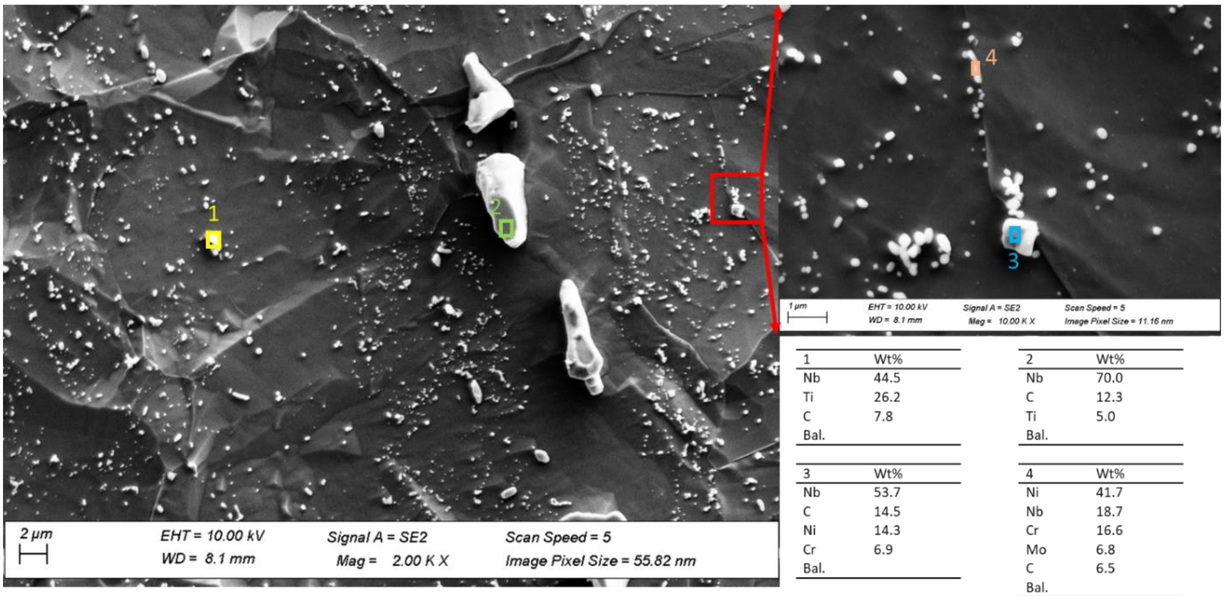

1	Wt%
Nb	44.5
Ti	26.2
C	7.8
Bal.	

2	Wt%
Nb	70.0
C	12.3
Ti	5.0
Bal.	

3	Wt%
Nb	53.7
C	14.5
Ni	14.3
Cr	6.9
Bal.	

4	Wt%
Ni	41.7
Nb	18.7
Cr	16.6
Mo	6.8
C	6.5
Bal.	

Fig. 5. 21 SEM observation for surface microstructure of Inconel 625 after chemical etching and elemental analysis by EDS

Fig. 5. 21 presents the SEM micrographs of Inconel 625 after chemical etching with EDS analysis attached. The grain boundaries are clearly visible in some parts of the image because the surface has been etched too much. On the surface of Inconel 625, a great number of small precipitates is observed. Furthermore, precipitations of over 2 µm diameters exists as well. To confirm the composition of the precipitates, a local magnification micrograph has been taken. It is presented on the right. It is found that the largest precipitate is niobium or titanium carbide, and a few chromium carbides are found as well. In the case of Inconel 625, the main carbides detected are Niobium or Titanium rich carbides. They cannot play the same role than Cr rich carbides in Inconel 600. Confirming this finding, Inconel 625 presents different passive behavior than Inconel 600.

In the basic borate buffer solution, Inconel 625 has the same passivation current density as model alloy NiCr20 and NiCr22Fe8, and exhibits a dissolution peak in secondary oxidation-repassivation potential region (shown in Fig. 5. 13). Moreover, Inconel 625 presents a quick repassivation behavior after transpassive dissolution. When it comes to the evolution of passive film thickness (Fig. 5. 15), unlike model alloys whose thickness decreases in the secondary potential range, the thickness of passive film grown on Inconel 625 has an increase in this potential range, despite it decreases in the beginning of dissolution. In terms of resistivity ρ_δ for Inconel 625, the resistivity ρ_δ evolution (Fig. 5. 16) is always in the same order of magnitude as other samples. In acidic solution, with addition of iron or molybdenum, the corrosion potential is increased to the stable passivation domain directly, seen in Fig. 5. 17. The thickness and CPE parameters are not modified with the presence of molybdenum. However, the resistivity ρ_δ for Inconel 625 is quite different from others with much lower order of magnitude, and a rapid increase with applied anodic potential. Hence, it is reasonable to assume that the molybdenum plays a critical role in the process of polarization on Inconel 625. However, that role may be different as a function of the considered solution. In general, the role of molybdenum on corrosion resistance are considered whether mitigating passive film breakdown [200,203] or promoting passive film repair [191].

The main difference of behavior is observed at the secondary oxidation-secondary passivation transition, it is interesting to understand the role of Mo during transpassive process. Considering its effect on the transpassive dissolution – repassivation process in basic solution, it is worth mentioning that the precipitation of molybdenum oxide appears at low pH condition and the solubility of Mo (VI) and MoO_4^{2-} as function of pH value is presented in Fig. 5. 22 shown below [204].

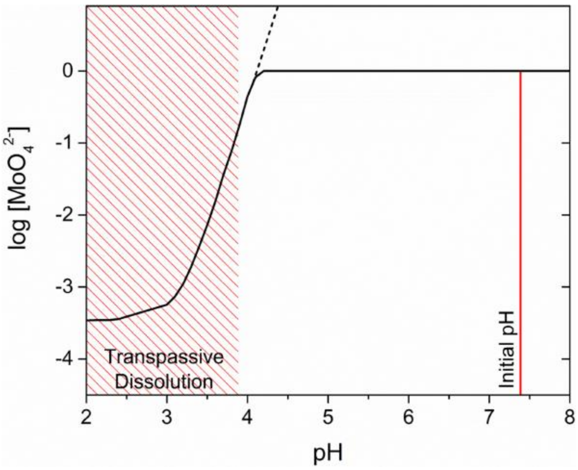

Fig. 5. 22 Solubility of Mo(VI), MoO_4^{2-}, as a function of pH value (calculation based on [MoO_4^{2-}] of 1 mol/L) [204]

It is evident that [MoO_4^{2-}] has a lower solubility in the condition of pH below 4, especially between 2 and 3. The solubility increases gradually and [MoO_4^{2-}] is almost totally soluble after pH=4. In low pH, the molybdenum could be in oxidation state of Mo (IV) in inner layer of passive film, with the reaction assumed below in equation (5.1):

$$Mo + 2H_2O \rightarrow MoO_2 + 4H^+ + 4e^- \tag{5.1}$$

With higher applied potential, molybdenum oxide might be oxidized to higher valence or in a soluble state. The equations are shown below:

$$MoO_2 + 2H_2O \rightarrow MoO_4^{2-} + 4H^+ \rightarrow MoO_3 + 2H_2O \tag{5.2}$$

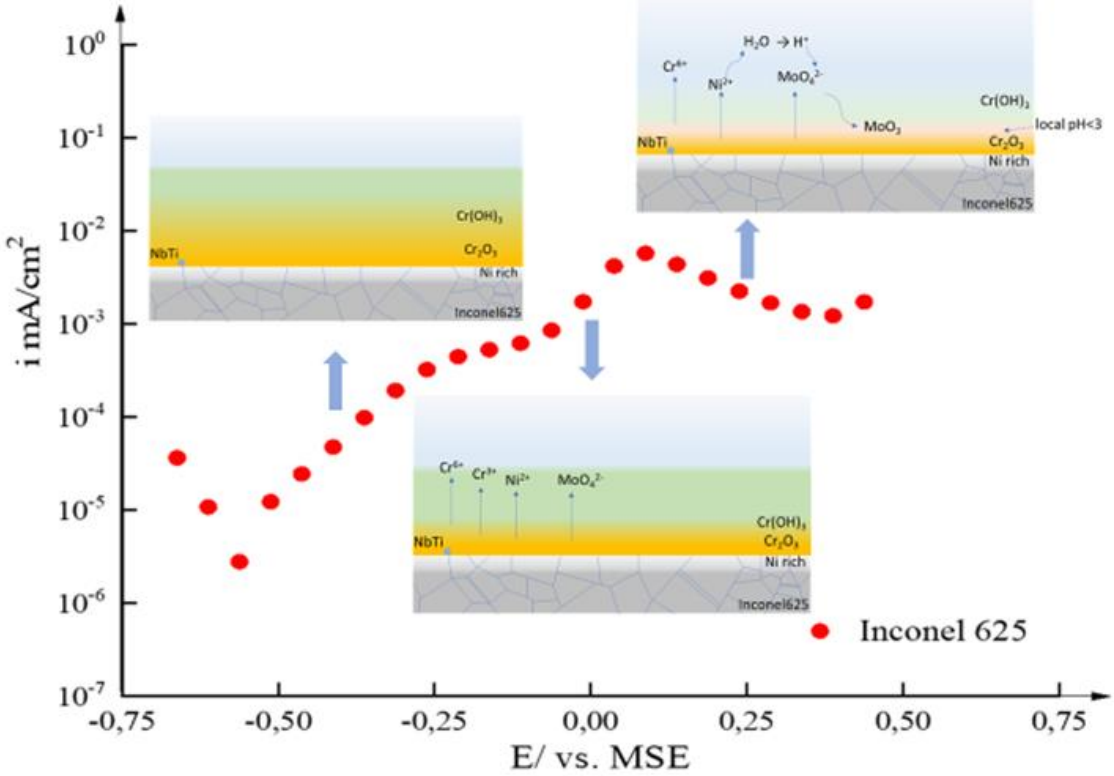

Fig. 5. 23 Schematic representation of Inconel 625 in aerated solution of 0.05 M H_3BO_3 + 0.075 M $Na_2B_4O_7$ $10H_2O$ (pH=9.2) during the polarization

The graphical representation of passive film evolution on Inconel 625 in basic borate buffer solution is shown in Fig. 5. 23. At the beginning, when the anodic polarization is performed on the material, the composition could mostly be Cr_2O_3 at inner layer whereas $Cr(OH)_3$ at outer layer. Considering the main role of chromium, nickel and other iron oxides or hydroxides are not presented in the diagram. After, in secondary oxidation region, Cr_2O_3 begins to dissolve, the metallic substrate begins to release cations into solution, accompanying with the dissolution of Cr^{3+}, Cr^{6+}, Ni^{2+} and Mo^{4+}. Note that Mo^{4+} could be oxidized to Mo^{6+} at higher potential. However, the dissolved ions like Ni^{2+} will hydrate with H_2O forming H^+ when the released ions reach a certain concentration, resulting in a local pH value < 3.

As discussed before in Fig. 5. 22, there might be a newly generated insoluble Mo (VI) film because of low local pH value. Hence, another protective oxide is formed again. As a result, the dissolution is inhibited, observing secondary repassivation from polarization curve.

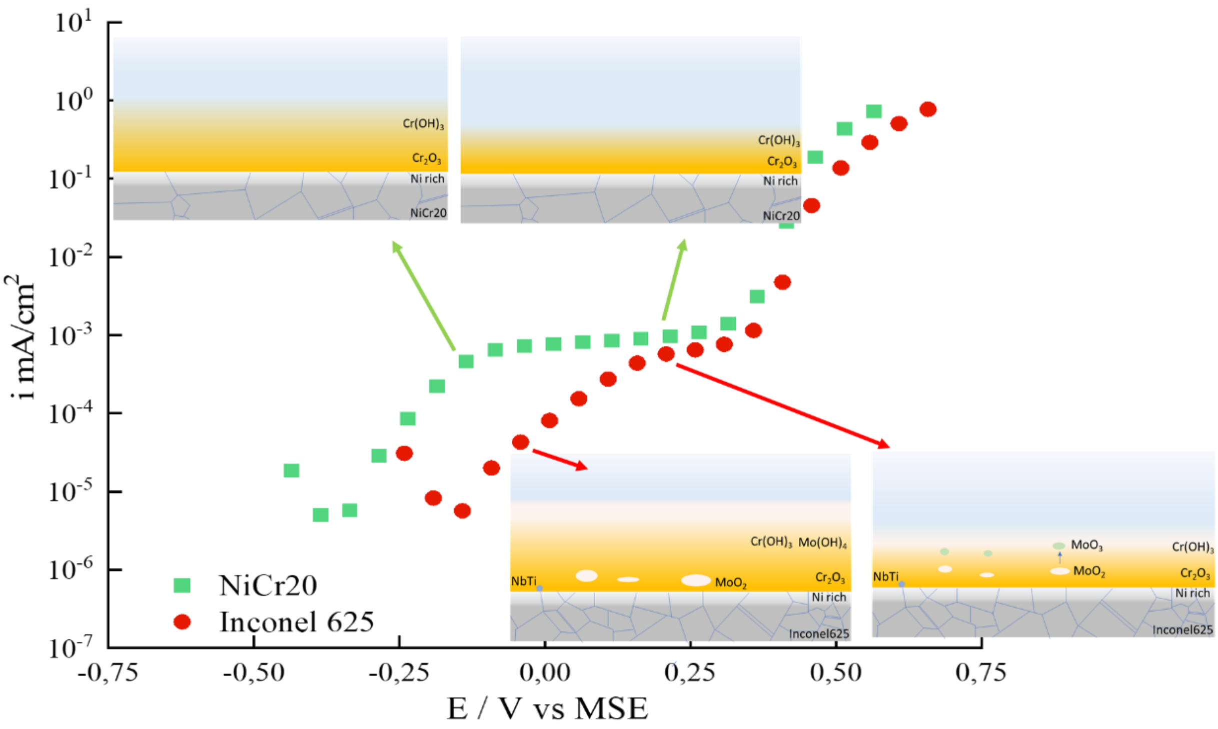

Fig. 5. 24 Schematic representation of NiCr20 and Inconel 625 in aerated solution of aerated solution of 10 g/L Na_2SO_4 with H_2SO_4 (pH=2) during the polarization

Fig. 5. 24 presents the graphical illustration of NiCr20 and Inconel 625 in aerated acidic solution. To simplify, the representation is only concerning chromium and molybdenum. In the case of NiCr20, the main compositions of passive film are Cr_2O_3 and $Cr(OH)_3$. Cr_2O_3 is supposed to enrich the inner layer of passive film whereas $Cr(OH)_3$ is concentrated in outer layer of passive film. The thickness of passive film is thin at higher potential from the testing result. Consequently, with anodic potential applied, the passive film formed on NiCr20 becomes thin but its resistivity is still high.

In the case of Inconel 625 alloy, the existence of Mo on the Ni-Cr surface favors oxygen chemisorption over binary Ni-Cr alloys on most surface oxide sites and may form oxides, such as MoO_2 or MoO_3 within the passive films. Moreover, Mo form strong bonds with adsorbed oxygen by donating more charge than either Ni or Cr [205]. Consequently, more oxygens tend to react with Mo other than Cr, resulting in the formation of complex non-stochiometric chromium oxide. Consequently, besides the Cr_2O_3 and $Cr(OH)_3$, there is also Mo (IV) exists in inner layer of passive film. The Mo (IV) is expressed as MoO_2 inside of passive film as non-continuous island, since it is suggested that molybdenum presents an inhomogeneous distribution and is enriched at local sites [206,207]. Moreover, MoO_2 islands are supposed to be dispersed into the passive film and standing at alloy/passive interface. This may explain that the fitted resistivity ρ_0 for Inconel 625 is the same as that of NiCr20. Otherwise, Mo likely become trapped as substitutional Mo^{4+} and Mo^{6+} cations in Ni^{2+} and Cr^{3+} oxides which may interact with negatively charged cation vacancies to reduce their mobility by electrostatic interactions [180]. Hence, the resistivity ρ_δ on Inconel 625 is much smaller in comparison with that of NiCr20 alloy.

With anodic potential applied, the Mo (IV) tends to be oxidized to Mo (VI). Mo (VI) is expressed as MoO_3 or as soluble Mo^{6+} here. Hence, there is less free doping cations as Mo^{4+} and Mo^{6+}, resulting in the increase of resistivity ρ_δ of passive film on Inconel 625 while anodic potential is applied, despite of thinner thickness. This assumption is in accordance with the XPS result that Mo(IV) in the Cr-rich inner layer becomes Mo(VI) enriched in the outer layer of the passive film during anodic polarization [206]. Thus, that might be the explanation to evolution of the resistivity of Inconel 625.

5.5 Conclusion

In this chapter, the successive impedance measurement was employed to study passivation behavior of commercial alloys: GILPHY 80, Inconel 600 and Inconel 625, respectively. They were compared with model alloys with close Cr content. It is found that:

1. The commercial alloy GILPHY 80 has the same corrosion behavior as model alloy NiCr20 in both acidic and basic solution. This finding indicates that for low alloyed Ni-based alloys, SEIS measurements displays similar results whatever the grain size.

2. Even though Inconel 600 has almost the same chemical composition as ternary model alloy NiCr14Fe8, the passivation behavior of Inconel 600 is more like alloy NiCr16 in basic and acidic solution. Microstructural characterization shows the precipitation of intergranular and intragranular chromium carbides, known to be detrimental for intergranular corrosion resistance. Hence, the presence of these carbides enriched in Cr affects the passivation behavior and limit the effect of Fe on the active-passive transition as well as the transpassive-second passivation transition. In this case, SEIS measurement evidences the influence of the microstructure.

3. When the electrochemical analysis was performed on Inconel 625, the passivation behavior of Inconel 625 was determined, and the role of molybdenum was considered. In this case, even if there is niobium and titanium carbides precipitation, the passivation behavior is more influenced by the molybdenum and its oxide/hydroxide forms rather than microstructural features. In basic solution, the existence of molybdenum could hinder a further dissolution of chromium oxide during transpassivation-second passivation transition. During the dissolution process, the ions like Ni^{2+} will be hydrated with H_2O releasing H^+, resulting in acidifying local pH. Molybdenum could form Mo(VI) as an insoluble film in a local acidic environment with pH value less than 3. Consequently, the further dissolution is hindered. To more anodic potential, Mo is more likely to adsorb O atoms as it stabilizes the oxidation reaction. Moreover, the Mo(IV) would be oxidized to Mo(VI) and enrich the outer layer of passive film with applied anodic potential. These could explain why the resistivity of ρ_δ increase with applied potential. Hence, SEIS method proves that niobium and titanium carbides play a minor role on the passivation behavior whereas the Mo content acts significantly on the passive and transpassive behavior of alloy 625 in acidic and basic solutions.

Therefore, it is evident that it is possible to better understand the passivation behavior of commercial alloys with successive impedance and relevant interpretation method (enhanced graphical method to extract CPE parameters and Power-Law Model to fit). The results obtained in this chapter prove that SEIS results may be correlated to different material factors. Consequently, when it concerns to the alloy designing, not only the optimized alloying element content or addition of different alloying elements needs to be considered, but also the microstructure of materials should be taken into account to modify or improve passivation behavior. Therefore, the thermomechanical history of the alloy still has a crucial influence on its corrosion behavior.

Chapter 6 General conclusion and perspectives

In this work, an electrochemical measuring method was developed to study passive films grown on Ni-based alloys and evidence the role of the alloying elements on the passive and transpassive behavior of such alloys. Using successive electrochemical impedance spectroscopy (SEIS) measurement aims to obtain specific information and their evolution about the passive film features during polarization. With this method, the staircase polarization curve could be acquired, coupled with a series of impedance diagrams which provides data about the passive state which complement results obtain by conventional polarization curves. For the interpretation of impedance diagrams, the enhanced graphical method and Power-Low Model were employed. On the one hand, the enhanced graphical method helps to estimate electrolyte resistance, CPE parameters (α and Q_{eff}) and infinite capacitance, which allow the calculation of the thickness of passive film. On the other hand, the Power-Law Model used to fit impedance diagrams provides physical parameters of passive film and their distributions, namely resistivity, including resistivity $\rho 0$ at interface alloy/passive film and resistivity ρ_δ at interface passive film/electrolyte. Those recent advanced impedance diagrams analyses and their coupling improve significantly our knowledge of the reactivity of passive film during polarization.

The first part of this work was dedicated to the validation of the methodology and some preliminary applications of the method. In this part, the proposed method was applied to characterize the passive film formed Ni–20Cr binary alloy in borate buffer solution of 0.05 M H_3BO_3 + 0.075 M $Na_2B_4O_7$ $10H_2O$ (pH=9.2). To validate this method, various experimental conditions were tested, including dwell times at each potential (30 s, 120 s, 600 s and 3600 s) and step sizes (25 mV and 50 mV), but also inversed scanning direction or the effect of dissolved oxygen in the electrolyte. The results obtained with the different experimental conditions were compared with each other and with a conventional polarization curves (scan rate of 0.5 mV/s). The comparisons of the average value of the current density and data of the fitted impedance diagrams indicate that the experimental parameters don't significantly affect the measurement, excepted the long term staying of 3600 s that exhibit different results from the polarization curve itself. A dwell time of 120 s and a step size of 50 mV were selected as optimized parameters to characterize passive film without unreasonably spending time.

The method was then applied on same binary Ni–20Cr alloy but with two others solutions with different pH values: 10 g/L Na_2SO_4 with H_2SO_4 (pH=2) and 0.01 M Na_2SO_4 (pH=5.8). The results reveal that this method shows great potential for the study of film passivity and evidence the dependence of the passive behavior with the pH of the solution. Thanks to enhanced graphical representation and the Power-Law Model, more parameters related to the passive film properties were determined from impedance diagram and the evolutionary nature of a passive film could be explored with SEIS. Since the evolution of the current density (measured at each potential step), the modification of the thickness, chemical composition, and reactivity can be assessed in situ. Moreover, XPS was also employed to study the composition of passive film, helping to prove the results from impedance diagram interpretation.

Then, the second part was devoted to the passive behaviors of Ni–xCr binary and Ni–xCr–8Fe ternary alloys. This part highlights the role of the chemical composition of Ni-based alloys, essentially the Cr content and the addition of Fe, on their passive and transpassive behaviors in borate buffer solution. The electrochemical behavior was characterized by SEIS. Furthermore, XPS were employed to better understand the modification within the passive film during polarization. The results show that the Cr content has no obvious influence on the passivation behavior of Ni–xCr in passive potential domain. Despite of the increased Cr content in the alloy, the same duplex distribution and evolution was obtained from normalized resistivity profiles. However, the Cr content influences straightforwardly the secondary oxidation and repassivation processes. The increased Cr content might cause a higher current density peak in the transpassivation-second passivation process. Conversely, the second passivation current density was not dependent of the Cr content within the alloy and is mainly due to the high amount of Ni which is still passive at these potentials. Furthermore, an enrichment of Ni hydroxide in the passive film was also detected and might contribute to inhibit the secondary oxidation of Cr. Secondary oxidation peak could also be limited by the addition of 8 wt.% Fe, especially for low Cr content. Indeed, the presence of Fe could maintain the passive layer at the surface to limit the dissolution of Cr_2O_3 at high anodic potential.

Finally, in the third part, the successive impedance measurement was employed to study passive behavior of commercial alloys, namely GILPHY 80, Inconel 600 and Inconel 625. The results were compared with that of model alloys regards to same Cr content as commercial one. Since commercial alloy GILPHY 80 presents the same corrosion behavior as model alloy NiCr20 in both acidic and basic solution, it is found that, for low alloyed materials, the measurement of the corrosion behavior is not dependent with the grain size. In the case of Inconel 625, the existence of molybdenum could hinder a further dissolution of chromium oxide in basic solution, since molybdenum could form Mo(VI) as a insoluble film in outer layer of passive film, due to a local acidic environment. Whereas the resistivity of passive film on Inconel 625 is very low in acidic solution, caused by the existence of Mo(IV) in the film. However, the proposed method demonstrate also that the microstructure may play a major role on passive and transpassive behavior. The passive behavior of Inconel 600 is far away from corresponding model alloy NiCr14Fe8, even though they have almost the same chemical composition. The SEIS results show that the resistivity of Inconel 600 is significantly different in comparison with other two samples. The existence of precipitation of chromium carbides and titanium carbides in Inconel 600 was confirmed by SEM and EDS characterizations. It is known that those Cr carbides at grain boundaries result in the formation of a depletion zone of chromium which is detrimental to intergranular corrosion resistance. The inhomogeneous distribution of chromium likely affects the passive and transpassive behavior, attenuating the positive effect of the Fe on the transpassive behavior.

Even though this work already demonstrated the potentiality of the proposed method (SEIS and advance interpretation) to study passive film, there are some limitations on the use of this method. Firstly, the comparison between short term and long term staying indicates that this measurement is more dependent on dwell time and that the interpretation of the passive film characteristics has to be considered regarding conventional polarization curve and not steady-state studies. Indeed, the polarization curve has to be compared to conventional polarization curve and describes quasi-steady state or transient state rather than steady state. For studying achieved steady state, long term potentiostatic measurements are required and sometimes more samples and tests also. Consequently, this analyzing method should be considered as a complementary method from polarization curve. Secondly, it is about the sensitivity of this methodology. For example, it is difficult to discern the effect of chemistry or microstructure of samples. In the case of Ni20Cr and GILPHY80, the two samples showed almost the same electrochemical behavior, even if they have different grain size. However, when it comes to study on commercial alloys, not only chemistry but also microstructure need to be considered. Nevertheless, it is not always easy to know which factor might be the most influential to electrochemical behavior. Consequently, it is still interesting to work with model alloy or model microstructure to evidence the role of each features on the passive and transpassive behavior. Furthermore, the presented method is adapted to study the passive behavior but is not sufficient for its understanding when complex alloys are considered.

Regarding the perspectives, this work and the proposed methodology evidence the role of the solution pH, the composition of the alloy and its microstructure on the passive and transpassive behavior of some Ni-based alloys. However, there are still some work to do in terms of methodology and understanding of passivity and transpassivity of Ni-based alloys. In the first place, it is worth mentioning that an in-depth understanding of the mechanisms of active-passive transition and second oxidation-second passivation transition is required for designing of choosing alloys. For that, the proposed may be complemented by inductively coupled plasma atomic emission spectroscopy (ICP-AES) and specific chromatography to determine the ions releasing and their speciation. Those techniques provide the concentration of the different cations within solution and their oxidation degree. Indeed, it is of prime interest to quantify the cations releasing but also to know exactly on which form there are in solution. Those results coupled with XPS measurements and the analysis of the current signal may provide some relevant information on the dissolution process during active and transpassive dissolution but also during passive film nucleation or growth. Secondly, the effect of other alloying elements on passivation of Ni-based alloys has not extensively been studied. It could be interesting to determine how other alloying elements affect electrochemical behavior of Ni-based alloys, especially in second oxidation-second passivation domain. Since other elements may hinder or accelerate the dissolution of Cr, the mechanism still remains under question. In another word, it could be very motivating for the corrosion field to better apprehend and classify the way of action on the passive behavior of the different alloying elements. Then, in the presented work, impedance diagrams were not fully adjusted within transpassive domain or during active-passive transition. Probably, some information is missing. It could be interesting to pay more attention on this impedance diagrams and on their interpretation to extract supplementary data. Finally, one of the possible extensions of the present work is the use of the methodology for oxide film study in different corrosive media. Indeed, as Ni-based alloys are generally used for high temperature applications, in-situ measurements, like in PWR environment, may provide information on the evolution of oxide film grown in high pressure and high temperature environment.

Reference

[1] A. J. Sedriks, Encyclopedia of Materials: Science and Technology, 2001. https://doi.org/10.1201/9781482270570.

[2] T.H. Bassford, J. Hosier, Nickel and Its Alloys, in: M. Kutz (Ed.), Mech. Eng. Handb. (Second Ed., John Wiley & Sons, Inc., 1998.

[3] F. M, Experimental researches in chemistry and physics, 1859. https://doi.org/10.1016/0160-9327(91)90184-d.

[4] S. Noris, G. Okamoto, Electrochemical Passivation of Metals, in: Electrochem. Mater. Sci., 1981: pp. 193–245.

[5] V. Maurice, P. Marcus, Progress in corrosion science at atomic and nanometric scales, Prog. Mater. Sci. 95 (2018) 132–171. https://doi.org/10.1016/j.pmatsci.2018.03.001.

[6] C. Blanc, I. Aubert, “Mechanics – Microstructure – Corrosion” Coupling, 2019. https://doi.org/10.1016/b978-1-78548-309-7.50023-5.

[7] E. McCafferty, Introduction to corrosion science, 2010. https://doi.org/10.1007/978-1-4419-0455-3.

[8] S. Fujimoto, H. Tsuchiya, Semiconductor properties and protective role of passive films of iron base alloys, Corros. Sci. 49 (2007) 195–202.

[9] J. Sikora, E. Sikora, D.D. Macdonald, The electronic structure of the passive film on tungsten, Electrochim. Acta. 45 (20000) 1875–1883.

[10] J. Kang, Y. Yang, X. Jiang, H. Shao, Semiconducting properties of passive films formed on electroplated Ni and Ni – Co alloys, Corros. Sci. 50 (2008) 3576–3580. https://doi.org/10.1016/j.corsci.2008.09.005.

[11] D.-S. Kong, S.-H. Chen, C. Wang, W. Yang, A study of the passive films on chromium by capacitance measurement, Corros. Sci. (2003) 747–758.

[12] B. Ter-Ovanessian, B. Normand, Passive films growth on different Ni-Cr alloys from the migration of cation vacancies, J. Solid State Electrochem. 20 (2016) 9–18. https://doi.org/10.1007/s10008-015-2981-x.

[13] N. Sato, Electrochemistry at Metal and Semiconductor Electrodes, Elsevier, 1998. https://doi.org/10.1016/b978-0-444-82806-4.x5000-4.

[14] Y.-M. Chen, N.G. Rudawski, E. Lambers, M.E. Orazem, Application of Impedance Spectroscopy and Surface Analysis to Obtain Oxide Film Thickness, J. Electrochem. Soc. 164 (2017) C563–C573. https://doi.org/10.1149/2.1061709jes.

[15] Y.W. Jung, J.S. Byun, D.H. Woo, Y.D. Kim, Ellipsometric analysis of porous anodized aluminum oxide films, Thin Solid Films. 517 (2009) 3726–3730. https://doi.org/10.1016/j.tsf.2008.12.051.

[16] P. Marcus, On some fundamental factors in the effect of alloying elements on passivation of alloys, Corros. Sci. 36 (1994) 2155–2158. https://doi.org/10.1016/0010-938X(94)90013-2.

[17] N. Sato, Toward a More Fundamental Understanding of Corrosion Processes, Corrosion. 45 (1989) 354–368.

[18] G. Okamoto, Passive film of 18-8 stainless steel structure and its function, Corros. Sci. 13 (1973)

471–489. https://doi.org/10.1016/0010-938X(73)90031-0.

[19] G. Okamoto, T. Shibata, Stability of passive stainless steel in relation to the potential of passivation treatment, Corros. Sci. 10 (1970) 371–378. https://doi.org/10.1016/S0010-938X(70)80027-0.

[20] M. Pourbaix, Atlas of Electrochemical Equilibria in Aqueous Solutions, 1974.

[21] E. McCafferty, Introduction to corrosion science, Springer Science & Business Media, 2010.

[22] D.D. Macdonald, Passivity - The key to our metals-based civilization, Pure Appl. Chem. 71 (1999) 951–978. https://doi.org/10.1351/pac199971060951.

[23] D.D. Macdonald, Some personal adventures in passivity - A review of the point defect model for film growth, Russ. J. Electrochem. 48 (2012) 235–258. https://doi.org/10.1134/S1023193512030068.

[24] A. Mishra, Performance of corrosion-resistant alloys in concentrated acids, Acta Metall. Sin. (English Lett. 30 (2017) 306–318. https://doi.org/10.1007/s40195-017-0538-y.

[25] D.D. Macdonald, On the Existence of Our Metals-Based Civilization: I. Phase-Space Analysis, J. Electrochem. Soc. 153 (2006) B213. https://doi.org/10.1149/1.2195877.

[26] P. Kinnunen, Electrochemical characterisation and modelling of passive films, Helsinki University of Technology, 2002.

[27] A.K. Mishra, S. Ramamurthy, M. Biesinger, D.W. Shoesmith, The activation/depassivation of nickel-chromium-molybdenum alloys in bicarbonate solution: Part I, Electrochim. Acta. 100 (2013) 118–124. https://doi.org/10.1016/j.electacta.2013.03.161.

[28] A.K. Mishra, D.W. Shoesmith, The activation/depassivation of nickel-chromium-molybdenum alloys: An oxyanion or a pH effect - Part II, Electrochim. Acta. 102 (2013) 328–335. https://doi.org/10.1016/j.electacta.2013.03.177.

[29] M. Okuyama, M. Kawakami, K. Ito, Anodic dissolution of chromium in acidic sulphate solutions, Electrochim. Acta. 30 (1985) 757–765. https://doi.org/10.1016/0013-4686(85)80124-9.

[30] H. Takahashi, K. Fujiwara, M. Seo, The cathodic polarization of aluminum covered with anodic oxide films in a neutral borate solution-II. Film breakdown and pit formation, Corros. Sci. 36 (1994) 689–705. https://doi.org/10.1016/0010-938X(94)90074-4.

[31] M.M.L. A. W. Hassel, INITIAL STAGES OF CATHODIC ANODIC ALUMINIUM BREAKDOWN OXIDE FILMS OF THIN Metal Oxide Electrolyte, Electrochim. Acta. 40 (1995) 433–437.

[32] S.F. Bubar, D.A. Vermilyea, Deformation of Passive Films, J. Electrochem. Soc. 114 (1967) 882. https://doi.org/10.1149/1.2426770.

[33] B. Ter-Ovanessian, N. Mary, B. Normand, Passivity Breakdown of Ni-Cr Alloys: From Anions Interactions to Stable Pits Growth, J. Electrochem. Soc. 163 (2016) C410–C419. https://doi.org/10.1149/2.0381608jes.

[34] V. Maurice, L.H. Klein, P. Marcus, Atomic structure of metastable pits formed on nickel, Electrochem. Solid-State Lett. 4 (2001) 1–4. https://doi.org/10.1149/1.1344277.

[35] P. Marcus, V. Maurice, H.H. Strehblow, Localized corrosion (pitting): A model of passivity breakdown including the role of the oxide layer nanostructure, Corros. Sci. 50 (2008) 2698–2704. https://doi.org/10.1016/j.corsci.2008.06.047.

[36] A. Almubarak, W. Abuhaimed, A. Almazrouee, Corrosion Behavior of the Stressed Sensitized

Austenitic Stainless Steels of High Nitrogen Content in Seawater, Int. J. Electrochem. 2013 (2013) 970835.

[37] S. Li, Y. He, S. Yu, P. Zhang, Evaluation of the effect of grain size on chromium carbide precipitation and intergranular corrosion of 316L stainless steel, Corros. Sci. 66 (2013) 211–216. https://doi.org/10.1016/j.corsci.2012.09.022.

[38] J. Kil, Y. Ho, B. Ho, K. Young, New findings on intergranular corrosion mechanism of stabilized stainless steels, Electrochim. Acta. 56 (2011) 1701–1710. https://doi.org/10.1016/j.electacta.2010.08.042.

[39] A. Pardo, M.C. Merino, A.E. Coy, F. Viejo, M. Carboneras, R. Arrabal, Influence of Ti , C and N concentration on the intergranular corrosion behaviour of AISI 316Ti and 321 stainless steels, Acta Mater. 55 (2007) 2239–2251. https://doi.org/10.1016/j.actamat.2006.11.021.

[40] B. Zhao, W. Zhao, H. Shi, G. Li, Y. Ding, The effects of stabilizing treatment on microstructure and corrosion resistance of 316Ti stainless steel, Eng. Fail. Anal. 105 (2019) 961–969. https://doi.org/10.1016/j.engfailanal.2019.07.047.

[41] J.D. Henderson, N. Ebrahimi, V. Dehnavi, M. Guo, D.W. Shoesmith, Electrochimica Acta The role of internal cathodic support during the crevice corrosion of Ni-Cr-Mo alloys, Electrochim. Acta. 283 (2018) 1600–1608. https://doi.org/10.1016/j.electacta.2018.07.048.

[42] S. Pumps, Chapter eight: MaterialsMaterials and Corrosion, in: Centrif. Pump Handb. (Third Ed., 2010: pp. 227–250. https://doi.org/10.1016/B978-0-7506-8612-9.00008-5.

[43] N. Ebrahimi, P. Jakupi, J.J. Noël, D.W. Shoesmith, The Role of Alloying Elements on the Crevice Corrosion Behaviour of Ni-Cr-Mo Alloys, Corrosion. 71 (2015) 1441–1451.

[44] I.L. Rosenfeld, I.K. Marshakov., Mechanism of Crevice Corrosion, Corrosion. 20 (1964) 115t-125t.

[45] A.K. Mishra, D.W. Shoesmith, Effect of Alloying Elements on Crevice Corrosion Inhibition of Nickel-Chromium-Molybdenum- Tungsten Alloys Under Aggressive Conditions : An Electrochemical Study, Corrosion. 70 (2014) 721–730.

[46] J.N. Wanklyn, The role of molybdenum in the crevice corrosion of stainless steels, Corros. Sci. 21 (1981) 211–225.

[47] A.K. Mishra, X. Zhang, D.W. Shoesmith, The Role of Copper on the Crevice Corrosion Behavior of Nickel-Chromium-Molybdenum Alloys in Aggressive Solutions, Corrosion. 72 (2016) 356–367.

[48] A. Nazarov, V. Vivier, F. Vucko, D. Thierry, Effect of Tensile Stress on the Passivity Breakdown and Repassivation of AISI 304 Stainless Steel: A Scanning Kelvin Probe and Scanning Electrochemical Microscopy Study, J. Electrochem. Soc. 166 (2019) C3207–C3219. https://doi.org/10.1149/2.0251911jes.

[49] S.P. Knight, K. Pohl, N.J.H. Holroyd, N. Birbilis, P.A. Rometsch, B.C. Muddle, R. Goswami, S.P. Lynch, Some effects of alloy composition on stress corrosion cracking in Al–Zn–Mg–Cu alloys, Corros. Sci. 98 (2015) 50–62. https://doi.org/10.1016/j.corsci.2015.05.016.

[50] B.T. Lu, J.L. Luo, Relationship Between Yield Strength and Near- Neutral pH Stress Corrosion Cracking Resistance of Pipeline Steels — An Effect of Microstructure, Corrosion. 62 (2006) 129–140.

[51] B.J. Wang, D.K. Xu, J. Sun, E. Han, Effect of grain structure on the stress corrosion cracking (SCC) behavior of an as-extruded Mg-Zn-Zr alloy, Corros. Sci. 157 (2019) 347–356.

https://doi.org/10.1016/j.corsci.2019.06.017.

[52] S.P. Knight, N. Birbilis, B.C. Muddle, A.R. Trueman, S.P. Lynch, Correlations between intergranular stress corrosion cracking , grain-boundary microchemistry , and grain-boundary electrochemistry for Al – Zn – Mg – Cu alloys, Corros. Sci. 52 (2010) 4073–4080. https://doi.org/10.1016/j.corsci.2010.08.024.

[53] V.S. Raja, T. Shoji, Stress corrosion cracking: theory and practice, Elsevier, 2011.

[54] K.J. Miller, The behaviour of short fatigue cracks and their initiation part ii-a general summary, Fatigue Fract. Eng. Mater. Struct. 10 (1987) 93–113.

[55] P.P. Milella, Fatigue and Corrosion in Metals, Springer Science & Business Media, 2012.

[56] P. Jemmely, S. Mischler, D. Landolt, Electrochemical modeling of passivation phenomena in tribocorrosion, Wear. 237 (2000) 63–76. https://doi.org/10.1016/S0043-1648(99)00314-2.

[57] N. Diomidis, J. Celis, P. Ponthiaux, F. Wenger, A methodology for the assessment of the tribocorrosion of passivating metallic materials, Lubr. Sci. 21 (2009) 53–67. https://doi.org/10.1002/ls.

[58] M. Stemp, S. Mischler, D. Landolt, The effect of mechanical and electrochemical parameters on the tribocorrosion rate of stainless steel in sulphuric acid, Wear. 255 (2003) 466–475. https://doi.org/10.1016/S0043-1648(03)00085-1.

[59] V. Dalbert, N. Mary, B. Normand, C. Verdu, T. Douillard, S. Saedlou, The effects of microstructures and repassivation kinetics on the tribocorrosion resistance of ferrite and ferrite-martensite stainless steels, Wear. 420–421 (2019) 245–256. https://doi.org/10.1016/j.wear.2018.10.023.

[60] S. Mischler, A. Spiegel, D. Landolt, The role of passive oxide films on the degradation of steel in tribocorrosion systems, Wear. 225 (1999) 1078–1087.

[61] V. Dalbert, N. Mary, B. Normand, C. Verdu, S. Saedlou, Tribology International In situ determinations of the wear surfaces , volumes and kinetics of repassivation : Contribution in the understanding of the tribocorrosion behaviour of a ferritic stainless steel in various pH, Wear. 150 (2020) 106374.

[62] I. Olefjord, L. Wegrelius, Surface analysis of passive state, Corros. Sci. 31 (1990) 89–98.

[63] W. Dec, M. Mosiałek, R.P. Socha, M. Jaworska-Kik, W. Simka, J. Michalska, The effect of sulphate-reducing bacteria biofilm on passivity and development of pitting on 2205 duplex stainless steel, Electrochim. Acta. 212 (2016) 225–236. https://doi.org/10.1016/j.electacta.2016.07.043.

[64] I.B. Beech, J. Sunner, Biocorrosion: Towards understanding interactions between biofilms and metals, Curr. Opin. Biotechnol. 15 (2004) 181–186. https://doi.org/10.1016/j.copbio.2004.05.001.

[65] J. Duan, B. Hou, Z. Yu, Characteristics of sulfide corrosion products on 316L stainless steel surfaces in the presence of sulfate-reducing bacteria, Mater. Sci. Eng. C. 26 (2006) 624–629. https://doi.org/10.1016/j.msec.2005.09.108.

[66] Y. SHU, M. YAN, et al. WEI, Yinghua, Characteristics of SRB Biofilm and Microbial Corrosion of X80 Pipeline Steel, Acta Met. Sin. 54 (2018) 1408–1416. https://doi.org/10.11900/0412.1961.2018.00069.

[67] S. Boudin, J. -L Vignes, G. Lorang, M. Da Cunha Belo, G. Blondiaux, S.M. Mikhailov, J.P. Jacobs,

H.H. Brongersma, Analytical and electrochemical study of passive films formed on nickel—chromium alloys: Influence of the chromium bulk concentration, Surf. Interface Anal. 22 (1994) 462–466. https://doi.org/10.1002/sia.740220198.

[68] A. Kawashima, K. Asami, K. Hashimoto, An XPS study of passive films on nickel and alloy 600 in acids, Corros. Sci. 25 (1985) 1103–111.

[69] A. Machet, A. Galtayries, S. Zanna, L. Klein, V. Maurice, P. Jolivet, M. Foucault, P. Combrade, P. Scott, P. Marcus, XPS and STM study of the growth and structure of passive films in high temperature water on a nickel-base alloy, Electrochim. Acta. 49 (2004) 3957–3964. https://doi.org/10.1016/j.electacta.2004.04.032.

[70] J.A. Bardwell, G.I. Sproule, B. Macdougall, M.J. Graham, In situ XANES detection of Cr (VI) in the passive film on Fe-26Cr, J. Electrochem. Soc. 193 (1992) 371.

[71] A.J. Davenport, M. Sansone, High Resolution In Situ XANES Investigation of the Nature of the Passive Film on Iron in a pH 8 . 4 Borate Buffer, J. Electrochem. Soc. 142 (1995) 725.

[72] L. Wang, A. Seyeux, P. Marcus, Thermal stability of the passive film formed on 316L stainless steel surface studied by ToF-SIMS, Corros. Sci. 165 (2020) 108395. https://doi.org/10.1016/j.corsci.2019.108395.

[73] L. Wang, D. Mercier, S. Zanna, A. Seyeux, M. Laurent-brocq, L. Perrière, I. Guillot, P. Marcus, Study of the surface oxides and corrosion behaviour of an equiatomic CoCrFeMnNi high entropy alloy by XPS and ToF-SIMS, Corros. Sci. 167 (2020) 108507. https://doi.org/10.1016/j.corsci.2020.108507.

[74] L. Wang, A. Seyeux, P. Marcus, Ion Transport Mechanisms in the Oxide Film Formed on 316L Stainless Steel Surfaces Studied by ToF-SIMS with 18 O 2 Isotopic Tracer Ion Transport Mechanisms in the Oxide Film Formed on 316L Stainless Steel Surfaces Studied by ToF-SIMS with 18 O 2 Isotopic, J. Electrochem. Soc. 167 (2020) 101511. https://doi.org/10.1149/1945-7111/ab9c87.

[75] J. Li, D.J. Meier, An AFM study of the properties of passive films on iron surfaces, J. Electroanal. Chem. 454 (1998) 53–58.

[76] J. Li, D. Lampner, In-situ AFM study of pitting corrosion of Cu thin films, Colloids Surfaces A Physicochem. Eng. Asp. 154 (1999) 227–237.

[77] V. Maurice, W.P. Yang, P. Marcus, XPS and STM investigation of the passive film formed on Cr (110) single-crystal surfaces, J. Electrochem. Soc. 141 (1994) 3016.

[78] V. Maurice, W.P. Yang, P. Marcus, XPS and STM study of passive films formed on Fe-22Cr (110) single-crystal surfaces, J. Electrochem. Soc. 143 (1996) 11182.

[79] Y. Yi, P. Cho, A. Al Zaabi, Y. Addad, C. Jang, Potentiodynamic polarization behaviour of AISI type 316 stainless steel in NaCl solution, Corros. Sci. 74 (2013) 92–97. https://doi.org/10.1016/j.corsci.2013.04.028.

[80] R.J. Wilbraham, C. Boxall, Electrochemistry Communications The effect of acetohydroxamic acid on stainless steel corrosion in nitric acid, Electrochem. Commun. 62 (2016) 52–55. https://doi.org/10.1016/j.elecom.2015.11.009.

[81] C. Boissy, B. Normand, Electrochemistry Communications EIS evaluation of steady-state characteristic of 316L stainless steel passive film grown in acidic solution, Electrochem. Commun. 26 (2013) 10–12. https://doi.org/10.1016/j.elecom.2012.09.040.

[82] I. Bösing, G. Marquardt, J. Thöming, Effect of Heat Treatment of Martensitic Stainless Steel on

Passive Layer Growth Kinetics Studied by Electrochemical Impedance Spectroscopy in Conjunction with the Point Defect Model, Corros. Mater. Degrad. 1 (2020) 77–91.

[83] C. Boissy, N. Mary, B. Normand, Electrochimica Acta Correlation between predictive and descriptive models to characterize the passive film – Study of pure chromium by electrochemical impedance spectroscopy, Electrochim. Acta. 174 (2015) 430–437. https://doi.org/10.1016/j.electacta.2015.05.179.

[84] S. Marcelin, B. Ter-ovanessian, B. Normand, Electronic properties of passive films from the multi-frequency Mott – Schottky and power-law coupled approach, Electrochem. Commun. 66 (2016) 62–65. https://doi.org/10.1016/j.elecom.2016.03.003.

[85] B. Ter-ovanessian, B. Normand, Passive films growth on different Ni-Cr alloys from the migration of cation vacancies, J. Solid State Electrochem. 20 (2016) 9–18. https://doi.org/10.1007/s10008-015-2981-x.

[86] E.J.W. Verwey, Electrolytic conduction of a solid insulator at high fields The formation of the anodic oxide film on aluminium, Physica. 2 (1935) 1059–1063. https://doi.org/10.1016/S0031-8914(35)90193-8.

[87] N. Cabrera, N.F. Mott, Theory of the oxidation of metals, Reports Prog. Phys. 12 (1949) 163–184.

[88] L.F. Lin, C.Y. Chao, D.D. Macdonald, A Point Defect Model for Anodic Passive Films: II . Chemical Breakdown and Pit Initiation, J. Electrochem. Soc. 128 (1981) 1194–1198. https://doi.org/10.1149/1.2127592.

[89] D.D.M. C.Y. Chao, L.F. Lin, A Point Defect Model for Anodic Passive Films, J. Electrochem. Soc. 128 (1981) 1187–1194. http://jes.ecsdl.org/cgi/doi/10.1149/1.2127591.

[90] D. Macdonald, The Point Defect Model for the Passive State, J. Electrochem. Soc. 139 (1992) 3434. https://doi.org/10.1149/1.3496427.

[91] D.D. Macdonald, PassivityÐthe key to our metals-based civilization *, Pure Appl. Chem. 71 (1999) 951–978.

[92] D.D. Macdonald, G.R. Engelhardt, The Point Defect Model for Bi-Layer Passive Films Center for Electrochemical Science and Technology , Department of Materials The Point Defect Model (PDM) has been shown to accurately describe the properties of passive films that form on metal surfaces , 28 (2010) 123–144.

[93] S. Sharifi-Asl, M.L. Taylor, Z. Lu, G.R. Engelhardt, B. Kursten, D.D. Macdonald, Modeling of the electrochemical impedance spectroscopic behavior of passive iron using a genetic algorithm approach, Electrochim. Acta. 102 (2013) 161–173. https://doi.org/10.1016/j.electacta.2013.03.143.

[94] S. Sharifi-asl, M.L. Taylor, Z. Lu, G.R. Engelhardt, B. Kursten, D.D. Macdonald, Modeling of the electrochemical impedance spectroscopic behavior of passive iron using a genetic algorithm approach, Electrochim. Acta. 102 (2013) 161–173. https://doi.org/10.1016/j.electacta.2013.03.143.

[95] E. Sikora, J. Sikora, D.D. Macdonald, A new method for estimating the diffusivities of vacancies in passive films, Electrochim. Acta. 41 (1996) 783–789. https://doi.org/10.1016/0013-4686(95)00312-6.

[96] D.D. Macdonald, K.M. Ismail, E. Sikora, Characterization of the Passive State on Zinc, J. Electrochem. Soc. 145 (1998) 3141–3149. https://doi.org/10.1149/1.1838777.

[97] D. Ellerbrock, D.D. MacDonald, Passivity of titanium, part 1: Film growth model diagnostics, J. Solid State Electrochem. 18 (2014) 1485–1493. https://doi.org/10.1007/s10008-013-2334-6.

[98] B. Roh, D.D. Macdonald, Passivity of titanium: part II, the defect structure of the anodic oxide film, J. Solid State Electrochem. 23 (2019) 1967–1979. https://doi.org/10.1007/s10008-019-04254-0.

[99] B. Roh, D.D. Macdonald, Passivity of titanium: part III: characterization of the anodic oxide film, J. Solid State Electrochem. 23 (2019) 1967–1979. https://doi.org/10.1007/s10008-019-04254-0.

[100] B. Roh, D.D. Macdonald, Passivity of titanium, part IV: reversible oxygen vacancy generation/annihilation, J. Solid State Electrochem. 23 (2019) 2863–2879. https://doi.org/10.1007/s10008-019-04363-w.

[101] I. Nicic, D.D. Macdonald, The passivity of Type 316L stainless steel in borate buffer solution, J. Nucl. Mater. 379 (2008) 54–58. https://doi.org/10.1016/j.jnucmat.2008.06.014.

[102] P. Lu, G.R. Engelhardt, B. Kursten, D.D. Macdonald, The Kinetics of Nucleation of Metastable Pits on Metal Surfaces: The Point Defect Model and Its Optimization on Data Obtained on Stainless Steel, Carbon Steel, Iron, Aluminum and Alloy-22, J. Electrochem. Soc. 163 (2016) C156–C163. https://doi.org/10.1149/2.0401605jes.

[103] T. Haruna, D. Macdonald, Pitting Potential and the Probabilily Dstribution, J. Electrochem. Soc. 144 (1997) 1574–1581.

[104] S. Ahn, H. Kwon, D.D. Macdonald, Role of Chloride Ion in Passivity Breakdown on Iron and Nickel, J. Electrochem. Soc. 152 (2005) B482–B490. https://doi.org/https://doi.org/10.1149/1.2048247.

[105] Y. Zhang, D.D. Macdonald, M. Urquidi-Macdonald, G.R. Engelhardt, R.B. Dooley, Passivity breakdown on AISI Type 403 stainless steel in chloride-containing borate buffer solution, Corros. Sci. 48 (2006) 3812–3823. https://doi.org/10.1016/j.corsci.2006.01.009.

[106] S. Yang, D.D. Macdonald, Theoretical and experimental studies of the pitting of type 316L stainless steel in borate buffer solution containing nitrate ion, Electrochim. Acta. 52 (2007) 1871–1879. https://doi.org/10.1016/j.electacta.2006.07.052.

[107] M. Bojinov, G. Fabricius, P. Kinnunen, T. Laitinen, K. Mäkelä, T. Saario, G. Sundholm, Electrochemical study of the passive behaviour of Ni-Cr alloys in a borate solution- A mixed-conduction model approach, J. Electroanal. Chem. 504 (2001) 29–44. https://doi.org/10.1016/S0022-0728(01)00423-5.

[108] M. Bojinov, G. Fabricius, T. Laitinen, K. Mäkelä, T. Saario, G. Sundholm, Coupling between ionic defect structure and electronic conduction in passive films on iron, chromium and iron-chromium alloys, Electrochim. Acta. 45 (2000) 2029–2048. https://doi.org/10.1016/S0013-4686(99)00423-5.

[109] M. Bojinov, A. Galtayries, P. Kinnunen, A. Machet, P. Marcus, Estimation of the parameters of oxide film growth on nickel-based alloys in high-temperature water electrolytes, Electrochim. Acta. 52 (2007) 7475–7483. https://doi.org/10.1016/j.electacta.2007.06.002.

[110] B. Beverskog, M. Bojinov, A. Englund, P. Kinnunen, T. Laitinen, K. Mäkelä, T. Saario, P. Sirkiä, A mixed-conduction model for oxide films on Fe, Cr and Fe-Cr alloys in high-temperature aqueous electrolytes - I. Comparison of the electrochemical behaviour at room temperature and at 200 °C, Corros. Sci. 44 (2002) 1901–1921. https://doi.org/10.1016/S0010-938X(02)00008-2.

[111] A. Seyeux, V. Maurice, P. Marcus, Oxide Film Growth Kinetics on Metals and Alloys I . Physical Model, J. Electrochem. Soc. 160 (2013) C189–C196. https://doi.org/10.1149/2.036306jes.

[112] K. Leistner, C. Toulemonde, B. Diawara, A. Seyeux, P. Marcus, Oxide Film Growth Kinetics on Metals and Alloys II . Numerical Simulation of Transient Behavior, 160 (2013). https://doi.org/10.1149/2.037306jes.

[113] C. Bataillon, F. Bouchon, C. Chainais-Hillairet, C. Desgranges, E. Hoarau, F. Martin, S. Perrin, M. Tupin, J. Talandier, Corrosion modelling of iron based alloy in nuclear waste repository, Electrochim. Acta. 55 (2010) 4451–4467. https://doi.org/10.1016/j.electacta.2010.02.087.

[114] C. Bataillon, F. Bouchon, C. Chainais-Hillairet, J. Fuhrmann, E. Hoarau, R. Touzani, Numerical methods for the simulation of a corrosion model with moving oxide layer, J. Comput. Phys. 231 (2012) 6213–6231. https://doi.org/10.1016/j.jcp.2012.06.005.

[115] A. Couet, A.T. Motta, A. Ambard, The coupled current charge compensation model for zirconium alloy fuel cladding oxidation: I. Parabolic oxidation of zirconium alloys, Corros. Sci. 100 (2015) 73–84. https://doi.org/10.1016/j.corsci.2015.07.003.

[116] A. Coueta, L. Borrela, J. Liu, J. Hu, C. Grovenorb, An integrated modeling and experimental approach to study hydrogen pickup mechanism in zirconium alloys, Corros. Sci. 159 (2019) 108134.

[117] A. Veluchamy, D. Sherwood, B. Emmanuel, I.S. Cole, Critical review on the passive fi lm formation and breakdown on iron electrode and the models for the mechanisms underlying passivity, J. Electroanal. Chem. 785 (2017) 196–215. https://doi.org/10.1016/j.jelechem.2016.12.020.

[118] S. Sharifi-asl, M.L. Taylor, Z. Lu, G.R. Engelhardt, B. Kursten, D.D. Macdonald, Electrochimica Acta Modeling of the electrochemical impedance spectroscopic behavior of passive iron using a genetic algorithm approach, Electrochim. Acta. 102 (2013) 161–173. https://doi.org/10.1016/j.electacta.2013.03.143.

[119] ASTM, Standard Test Methods for Determining Average Grain Size, 2004. https://doi.org/10.1520/E0112-10.Copyright.

[120] D. Rai, B.M. Sass, D.A. Moore, Chromium(III) Hydrolysis Constants and Solubility of Chromium(III) Hydroxide, Inorg. Chem. 26 (1987) 345–349. https://doi.org/10.1021/ic00250a002.

[121] S. EL Euch, D. Bricault, H. Cachet, E.M.M. Sutter, M.T.T. Tran, V. Vivier, N. Engler, A. Marion, M. Skocic, B. Huerta-Ortega, Temperature dependence of the electrochemical behavior of the 690 Ni-base alloy between 25 and 325 °C, Electrochim. Acta. 317 (2019) 509–520. https://doi.org/10.1016/j.electacta.2019.05.131.

[122] V. Jovancicevic, P. Zelenay, B.R. Scharifker, The transport properties of oxygen in aqueous borate solutions, Electrochim. Acta. 32 (1987) 1553–1555. https://doi.org/10.1016/0013-4686(87)90002-8.

[123] L. Hamadou, L. Aïnouche, A. Kadri, S.A.A. Yahia, N. Benbrahim, Electrochemical impedance spectroscopy study of thermally grown oxides exhibiting constant phase element behaviour, Electrochim. Acta. 113 (2013) 99–108. https://doi.org/10.1016/j.electacta.2013.09.054.

[124] M. Urquidi-Macdonald, S. Real, D.D. Macdonald, Applications of Kramers-Kronig transforms in the analysis of electrochemical impedance data-III. Stability and linearity, Electrochim. Acta. 35 (1990) 1559–1566. https://doi.org/10.1016/0013-4686(90)80010-L.

[125] M.E. Orazem, B. Tribollet, Electrochemical Impedance Spectroscopy (Second Edition), 2017.

[126] B. Hirschorn, M.E. Orazem, B. Tribollet, V. Vivier, I. Frateur, M. Musiani, Constant-phase-element behavior caused by resistivity distributions in films: I. theory, J. Electrochem. Soc. 157 (2010) 458–463. https://doi.org/10.1149/1.3499565.

[127] B. Hirschorn, M.E. Orazem, B. Tribollet, V. Vivier, I. Frateur, M. Musiani, L. Interfaces, U.P.R. Cnrs, U. Pierre, Constant-Phase-Element Behavior Caused by ResistivityDistributions in Films II. Applications, J. Electrochem. Soc. 157 (2010) C458–C463. https://doi.org/10.1149/1.3499565.

[128] B. Tribollet, V. Vivier, M.E. Orazem, EIS Technique in Passivity Studies : Determination of the Dielectric Properties of Passive Films, Elsevier Inc., 2017. https://doi.org/10.1016/B978-0-12-409547-2.13817-X.

[129] M.E. Orazem, I. Frateur, B. Tribollet, V. Vivier, S. Marcelin, N. Pébère, A.L. Bunge, E.A. White, D.P. Riemer, M. Musiani, Dielectric Properties of Materials Showing Constant-Phase-Element (CPE) Impedance Response, J. Electrochem. Soc. 106 (2013) C215–C225.

[130] M.E. Orazem, N. Pébère, B. Tribollet, Enhanced Graphical Representation of Electrochemical Impedance Data, J. Electrochem. Soc. 153 (2006) B129–B136. https://doi.org/10.1149/1.2168377.

[131] S. Chakri, I. Frateur, M.E. Orazem, E.M.M. Sutter, T.T.M. Tran, B. Tribollet, V. Vivier, Improved EIS Analysis of the Electrochemical Behaviour of Carbon Steel in Alkaline Solution, Electrochim. Acta. 246 (2017) 924–930. https://doi.org/10.1016/j.electacta.2017.06.096.

[132] B. Lovreček, J. Sefaja, Semiconducting aspects of the passive layer on chromium, Electrochim. Acta. 17 (1972) 1151–1155. https://doi.org/10.1016/0013-4686(72)90031-X.

[133] M. Benoit, C. Bataillon, B. Gwinner, F. Miserque, M.E. Orazem, C.M. Sánchez-sánchez, B. Tribollet, V. Vivier, Comparison of different methods for measuring the passive fi lm thickness on metals, Electrochim. Acta. 201 (2016) 340–347. https://doi.org/10.1016/j.electacta.2015.12.173.

[134] P.E. Sobol, J. Chastain, Handbook of X-ray Photoelectron Spectroscopy, 1992.

[135] M.C. Biesinger, B.P. Payne, A.P. Grosvenor, L.W.M. Lau, A.R. Gerson, R.S.C. Smart, Resolving surface chemical states in XPS analysis of first row transition metals, oxides and hydroxides: Cr, Mn, Fe, Co and Ni, Appl. Surf. Sci. 257 (2011) 2717–2730. https://doi.org/10.1016/j.apsusc.2010.10.051.

[136] A.R. Brooks, C.R. Clayton, K. Doss, Y.C. Lu, On the role of Cr in the passivity of stainless steel, J. Electrochem. Soc. 133 (1986) 2459.

[137] B. Stypula, J. Stoch, The characterization of passive films on chromium electrodes by XPS, Corros. Sci. 36 (1994) 2159–2167. https://doi.org/10.1016/0010-938X(94)90014-0.

[138] C.M. Abreu, M.J. Cristóbal, R. Losada, X.R. Nóvoa, G. Pena, M.C. Pérez, Comparative study of passive films of different stainless steels developed on alkaline medium, Electrochim. Acta. 49 (2004) 3049–3056. https://doi.org/10.1016/j.electacta.2004.01.064.

[139] C.O.A. Olsson, D. Landolt, Passive films on stainless steels - Chemistry, structure and growth, Electrochim. Acta. 48 (2003) 1093–1104. https://doi.org/10.1016/S0013-4686(02)00841-1.

[140] V. Maurice, S. Cadot, P. Marcus, XPS, LEED and STM study of thin oxide films formed on Cr(110), Surf. Sci. 458 (2000) 195–215. https://doi.org/10.1016/S0039-6028(00)00439-8.

[141] V. Maurice, P. Marcus, Passive films at the nanoscale, Electrochim. Acta. 84 (2012) 129–138.

https://doi.org/10.1016/j.electacta.2012.03.158.

[142] Y.T. Chin, B.D. Cahan, An Ellipsometric Spectroscopic Study of the Passive Film on Iron-Potential and Chloride Ion Dependence, J. Electrochem. Soc. 139 (1992) 2432–2442. https://doi.org/10.1149/1.2221245.

[143] B. Cahan, C.T. Chen, The Nature of the Passive Film on Iron I. Automatic Ellipsometric Impedance Studies, J. Electrochem. Soc. 129 (1982) 2872–2873. https://doi.org/10.1149/1.2123703.

[144] M. Iida, T. Ohtsuka, Ellipsometry of passive oxide films on nickel in acidic sulfate solution, Corros. Sci. 49 (2007) 1408–1419. https://doi.org/10.1016/j.corsci.2006.08.002.

[145] D.D. Macdonald, The Point Defect Model for the Passive State, J. Electrochem. Soc. 139 (1992) 3434–3449.

[146] D.D. Macdonald, The history of the Point Defect Model for the passive state : A brief review of film growth aspects, Electrochim. Acta. 56 (2011) 1761–1772. https://doi.org/10.1016/j.electacta.2010.11.005.

[147] D.D. Macdonald, S.I. Smedley, Characterization of vacancy transport in passive films using low frequency electrochemical impedance spectroscopy, Corros. Sci. 31 (1990) 667–672. https://doi.org/10.1016/0010-938X(90)90178-8.

[148] D.D. Macdonald, S.I. Smedley, An electrochemical impedance analysis of passive films on nickel(111) in phosphate buffer solutions, Electrochim. Acta. 35 (1990) 1949–1956. https://doi.org/10.1016/0013-4686(90)87104-A.

[149] M.A. Vorotyntsev, J.P. Badiali, E. Vieil, Multi-component diffusion approach to transport across electroactive-polymer films with two mobile charge carriers, Electrochim. Acta. 41 (1996) 1375–1381. https://doi.org/10.1016/0013-4686(95)00459-9.

[150] S. Marcelin, B. Ter-Ovanessian, B. Normand, Electronic properties of passive films from the multi-frequency Mott-Schottky and power-law coupled approach, Electrochem. Commun. 66 (2016) 62–65. https://doi.org/10.1016/j.elecom.2016.03.003.

[151] M. Benoit, C. Bataillon, B. Gwinner, F. Miserque, M.E. Orazem, C.M. Sánchez-sánchez, B. Tribollet, V. Vivier, Comparison of different methods for measuring the passive film thickness on metals, Electrochim. Acta. 201 (2016) 340–347. https://doi.org/10.1016/j.electacta.2015.12.173.

[152] B. Hirschorn, M.E. Orazem, B. Tribollet, V. Vivier, I. Frateur, M. Musiani, Constant-Phase-Element Behavior Caused by Resistivity Distributions in Films: I . Theory, J. Electrochem. Soc. 157 (2010) C452–C457. https://doi.org/10.1149/1.3499564.

[153] B. Hirschorn, M.E. Orazem, B. Tribollet, V. Vivier, I. Frateur, M. Musiani, Constant-phase-element behavior caused by resistivity distributions in films: II. Applications, J. Electrochem. Soc. 157 (2010) 458–463. https://doi.org/10.1149/1.3499565.

[154] H. Krawiec, V. Vignal, E. Schwarzenboeck, J. Banasa, Role of plastic deformation and microstructure in the micro-electrochemical behaviour of Ti-6Al-4V in sodium chloride solution, Electrochim. Acta. 104 (2013) 400–406. https://doi.org/10.1016/j.electacta.2012.12.029.

[155] Z. Feng, X. Cheng, C. Dong, L. Xu, X. Li, Effects of dissolved oxygen on electrochemical and semiconductor properties of 316L stainless steel, J. Nucl. Mater. 407 (2010) 171–177. https://doi.org/10.1016/j.jnucmat.2010.10.010.

[156] M.C. Biesinger, B.P. Payne, L.W.M. Lau, A. Gerson, R.S.C. Smart, X-ray photoelectron

spectroscopic chemical state Quantification of mixed nickel metal, oxide and hydroxide systems, Surf. Interface Anal. 41 (2009) 324–332. https://doi.org/10.1002/sia.3026.

[157] S.T. Kunihiko Chiba, Rumi Ohmori, Hisashi Tanigawa, Toshiaki Yoneoka, H2O trapping on various materials studied by AFM and XPS, Fusion Eng. Des. 49–50 (2000) 791–797.

[158] H. Luo, H. Su, G. Ying, C. Dong, X. Li, Effect of cold deformation on the electrochemical behaviour of 304L stainless steel in contaminated sulfuric acid environment, Appl. Surf. Sci. 425 (2017) 628–638. https://doi.org/10.1016/j.apsusc.2017.07.057.

[159] L. Freire, M.J. Carmezim, M.G.S. Ferreira, M.F. Montemor, The passive behaviour of AISI 316 in alkaline media and the effect of pH : A combined electrochemical and analytical study, Electrochim. Acta. 55 (2010) 6174–6181. https://doi.org/10.1016/j.electacta.2009.10.026.

[160] C.T. Liu, J.K. Wu, Influence of pH on the passivation behavior of 254SMO stainless steel in 3.5% NaCl solution, Corros. Sci. 49 (2007) 2198–2209. https://doi.org/10.1016/j.corsci.2006.10.032.

[161] N. Sato, T. Noda, K. Kudo, Thickness and structure on iron in acidic and basic solution, Electrochim. Acta. 19 (1974) 471–475.

[162] B. Hirschorn, M.E. Orazem, B. Tribollet, V. Vivier, I. Frateur, M. Musiani, Determination of effective capacitance and film thickness from constant-phase-element parameters, Electrochim. Acta. 55 (2010) 6218–6227. https://doi.org/10.1016/j.electacta.2009.10.065.

[163] T. Jabs, P. Borthen, H.H. Strehblow, X-Ray Photoelectron Spectroscopic Examinations of Electrochemically Formed Passive Layers on Ni-Cr Alloys, J. Electrochem. Soc. 144 (1997) 1231–1243. https://doi.org/10.1149/1.1837577.

[164] E. McCaffert, Oxide networks, graph theory, and the passivity of binary alloys, Corros. Sci. 44 (2002) 1393–1409.

[165] M. Bojinov, G. Fabricius, P. Kinnunen, T. Laitinen, K. Ma, The mechanism of transpassive dissolution of Ni – Cr alloys in sulphate solutions, Electrochim. Acta. 45 (2000) 2791–2802.

[166] H.H. UHLIG, Electron Configuration in Alloys and Passivity, Zeitschrift Für Elektrochemie, Berichte Der Bunsengesellschaft Für Phys. Chemie. 62 (1958) 700–707.

[167] J.R. Myers, F.H. Beck, M.G. Fontana, Anodic polarization behavior of nickel-chromium alloys in sulfuric acid solutions, Corrosion. 21 (1965) 277–287.

[168] B. Ter-Ovanessian, N. Mary, B. Normand, Passivity Breakdown of Ni-Cr Alloys : From Anions Interactions to Stable Pits Growth, J. Electrochem. Soc. 163 (2016) 410–419. https://doi.org/10.1149/2.0381608jes.

[169] G. Song, Transpassivation of Fe–Cr–Ni stainless steels, Corros. Sci. 47 (2005) 1953–1987. https://doi.org/10.1016/j.corsci.2004.09.007.

[170] I. Betova, M. Bojinov, T. Laitinen, M. Kari, The transpassive dissolution mechanism of highly alloyed stainless steels I . Experimental results and modelling procedure, Corros. Sci. 44 (2002) 2675–2697.

[171] Z. Zhang, B. Ter-Ovanessian, S. Marcelin, B. Normand, Investigation of the passive behavior of a Ni–Cr binary alloy using successive electrochemical impedance measurements, Electrochim. Acta. 353 (2020) 136531. https://doi.org/10.1016/j.electacta.2020.136531.

[172] F. Hamdani, Improvement of the corrosion and oxidation resistance of Ni-based alloys by optimizing the chromium content, INSA Lyon, 2016.

[173] N. Jallerat, S.. Mischler, L. D., Influence of Fe and Mo Alloying Elements on the Composition of

Passive Films Formed on Ni-Cr Alloys in an Acidic Chloride Solution, in: Modif. Passiv. Film., 1993: pp. 26–34.

[174] S. Boudin, J.-L. Vignes, G. Lorang, M.D.C. Belo, G. Blondiaux, S.M. Mikhailov, J.P. Jacobs, H.H. Brongersma, Analytical and Electrochemical Study of Passive Films Formed on Nickel-Chromium Alloys: Influence of the Chromium Bulk Concentration, Suface Interface Anal. 22 (1994) 462–466.

[175] M. Da Cunha, N.E. Hakiki, M.G.S. Ferreira, Semiconducting properties of passive films formed on nickel–base alloys type Alloy 600 : influence of the alloying elements, Electrochim. Acta. 44 (1999) 2473–2481.

[176] B. Normand, N. Bererd, P. Martinet, S. Marcelin, M. Moine, J. Feirrera, D. Baux, T. Sauvage, N. Monco, Electrochemical behaviour of austenitic stainless steel under tribological stresses and irradiation, 176 (2020). https://doi.org/10.1016/j.corsci.2020.108945.

[177] K.T. Chiang, D.S. Dunn, G.A. Cragnolino, Effect of Simulated Groundwater Chemistry on Stress Corrosion Cracking of Alloy 22, Corrosion. 63 (2007) 940–950.

[178] W. Ye, Y. Li, F. Wang, The improvement of the corrosion resistance of 309 stainless steel in the transpassive region by nano-crystallization, Electrochim. Acta. 54 (2009) 1339–1349. https://doi.org/10.1016/j.electacta.2008.08.073.

[179] D. Marijan, M. Gojic, P. Industry, Electrochemical study of the chromium electrode behaviour in borate buffer solution, J. Appl. Electrochem. 32 (2002) 1341–1346.

[180] K. Lutton Cwalina, C.R. Demarest, A.Y. Gerard, J.R. Scully, Revisiting the effects of molybdenum and tungsten alloying on corrosion behavior of nickel-chromium alloys in aqueous corrosion, Curr. Opin. Solid State Mater. Sci. 23 (2019) 129–141. https://doi.org/10.1016/j.cossms.2019.03.002.

[181] W.-S. Kim, Electrochemical Characterization of Passive Films Formed on Ni Based Alloys, Osaka University, 2015.

[182] C. Man, C. Dong, Z. Cui, K. Xiao, Q. Yu, X. Li, A comparative study of primary and secondary passive films formed on AM355 stainless steel in 0.1 M NaOH, Appl. Surf. Sci. 427 (2018) 763–773. https://doi.org/10.1016/j.apsusc.2017.08.151.

[183] Z. Feng, X. Cheng, C. Dong, L. Xu, X. Li, Passivity of 316L stainless steel in borate buffer solution studied by Mott – Schottky analysis , atomic absorption spectrometry and X-ray photoelectron spectroscopy, Corros. Sci. 52 (2010) 3646–3653. https://doi.org/10.1016/j.corsci.2010.07.013.

[184] L.A. Toledo-matos, M.A. Pech-canul, Evolution of an iron passive film in a borate buffer solution (pH 8.4), J. Solid State Electrochem. 15 (2011) 1927–1934. https://doi.org/10.1007/s10008-010-1213-7.

[185] D. Marijan, M. Gojic, P. Industry, Electrochemical study of the chromium electrode behaviour in borate buffer solution, J. Appl. Electrochem. 32 (2003) 1341–1346.

[186] M. Bojinov, G. Fabricius, P. Kinnunen, T. Laitinen, K. Mäkelä, T. Saario, G. Sundholm, K. Yliniemi, Transpassive dissolution of Ni-Cr alloys in sulphate solutions - Comparison between a model alloy and two industrial alloys, Electrochim. Acta. 47 (2002) 1697–1712. https://doi.org/10.1016/S0013-4686(02)00018-X.

[187] H. Tsuchiya, S. Fujimoto, O. Chihara, T. Shibata, Semiconductive behavior of passive films formed on pure Cr and Fe–Cr alloys in sulfuric acid solution, Electrochim. Acta. 47 (2002) 4357–4366.

[188] B. Krishnamurthy, R.E. White, H.J. Ploehn, Simplified point defect model for growth of anodic passive films on iron, Electrochim. Acta. 47 (2002) 3375–3581.

[189] E.J. Calvo, C.D. Pallotta, S. Hild, E. Garcia, XPS and Electrochemical Studies of Chromium Modified Passive Iron Electrodes XPS and Electrochemical Studies of Chromium Modified Passive Iron Electrodes, J. Electrochem. Soc. 135 (1988) 314.

[190] https://www.aperam.com/product/imphy-gilphy-80/, (n.d.).

[191] W. YANG, R.-C. NI, H.-Z. HUA, The behavior of chromium and molybdenum in the propagation process of localized corrosion of steels, Corros. Sci. 24 (1984) 691–707.

[192] http://www.phase-trans.msm.cam.ac.uk/2005/Stainless_steels/stainless.html, (n.d.).

[193] A. Ben Rhouma, T. Amadou, H. Sidhom, C. Braham, Correlation between microstructure and intergranular corrosion behavior of low delta-ferrite content AISI 316L aged in the range 550-700 °C, J. Alloys Compd. 708 (2017) 871–886.

[194] Z.F. Yin, W.Z. Zhao, W.Y. Lai, X.H. Zhao, Electrochemical behaviour of Ni-base alloys exposed under oil/gas field environments, Corros. Sci. 51 (2009) 1702–1706.

[195] J.E. Indacochea, J.L. Smith, K.R. Litko, E.J. Karell, High-Temperature Oxidation and Corrosion of Structural Materials in Molten Chlorides, Oxid. Met. 55 (2001) 1–16.

[196] S. Khorsand, A. Sheikhi, K. Raeissi, M.A. Golozar, Hot Corrosion Behavior of Inconel 625 Superalloy in Eutectic Molten Nitrate Salts S., Oxid. Met. 90 (2018) 169–186.

[197] X. Ren, K. Sridharan, T.R. Allen, Corrosion Behavior of Alloys 625 and 718 in Supercritical Water, Corrosion. 63 (2007) 8–9.

[198] I. Olefjord, B. Brox, U. Jelvestam, Surface Composition of Stainless Steels during Anodic Dissolution and Passivation Studied by ESCA, J. Electrochem. Soc. 132 (1985) 2854–2861.

[199] K. Jung, S. Ahn, Y. Kim, S. Oh, W. Ryu, H. Kwon, Alloy design employing high Cr concentrations for Mo-free stainless steels with enhanced corrosion resistance, Corros. Sci. 140 (2018) 61–72. https://doi.org/10.1016/j.corsci.2018.06.021.

[200] J.E. CASTLE, J.H. QIU, A co-ordinated study of the passivation of alloy steels by plasma source mass spectrometry and x-ray photoelectron spectroscopy—1. characterization of the passive film, Corros. Sci. 29 (1989) 591–603.

[201] Y.C. Lu, C.R. Clayton, A.R. Brooks, A bipolar model of the passivity of stainless steels-II. The influence of aqueous molybdate, Corros. Sci. 29 (1989) 863–880. https://doi.org/10.1016/0010-938X(89)90058-9.

[202] P. Marcus, M.E. Bussell, XPS study of the passive films formed on nitrogen-implanted austenitic stainless steels, Appl. Surf. Sci. 59 (1992) 7–21. https://doi.org/10.1016/0169-4332(92)90163-R.

[203] J.E. Castle, J.H. Qiu, A co-ordinated study of the passivation of alloy steels by plasma source mass spectrometry and x-ray photoelectron spectroscopy—II. growth kinetics of the passive film, Corros. Sci. 29 (1989) 605–616.

[204] J.D. Hendersona, X. Li, D.W. Shoesmith, J.J. Noël, K. Ogle, Molybdenum surface enrichment and release during transpassive dissolution of Ni-based alloys, Corros. Sci. 147 (2019) 32–40.

[205] A.J. Samin, C.D. Taylor, First-principles investigation of surface properties and adsorption of oxygen on Ni-22Cr and the role of molybdenum, Corros. Sci. 134 (2018) 103–111. https://doi.org/10.1016/j.corsci.2018.02.017.

[206] V. Maurice, H. Peng, L.H. Klein, A. Seyeux, S. Zanna, P. Marcus, Effects of molybdenum on the composition and nanoscale morphology of passivated austenitic stainless steel surfaces, Faraday Discuss. 180 (2015) 151–170.

[207] P. Wang, Z., Carrière, C., Seyeux, A., Zanna, S., & Marcus, XPS and ToF-SIMS Investigation of Native Oxides and Passive Films Formed on Nickel Alloys Containing Chromium and Molybdenum, J. Electrochem. Soc. (2021).

Appendix

Appendix A. XPS analysis on Ni16Cr and Ni14Cr8Fe

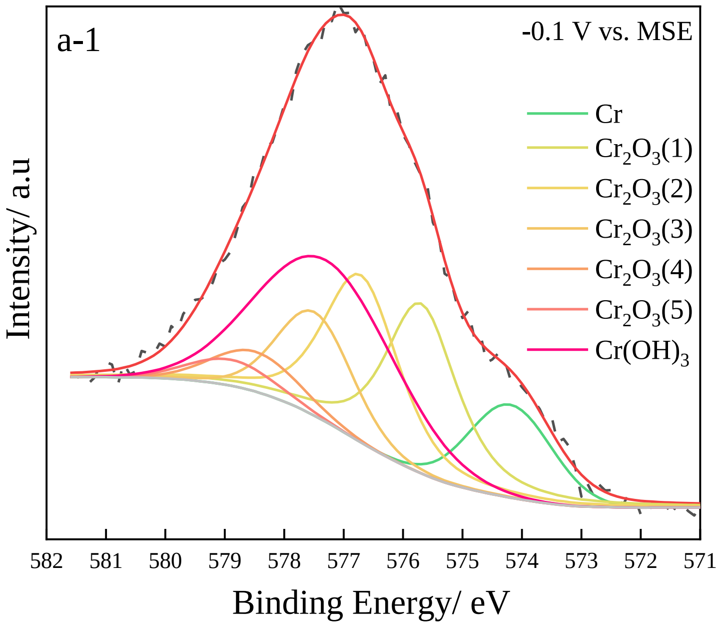

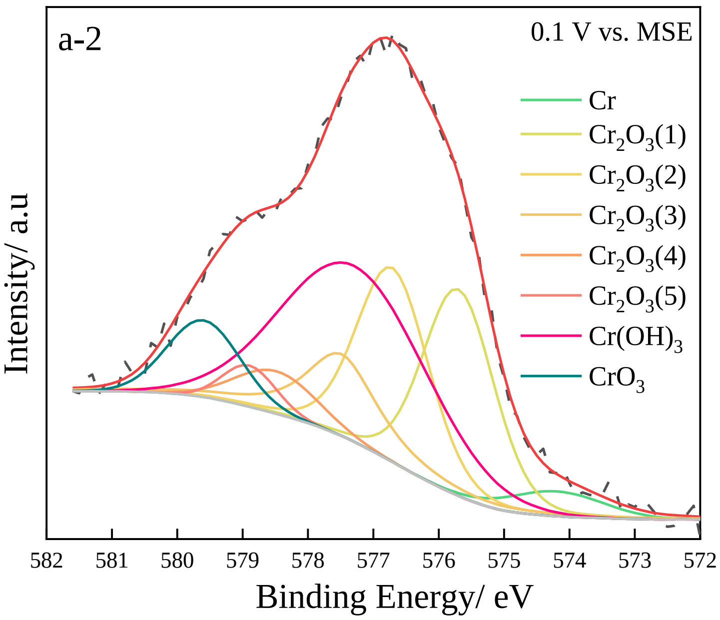

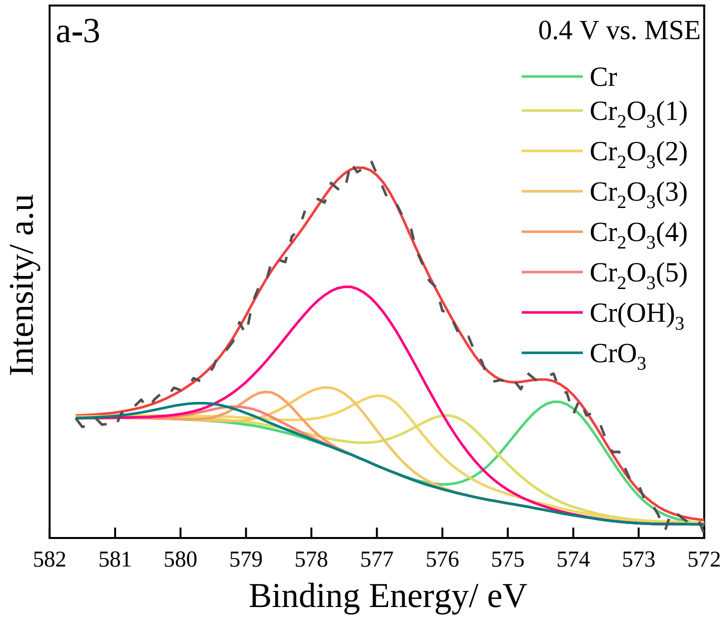
a-3
0.4 V vs. MSE
Cr
Cr_2O_3(1)
Cr_2O_3(2)
Cr_2O_3(3)
Cr_2O_3(4)
Cr_2O_3(5)
$Cr(OH)_3$
CrO_3
Intensity/ a.u
582
581
580
579
578
577
576
575
574
573
572
Binding Energy/ eV

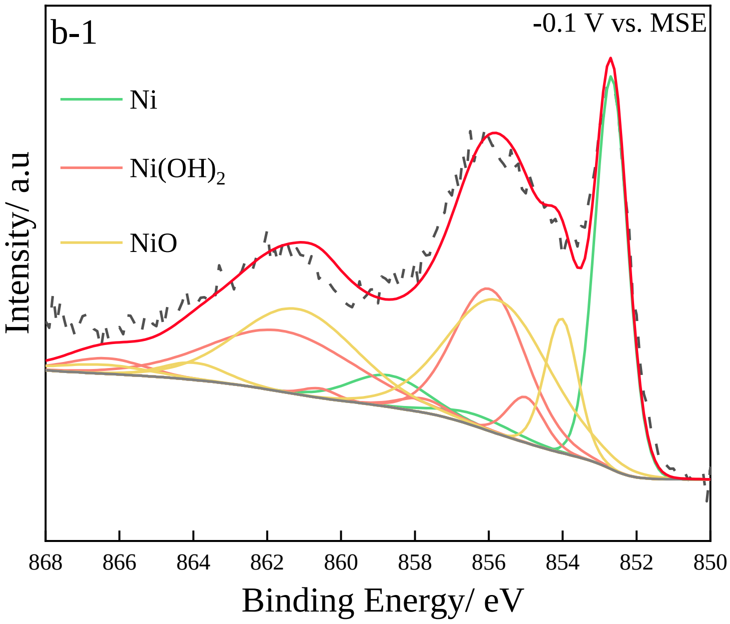
b-1
-0.1 V vs. MSE
Ni
$Ni(OH)_2$
NiO
Intensity/ a.u
868
866
864
862
860
858
856
854
852
850
Binding Energy/ eV

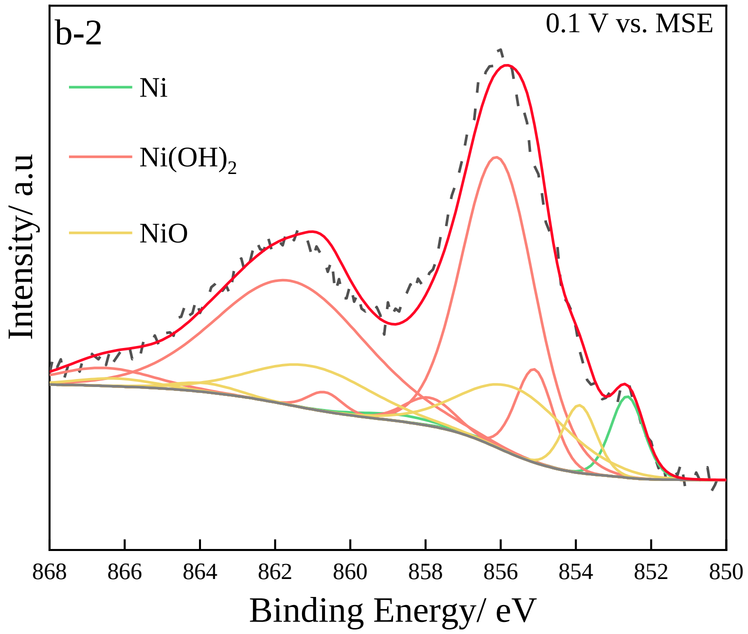
b-2
0.1 V vs. MSE
Ni
Ni(OH)$_2$
NiO
Intensity/ a.u
868
866
864
862
860
858
856
854
852
850
Binding Energy/ eV

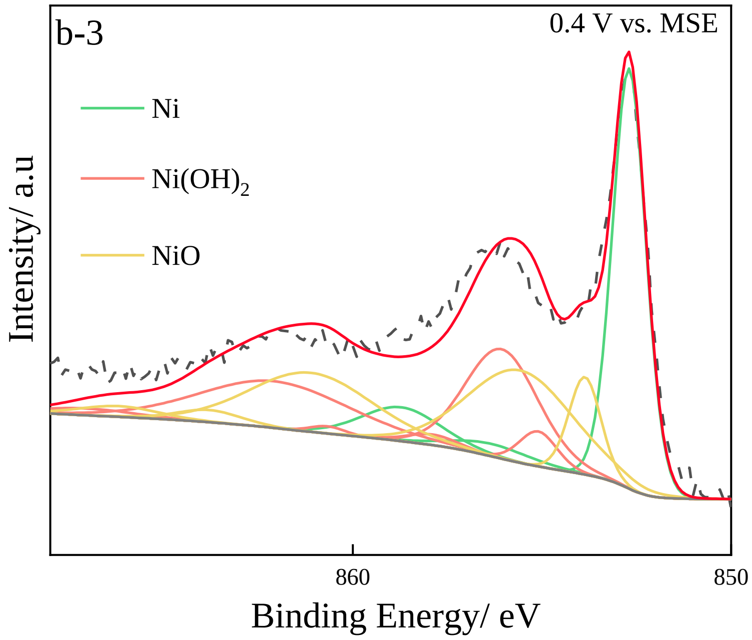
b-3
0.4 V vs. MSE
Ni
Ni(OH)$_2$
NiO
Intensity/ a.u
860
850
Binding Energy/ eV

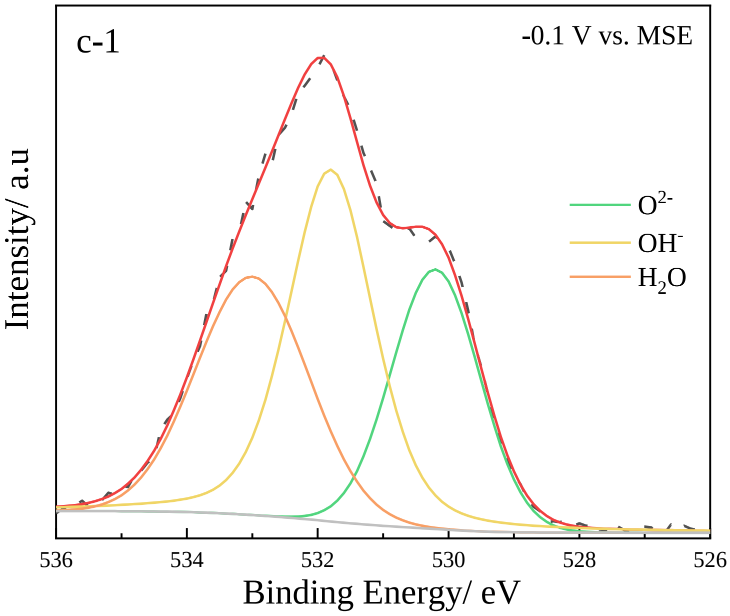
c-1
-0.1 V vs. MSE
Intensity/ a.u
O^{2-}
OH^-
H_2O
536
534
532
530
528
526
Binding Energy/ eV

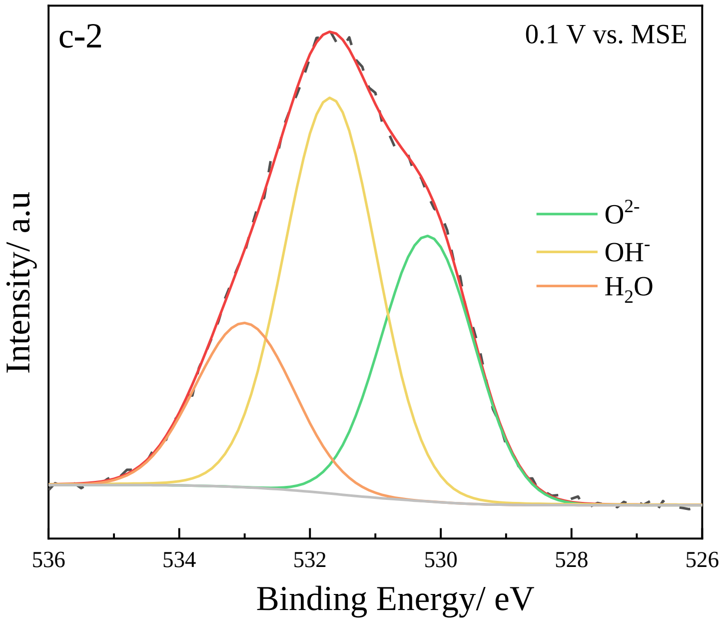
c-2
0.1 V vs. MSE
Intensity/ a.u
O^{2-}
OH^-
H_2O
536
534
532
530
528
526
Binding Energy/ eV

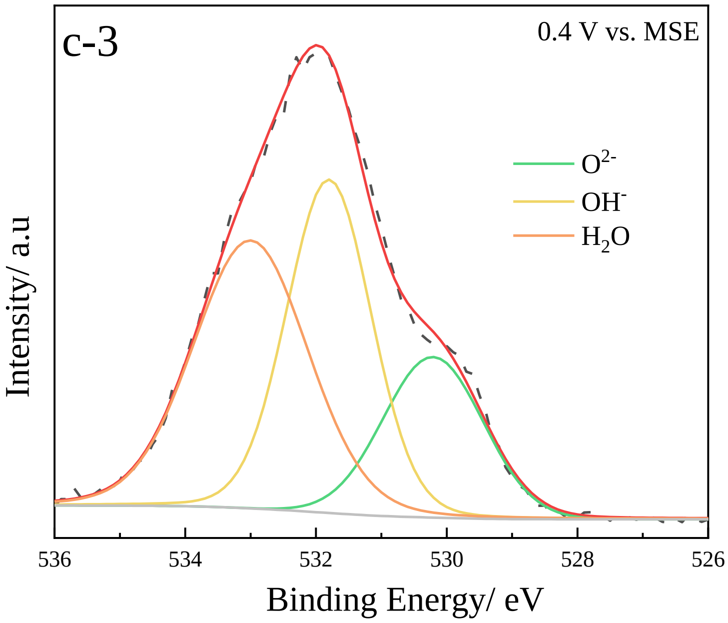

Figure App. 1 XPS spectra of (a) Cr 2p3/2, (b) Ni2p3/2, and (c) O 1s of the passive film formed on Ni–16Cr alloy at different potentials (vs MSE) staying for 12 h in 0.05 M H_3BO_3 + 0.075 M $Na_2B_4O_7$ 10H2O borate buffer solution (pH=9.2).

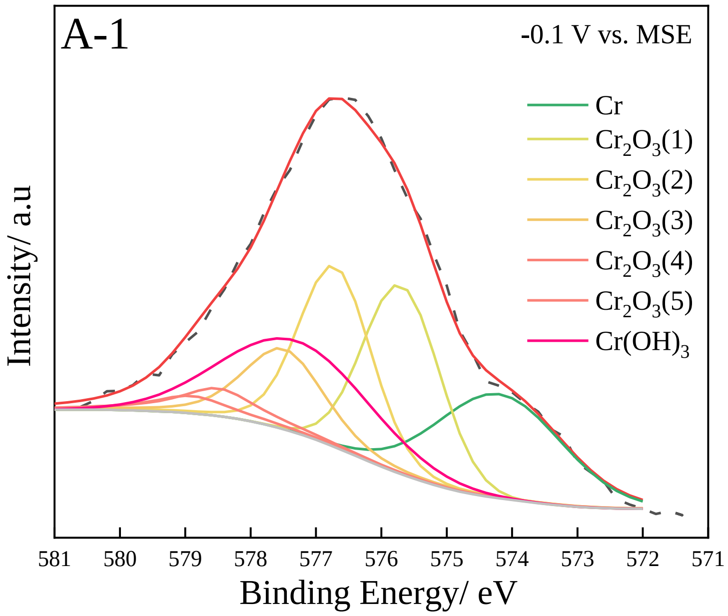

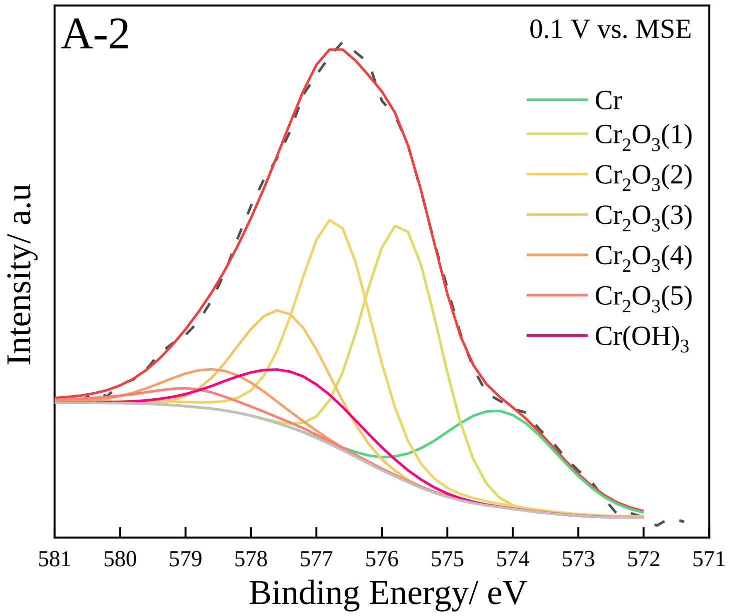
A-2
0.1 V vs. MSE
Cr
Cr_2O_3(1)
Cr_2O_3(2)
Cr_2O_3(3)
Cr_2O_3(4)
Cr_2O_3(5)
$Cr(OH)_3$
Intensity/ a.u
581
580
579
578
577
576
575
574
573
572
571
Binding Energy/ eV

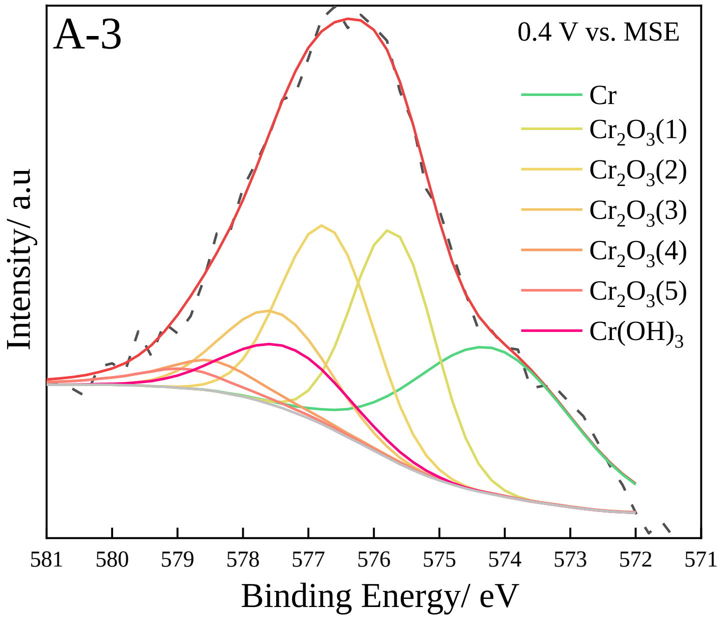
A-3
0.4 V vs. MSE
Cr
Cr_2O_3(1)
Cr_2O_3(2)
Cr_2O_3(3)
Cr_2O_3(4)
Cr_2O_3(5)
$Cr(OH)_3$
Intensity/ a.u
581
580
579
578
577
576
575
574
573
572
571
Binding Energy/ eV

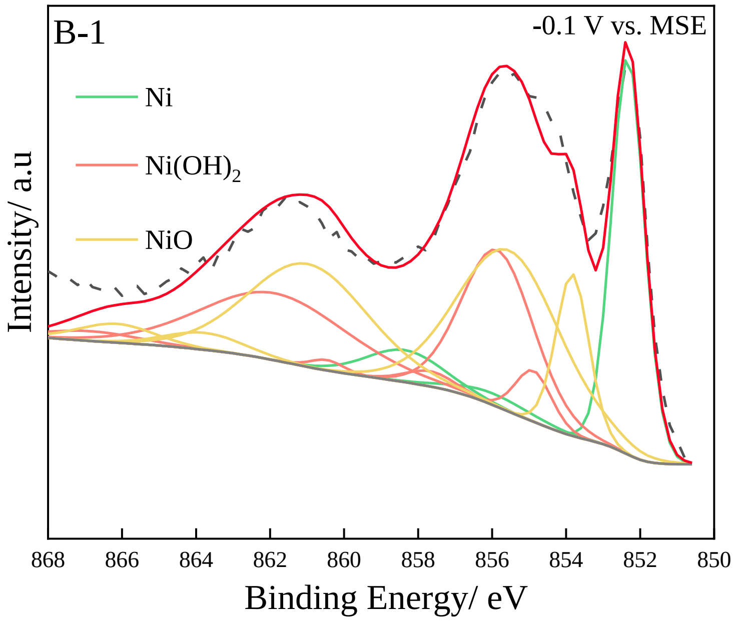
B-1
-0.1 V vs. MSE
Ni
Ni(OH)$_2$
NiO
Intensity/ a.u
868
866
864
862
860
858
856
854
852
850
Binding Energy/ eV

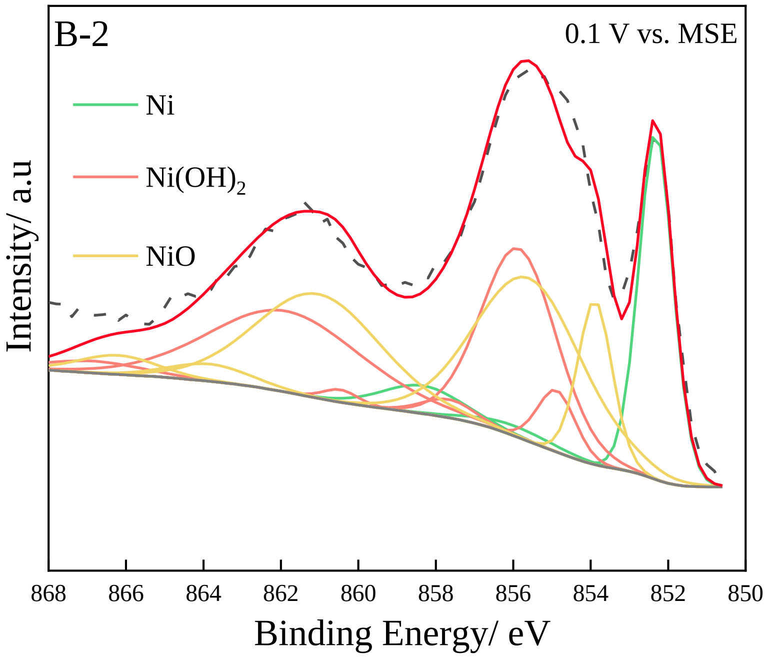
B-2
0.1 V vs. MSE
Ni
Ni(OH)$_2$
NiO
Intensity/ a.u
868
866
864
862
860
858
856
854
852
850
Binding Energy/ eV

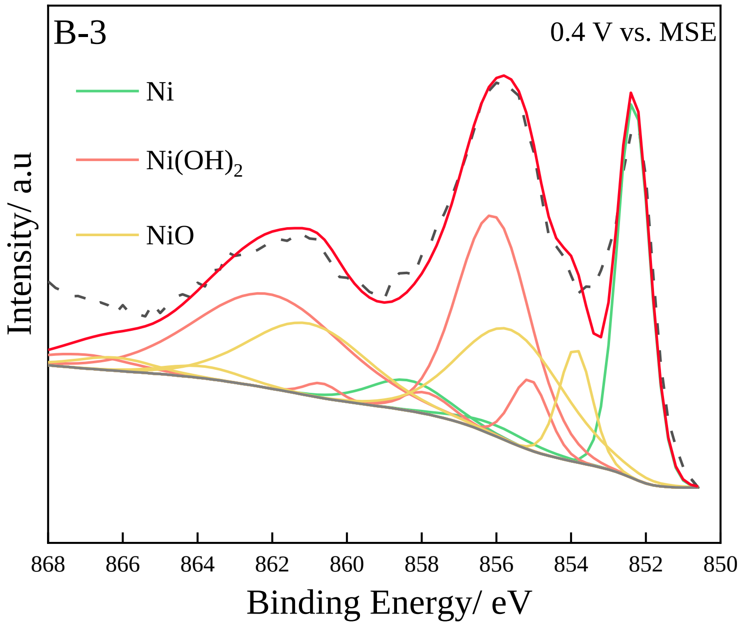
B-3
0.4 V vs. MSE
Ni
Ni(OH)$_2$
NiO
Intensity/ a.u
868
866
864
862
860
858
856
854
852
850
Binding Energy/ eV

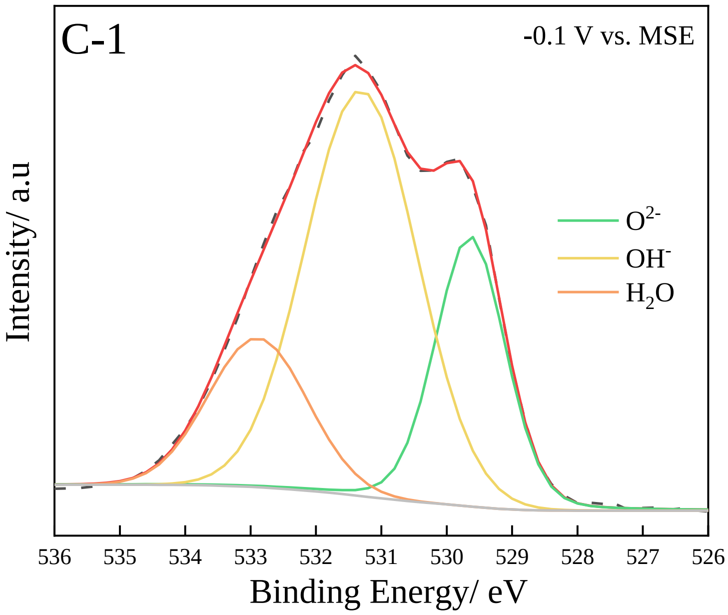
C-1
-0.1 V vs. MSE
O^{2-}
OH$^-$
H$_2$O
Intensity/ a.u
536
535
534
533
532
531
530
529
528
527
526
Binding Energy/ eV

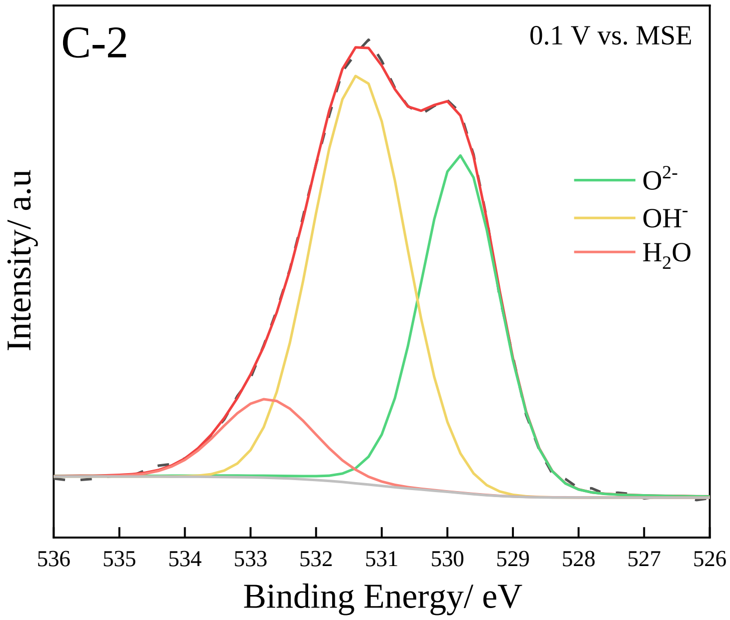
C-2
0.1 V vs. MSE
O^{2-}
OH^-
H_2O
Intensity/ a.u
536
535
534
533
532
531
530
529
528
527
526
Binding Energy/ eV

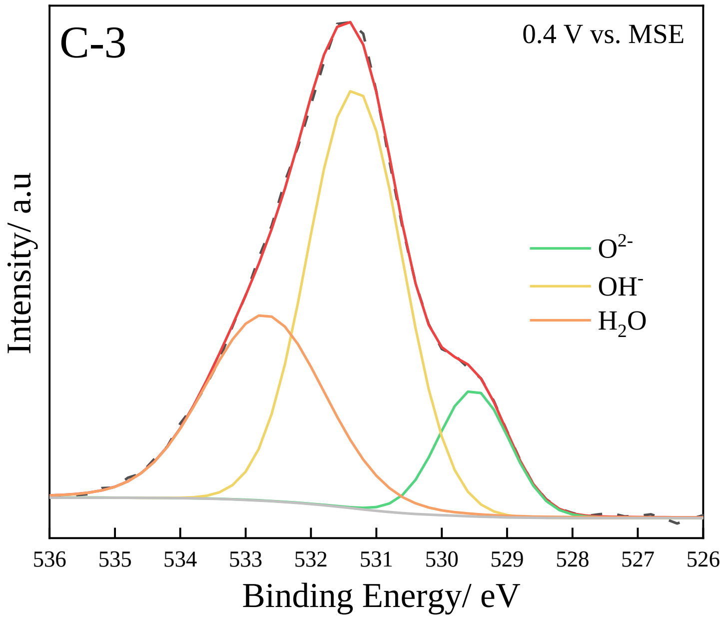
C-3
0.4 V vs. MSE
O^{2-}
OH^-
H_2O
Intensity/ a.u
536
535
534
533
532
531
530
529
528
527
526
Binding Energy/ eV

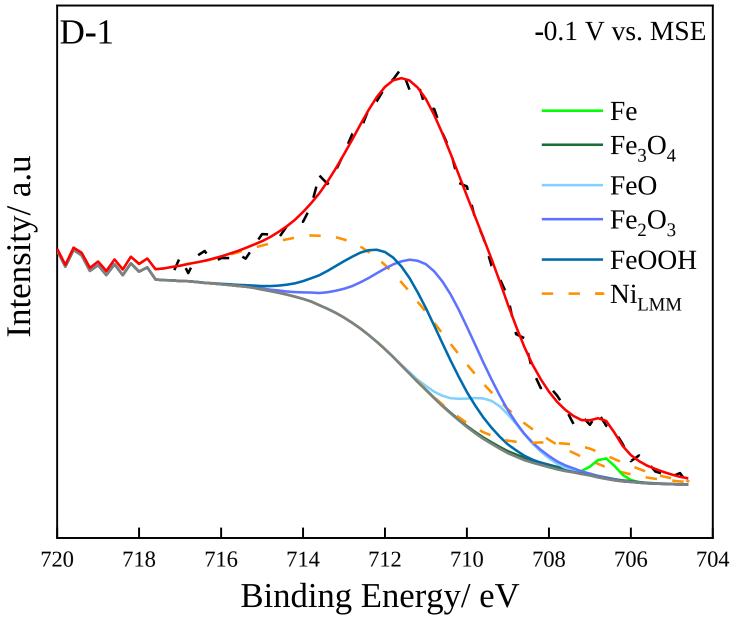
D-1
-0.1 V vs. MSE
Fe
Fe_3O_4
FeO
Fe_2O_3
FeOOH
Ni_{LMM}
Intensity/ a.u
720
718
716
714
712
710
708
706
704
Binding Energy/ eV

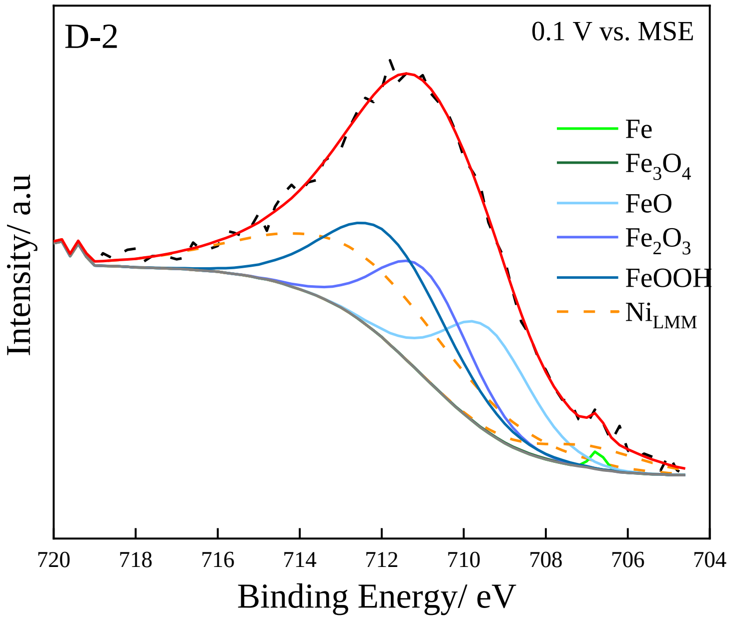
D-2
0.1 V vs. MSE
Fe
Fe_3O_4
FeO
Fe_2O_3
FeOOH
Ni_{LMM}
Intensity/ a.u
720
718
716
714
712
710
708
706
704
Binding Energy/ eV

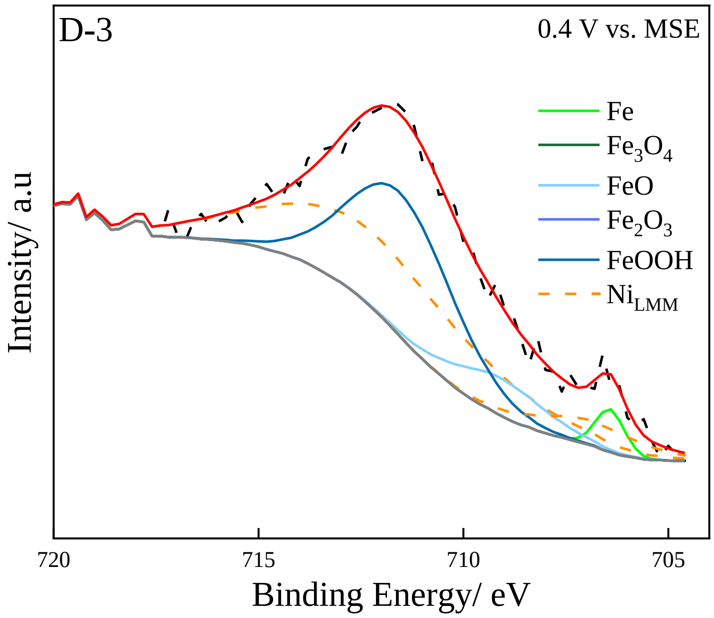

Figure App. 2 XPS spectra of (A) Cr 2p3/2, (B) Ni2p3/2, (C) O 1s and (D) Fe 2p3/2 of the passive film formed on Ni–14Cr–8Fe alloy at different potentials (vs MSE) staying for 12 h in 0.05 M H_3BO_3 + 0.075 M $Na_2B_4O_7$ $10H_2O$ borate buffer solution (pH=9.2).

XPS was used for detecting the different composition of passive film at different potential ranges. Figure App. 1 and Figure App. 2 show high-resolution spectra of the Cr 2p3/2, Ni 2p3/2, O 1s and Fe 2p3/2 regions of the passive film formed on Ni–16Cr and Ni–14Cr–8Fe alloy, separately. The binding energies corresponding to the different sorts of the chemical elements is summarized in Table App. 1.

Table App. 1 XPS binding energies Eb

$Cr2p_{3/2}$	peak	Cr(0)	Cr_2O_3 (1)	Cr_2O_3 (2)	Cr_2O_3 (3)	Cr_2O_3 (4)	Cr_2O_3 (5)
	E_b/eV	574.2	575.7	576.7	577.5	578.5	578.9
		$Cr(OH)_3$	CrO_3				
		577.3	579.6				
$Ni2p_{3/2}$	peak	Ni(1)	Ni(2)	Ni(3)			
	E_b/eV	852.6	856.3	858.7			
		NiO(1)	NiO(2)	NiO(3)	NiO(4)	NiO(5)	
		853.7	855.4	860.9	864.0	866.3	
		$Ni(OH)_2$(1)	$Ni(OH)_2$ (2)	$Ni(OH)_2$(3)	$Ni(OH)_2$(4)	$Ni(OH)_2$(5)	$Ni(OH)_2$(6)
		854.9	855.7	857.7	860.5	861.5	866.5
O 1s	peak	O^{2-}	OH^- metallic hydroxides	H_2O bonded water			
	E_b/eV	530.2	531.8	533			
$Fe2p_{3/2}$	peak	Fe(0)	Fe_3O_4	FeO	Fe_2O_3	FeOOH	
	E_b/eV	706.7	708.2	709.4	710.9	711.8	

The Cr $2p_{3/2}$ spectra were fitted with data from the literature, the binding energy differences, FWHM and area ratio are fixed for each peak, more detail was introduced in Chapter 2. The metallic chromium Cr(0) peaks is assigned to the binding energy of 574.2 eV, and those for chromium hydroxide $Cr(OH)_3$ is found at the higher binding energy of 577.4 eV. The peaks for chromium oxide Cr_2O_3 are at binding energies of 575.7, 576.7, 577.5, 578.5, and 578.9 eV. The binding energy differences, FWHM and area ratio are fixed for each peak. The binding energy of 579.6 eV is attributed to CrO_3.

The $2p_{3/2}$ region of Ni was fitted according to the method introduced in Chapter 2. The ones at the low binding energy of 852.6 eV, 856.3 eV and 858.7 can be attributed to Ni in the metallic state. There are five different peaks to account for nickel oxide NiO at 853.7 eV, 855.4 eV, 860.9 eV, 864.0 eV and 866.3 eV. The last six peaks corresponded to hydroxide $Ni(OH)_2$ locate at 854.9 eV, 855.7 eV, 857.7 eV, 860.5 eV, 861.5 eV and 866.5 eV, respectively.

The O 1s spectra were fitted with oxide O^{2-}, hydroxide OH^-, and water H_2O, respectively. The peak at 530.2 eV corresponds to O^{2-}, which can be attributed to the metallic oxides in the passive film. However, the peaks at 531.8 and 533 eV correspond to OH^- of metallic hydroxides and bonded water/adsorbed water or impurities on the surface of the sample.

The Fe $2p_{3/2}$ spectra were fitted with metallic Fe, Fe_3O_4, FeO, Fe_2O_3 and FeOOH [141]. Note that the information of Auger Ni_{LMM} was measured on a NiCr sample and excluded from the signal of iron in the NiCrFe samples within the binding energy 706 and 712 eV. The binding energy at 706.7 eV corresponds to the metallic Fe(0). The peaks at about 708.2, 709.4 and 710.9 eV are assigned to the iron oxides of Fe_3O_4, FeO and Fe_2O_3, respectively. The peak at 711.8 eV could be contributed to FeOOH.

This fitting procedure was employed on all the samples in this work, and allowed to extract ratios of different compounds on the samples surface. The accuracy of these measurements is estimated to a few percents.

Appendix B. XPS analysis on Ni16Cr during polarization test

This appendix is a comparison of composition of passive films formed at three different potentials, corresponding to stable passivation range, secondary oxidation and secondary passivation, respectively. In order to know the difference between instantaneous (5 minutes) polarization and long-term polarization (12 h) for composition of passive film. Consequently, it could be seen as a complementary test for the methodology of successive impedance measurement.

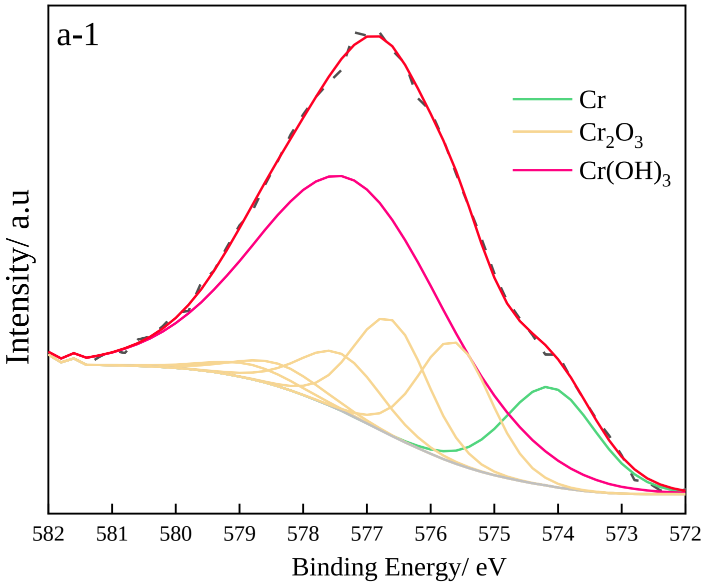

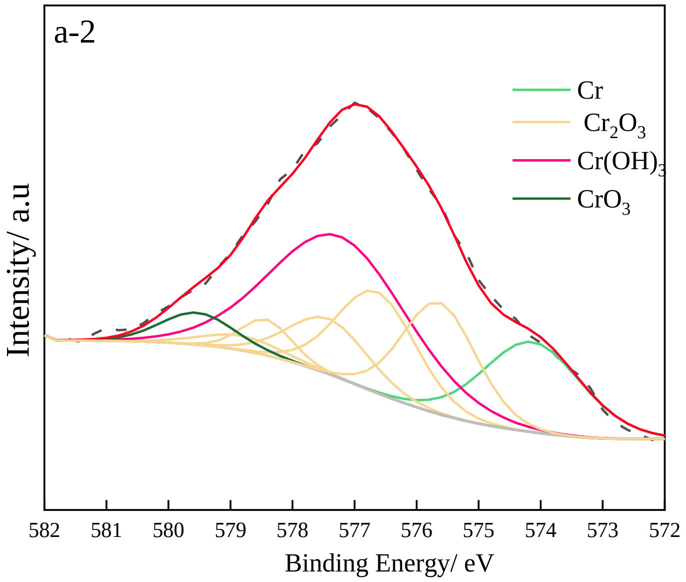

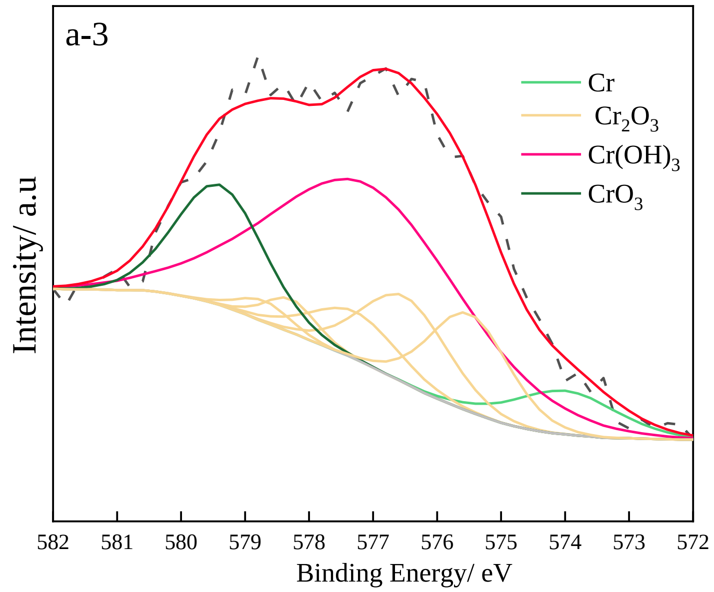
a-3
Cr
Cr$_2$O$_3$
Cr(OH)$_3$
CrO$_3$
Intensity/ a.u
582
581
580
579
578
577
576
575
574
573
572
Binding Energy/ eV

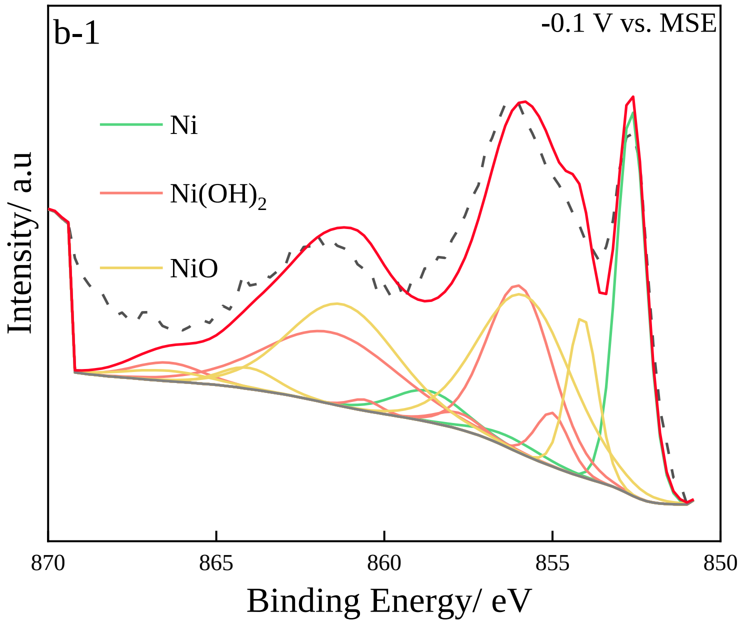
b-1
-0.1 V vs. MSE
Ni
Ni(OH)$_2$
NiO
Intensity/ a.u
870
865
860
855
850
Binding Energy/ eV

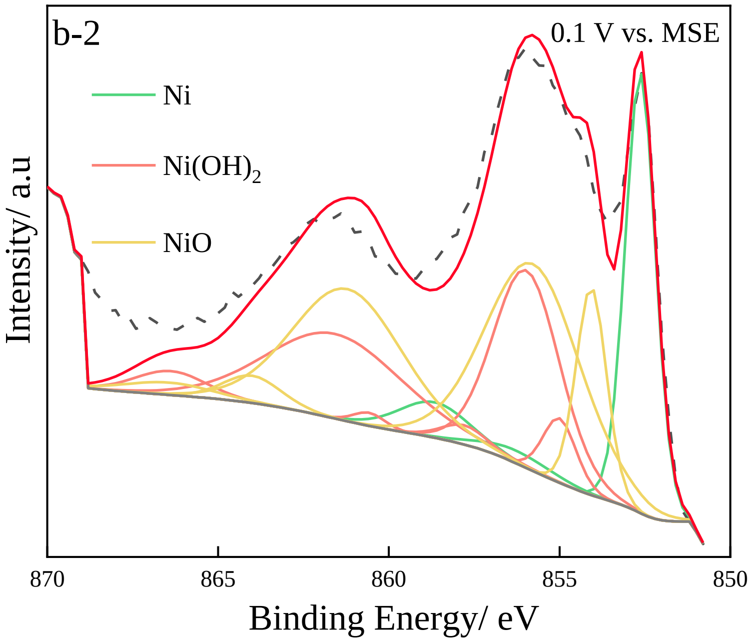
b-2
0.1 V vs. MSE
Ni
Ni(OH)$_2$
NiO
Intensity/ a.u
870
865
860
855
850
Binding Energy/ eV

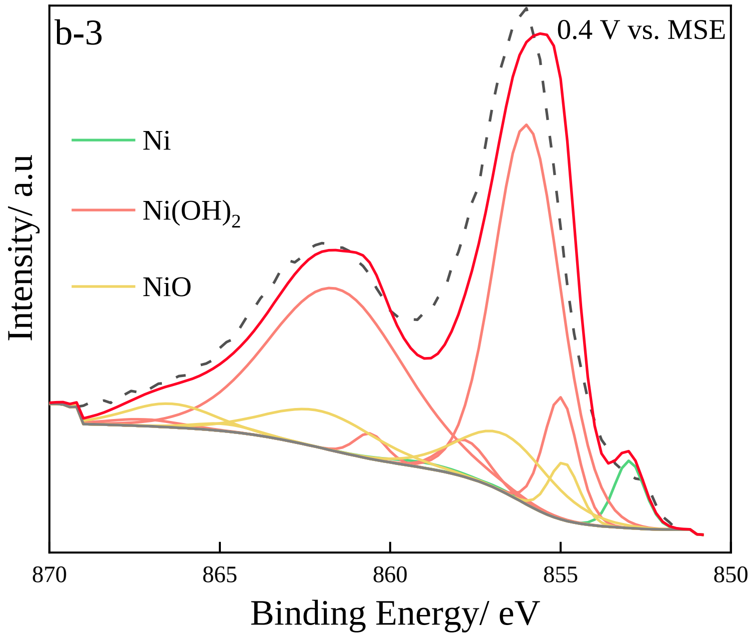
b-3
0.4 V vs. MSE
Ni
Ni(OH)$_2$
NiO
Intensity/ a.u
870
865
860
855
850
Binding Energy/ eV

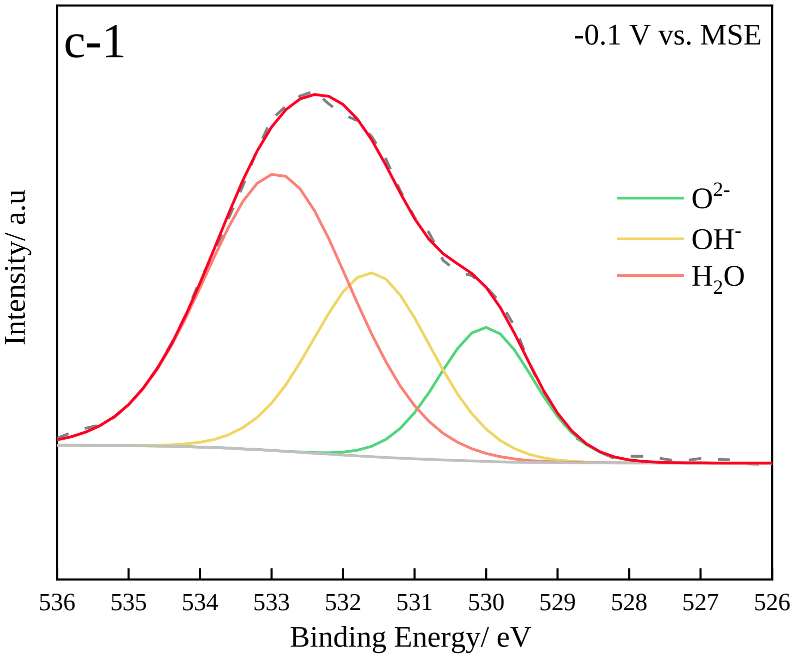
c-1
-0.1 V vs. MSE
O2-
OH-
H2O
Intensity/ a.u
536
535
534
533
532
531
530
529
528
527
526
Binding Energy/ eV

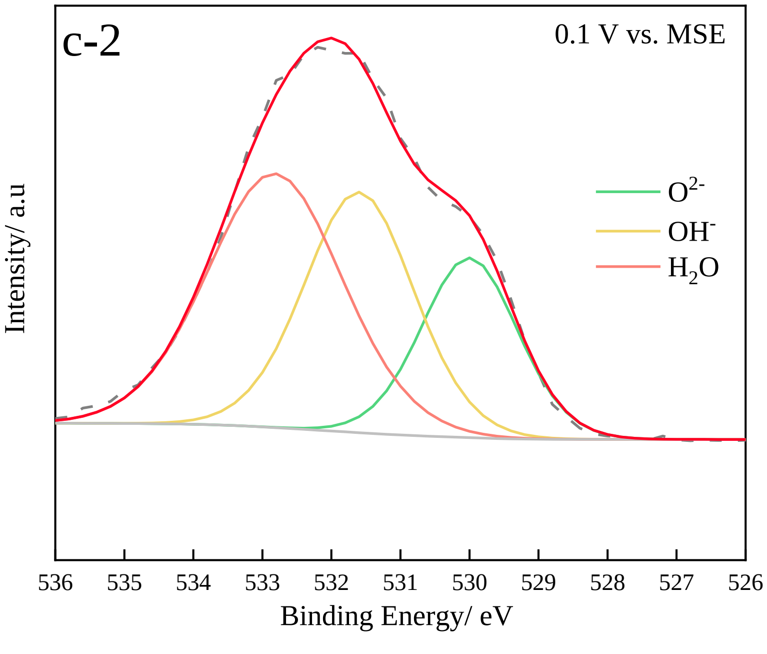
c-2
0.1 V vs. MSE
O2-
OH-
H2O
Intensity/ a.u
536
535
534
533
532
531
530
529
528
527
526
Binding Energy/ eV

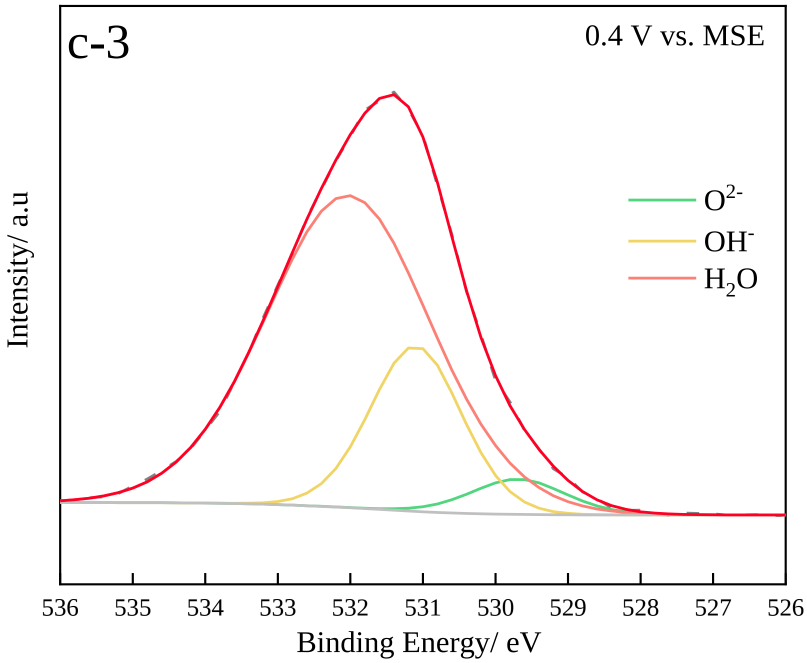

Figure App. 3 XPS spectra of (a) Cr 2p3/2, (b) Ni2p3/2, and (c) O 1s of the passive film formed on Ni–16Cr alloy at different potentials (vs MSE) in 0.05 M H_3BO_3 + 0.075 M $Na_2B_4O_7$ 10H2O borate buffer solution (pH=9.2) during the poentiostatic polarization test.

The XPS spectra of Cr 2p3/2, Ni2p3/2 and O 1s of the passive film formed on Ni–16Cr alloy at different potentials for 12 h is presented in Figure App. 3. The binding energies corresponding to the different sorts of the chemical elements can be found in Table App. 1.

For the XPS spectra of Cr 2p3/2 of passive film formed for 12 h for each potential, the portion of Cr_2O_3, $Cr(OH)_3$ and CrO_3 at potential of -0.1 V vs MSE are 58%, 42% and 0, at potential of 0.1 V vs MSE are 47%, 43% and 10%, and at potential of 0.4 V vs MSE are 40%, 57% and 3%. While for the XPS spectra of Cr 2p3/2 of passive film formed during potentiostatic polarization test, the portion of Cr_2O_3, $Cr(OH)_3$ and CrO_3 at potential of -0.1 V vs MSE are 36%, 64% and 0, at potential of 0.1 V vs MSE are 52%, 43% and 5%, and at potential of 0.4 V vs MSE are 33%, 52% and 15%. It is obvious that with long term anodic potential applied on alloys in passivation domain, there are more chromium oxide because of dehydrate effect. Meanwhile, there are more CrO_3 kept in the passive film at 0.4 V vs MSE during potentiostatic polarization test due to less polarization.

For the XPS spectra of Ni 2p3/2 of passive film formed for 12 h for each potential, the portion of NiO, and $Ni(OH)_2$ at potential of -0.1 V vs MSE are 55% and 45%, at potential of 0.1 V vs MSE are 24% and 76%, and at potential of 0.4 V vs MSE are 57% and 47%. While for the XPS spectra of Ni 2p3/2 of passive film formed during potentiostatic polarization test, the portion of NiO, and $Ni(OH)_2$ at potential of -0.1 V vs MSE are 57% and 42%, at potential of 0.1 V vs MSE are 60% and 40%, and at potential of 0.4 V vs

MSE are 18% and 82%. It is found that the transformation of oxide to hydroxide because of long term polarization is less obvious. However, it is interesting to see that there is much more $Ni(OH)_2$ formed in the first place of polarization. It could conclude that nickel hydroxide hinders a further dissolution of chromium and have transform to nickel oxide at secondary passivation domain.

For the XPS spectra of O 1s, the change of $O2^-$ and OH^- portion is almost in accordance with the fitted results from Cr 2p3/2 and Ni 2p3/2.

Appendix C. Evolution of interpreted parameters of GILPHY 80

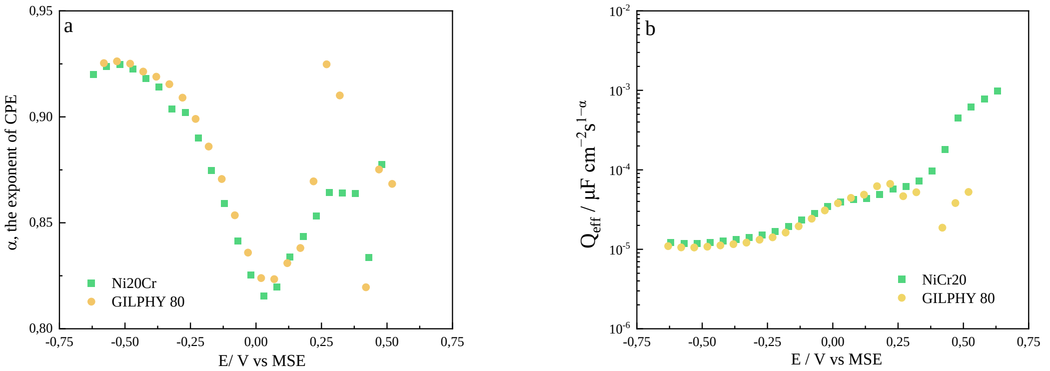

Figure App. 4 Evolution of CPE parameters (a) α and (b) Q_{eff} with potential for NiCr20 and GHILPHY 80 in aerated solution of 0.05 M H_3BO_3 + 0.075 M $Na_2B_4O_7$ $10H_2O$ (pH=9.2).

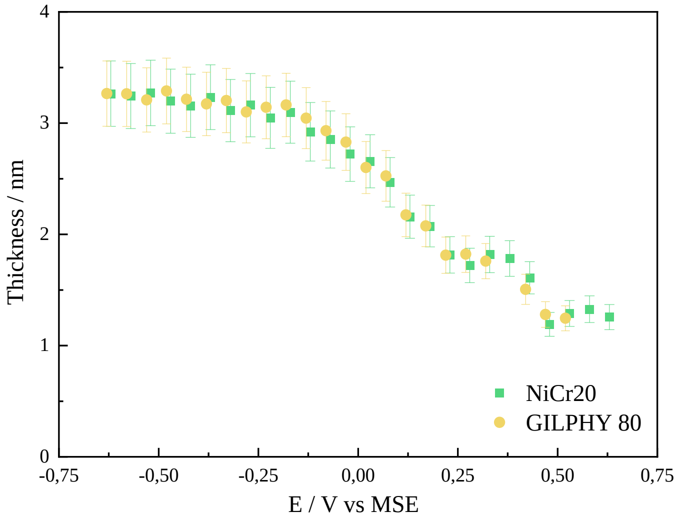

Figure App. 5 Evolution of thickness of NiCr20 and GILPHY 80 in aerated solution of 0.05 M H_3BO_3 + 0.075 M $Na_2B_4O_7$ $10H_2O$ (pH=9.2).

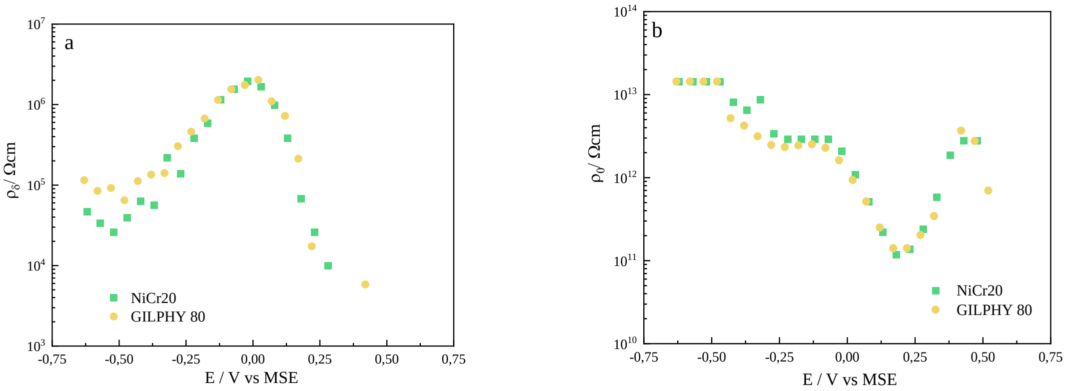

Figure App. 6 Evolution of resistivity a) ρ_0 and b) ρ_δ of NiCr20 and GILPHY 80 in aerated solution of 0.05 M H_3BO_3 + 0.075 M $Na_2B_4O_7$ $10H_2O$ (pH=9.2).

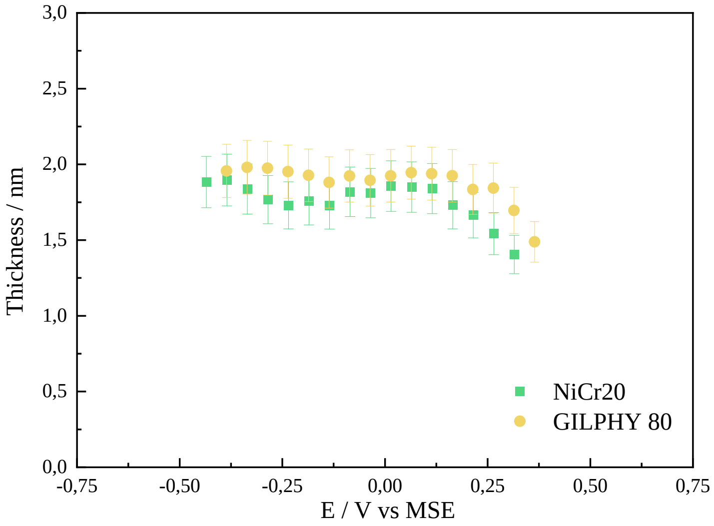

Figure App. 7 Evolution of thickness of NiCr20 and GILPHY 80 in aerated solution of 10 g/L Na_2SO_4 with H_2SO_4 (pH=2).

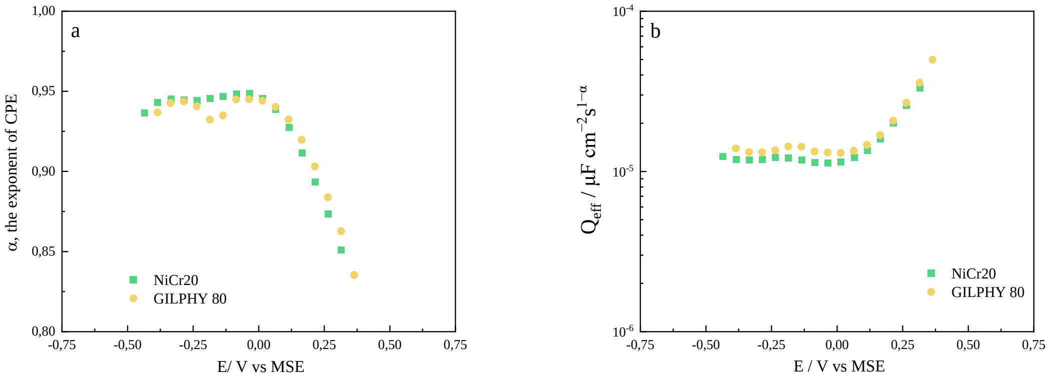

Figure App. 8 Evolution of CPE parameters (a) α and (b) Q_{eff} with potential for NiCr20 and GHILPHY in aerated solution of 10 g/L Na_2SO_4 with H_2SO_4 (pH=2).

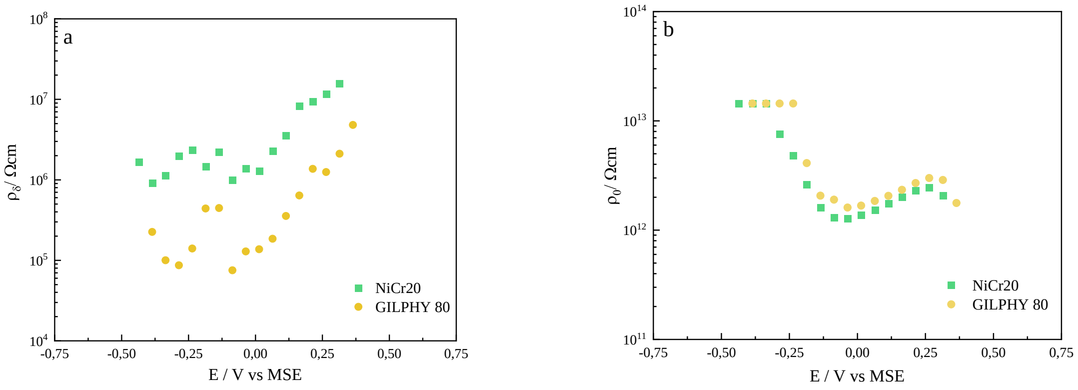

Figure App. 9 Evolution of resistivity a) ρ_0 and b) ρ_δ of NiCr20 and GILPHY 80 in aerated solution of 10 g/L Na_2SO_4 with H_2SO_4 (pH=2).

FOLIO ADMINISTRATIF

THESE DE L'UNIVERSITE DE LYON OPEREE AU SEIN DE L'INSA LYON

NOM : ZHANG DATE de SOUTENANCE : 19/07/2021

Prénoms : Zhiheng

TITRE :
Determination and understanding of the role of alloying elements on the passive behavior of Ni-based alloys by electrochemical investigation

NATURE : Doctorat Numéro d'ordre : 2021LYSEI050

Ecole doctorale : L'École Doctorale Matériaux de Lyon

Spécialité : Science et génie des matériaux

RESUME :

Les alliages base nickel sont largement utilisés dans divers domaines d'application, tels que le pétrole et le gaz, le nucléaire et la chimie, grâce à leur excellente résistance à la corrosion et leurs bonnes propriétés mécaniques à haute température. Dans le but de prolonger la durée de vie de certains composants stratégiques, de nombreuses études sur l'influence des éléments d'alliage sur les propriétés et la résistance à la corrosion des alliages base nickel ont été réalisées ou sont toujours en cours. Dans ce cadre, l'objectif principal de cette thèse est de développer une méthodologie basée sur la caractérisation et l'analyse électrochimique permettant de comprendre l'effet des éléments d'alliage sur les propriétés du film passif des alliages base nickel. La méthodologie proposée se base sur des mesures successives de spectroscopie d'impédance électrochimique et sur une analyse approfondie des diagrammes d'impédance, permettant de suivre l'évolution des propriétés du film passif formé sur différents alliages binaires (Ni-Cr) et ternaires (Ni-Cr-Fe) à différents potentiels. Les diagrammes d'impédance obtenus ont été interprétés avec une méthode graphique avancée et ajustés par le modèle en loi de puissance fournissant ainsi des informations caractéristiques du film passif. Cette méthodologie permet ainsi de déterminer et d'obtenir des informations complémentaires aux traditionnelles courbes de polarisation, telles que l'évolution de l'épaisseur du film et des profils de résistivité au travers de son épaisseur. Cette méthodologie a aussi été appliquée à des alliages commerciaux. Leurs réponses ont été comparées à celles obtenues pour les alliages binaires ou tertiaires dont les compositions sont les plus proches afin de mettre en évidence quels sont les paramètres microstructuraux ou chimiques les plus discriminants. Dans ce travail, le rôle des éléments d'alliage, en particulier le chrome et le fer, sur les propriétés et la réactivité du film passif a été étudié. Comprendre comment les éléments d'alliage agissent sur la nature, la structure et les propriétés du film passif fournira quelques lignes directrices aux ingénieurs et scientifiques pour la conception ou le choix des alliages les plus adaptés.

MOTS-CLÉS : Alliages à base de Nickel; Passivation; Spectroscopie d'Impédance Electrochimique

Laboratoire (s) de recherche : MatéIS

Directeur de thèse: Bernard Normand

Président de jury : MARCUS, Philippe

Composition du jury :

BOJINOV, Martin	Professeur des Université – University of Chemical Technology and Metallurgy	
PEBERE, Nadine	Directrice de Recherche – CNRS(CIRIMAT)	
MARCUS, Philippe	Directeur de Recherche – CNRS(Chimie ParisTech)	
COUET, Adrien	Maître de Conférences – University of Wisconsin–Madison	
NORMAND, Bernard	Professeur des Université – INSA de Lyon	Directeur de thèse
TER-OVANESSIAN, Benoît	Maître de Conférences – INSA de Lyon	Co-directeur de thèse
MARCELIN, Sabrina	Ingénieur – INSA de Lyon	Invitée